

THE UNIVERSITY OF HULL

**Computer Simulations of
Hybrid Aligned Nematic Liquid Crystal Cells
and Liquid Droplets**

being a Thesis submitted for the Degree of PhD

in the University of Hull

by

Nicola. T. Kirkman, BSc.

May 2004

Dedicated to:

Dr Thomas Stirner, for his continuing help and support;
Disabilities Services, in particular Avril Johnson and Peter
Robinson, for a myriad of reasons;

My parents, for not questioning that I would finish;

My students, for giving me practice at proof reading and an
excellent reason to practice what I preach;

Prof Winston Hagston, for his additional help with some of the
maths;

EPSRC, for their financial support;

And my friends,

in particular Tom Aitken, Peter Adman, Norma Romm, Mary
Precious and Anita Hunter,
for more of the same and everything else.

Preface

This thesis is divided into two parts. The common denominator connecting these two parts is that they both involve computational modelling approximating real systems. However, these two chapters investigate two very different types of systems: the first is a liquid crystal cell and the second is a simple monatomic liquid droplet. Parts of this thesis have been published in *Liquid Crystals*, Vol. 30, No. 9, September 2003, 1115-1122, N. T. Kirkman, T. Stirner and W. E. Hagston, "Continuum modelling of hybrid-aligned nematic liquid crystal cells: optical response and flexoelectricity-induced voltage shift" and presented at the XI Workshop on Computational Materials Science, Cagliari/Italy, September 17-23, 2001, N. T. Kirkman, "A new method for investigating the surface tension from molecular dynamics simulations applied to liquid droplets" which has since lead to its publication: N. T. Kirkman, T. Stirner and W. E. Hagston, A new method for investigating the surface tension from molecular dynamics simulations applied to liquid droplets, *Comp. Mater. Sci.*, Vol. 30, 126 (2004)

Abstract

1. Continuum Modelling of Hybrid Aligned Nematic Liquid Crystal Cells

Hybrid Aligned Nematic (HAN) cells provide an interesting tool to investigate liquid crystalline properties, such as flexoelectricity. They are Liquid Crystal Devices (LCDs) that employ two different alignment layers to produce distortions in the director profile across the cell. As a result of their geometry, they exhibit some unusual properties. These can be examined experimentally by investigating the transmittance of light through these cells as a function of voltage.

There are two main foci of this work, the first is to perform a theoretical study of how the different physical and optical parameters affect the behaviour of the cells. In the process, we also hope to gain an understanding of why these parameters exert such influences. The second motivation for this study is to see if this model can reproduce the experimental transmittance curves and if these curve fits can be gained using meaningful input parameters. From this we would be able to obtain values for the flexoelectric coefficient e ($= e_{11} + e_{33}$). Previous to this study there have been numerous attempts to find the flexoelectric coefficient. However, we doubt the validity of many of these findings: a preliminary investigation revealed that this was a rich area of study and without further investigation previous results might not only be superficial but also erroneous.

These input parameters are employed in a continuum model of the system, using the finite difference method (performed using C on a UNIX workstation). Having initially employed a self consistent method (adhering to Takahashi et al. [Jpn. J. Appl. Phys. **37**, 1865 (1998)]) to find solutions to the partial differential equations used to describe this system we found that it resulted in non-physical solutions. To overcome this problem we propose, and then use, a new method in which the variables remain coupled throughout. In the course of our investigations the new method was examined extensively and, as a result, we have confidence in the physicality / validity of the solution curves resulting from our simulations.

Having divided the results section of this chapter into two, firstly, we shall look at the major findings of the theory section. In this section there are three major findings. The first is unsurprising, finding that increasing birefringence or cell thickness increases the phase difference accumulated across the cell. The second pertains to the elastic constants, finding that the one-constant approximation is ill-advised, unless the choice of K is closer to the bend elastic coefficient, K_{33} , and only then if one is restricting the examination to the magnitude of the flexoelectric voltage shift. The third and final finding relates to the interaction between the parameters dielectric anisotropy, $\Delta\epsilon$, flexoelectric coefficient, e , and homeotropic anchoring energy, A_{θ} . While, when the homeotropic anchoring energy is large the flexoelectric voltage shift is proportional to the size of the flexoelectric coefficient (where the constant of proportionality is largely governed by the sign and magnitude of $\Delta\epsilon$), when the homeotropic anchoring energy is reduced other (non-linear) trends are observed. Reducing the homeotropic anchoring energy

(for $e \neq 0 \text{ C m}^{-1}$) introduces asymmetries into the transmittance curves; the nature of these asymmetries is dictated by the sign of $\Delta\epsilon$. As a result of the asymmetries, the flexoelectric voltage shifts can cease to be a guide to both the magnitude and (more alarmingly) the sign of the flexoelectric coefficient, in particular when $\Delta\epsilon$ is negative.

The major findings from curve fitting experimental results are that we are generally able to reproduce the experimental curves using this model and that these curve fits provide reasonable values for the input parameters. The fitting parameters for the E7 systems [K. Bartle, PhD Thesis, Hull University, Hull, 2003] are shown below.

Curve fitting parameters used for the E7 systems, where the JHW materials are dopant materials dissolved (10% by weight) in E7.

	D μm	$\Delta\epsilon$	A_{ω} $\times 10^{-6} \text{ Jm}^{-2}$	$\times 10^{-11} \text{ Cm}^{-1}$
E7	27.5 ± 0.5	13.8	9.0 $3.0 < A_{\omega} < 9.0$	0.0 ± 0.5
JHW29	16.9 ± 0.5	15.8 ± 0.5	5.0 $3.0 < A_{\omega} < 10.0$	-1.0 ± 1.0
JHW33	18.0 ± 0.5	13.8 ± 0.5	5.0 $3.0 < A_{\omega} < 10.0$	-0.5 ± 1.0
JHW131	17.4 ± 0.5	8.8 ± 0.5	5.0 $3.0 < A_{\omega} < 10.0$	-0.5 ± 0.5
JHW172	26.6 ± 0.5	7.8 ± 0.5	5.0 $3.0 < A_{\omega} < 10.0$	0.0 ± 0.5

We find that, for all these systems, the flexoelectric coefficients and the homeotropic anchoring energies are small. While we are unable to obtain a meaningful curve fit for Takahashi's MBBA data we believe the same is true of this system, i.e. e and A_{ω} are small.

Our studies examine systems with positive and negative dielectric anisotropies. Along with varying other input parameters, this provides a comprehensive, near to exhaustive, study of the behaviour of these systems. Many of the properties of these systems can be (and are) explained using this model.

2. Calculating the Surface Tension of Sub-Microscopic Liquid Droplets for Lennard-Jones Fluids.

Surface tension is an interesting macroscopic phenomenon with microscopic origins. Its technological applications are wide ranging, from aerosols, through waterproofing, to producing good electrical contacts.

Being able to model and interpret the surface regions of liquids can have many theoretical, practical and potential technical applications. Surface tension is such an important phenomenon technologically that being able to predict its value for new systems can avoid the expenses of producing unfruitful systems. Having the capability

to predict how the size of droplets can affect a material's properties (e.g. surface tension, rates of evaporation, density), can provide an important tool for designing such systems as aerosols. Also, being able to define the surface region opens a direct route via which contact angles, important in describing wetting phenomena, can be calculated.

Having found numerous limitations to previous methods we propose a new model here. Our method treats a liquid as a potential well, finding a meaningful definition of the surface region; then the energy required to remove a particle from the surface to infinity (as a function of surface area) is calculated. This provides a measure of surface tension.

This is the general version of our theory; from this it can be seen that this theory is easily adaptable to a wide range of different systems. For several reasons we choose to apply this theory to small, spherical Lennard-Jones 12-6 droplets. The reasons for choosing small (of radii circa 4 nm) droplets are twofold. Firstly, it is interesting from the aspect of examining how surface tension varies for aerosol sized droplets and, secondly, smaller systems are less time consuming than larger systems computationally. The choice to examine spherical systems was their prevalence and their technological importance: free of external forces or constraints, liquids tend to coalesce to form spheres; consequently, this geometry is relevant to a wide range of systems, including aerosols. And finally, the reasons for choosing to use a Lennard-Jones pair potential are that firstly it is simple, therefore computationally undemanding, and secondly that, in addition to providing an accurate approximation to the Van der Waals interactions of noble gases, it is necessary to compare the results from our method with those of other researchers, of which there are numerous available in the literature for this pair potential, in order to test the validity of our new method.

Molecular Dynamics is employed to create and equilibrate the spherical droplets. The positional data is then used to calculate the forces and energies on the particles.

While this method needs honing, principally by averaging over a greater number of data sets and over longer periods of time, in order to reduce statistical fluctuations, this method produces results that are consistent with the predictions of thermodynamical and statistical dynamical models. For example, the model predicts there was a reduction in surface tension for both decreasing radius of a droplet and increasing temperature. We are also able to infer a phase transition between 30 and 40 K, in agreement with the molecular dynamic simulations of Rusanov and Brodskaya [J. Colloids Interf. Sci. **62**, 543 (1977)].

Contents

page
number

1	Continuum Modelling of Hybrid Aligned Nematic Liquid Crystal Cells	1
1.1	Introduction.	1
1.2	What are Liquid Crystals?	3
1.3	Liquid Crystal Properties	8
1.3.1	Steric Effects	8
1.3.2	Elasticity	12
1.3.3	Dielectric Properties	14
1.3.4	Flexoelectricity	15
	<i>Summary</i>	17
1.3.5	Birefringence	18
1.4	Wave Plates	20
1.5	Liquid Crystal Devices	24
1.5.1	Twisted Nematic, TN.	26
1.5.2	Super Twisted Nematics, STN.	26
1.5.3	Ferroelectric LC Cells	28
1.5.4	Hybrid Aligned Nematic, HAN, Cells.	29
1.6	Experimental Set-Up	30
1.6.1	Takahashi's Experimental Set-Up	30
1.6.2	K. Bartle's Experimental Set-Up	31
1.7	Continuum Modelling	34
1.8	Computer Simulation - Finite Difference Method	38
1.8.1	Takahashi's Method	39
1.8.2	Our New Method	41
1.8.2.1	Flexoelectric Voltage and the Flexoelectric Voltage Shift	44
1.8.2.2	Boundary Conditions	46
1.8.3	Flow Diagram describing how the program is executed.	48
1.8.4	Phase Difference and Transmittance	49

1.9	Results and Discussion	51
1.9.1	Theory and Trends	54
1.9.1.1	Introduction to figure types	57
1.9.1.2	Varying cell thickness, D	59
1.9.1.3	Varying birefringence, Δn	62
1.9.1.4	Varying elastic constants, K_{11} and K_{33}	65
1.9.1.4.1	When flexoelectric coefficient small,	66
1.9.1.4.2	When flexoelectric coefficient large,	75
1.9.1.5	Varying angles of easy axes, θ_{easy}	84
1.9.1.5.1	Homeotropic angle of easy axis,	84
1.9.1.5.2	Homogeneous angle of easy axis,	86
	θ_{Deasy}	
1.9.1.6	Varying flexoelectric coefficient, e	88
1.9.1.6.1	Large homeotropic anchoring energy	89
1.9.1.6.2	Medium homeotropic anchoring energy	92
1.9.1.6.3	Small homeotropic anchoring energy	95
1.9.1.7	Varying homeotropic anchoring energy, A_{θ}	99
1.9.1.7.1	Negative Dielectric Anisotropy	100
1.9.1.7.2	Positive Dielectric Anisotropy	102
1.9.1.8	Varying Dielectric Anisotropy, $\Delta\epsilon$	104
1.9.1.8.1	General effect of varying $\Delta\epsilon$	104
1.9.1.8.2.1	Effect of varying $\Delta\epsilon$ for MBBA	107
1.9.1.8.2.2	Effect of varying $\Delta\epsilon$ for E7	108
1.9.1.9	Varying homeotropic anchoring energy and flexoelectric	109
1.9.1.9.1	For MBBA, i.e. negative $\Delta\epsilon$	109
1.9.1.9.2	For E7, i.e. positive $\Delta\epsilon$	110
1.9.1.10	Summary and Conclusion	111
1.9.2	Experimental Results sections	115
1.9.2.1	Introduction	115
1.9.2.2	Normalising the curves	118
1.9.2.3	Simulations	123

	1.9.2.3.1	E7	125
	1.9.2.3.2	Curve fits and discussion of the 10% solutions	131
		Molecular modelling	140
	1.9.2.3.2	Parameter fitting for MBBA and Discussion.	144
	1.9.2.4	Conclusion to experimental curve fitting	152
1.10	Conclusion		156
1.11	Further Work		158
	Bibliography		159
2	A New Method for Investigating Surface Tension of Liquid Droplets from Molecular Dynamics Simulations.		162
2.1	Introduction		162
2.2	Historical background		168
	2.2.1	Thermo-dynamical Theories	168
	2.2.2	Quasi-Thermodynamical Theories	170
		2.2.2.1 Gibbs' Theory	170
		2.2.2.2 Van der Waals' Theory	172
	2.2.3	Statistical Mechanics	173
2.3	New Theoretical Method		178
2.4	Computer Simulation Details		179
	2.4.1	The System.	179
	2.4.2	The Pair Potential.	180
		2.4.2.1 Creating Spherical Droplets.	181
		2.4.2.2 Running the Molecular Dynamic Simulations.	181
		2.4.2.3 Analysing the Droplets.	182
		2.4.2.4 Calculating Density Profiles.	183
		2.4.2.5 Calculating Forces and Energies	184
		2.4.2.6 Calculating Radial Averages.	185
		2.4.2.7 Calculating Temporal Averages.	186

2.4.2.8	Implementation on Computer: The Program	186
	Density	188
	Energies and Forces	188
	Spatial averaging	188
2.4.2.9	Calculating Surface Tension.	190
2.4.2.10	<i>Density Profile fitting (tanh-Fitting)</i>	192
2.5	Results and Discussion	197
2.5.1	Surface Tension in Relation to Temperature and N .	197
2.5.2	Surface Tension in Relation to Temperature and Surface of Tension, r_s .	200
	Comparing Radii for Different Sized Droplets:	203
	Comparing Surface Energies for Different Sized Droplets:	203
2.6	Conclusions	204
2.7	Further work	204
	Bibliography	206

APPENDICES:

A.	The Frank energy density	206
B.	Derivation of the Free Energy density for the HAN cell	210
C.	Energy Minimising the Laplacian	213
D.	Anchoring Energies	217
E.	Self consistent method	221
F.	Infinite Anchoring Energies Case	222
G.	Takahashi's In-Plain Device Formalism	224
H.	Relationship between Dipole Moments, Permittivities and Order Parameters	226
I.	Parameters used in Normalization of Experimental Data For HAN Cells	230
J.	Ansi C code used to solve PDEs	231
K.	The Equimolar surface	238
L.	Exponential Regression on Temperature versus Surface Tensions Graph	240
M.	Ansi C code used to on Cerius ² output data for 10 sets of Droplet Data.	244

Chapter 1

Continuum Modelling of Hybrid Aligned Nematic Liquid Crystal Cells

1.1 Introduction

This chapter will investigate hybrid aligned nematic liquid crystal cells (HAN cells) using a continuum method. HAN cells are interesting liquid crystal devices as, among their traits, they utilise a linear electro-optic effect [1, 2]. There are two main objectives of modelling this system (performed using a UNIX workstation). The first of these is to investigate whether the effects (theoretically) of varying input parameters alters the optical behaviour of such cells, in order to gain understanding of the effects of each parameter. The second purpose is to see if it possible to produce simulations that emulate experimental data obtained from existing HAN cells. The results section is divided into two subsections to reflect these two objectives.

Previous work in this area has focused on the effects of changing the flexoelectric coefficient, e ($= e_{11} + e_{33}$) and was employed to isolate the flexoelectric effect from elastic and dielectric effects. We challenge this viewpoint and suggest an alternative procedure to evaluate the flexoelectric effect. We also discuss how the findings of continuum modelling can be employed to design new liquid crystal devices with specific properties.

Continuum modelling is a well-established mathematical modelling method used to describe such systems. In this work a new method of finding numerical solutions to partial differential equations (PDEs) for HAN cells is proposed.

Before revealing this new method, it is important to have a general grounding in this subject area. Describing what liquid crystals are, expounding on some of their applications (e.g. devices), and discussing their physical properties (such as birefringence and flexoelectricity), will therefore be presented prior to describing the mathematical and computational tools necessary to find numerical solutions to the PDEs that will be used to model this system.

1.2 What are Liquid Crystals?

The term 'liquid crystal' (LC) is used to describe several states of matter, and the materials that exhibit one or more of them. They are similar to other liquids in that the molecules are relatively free to move, and so the materials possess the ability to flow. However, they are also *unlike* liquids because they exhibit anisotropy in their optical and electro-magnetic characteristics, much like a conventional crystal [3]. LCs are usually organic steric *rod-* or *disk-*shaped molecules [4]; the anisotropy / ordering of the molecules¹ within liquid crystal phases is thought to be due to the packing constraints of the molecules as well as induced dipole interactions (Onsager and Maier-Saupe theory)[3].

There are two main types of liquid crystals, lyotropic and thermotropic LCs. If transitions between the phases are governed by temperature the material is thermotropic. If, in mixtures of two or more different components, the phase transitions are governed by the concentration of an isotropic mixture component then the liquid crystals are called lyotropic [4].

Lyotropic liquid crystals are 'mixtures' of two or more semi-immiscible materials. The materials separate to form structures (with both short range and long range order) that allow them to coexist within a volume. They are prevalent in biological organisms as they can be utilized to form selectively permeable membranes, such as those found in cell walls. Examples of how the structures are formed in two and three-component lyotropic mixtures (for example in an ordered cubic phase) are shown below, in figure (1.1) (*a* and *b* respectively).

¹ For example the average direction of the long axes of rod-shaped molecules may align parallel with one another.

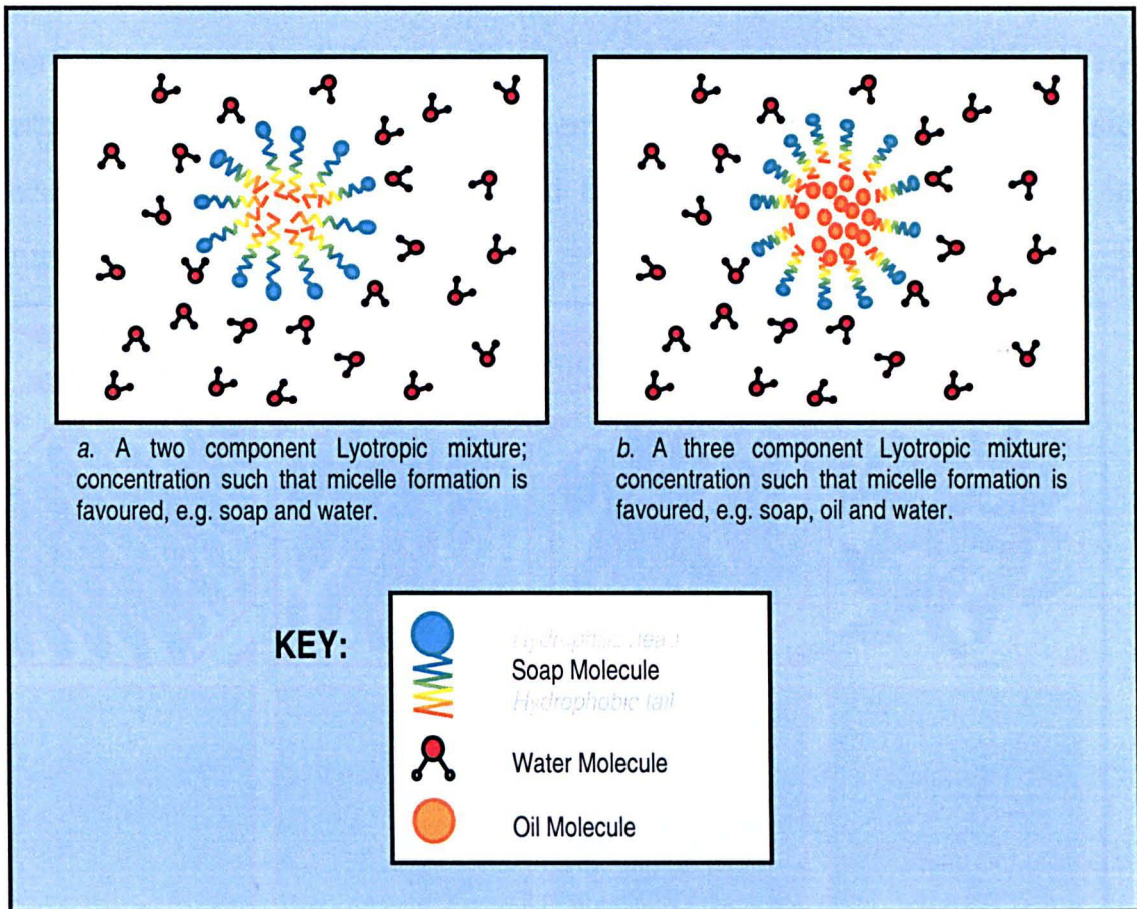


Figure 1.1: Different concentrations result in different structures to be favoured. Examples of these can be found in *The lyotropic state of matter: molecular physics and living matter physics*. [5].

The structures shown in figure (1.1) are called *micelles*; different concentrations of the constituent parts would result in different structure formations (e.g. lamina).

Thermotropic LCs however exhibit ‘*truer*’ liquid crystal mesophases, where the phase transitions are temperature dependent, occurring at temperatures intrinsic to a given material. Thermotropic LC phases may occur in pure substances or in mixtures of miscible ones. It is thermotropic liquid crystals that are employed in liquid crystal devices (LCDs), e.g. HAN cells.

There are several different liquid crystal mesophases exhibited by thermotropics; the main two are nematics and smectics². These basic phases (in relation to crystalline and liquid phases) are shown below in figure (1.2).

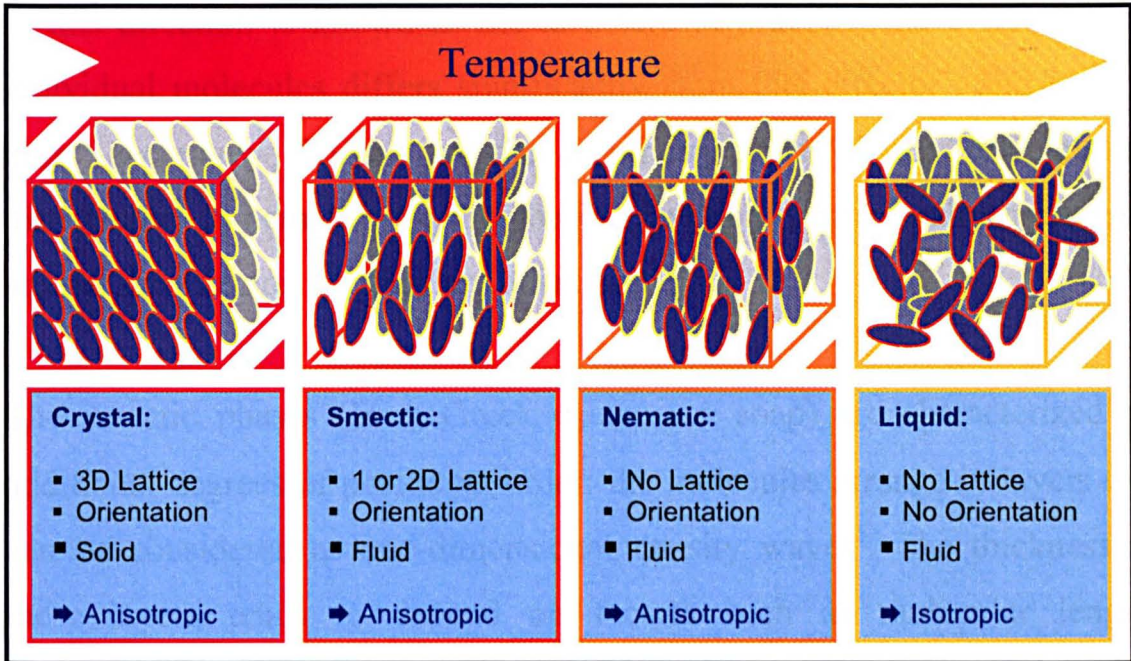


Figure 1.2: Shows the basic phase transitions that may occur between crystal and liquid. N.B. Not all materials exhibit liquid crystalline phases and not all LCs exhibit all the liquid crystalline mesophases either.

Nematic liquid crystals acquired their name from the Greek νημος meaning *thread*, due to the thread-like textures³ observed under a polarizing microscope [4]. An example of a typical nematic texture can be seen in figure (1.3) below:



Figure 1.3: Example of nematic Schlieren texture: often observed when viewing nematics through cross polarisers. The thread-like *structures* are not actually present in the material, but are artefacts due to defects and viewing the sample through cross polarisers. Despite the absence of real threads, these thread-like artefacts gave rise to the name 'nematics', from the Greek meaning "thread". [6 - 8]

² These are further divided into numerous subcategories, e.g. smectic A and smectic C [8].

³ Due to defects in the liquid crystalline structure, see Schlieren defects [8, 9].

In nematics there is no ordering of the molecular centres of mass but there is a general ordering of their orientation. The molecules of nematic LCs tend to have a long axis (for example they may be rod-shaped molecules) and these long axes tend to line up in a particular direction. The unit vector in this direction is known as the *director*. In practice, the orientation of individual molecules differs significantly from this director⁴, and so it is more accurately defined as the symmetry axis of the orientational distribution. In nematics the distribution function is rotationally symmetric around the director, i.e. they are uniaxial [4].

The smectic phases (from Greek $\sigma\mu\epsilon\gamma\mu\alpha$ = soap) are characterized by additional degrees of positional order: the molecules arrange in layers that can be considered as one-dimensional density waves⁵. The thickness of these layers tends to depend on factors such as molecular length, temperature of the medium, etc. [10]. Because liquid crystal displays made with Chiral Smectic C materials exhibit better viewing angle characteristics, contrast ratios and can operate at high speed, they have potential advantages over nematics [3].

⁴ This has led to the need to have a quantitative description of *how* ordered a nematic liquid crystal is; the equation that has allowed us to do this is called the 'Order Parameter', S . One of the forms it takes is this:

$$S = \frac{1}{2} \langle (3 \cos^2 \theta - 1) \rangle$$

where θ is the angle a molecule's long axis makes with the director, and $\langle \rangle$ denotes the average found for all the molecules. If all the molecules are aligned $S = 1$, if the medium is isotropic $S = 0$.

⁵ "This positional ordering may be described in terms of the density of the centres of mass of the molecules using the following equation:

$$\rho(z) = \rho_0 (1 + \psi \cos(2\pi z/d))$$

where z is the coordinate parallel to the layer normal, the average density of the fluid is ρ_0 , d is the distance between layers and ψ is the order parameter. When $|\psi|=0$ there is no layering and the material is nematic but if $|\psi|>0$ then some amount of sinusoidal layering exists and the material is smectic." [3]

The hybrid aligned nematic liquid crystal cell, as the name implies, utilizes thermotropic liquid crystals in their nematic mesophase temperature range. For this reason this thesis will limit its examination to thermotropic liquid crystals. Before liquid crystal devices are examined in detail (in particular HAN cells), an appreciation of some of their physical and optical properties is desirable. These properties are dealt with in sections 1.3 and 1.4.

1.3 Liquid Crystal Properties

In this section, we detail some of the interesting properties of liquid crystalline materials that make them appropriate for electro-optic devices. We introduce: steric effects, including chirality, elastic properties, dielectric properties, flexoelectricity and finally, birefringence. Then, in section 1.5 (after a brief examination of wave plates in section 1.4), we provide examples of liquid crystal devices showing how they utilise these properties in various ways to produce effective electro-optic devices.

1.3.1 Steric Effects

Molecules have physical shape; in the case of liquid crystal molecules, this physical shape tends to be roughly rod or disc-like. It is believed that these shapes result in packing constraints [11] which gives rise to the various liquid crystalline phases being possible; these are known as 'steric effects'. However, it should be noted that not all rod and disc-shaped molecules exhibit liquid crystalline phases, so steric effects are not the only contributing factor determining the presence of such LC mesophases.

Steric effects can also contribute to such phenomena as chirality and flexoelectricity (see below).

Chirality

Chirality is a *handedness* quality possessed by some molecules. If there is an atom that is able to bond with four⁶ other atoms/groups of atoms, chirality may occur. However, chirality *only* occurs when these four atoms/groups of atoms are different from one another. Such an atom is

⁶ Mathematically any number greater than three would result in permutations allowing 'handed' molecules; the number four is specified here because group IV elements, such as carbon, are of interest here and not transition metal complexes.

called a *chiral centre* (we identify this by a star, *) and an example of left and right-handed permutations about a chiral centre is shown below in figure (1.4).

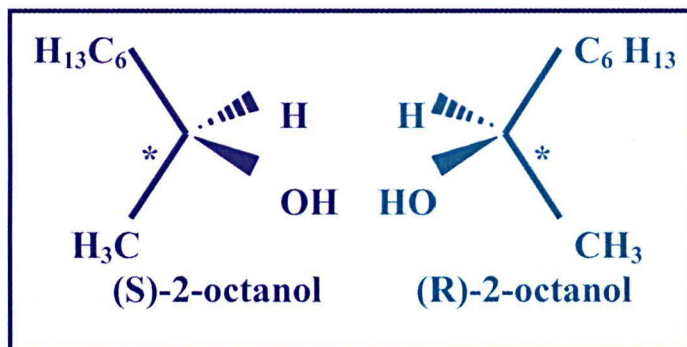


Figure 1.4: Chiral centres are identified by a star *, as are chiral molecules [9]

Chiral molecules are conventionally identifiable by a star beside their name.

While chirality results in interesting optical properties even in isotropic fluids, it is of particular interest in liquid crystals as it results not only in an optical handedness but also (obviously) in a *physical* handedness. This has steric implications: it becomes energetically more favourable for these molecules to line up at some angle to their neighbouring molecules, instead of parallel to them. As this angle is in one direction, rather than both directions, helical 'structures' are formed.

In the case of nematic liquid crystals this helical structure occurs at right angles to the molecules' long axis, see fig (1.5) below

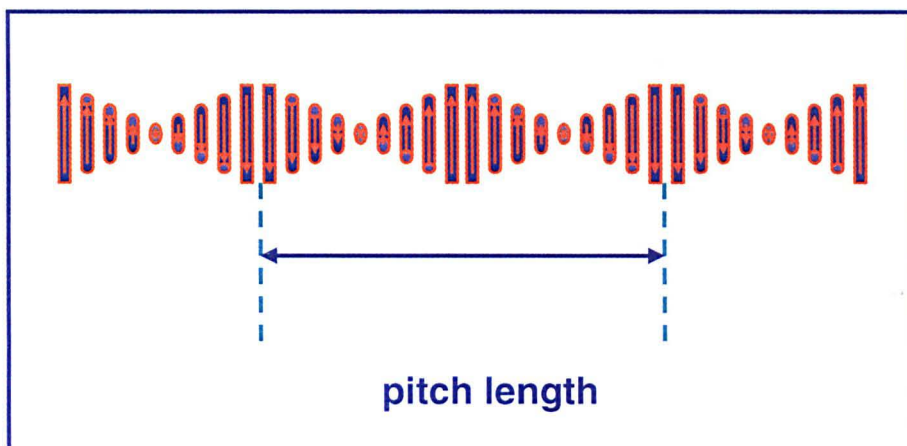


Figure 1.5: Shows a simplified representation of the helical structure formed by chiral nematic (N^*) liquid crystals.

where the pitch length is the length corresponding to the length of the repeat unit of the helix. Chiral nematics are also called *cholesterics*.

In chiral smectic phases, e.g. chiral smectic C, ($Sm C^*$), the helical structure is oriented along the axis normal to the smectic layers, as shown in figure (1.6),

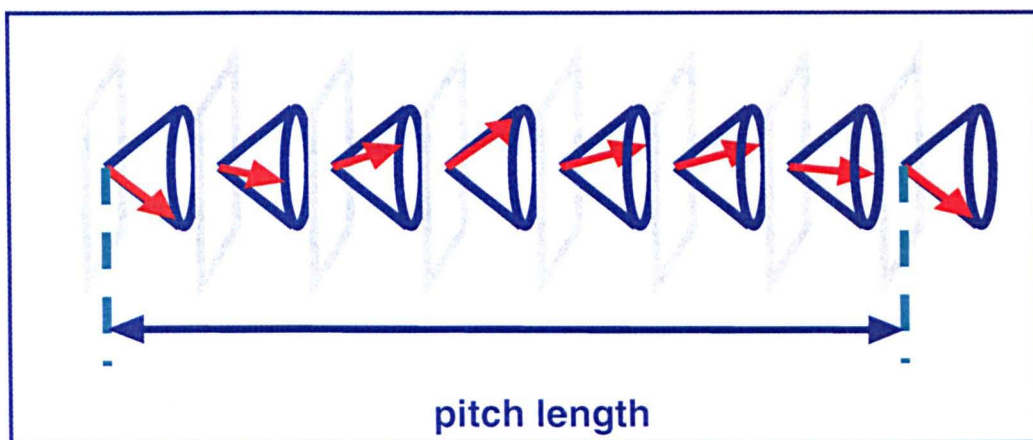


Figure 1.6: Shows a schematic representation of a single pitch length of a chiral smectic helix.

where the blue cones represent the angles of easy axis of the molecules with respect to the smectic planes, depicted by the grey parallelograms. The red arrows show the statistical average director orientation for a given smectic plane.

The helices above do not only demonstrate different chiral liquid crystal types they also demonstrate the two types of handedness: the nematic helix is right handed and the smectic helix is left handed in these two figures. These different types can be distinguished by thinking in terms of left and right-handed corkscrews (see figure (1.7))

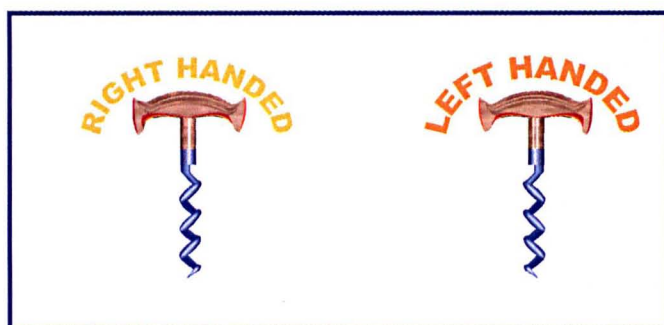


Figure 1.7: Shows right and left-handed corkscrews respectively.

In both chiral smectic and chiral nematic liquid crystals, the pitch length shows a temperature dependency [12].

It should be noted that if a material that does not exhibit chirality is required, then either a material with no chiral centres must be used or a 50:50 mixture of right-handed and left-handed species of a given molecule (known as racemic) must be used.

Chiral nematics are called cholesterics, so when we are referring to nematics, the reader may assume that we are referring to either achiral or racemic nematic liquid crystals. The importance of this distinction becomes apparent in the section about elastic properties of nematic LCs.

1.3.2 Elasticity

In nematic liquid crystals the director orientations n and $-n$ are indistinguishable. If a molecule shape can be approximated by a cylinder, for example due to complete rotational freedom around its long molecular axis, the phase is uniaxial. Thus, left is indistinguishable from right. As a consequence of this symmetry the energy required to induce a distortion is equal to the energy required to produce its mirror distortion. The equilibrium configuration favours no long-range disorder of the director profile.

The different elastic distortions that can be produced are shown below. In figure (1.8) we see for example how steric properties, e.g. the pear-drop shape, of the molecules may lend themselves to splay distortions.

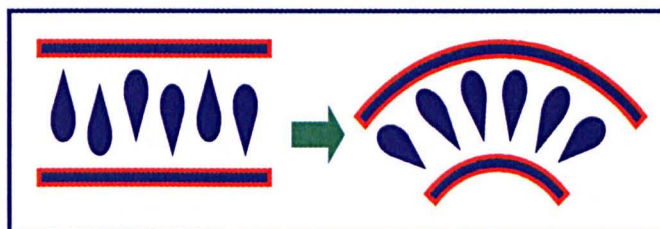


Figure 1.8: Splay deformation

Below, in figure (1.9), it can be seen that the molecules' steric properties, e.g. their banana shape, lend themselves to bend distortions.

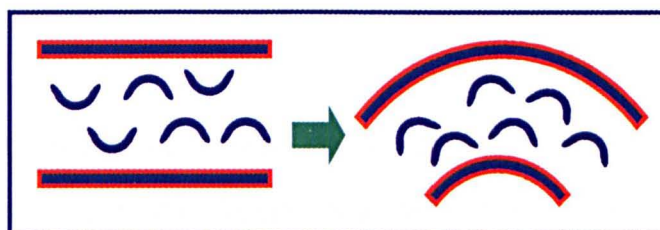


Figure 1.9: Bend deformation

And finally, this dumb-bell shaped molecule (see figure (1.10)) demonstrates how it is possible to have molecules that can be packed in both left and right-handed helices. Under normal circumstances helices would not form in a nematic material. However, by using alignment layers

and rotating them with respect to each other (with a nematic phase between them), it is possible to induce twists up to 90° . In contrast with cholesterics, the pitch length of these helices is not material or temperature dependent but is instead dictated by the choice of alignment layers.

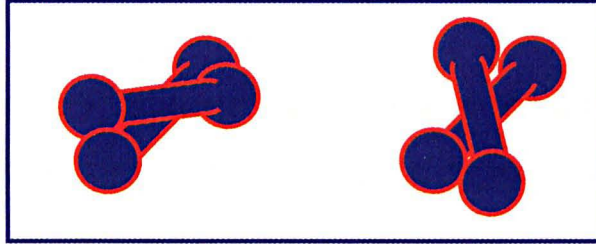


Figure 1.10: Twist deformation

It is also possible to obtain bend-splay deformations but, as this is not a bulk distortion, it is of no consequence here.

For all three cases shown above, it is known that an equilibrate system exhibits *no* net distortions; from this it is possible to deduce that the elastic constant associated with these distortions is positive [8]. Furthermore, from the knowledge that inducing distortions is equally easy in both directions (e.g. bending up is equally easy as bending down), it can be stated that the elastic terms are *even* functions. In continuum modelling, the elastic energy terms can be expressed by the following formula [13]

$$F_{Frank} = \frac{1}{2} K_{11} (\nabla \cdot \vec{n})^2 + \frac{1}{2} K_{22} (\vec{n} \cdot \nabla \times \vec{n})^2 + \frac{1}{2} K_{33} (\vec{n} \times \nabla \times \vec{n})^2 \quad (\text{A.1})^7$$

where the three terms represent the splay, twist and bend deformation of the director field \vec{n} respectively (and where we have ignored the saddle splay elastic deformation for the reason given above). This is known as the Frank expression for the elastic energy density of a deformed nematic LC (see Appendix A).

⁷ If the one constant approximation is used, i.e. ($K_{11} = K_{22} = K_{33} = K$), then equation (A.1) becomes $F_d = \frac{1}{2} K [(\nabla \cdot \vec{n})^2 + (\nabla \times \vec{n})^2]$.

1.3.3 Dielectric Properties

Dielectric anisotropy is a measure of the ease with which a molecule can be reoriented by an electric field \vec{E} . Its origins are the molecular polarity, i.e. the permanent dipole moment, and polarisability of a molecule.

Due to their geometry, nematic liquid crystals are uniaxial mediums, i.e. their dielectric anisotropy can be described in terms of two components: one parallel to the molecular long axis and the other perpendicular to it, ϵ_{\parallel} and ϵ_{\perp} respectively. The dielectric anisotropy is the difference between these components and is given as:

$$\Delta\epsilon = \epsilon_{\parallel} - \epsilon_{\perp}$$

which, in turn, leads to the dielectric component of the energy term via the electric displacement \vec{D}

$$\vec{D} = \epsilon'_{\perp} \cdot \vec{E} + (\epsilon'_{\parallel} - \epsilon'_{\perp}) \cdot (\vec{n} \cdot \vec{E}) \cdot \vec{n}$$

This gives the dielectric free energy density in the form [1, 8]

$$\begin{aligned} F_{diel} &= -\frac{1}{2} \vec{D} \cdot \vec{E} \\ &= -\frac{1}{2} \left[\epsilon'_{\perp} \cdot E^2 + (\epsilon'_{\parallel} - \epsilon'_{\perp}) \cdot (\vec{n} \cdot \vec{E})^2 \right] \\ &= -\frac{1}{2} \left[\epsilon'_{\perp} \cdot E^2 + \Delta\epsilon' \cdot E^2 \cdot \cos^2(\vec{n} \cdot \vec{E}) \right] \\ &= -\frac{1}{2} \epsilon_0 (\epsilon_{\perp} + \Delta\epsilon \cdot \sin^2 \theta) \cdot E^2 \\ &= -\frac{1}{2} \cdot f_{diel}(\theta) \cdot \left(\frac{\partial \phi}{\partial z} \right)^2 \end{aligned}$$

where $f_{diel}(\theta) = \epsilon_0 (\epsilon_{\perp} + \Delta\epsilon \cdot \sin^2 \theta)$, $E = \frac{\partial \phi}{\partial z}$ θ is the polar angle and ϕ is the electrical potential.

1.3.4 Flexoelectricity

In a single crystal domain of an achiral liquid crystal the molecules will naturally tend to orient parallel to a common director as this is energetically and statistically the most favourable configuration. However, if some external force is applied to such a domain, e.g. as could be provided by two different alignment layers or if there are some asymmetries in the molecule, it may become energetically more favourable for the director to orient one way rather than another (see figures from (1.8) to (1.10)). If these molecules also possess dipoles, this reorientation will result in a net polarization of the domain (see figure (1.11) below). This polarization of the liquid crystal is called the flexoelectric polarization.

As the origin of the flexoelectric distortions is external stress it was originally called ‘piezoelectric effect in liquids’ [15]. However this was misleading as pressure cannot result in these distortions in the director profile [14]

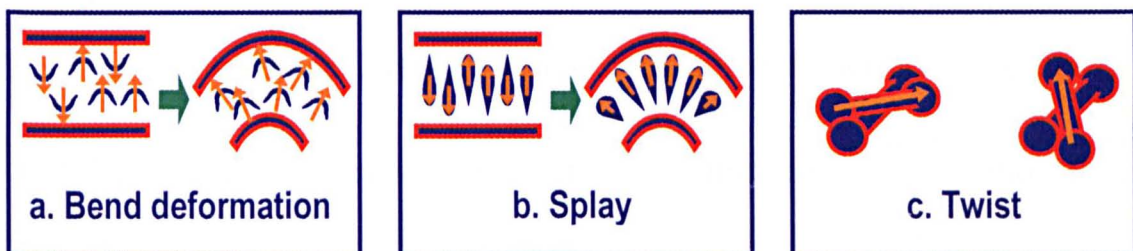


Figure 1.11: Shows how elastic deformations can result in net polarizations of a flexoelectric material.

In the case of twist deformation (due to some external twisting stress being placed on the system) a helical deformation could be induced (left-handed and right-handed helices can be induced with equal ease). This would result in a periodicity in the polarisation of the medium, i.e. no net flexoelectric polarization.

For similar arguments to those presented for elastic deformations (as there is no net flexoelectric polarisation when the system is in its equilibrium state), we can again assume that a flexoelectric function will be zero when the medium is not distorted. Similarly, it will be as easy to induce one distortion as it will be to produce one of equal magnitude but in the opposite direction (i.e. with the dipoles pointing down instead of up); consequently, this distortion will result in the opposite sign of the flexoelectric polarisation of the medium. For this reason we know that the function that will represent the flexoelectric properties of a nematic must necessarily be an *odd* function, rather than the even one used to represent elasticity. In continuum modelling the following expression is used to describe the flexoelectric contribution to the energy term (see Appendix B.3) [16],

$$F_{flex} = -\vec{P} \cdot \vec{E}$$

where the flexoelectric polarisation $\vec{P} = e_{11}(\nabla \cdot \vec{n}) \cdot \vec{n} + e_{33}(\nabla \times \vec{n}) \times \vec{n}$. In this form, the equation results in the sign convention preferred by Rudquist et

al. [17]. For this particular system, the substitutions $\vec{n} = \begin{pmatrix} \cos \theta \\ 0 \\ \sin \theta \end{pmatrix}$ and $\vec{E} = \begin{pmatrix} 0 \\ 0 \\ E \end{pmatrix}$

can be made. In so doing, the following simplifications can be achieved:

$$\begin{aligned} F_{flex} &= e_{11} \cos \theta \frac{\partial \theta}{\partial z} \vec{n} \cdot \vec{E} + e_{33} \left(-\sin^2 \theta \frac{\partial \theta}{\partial z} \hat{i} + \sin \theta \cos \theta \frac{\partial \theta}{\partial z} \hat{k} \right) \vec{E} \\ &= e_{11} \cos \theta \frac{\partial \theta}{\partial z} \vec{E} \sin \theta + e_{33} \sin \theta \cos \theta \frac{\partial \theta}{\partial z} \vec{E} \\ &= (e_{11} + e_{33}) \sin \theta \cos \theta \frac{\partial \theta}{\partial z} \vec{E} \\ &= f_{flex}(\theta) \frac{\partial \theta}{\partial z} \frac{\partial \phi}{\partial z} \end{aligned}$$

where $f_{flex}(\theta) = (e_{11} + e_{33})\sin\theta \cos\theta$ and the following has been used

$$E = \frac{\partial\phi}{\partial z}$$

where E is the electrical potential and $\partial\phi/\partial z$ is the rate of change in the electric field potential, ϕ , with changes in distance, z .

Summary

Collecting the contribution from all the terms together (i.e. elasticity, dielectric and flexoelectric effects) provides an expression for the total free energy density, as a function of z , in the form:

$$f_z = \frac{1}{2} f_{elas}(\theta) \left(\frac{\partial\theta}{\partial z} \right)^2 - \frac{1}{2} f_{diel}(\theta) \left(\frac{\partial\phi}{\partial z} \right)^2 + f_{flex}(\theta) \left(\frac{\partial\theta}{\partial z} \right) \left(\frac{\partial\phi}{\partial z} \right)$$

thus, providing a description of a HAN cell in the form of a partial differential equation (PDE).

Having examined the physical properties of liquid crystals and applying this specifically to a HAN cell configuration, it is now appropriate to examine the optical properties of liquid crystals prior to discussing how solutions are found for this PDE. This is addressed in the next section, where birefringence is examined.

1.3.5 Birefringence

The name birefringence means ‘two refractive indices’. Also, biaxial materials are birefringent, but have three principle refractive indices. Therefore, in birefringent materials, different polarisations of the electric field component of the light experience different refractive indices. This is shown in figure (1.12) below where un-polarised light is incident upon two different materials, the first is isotropic (no birefringence) and the second is a birefringent material (such as calcite or a liquid crystal).

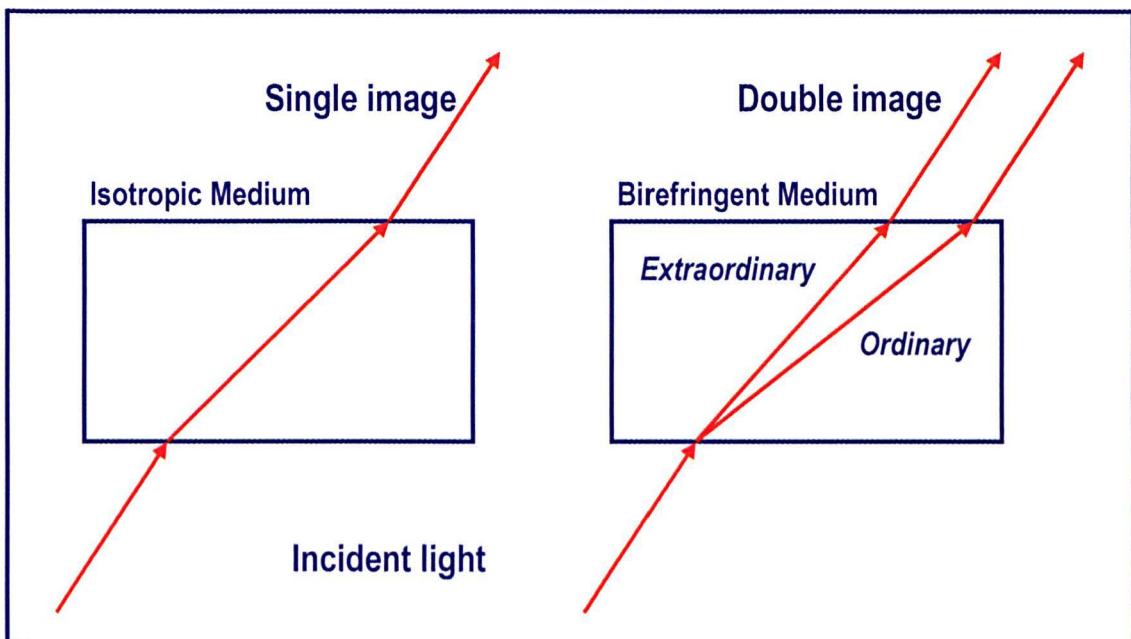


Figure 1.12: Shows the difference between passing un-polarised light through isotropic and birefringent materials.

As can be seen in the above diagram, the birefringent material splits the incident light into two beams, resulting in a double image emerging from the medium [18].

The reason why birefringence is present in liquid crystals is the presence of certain electronic structures (e.g. benzene rings) which make it easier to polarise the molecules in certain directions [19]. When this is coupled with the statistical alignment of the molecules, the different components of the

incident electromagnetic radiation will propagate with differing ease through the medium, according to their polarisations. However, above the clearing temperature, T_c , the statistical alignment of the molecules is lost (i.e. the order parameter, $S = 0$) and the material becomes isotropic, both in its physical and optical properties, thus the material loses its birefringence [20].

1.4 Wave Plates

In the previous section birefringence was discussed. Here, however, we shall discuss one of the applications of birefringent materials: they can be used to make a device called a 'wave plate'. We shall explain *what* a wave plate is and how a *variable* wave plate can be used to produce a *variable* intensity device. Then, in the next section, we shall examine some specific examples of liquid crystal devices, showing how some of the properties of liquid crystals are exploited to achieve such variable intensity devices.

Firstly, we examine how a birefringent material behaves if we have a uniform polarized wave front incident upon it. We observe that the polarisation of the light changes as it passes through the material (shown below in figure (1.13)), rather than seeing a double image as had been the case in figure (1.12).

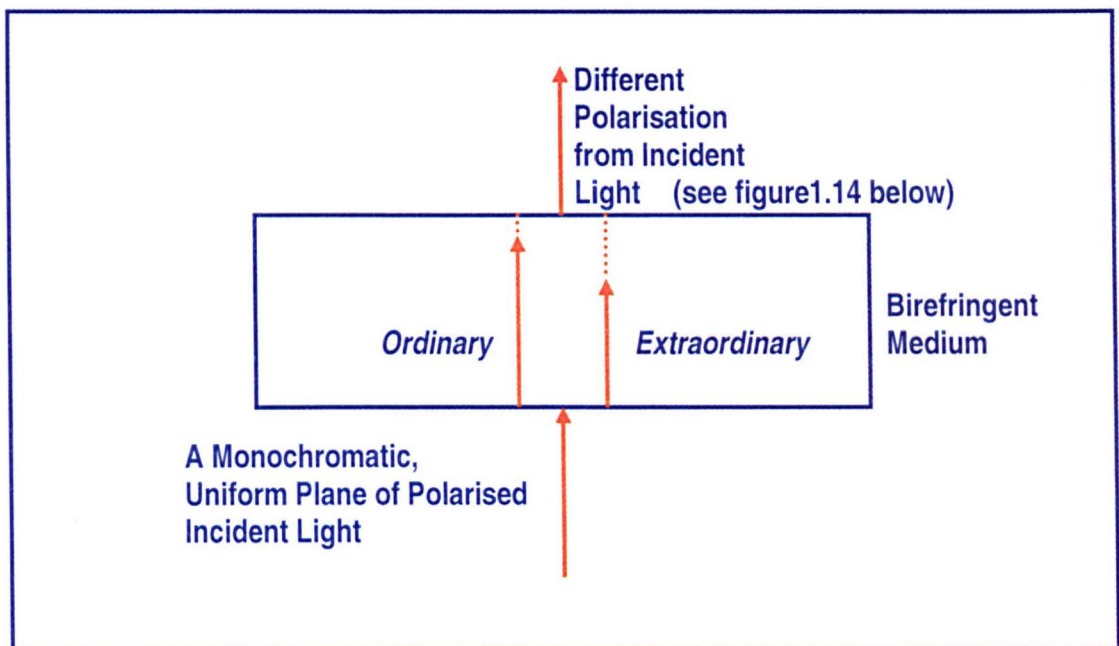


Figure 1.13: Shows what happens to a uniform, monochromatic, polarised wave-front incident on a sample of a birefringent material

N.B. the different arrow lengths in figure (1.13) denote the different apparent speeds of the two polarisations of light through the medium. The

resulting polarisation of the emergent light can be altered by changing the thickness of the sample. This ability to change light's polarisation earns this device the name 'wave plate'. The name denotes a phase difference, measured in radians, between emergent ordinary and extraordinary rays.

Some wave plates are given special names to denote that they are considered significant, due to producing a specific type of polarisation (specific to a given wavelength of light). Below is a diagram (figure (1.14)) from Feynman [21] showing different polarisations of light. If ordinary and extraordinary rays are in phase with each other we have linearly polarised light (top left and bottom right); wave plates that produce these polarisations are considered 'trivial' as they appear to have no effect on the incident light, if they are to have a name it is '*zero wave plate*'. However, if the emergent radiations are *half* a wavelength out of phase with each other we get linearly polarised light at right angles to the incident radiation (top right, figure (1.14)); a wave plate that results in this polarisation is called a '*half-plate*'. If the wave plate produces circularly polarised light then one of the rays lags a *quarter* of a wavelength behind the other; a plate that produces left handed circularly (LHC) polarised light is called a '*quarter wave plate*' and a plate that results in right handed circularly (RHC) polarised light is called a '*three-quarter wave plate*'.

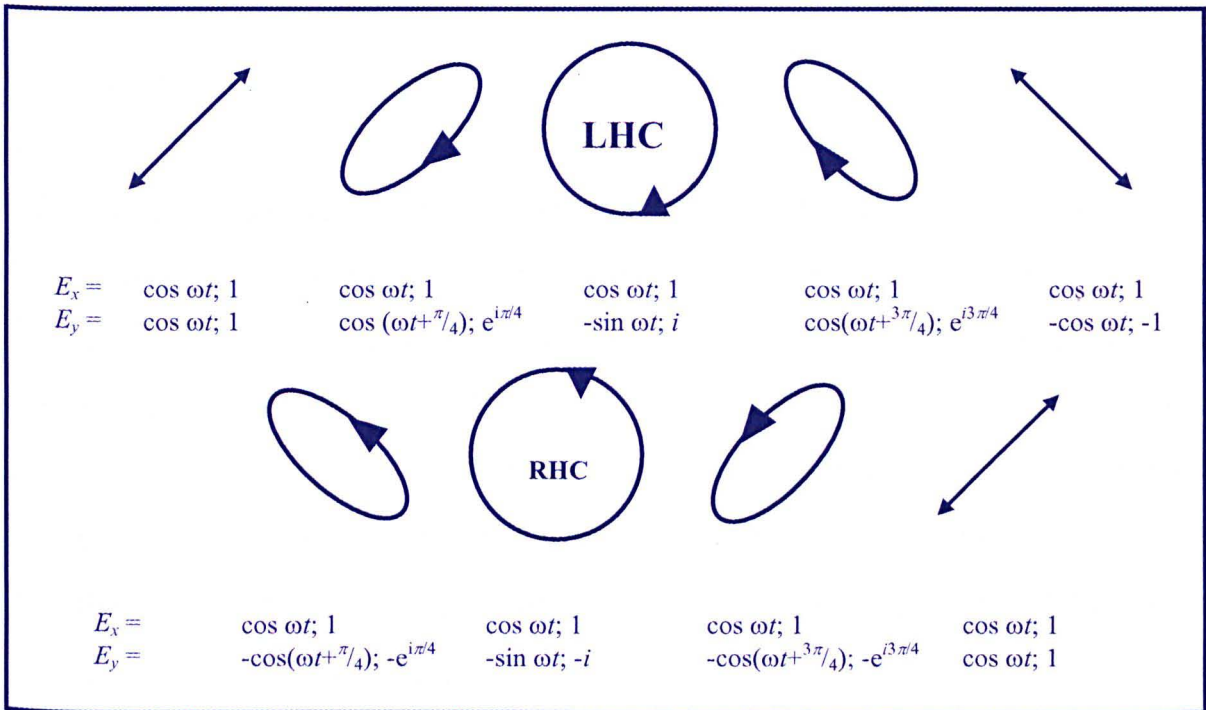


Figure 1.14: Shows polarization due to differing phase differences between two components of incident rays [21] (direction of propagation is out of the page).

It should be noted that wave plates that produce phase differences of a one quarter wavelength are optically indistinguishable from wave plates that produce phase differences of $1\frac{1}{4}$, $2\frac{1}{4}$, $3\frac{1}{4}$, ... $n\frac{1}{4}$, so when naming wave plates the integer number of wavelengths is ignored; all these wave plates are called ‘quarter wave plates’. However, the integer number becomes important in the experimental subsection of the results when simulations are being performed.

Liquid crystals are birefringent; a device that consists of a certain thickness of liquid crystalline material is therefore a wave plate. By using either the molecules’ electric or magnetic dipole (and applying an electric/magnetic field), it is possible to reorient the molecules. In so doing, it is possible to vary the effective birefringence of a given thickness of liquid crystalline material, i.e. this device becomes a *variable* wave plate. By placing such a

device between two polarisers, typically crossed polarisers, a variable intensity device is formed.

Crossed polarisers are two parallel sheets of polarising material, but one is rotated by an angle of 90° with respect to the other around the normal to the plane. In the absence of an intervening material, or a *zero* wave plate, crossed polarisers transmit no light. In contrast, placing a half wave plate between crossed polarisers results in a maximum in transmittance. All other wave plates result in values between 0 and 100% transmittance. In fact, the phase difference, $\Delta\Phi$, occurring between ordinary and extraordinary light, of wavelength λ , is expressed as

$$\Delta\Phi = \frac{2\pi n_O \left(\int_{z=0}^{z=D} \frac{1}{\sqrt{1-R(\sin^2(\frac{\pi}{2}-\theta(z)))}} dz - D \right)}{\lambda}$$

and can be thought of as an 'effective' birefringence of the cell, where R is

$R = \frac{n_E^2 - n_O^2}{n_E^2}$. Due to the crossed polarisers the emergent light intensity from

the cell is expressed in terms of the ratio:

$$T = \frac{1 - \cos \Delta\Phi}{2}$$

Hence, these variable wave plates are converted into variable intensity devices. These equations will be revisited at the end of the computer modelling section. The purpose of this will be to take the director profiles and convert them into light transmittance for each voltage across a given cell. However, prior to this, some different ways of achieving variable wave plates will be examined.

1.5 Liquid Crystal Devices

At present, liquid crystal displays (LCDs) represent the dominant flat panel device technology [22]. The three main reasons why liquid crystal devices are so important are that they are compact, light and low-voltage devices. Thus they are in marked contrast with cathode ray tubes in the field of display technology. The devices below demonstrate a range of different methods employed to exploit the different properties of liquid crystal materials in order to re-orientate the molecules (obtaining variable wave plate devices), resulting in variable intensity devices when combined with crossed polarisers.

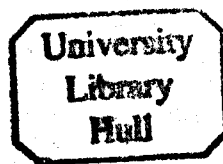
Firstly, it is important to introduce 'alignment layers' as they are paramount in determining the properties of liquid crystal cells. An alignment layer is a layer that makes it energetically more favourable for liquid crystal molecules adjacent to it to align in a particular direction, in the absence of any other factors. The alignment layers also provide some constraints to the orientation of the liquid crystal molecules throughout the cell, including acting to restore them to a desired configuration in the absence of any other external forces, such as a potential difference across the cell.

While this is an enormous research area in its own right, here we shall concentrate on only the very basics. The two particular types of alignment layers that are important in this work are called 'homeotropic' and 'homogeneous planar': the first of these acts to keep the liquid crystal molecules nearby approximately perpendicular to the cell wall; whereas the second acts to keep the LC molecules nearby approximately parallel to the cell wall. By using these two alignment layers it is possible to produce LC cells with macroscopic distortions in their director profiles.

Not only do we need to know about the anchoring angle that these alignment layers induce but we also need to know how effectively they anchor the liquid crystal molecules at these angles. Their effectiveness (in aligning molecules) is described in terms of an 'anchoring energy', A_θ : high anchoring energies mean that the molecules are held quite rigidly in a particular direction, and weak anchoring energies mean the molecules can easily be re-orientated by other factors (e.g. applying a voltage, or having a narrow cell with a different alignment at the other surface).

Anchoring energies are further subdivided into two types, azimuthal and zenithal. The first describes the ease with which the molecules can be rotated around the normal to the cell plane, and the second describes the ease with which the angle to the cell normal can be changed [23, 24, 25, 26]. For the main subject of this work, i.e. HAN cells, it will be the zenithal anchoring energy that will be relevant and so we shall not consider the azimuthal anchoring energy further.

Now we will examine some of the different configurations of LC molecules produced by these alignment layers in LCDs, and an effort will be made to demonstrate how versatile liquid crystals are. Firstly we will look at the twisted nematic, TN: one of the original LCDs, produced by Fergusson, Schadt and Helfrich in the late 1960s. Then we will look at the super twisted nematic, STN, which provides better viewing angles and is capable of faster switching than a TN. We will go on to look at a ferroelectric LCD, which uses a chiral smectic C phase, Sm C*, and discuss in brief its advantages. Finally we will describe the HAN cell, the topic of this chapter, and explain some of the reasons why it is of interest.



1.5.1 Twisted Nematic, TN.

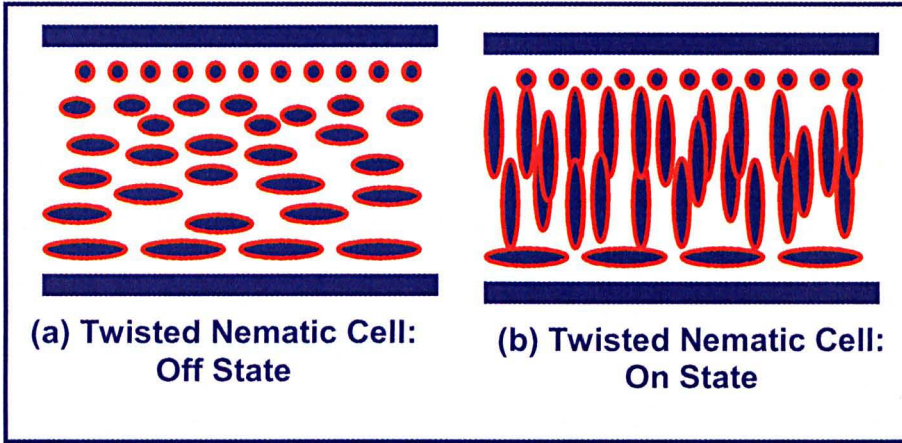


Figure 1.15: Shows a schematic depiction of a twisted nematic liquid crystal cell in (a) an off-state, and (b) an on-state (if placed between crossed polarisers). N.B. Twisted nematics use materials with positive dielectric anisotropies.

This configuration, (a) of figure (1.15), is of great practical interest. It is created by sandwiching a liquid crystal material between two homogenous alignment layers; a twist is then imposed upon the system by rotating one of the alignment layers in its own plane [27]. Switching can then be achieved by placing the cell in a magnetic field parallel to the twist axis⁸. A magnetic field above a critical value, H_c , will result in the cell switching to the on-state, (b) of figure (1.15) [27].

1.5.2 Super Twisted Nematics, STN.

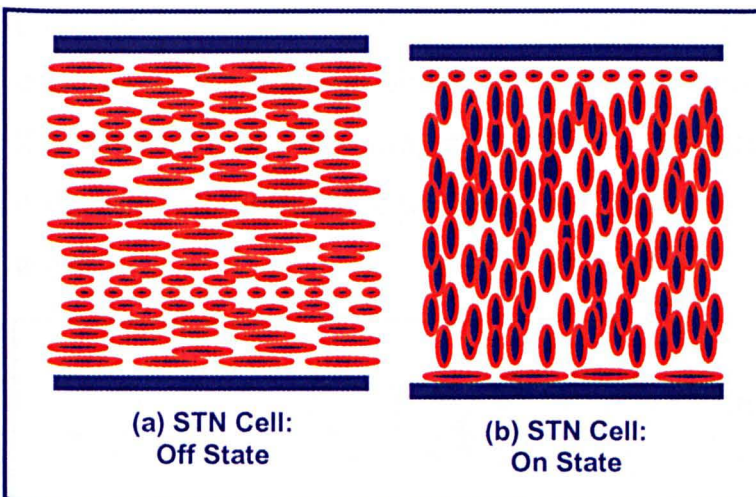


Figure 1.16: Shows a schematic depiction of a super twisted nematic liquid crystal cell in (a) an off-state, and (b) an on-state. Again, super twisted nematics use materials with positive dielectric anisotropies.

⁸ Or by applying an electric field parallel to the cell normal.

Clearly, both from figure (1.16) and this cell's name, the *super* twisted nematic LC cell is similar to its predecessor the twisted nematic LC cell. However, instead of the liquid crystal material only being twisted by 90° , it is twisted by some other multiple, e.g. 180° or 270° . This cell configuration is achieved by using chiral nematics, or by choosing chiral dopant molecules in order to change the LCs' pitch length to fit a particular cell thickness. The benefits of this technology are examined in detail in the literature [27]. However, the main benefit can be summarised by stating that most nematic LC devices achieve high contrast by resorting to significant reorientation of the director profile, whereas STNs do not [28]. This quality makes STNs excellent switching devices, operating on low voltages [29].

1.5.3 Ferroelectric LC Cells

These liquid crystal cell devices, which employ chiral smectic ($Sm\ C^*$) LCs, are of particular interest because they are bistable. Below, in figure (1.17a), numerous features of a $Sm\ C^*$ phase are shown. A chiral smectic phase has a layered structure (indicated by the periodicity of the cones). Within these layers the molecules are tilted by some angle (described by the cone surfaces). In turn, in the absence of external forces, the directors (represented by the arrows) from each layer follow a helical path. In contrast with a nematic phase, here, the molecular dipoles (at some angle to the director) are no longer randomly oriented; instead, each layer is polarised. However, due to the helical structure, a net polarisation does not arise.

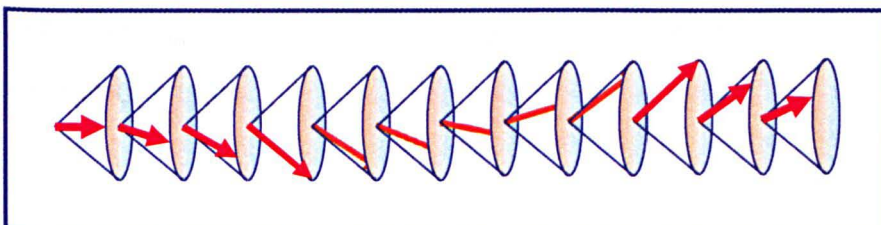


Figure 1.17a:
Represents a
chiral smectic, $Sm\ C^*$,
phase in the
absence of
external forces.

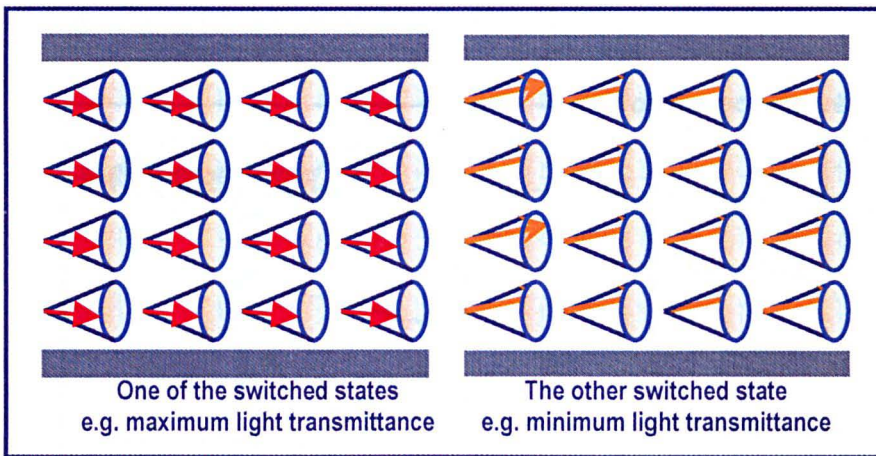


Figure 1.17b: Shows a ferro-electric liquid crystal device. Alignment layers are used to suppress the helical structure seen in figure 1.17a by ensuring that only two director orientations are energetically stable. Thus, the device achieves bistability.

In Ferroelectric LC devices this helical characteristic is suppressed by specialised anchoring layers, resulting in a spontaneous polarisation. The resulting configuration can be seen in figure (1.17b) where the director in each smectic layer is parallel to the director in its neighbouring layers; this is referred to as a surface stabilised SmC*.

Due to the spontaneous polarisation of the domain, applying an electric field (depending on its sign) can reorient the directors when it reorients the molecular dipoles; when the device is switching, the molecular directors (denoted by the arrows) follow the arc of the cone. The specialised alignment layers ensure that none of these intermediate director orientations is energetically stable. Consequently, when the applied voltage is removed the molecules do not find it energetically favourable to go through any of these intermediate states in order to revert to their previous state. As a result the device is bistable, making it an excellent switching device, especially as it exhibits 'memory'.

Once again, the optical properties of these devices depend upon the birefringence of their liquid crystal material and on being placed between cross polarisers.

1.5.4 Hybrid Aligned Nematic, HAN, Cells.

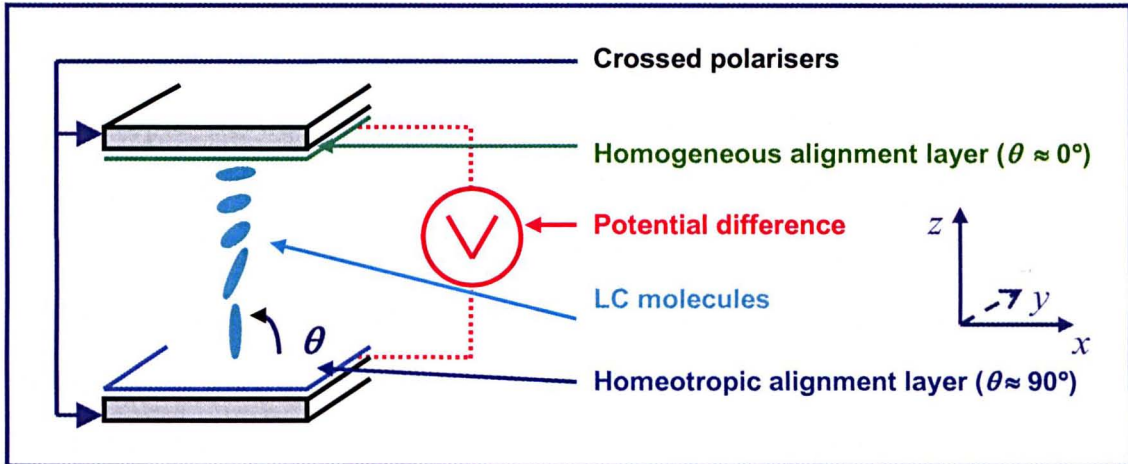


Figure 1.18: Schematic of a HAN cell. The potential difference (red) is applied in the z -direction. The homeotropic (blue) and homogeneous (green) alignment layers impose a distortion in the director profile, which is depicted here as a change in the angle, θ , of the molecules (turquoise).

As previously stated, the hybrid aligned nematic LC cell gets its name from the fact that it is a nematic liquid crystal material sandwiched between two different alignment layers. While it should be noted that there are many different configurations possible, resulting in a range of alternative director profiles (see Ref. [39]), the HAN cell under investigation in this thesis is shown, schematically, in figure (1.18), where θ denotes the angle between the director and the x - y plane. The cell of LC material, constrained by two alignment layers, is placed between crossed polarisers. A potential difference is applied along the cell normal (z direction). One alignment layer gives rise to homeotropic alignment (i.e. $\theta \approx 90^\circ$ to the x and y axes) whilst the other gives rise to homogeneous alignment (i.e. $\theta \approx 0^\circ$, that is, the director is nearly parallel to the plate). Because small changes in applied voltage result in small changes in the director profile⁹, this device can be used to achieve gradations in light transmittance, i.e. HAN cells are one type of grey-scaling device [39].

⁹ Director profile shows how the orientation of the molecules varies through the cell.

1.6 Experimental Set-Up

Having provided an outline to this subject area, and as HAN cells are the main topic of this chapter, the discussion will now focus on HAN cell devices. The discussion will initially examine the experimental set-up adopted by Takahashi et al. [1] and Bartle [30], whose experimental data is examined in the second part of the results section. Details of the sample preparation and the experimental procedures can be found in Takahashi et al. [1] and Bartle [30]. Other works in this area that may be of interest to the reader include Refs. [31, 32, 33, 34, 35]. After the description of the experimental set-ups, sections 1.7 and 1.8 will detail how theoretical models and computational simulations can be used to describe HAN cells.

1.6.1 Takahashi's Experimental Set-Up

With reference to the experimental set-up, over and above the information provided in figure (1.18), most of the information given by Takahashi et al. [1] pertains to the production of the HAN cell. Briefly, as regards the sample in Takahashi et al.'s work, one of the substrates was coated with a polyimide film and treated by rubbing to introduce homogeneous alignment. The other substrate was coated with another type of polyimide film to introduce homeotropic alignment. These substrates induced alignments of approximately 90° and 2° at the homeotropic and homogeneous alignment layers respectively when the HAN cell, of thickness $D = 28.5 \mu\text{m}$, was filled with MBBA.

N-(4-methoxybenzylidene)-4'-*n*-butylaniline (MBBA) is a commercially available nematic liquid crystal; its properties are detailed in the results section. The measurements were carried out at a temperature of 30°C and the wavelength of the laser light used was 550 nm .

1.6.2 K. Bartle's Experimental Set-Up

In contrast to Takahashi et al. [1], Bartle provides rather more information about his experimental set-up [30]. In addition to elaborating on how the cell was produced, he also provides information on how the experiments were performed, including steps taken to minimise problems caused by ion impurities and material viscosities.

Commencing with the similarities between the Takahashi and Bartle cells we see that Bartle's cells also had one of the substrates coated with a polyimide film and treated by rubbing (to introduce homogeneous alignment) and the other substrate coated with another type of polyimide film (to introduce homeotropic alignment). Furthermore, these alignment layers also produced alignments of approximately 2° and 90° at their respective surfaces, as had been the case for the Takahashi cell.

The experimental set-up used by Bartle can be seen in figure (1.19).

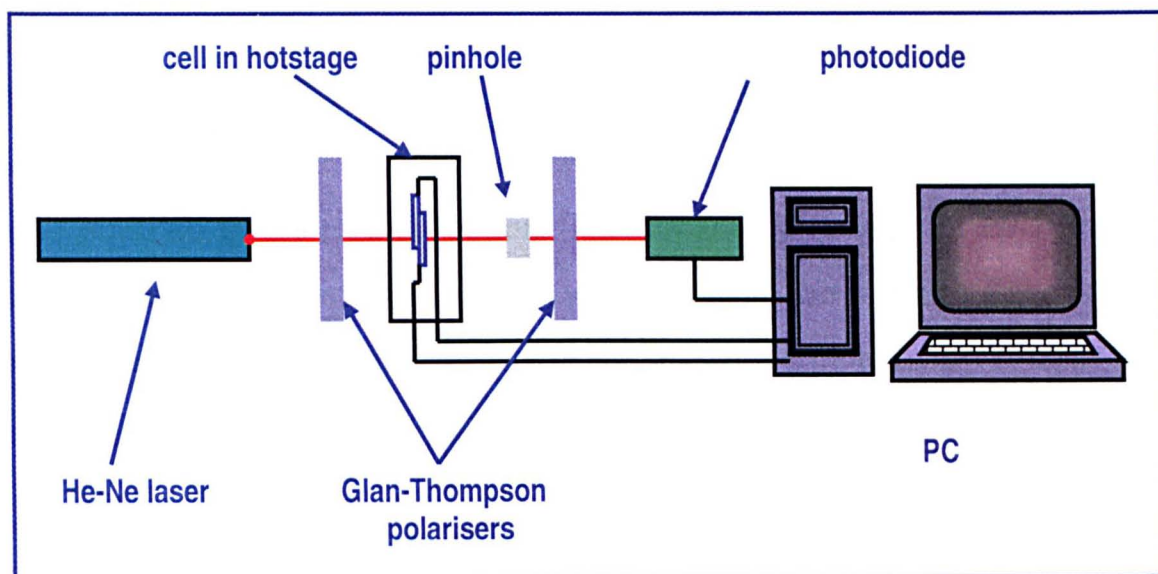


Figure 1.19: Schematic experimental set-up used by Bartle [30]

The polarisers are oriented such that they are at $+45^\circ$ and -45° to the rubbing direction of the polymer of the homogeneous alignment layer.

At this stage the main discernible difference between Bartle's set-up and that used by Takahashi et al. [1] is Bartle's use of a He-Ne laser, which has a wavelength of 633 nm. Furthermore, the hot-stage allowed the ambient temperature to be controlled. As a result temperature dependent readings could be taken. To aid comparison between data sets, all the measurements were carried out at 90% of the mixtures' clearing temperatures¹⁰, T_c [36].

A computer program was used to control the voltage across the cell and, simultaneously, to record the light intensity incident on a photodiode. The form of the input voltage was chosen to minimise the problems due to ion impurities and to erase any memory effect the cell may experience [30], which may be caused by factors such as viscosity.

In addition to these deviations from the experiments performed by Takahashi et al. [1], Bartle had a number of different samples; their thicknesses ranged between $D = 24.9$ and $35.4 \mu\text{m}$, and the cells were filled with either E7 or 10% solutions of other dopant liquid crystal materials in E7. Like MBBA, E7 is a commercially available nematic LC material, whose properties are well documented in the literature [30, 37]; they are also outlined in the results section. The dopants, dissolved in E7 to make 10% solutions (by weight), were synthesized in the author's laboratory. Their names and molecular structures are shown below in table (1.4.6).

¹⁰ The clearing temperature, T_c , of a liquid crystal is the temperature above which it becomes isotropic (details can be found in reference [30]).

Table 1.4.6: Shows molecular structures of the molecules placed in 10% (by weight) solutions in E7

Sample Code	Molecular Structure
JHW33	
JHW29	
JHW128	
JHW131	
JHW172	

1.7 Continuum Modelling

Continuum modelling is a technique in which some properties of a physical system are represented mathematically. It can be particularly appropriate when properties vary gradually and continuously through the system to model these properties using partial differential equations (PDEs). On first inspection, the properties and behaviour of any liquid crystal device are complex (appearing between order and disorder), and so the prospect of modelling them is fraught with difficulties. However, the continuum modelling method allows us to take a mesoscopic approach to this problem, smoothing out the microscopic noise inherent to the system. The director profile of the liquid crystal molecules and the electrical potential through the HAN cell are appropriate properties to be modelled by the continuum method, thus allowing us to gain a greater understanding of the system without becoming distracted by the minutia, as would often be the case with molecular dynamic simulations of liquid crystal systems.

The PDE used to represent the system is a Laplacian, where the free energy density of the system is given by equation (1.1) [1, 31] (see Appendix B),

$$f_z = \frac{1}{2} f_{elas}(\theta) \left(\frac{\partial \theta}{\partial z} \right)^2 - \frac{1}{2} f_{diel}(\theta) \left(\frac{\partial \phi}{\partial z} \right)^2 + f_{flex}(\theta) \left(\frac{\partial \theta}{\partial z} \right) \left(\frac{\partial \phi}{\partial z} \right) \quad (1.1).$$

Here, the variable θ is the angle of the director to the x - y plane and ϕ is the electrical potential, both are functions of z . The $f_{elas}(\theta)$ term gives the elastic free energy contribution, i.e.

$$f_{elas}(\theta) = K_{11} \cos^2(\theta) + K_{33} \sin^2(\theta), \quad (1.2)$$

where K_{11} (K_{33}) is the splay (bend) elastic constant. The $f_{diel}(\theta)$ term gives the dielectric contribution, i.e.

$$f_{diel}(\theta) = \epsilon_o (\Delta \epsilon \sin^2(\theta) + \epsilon_n), \quad (1.3)$$

where the dielectric anisotropy is

$$\Delta \varepsilon = \varepsilon_p - \varepsilon_n. \quad (1.4)$$

The $f_{flex}(\theta)$ term provides the flexoelectric free energy contribution, i.e.

$$f_{flex}(\theta) = (e_{11} + e_{33}) \cos(\theta) \sin(\theta), \quad (1.5)$$

where e_{11} (e_{33}) is the flexoelectric coefficient for splay (bend).

The physical system will seek to minimise its free energy. By minimising equation (1.1) with respect to (w.r.t.) θ and ϕ we can find the minimum energy configurations. Minimizing equation (1.1) w.r.t. θ gives (see Appendix C):

$$f'_{elas}(\theta) \left(\frac{\partial \theta}{\partial z} \right)^2 + 2f_{elas}(\theta) \left(\frac{\partial^2 \theta}{\partial z^2} \right) + f'_{diel}(\theta) \left(\frac{\partial \phi}{\partial z} \right)^2 + 2f_{flex}(\theta) \left(\frac{\partial^2 \phi}{\partial z^2} \right) = 0 \quad (1.6)$$

Similarly, minimizing equation (1.1) with respect to ϕ gives (see Appendix C):

$$f'_{diel}(\theta) \left(\frac{\partial \theta}{\partial z} \right) \left(\frac{\partial \phi}{\partial z} \right) + f_{diel}(\theta) \left(\frac{\partial^2 \phi}{\partial z^2} \right) - f'_{flex}(\theta) \left(\frac{\partial \theta}{\partial z} \right)^2 - f_{flex}(\theta) \left(\frac{\partial^2 \theta}{\partial z^2} \right) = 0. \quad (1.7)$$

Equation (1.7) can be rewritten as:

$$\frac{d}{dz} \left[f_{diel}(\theta) \left(\frac{\partial \phi}{\partial z} \right) - f_{flex}(\theta) \left(\frac{\partial \theta}{\partial z} \right) \right] = 0, \quad (1.8)$$

therefore we know that:

$$f_{diel}(\theta) \left(\frac{\partial \phi}{\partial z} \right) - f_{flex}(\theta) \left(\frac{\partial \theta}{\partial z} \right) = Const \quad (1.9)$$

The properties of the cell are largely governed by the boundary conditions. Initially fixed angles were used ($\theta_0 = 90^\circ$ and $\theta_D = 2^\circ$ at $z = 0$ and $z = D$ respectively) as the boundary conditions. However, in the real system, such rigidity would not occur, therefore finite anchoring energies are employed.

These angles were instead adopted ($\theta_0 = 90^\circ$ and $\theta_D = 2^\circ$ at $z = 0$ and $z = D$ respectively) as the ‘angles of easy axis’ at each surface, i.e. the preferred direction of orientation ($\theta_{0\text{easy}} = 90^\circ$ and $\theta_{D\text{easy}} = 2^\circ$ respectively), and incorporated into a surface anchoring energy term. Thus the surface anchoring energies can be described by equations (1.10) and (1.11) below [1],

$$f_{s_0}(\theta) = \frac{1}{2} A_{\theta_0} \sin^2(\theta_0 - \theta_{0\text{easy}}), \quad (1.10)$$

and

$$f_{s_D}(\theta) = \frac{1}{2} A_{\theta_D} \sin^2(\theta_D - \theta_{D\text{easy}}). \quad (1.11)$$

Equations (1.10) and (1.11) approximate the energy contributions to the system from the homeotropic and homogeneous alignment layers respectively (i.e. at $z = 0$ and $z = D$) with a Hook’s Law (i.e. the Rapini-Papoular approximation [1, 22]). $\theta_{0\text{easy}}$ and $\theta_{D\text{easy}}$ are the angles of the easy axis at $z = 0$ and $z = D$ respectively, whereas θ_0 and θ_D are the actual angles that the directors make with the homeotropic and homogeneous alignment layers respectively. A_{θ_0} and A_{θ_D} are the Hook’s constants used to describe the anchoring strengths [2].

Finally, our boundary conditions are found by minimising the energies at the surfaces ($z = 0$ and $z = D$):

$$f_{\text{elas}}(\theta_0) \frac{\partial \theta}{\partial z} \Big|_{z=0} + f_{\text{flex}}(\theta_0) \frac{\partial \phi}{\partial z} \Big|_{z=0} - \frac{1}{2} A_{\theta_0} \sin[2(\theta_0 - \theta_{0\text{easy}})] = 0 \quad (1.12)$$

and

$$f_{\text{elas}}(\theta_D) \frac{\partial \theta}{\partial z} \Big|_{z=D} + f_{\text{flex}}(\theta_D) \frac{\partial \phi}{\partial z} \Big|_{z=D} + \frac{1}{2} A_{\theta_D} \sin[2(\theta_D - \theta_{D\text{easy}})] = 0 \quad (1.13)$$

respectively (see Appendix D for derivation [37]).

All the above equations are currently in a form where changes in z are infinitesimally small. In order to implement and solve these equations by computer it will be necessary to convert them into a form involving small but finite changes in z . To achieve this we employ a finite difference method, described in the following section.

1.8 Computer Simulation – Finite Difference Method

In the previous section we outlined the mathematical formalism needed to describe the coupled partial differential equations, used to express the director and potential profiles (i.e. equations (1.6) and (1.7)). In this section, it is necessary to rewrite the equations, manipulating them in order to implement them on computer. To do this we employ a finite difference method, which uses the fact that:

$$\frac{dy}{dx} = \lim_{\Delta x \rightarrow 0} \frac{y_{i+1} - y_i}{x_{i+1} - x_i}$$

and

$$\frac{d^2 y}{dx^2} = \lim_{\Delta x \rightarrow 0} \frac{y_{i+2} - 2y_{i+1} + y_i}{(x_{i+1} - x_i)^2}.$$

If Δx (where $\Delta x = x_{i+1} - x_i$) is chosen to be sufficiently small, but finite, these equations can be used to approximate a continuous function.

Once we have found a numerical solution to the PDEs, we need to use the θ curve to calculate the phase difference that accrues between the ordinary and extraordinary components of light as it passes through the HAN cell (this can be found from equation (1.31) below); the accompanying ϕ curve enables us to calculate the corresponding voltage. By finding numerous pairs of θ and ϕ curves that are numerical solutions to our PDEs (i.e. satisfying given boundary conditions), we are able to calculate relative intensities of light transmitted (see equation (1.33)) against potential difference. This enables us to compare theoretical results with those obtained experimentally.

Firstly, we need a method by which we can integrate across the cell, i.e. a method by which, if θ_i , θ_{i+1} , ϕ_i and ϕ_{i+1} are known, θ_{i+2} and ϕ_{i+2} can be

calculated. This will allow us to integrate the PDEs across the cell and so find numerical solutions. The two methods we shall discuss are a self consistent method (in § 1.8.1) as proposed by Takahashi et al. [1], and our new method (in § 1.8.2) which allows us to calculate both curves simultaneously.

1.8.1 Takahashi's Method

Takahashi et al. [1] employ a self-consistent method. This method requires one function (e.g. tilt angle) to be calculated and then that function is used to calculate the other (e.g. electrical potential); after that, the second function is used to recalculate the first function. This process is repeated until there are no significant changes in each function between successive iterations, i.e. it is self-consistent. To enter into this cycle of iterations, an approximation for one of the functions (e.g. electrical potential) must initially be provided for the computer program.

Specifically, when applied to the HAN cell problem, Takahashi's method involves integrating one of the curves across the cell, say the $\theta(z)$ curve, and then he uses *this* curve to help integrate the other function (i.e. $\phi(z)$) across the cell. This $\phi(z)$ curve is then used to recalculate the $\theta(z)$ curve. The process is repeated until the $\theta(z)$ and the $\phi(z)$ curves are indistinguishable from those obtained during the previous iteration. His initial approximation is that the potential across the cell is uniform, that is to say $\phi(z) = \text{Const} \cdot z$ (i.e. $\phi(z) = 0$ when $z = 0$, and $\phi(z) = V$ when $z = D$).

We initially tried this method, while assuming infinite anchoring energies, but it did not result in physical solutions. We were initially alerted to this

due to our transmittance curves showing the ‘wrong kind’ of asymmetry. On further investigation we found that the director profiles across the cell typically exhibited unphysical oscillations as depicted below:

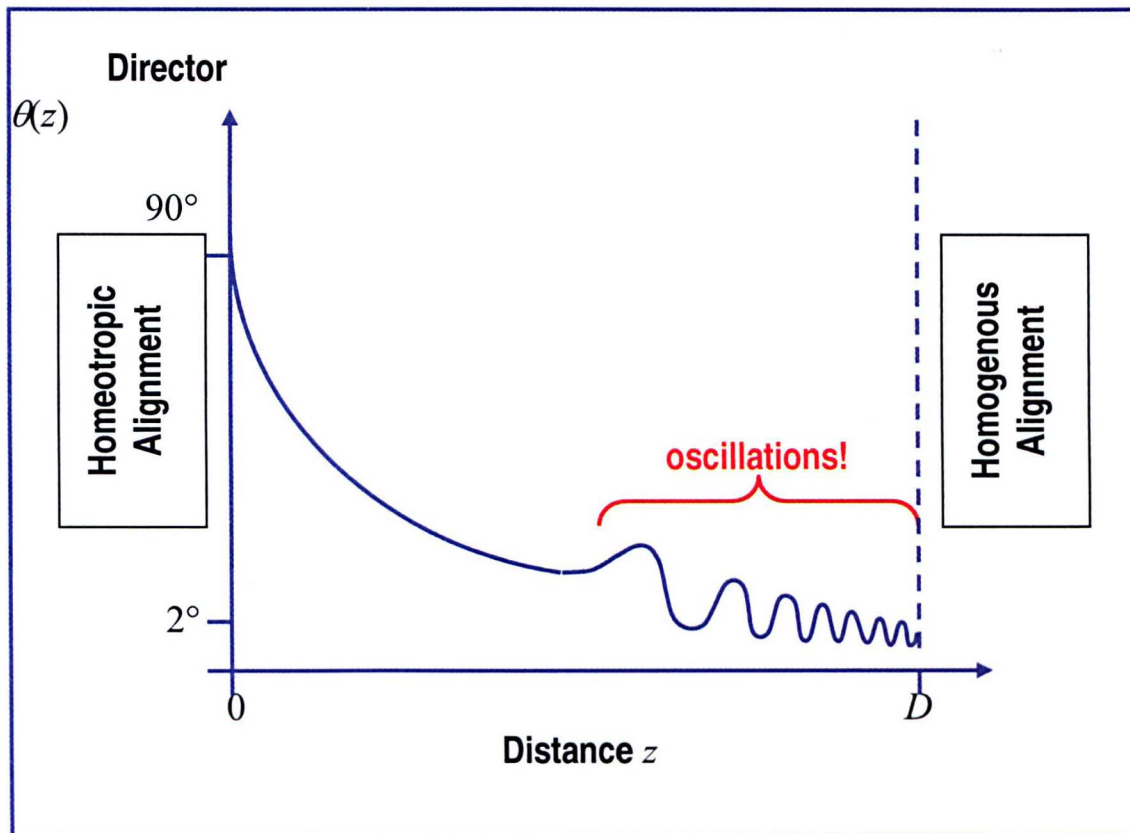


Figure 1.20: Shows a typical shape of the director profile across a cell as produced by the self-consistent method employed by Takahashi et al [1]. As acceptability of solutions was determined solely by the end points, we conclude that the number of oscillations is arbitrary and therefore that such solutions are non physical.

Subsequently, we found from our new method that the initial assumption made by Takahashi et al. [1] (i.e. of a constant electric field across the cell) was very close to what was observed (see section 1.9 below). Consequently, it appears that the self-consistent method *itself* is inappropriate for finding solutions to this particular system.

1.8.2 Our New Method

In this section the mathematics used to integrate the PDEs across the cell are demonstrated; a flow diagram has been included to show how this was implemented by computer. This method is a new way of finding numerical solutions to these PDEs and does not appear to succumb to the same pitfalls as the self-consistent method used by Takahashi et al. [1]. That is, the solution θ -curves found by Takahashi's method did not appear to represent physical solutions, whereas the solution curves found by our new method appear more plausible. Consequently, we have greater confidence in this new method and its ensuing results.

The aim of this section is to convert the relevant equations into finite difference notation. Recall that, to calculate θ_{i+2} and ϕ_{i+2} , we must know θ_i , θ_{i+1} , ϕ_i and ϕ_{i+1} . If we are to start at $z = 0$, with the intention of integrating across the cell (to $z = D$), θ_0 , θ_1 , ϕ_0 and ϕ_1 must be known. Note that where we choose our zero electrical potential is arbitrary, so for simplicity we choose it to be at $z = 0$, i.e. $\phi_0 = 0$. Due to the finite anchoring energies, θ_0 and θ_1 are unknown, and because the way in which the potential difference varies across the cell is also unknown, we have no value for ϕ_1 . There are then, too many unknowns. This is where our new method begins in earnest.

We assume that for an initial $\Delta\phi$ (i.e. $\phi_1 - \phi_0$) there is only *one* solution to the Laplacian; we choose a value of $\Delta\phi$ for which we wish to find a solution. We have an equation for the anchoring energies at both surfaces and an equation that relates θ_0 , θ_1 , ϕ_0 and ϕ_1 to a constant across the cell. If we choose θ_0 to be a deliberately incorrect value, the homeotropic anchoring energy term allows us to calculate θ_1 . While this then results in an incorrect value of *Const* in equation 1.9, it allows us to do an initial

integration across the cell. We can then see if this value of θ_0 will result in a value of θ_D that is too big or too small. Once this is known we are able to vary θ_0 up or down, until we obtain a meaningful value of $Const$ leading to a meaningful value of θ_D , satisfying the homogeneous anchoring energy term. A range of initial $\Delta\phi$ s will result in a range of potential differences across the cell and their accompanying director profiles. Thus we are able to calculate light transmittance against potential difference.

Having established the framework used, it now remains to show how this was achieved. Recalling equations (1.6) and (1.9):

$$f'_{elas}(\theta)\left(\frac{\partial\theta}{\partial z}\right)^2 + 2f_{elas}(\theta)\left(\frac{\partial^2\theta}{\partial z^2}\right) + f'_{diel}(\theta)\left(\frac{\partial\phi}{\partial z}\right)^2 + 2f_{flex}(\theta)\left(\frac{\partial^2\phi}{\partial z^2}\right) = 0 \quad (1.14)$$

$$f_{diel}(\theta)\left(\frac{\partial\phi}{\partial z}\right) - f_{flex}(\theta)\left(\frac{\partial\theta}{\partial z}\right) = Const, \quad (1.15)$$

equation (1.15) can be rewritten as:

$$\frac{\partial\phi}{\partial z} = \frac{Const}{f_{diel}(\theta)} + \frac{f_{flex}(\theta)}{f_{diel}(\theta)}\left(\frac{\partial\theta}{\partial z}\right). \quad (1.16)$$

Rearranging equation (1.14) results in:

$$\frac{\partial^2\theta}{\partial z^2} = \frac{-1}{2f_{elas}(\theta)}\left[f'_{diel}(\theta)\left(\frac{\partial\phi}{\partial z}\right)^2 + 2f_{flex}(\theta)\left(\frac{\partial^2\phi}{\partial z^2}\right) + f'_{elas}(\theta)\left(\frac{\partial\theta}{\partial z}\right)^2\right]. \quad (1.17)$$

Using finite difference notation this becomes:

$$\theta_{i+2} = \frac{-\left[f'_{elas}(\theta)(\theta_{i+1} - \theta_i)^2 + f'_{diel}(\theta)(\phi_{i+1} - \phi_i)^2 + 2f_{flex}(\theta)(\phi_{i+2} - 2\phi_{i+1} + \phi_i)\right]}{2f_{elas}(\theta)} + 2\theta_{i+1} - \theta_i \quad (1.18)$$

and the finite difference version of ϕ_{i+2} (from equation 1.16) becomes:

$$\phi_{i+2} = \frac{Const \cdot \Delta z}{f_{diel}(\theta)} + \frac{f_{flex}(\theta)}{f_{diel}(\theta)} (\theta_{i+2} - \theta_{i+1}) + \phi_{i+1}. \quad (1.19)$$

We can substitute equation (1.18) into (1.19) to obtain:

$$\phi_{i+2} = \frac{f_{flex}(\theta)}{f_{diel}(\theta)} \left(\frac{-1}{2f_{elas}(\theta)} \left[\begin{array}{l} f'_{elas}(\theta)(\theta_{i+1} - \theta_i)^2 \\ + f'_{diel}(\theta)(\phi_{i+1} - \phi_i)^2 \\ + 2f_{flex}(\theta)(\phi_{i+2} - 2\phi_{i+1} + \phi_i) \end{array} \right] + 2\theta_{i+1} - \theta_i - \theta_{i+1} \right) + \phi_{i+1} + \frac{Const \cdot \Delta z}{f_{diel}(\theta)} \quad (1.20)$$

All that is required now is to rearrange equation (1.20) so that all ϕ_{i+2} s appear on the left-hand side, i.e.

$$\left[1 + \frac{f_{flex}^2(\theta)}{f_{diel}(\theta)f_{elas}(\theta)} \right] \phi_{i+2} = \frac{f_{flex}(\theta)}{f_{diel}(\theta)} \left(\frac{-1}{2f_{elas}(\theta)} \left[\begin{array}{l} f'_{elas}(\theta)(\theta_{i+1} - \theta_i)^2 \\ + f'_{diel}(\theta)(\phi_{i+1} - \phi_i)^2 \\ + 2f_{flex}(\theta)(\phi_i - 2\phi_{i+1}) \end{array} \right] + \theta_{i+1} - \theta_i \right) + \phi_{i+1} + \frac{Const \cdot \Delta z}{f_{diel}(\theta)} \quad (1.21)$$

This is then refined to:

$$\phi_{i+2} = \frac{f_{diel}(\theta)f_{elas}(\theta) \left[\frac{f_{flex}(\theta)}{f_{diel}(\theta)} \left(\frac{-1}{2f_{elas}(\theta)} \left[\begin{array}{l} f'_{elas}(\theta)(\theta_{i+1} - \theta_i)^2 \\ + f'_{diel}(\theta)(\phi_{i+1} - \phi_i)^2 \\ + 2f_{flex}(\theta)(\phi_i - 2\phi_{i+1}) \end{array} \right] + \theta_{i+1} - \theta_i \right) + \phi_{i+1} + \frac{Const \cdot \Delta z}{f_{diel}(\theta)} \right]}{f_{diel}(\theta)f_{elas}(\theta) + f_{flex}^2(\theta)} \quad (1.22)$$

It may be noted that in the above equations, thus far, no decision has been made as to where to evaluate the functions of θ , e.g. $f_{flex}(\theta)$, $f_{diel}(\theta)$, etc. By choosing sufficiently small step sizes, it becomes less critical where we evaluate these functions of θ , whether be it at i , $i+1$, $i+2$ or some average.

We chose to evaluate these functions at i , and $\Delta z (=D/N)$ was found to be sufficiently small for $N = 200$ points.

1.8.2.1 Flexoelectric Voltage and the Flexoelectric Voltage Shift

We will also need to lay down the criterion by which solutions are accepted or rejected, i.e. a systematic procedure to find numerical solutions that satisfy our boundary conditions. We start by setting $\phi_0 = 0$ (because the electrical potential can be chosen to be zero arbitrarily; for simplicity, we have chosen the zero to be located at $z = 0$). Then we choose a value for $\Delta\phi_0$, assuming that for each $\Delta\phi_0$ there will only be one possible solution for the system, resulting in a specific value of the nominal voltage across the cell. The nominal voltage is written as

$$V_{nom} = \int_0^D \frac{\partial\phi}{\partial z} dz. \quad (1.23)$$

It should be noted that there are two components of the nominal voltage across a HAN cell. The first is the applied voltage, which is provided by an external power source. The second component is the flexoelectric voltage, which arises from the net polarisation of the cell due to the flexoelectric effect. The voltage calculated by equation (1.23) includes both of these. The flexoelectric voltage can be expressed as [31, 37]

$$\psi(\theta_0, \theta_D) = 2\pi \frac{e_{11} + e_{33}}{\Delta\varepsilon \cdot \varepsilon_0} \cdot \ln \left[\frac{f_{diel}(\theta_D)}{f_{diel}(\theta_0)} \right]. \quad (1.24)$$

To find the applied voltage we need to subtract the flexoelectric part (equation (1.24)) from equation (1.23), giving:

$$V_{applied} = \int_0^D \frac{\partial\phi}{\partial z} dz - \psi(\theta_0, \theta_D). \quad (1.25)$$

It is important to note the difference between the flexoelectric voltage and the flexoelectric voltage *shift*. The flexoelectric voltage is the potential

difference across the cell due to the flexoelectric polarization of the cell. Whereas, the flexoelectric voltage *shift* is the voltage at which the central feature occurs (see figure (1.21)).

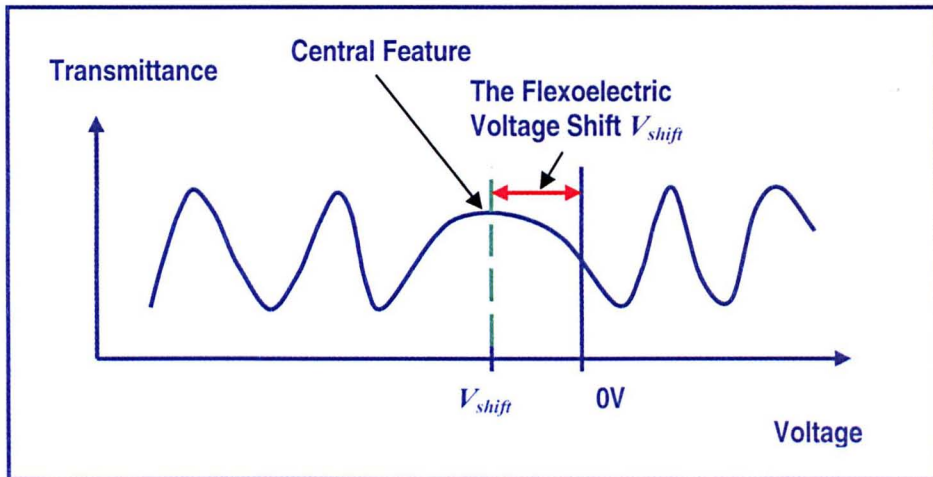


Figure 1.21: Shows the definition of both the central feature and of the flexoelectric voltage shift. The central feature is the approximate centre of reflection symmetry of the transmittance curve and the flexoelectric voltage shift is the voltage at which it occurs.

While the flexoelectric voltage is used in the calculations of the transmittance curves (and therefore the flexoelectric voltage shift), it is the flexoelectric voltage shift that is of explicit interest in the results section of this chapter.

1.8.2.2 Boundary Conditions

We then need to choose values of θ_0 and $\Delta\theta_0$ that will satisfy the boundary conditions. Having chosen $\phi_0 = 0$ and $\phi_1 = \text{variational parameter}$, we initially chose $\theta_0 = 90^\circ$; turning to equation (1.12) we were able to obtain θ_1 by rewriting the equation in finite difference notation and then rearranging it, to obtain the following relationship

$$\Delta\theta_0 = \frac{\Delta z \cdot A_{\theta_0} \sin[2(\theta_0 - \theta_{0_{\text{easy}}})]}{2f_{\text{elas}}(\theta_0)} - \frac{f_{\text{flex}}(\theta) \cdot \Delta\phi_0}{f_{\text{elas}}(\theta_0)}, \quad (1.26)$$

and hence

$$\theta_1 = \frac{\Delta z \cdot A_{\theta_0} \sin[2(\theta_0 - \theta_{0_{\text{easy}}})]}{2f_{\text{elas}}(\theta_0)} - \frac{f_{\text{flex}}(\theta) \cdot \Delta\phi_0}{f_{\text{elas}}(\theta_0)} + \theta_0. \quad (1.27)$$

This satisfies our boundary condition at the homeotropic alignment layer. Now enough information is known to enable us to calculate the value of $Const^{11}$ in equation (1.15): i.e.

$$f_{\text{diel}}(\theta_0) \left(\frac{\phi_1}{\Delta z} \right) - f_{\text{flex}}(\theta_0) \left(\frac{\theta_1 - \theta_0}{\Delta z} \right) = Const. \quad (1.28)$$

By using this value for $Const$, it becomes possible to integrate θ and ϕ across the cell. In so doing we are able to ascertain whether the initial choice of θ_0 (at $z = 0$) was appropriate to satisfy the boundary conditions at $z = D$. To do this we assign equation (1.13) (which should equal zero) to be equal to a new value, B .

¹¹ Only when both boundary conditions are satisfied will the correct value of $Const$ have been found.

Thus equation (1.13) becomes:

$$f_{elas}(\theta_N) \frac{\theta_N - \theta_{N-1}}{\Delta z} + f_{flex}(\theta_N) \frac{\phi_N - \phi_{N-1}}{\Delta z} + \frac{1}{2} A_{\theta_D} \sin[2(\theta_N - \theta_{D_{easy}})] = B. \quad (1.29)$$

We systematically¹² changed our initial conditions (i.e. the value of θ_0 , recalling that ϕ_0, ϕ_1 are fixed and θ_1 is defined in terms of θ_0) until B fell within an arbitrarily small range of $-\delta B \leq B \leq +\delta B$, where δB was small ($\delta B = 1 \times 10^{-6}$).

¹² We deliberately start with θ_0 too large (i.e. $\theta_0 = 90^\circ$) to satisfy equation (1.29). As a consequence, the resulting θ_D is very much greater than 2° . At the same time we initialise some *token* $T = +1$. We then integrate across the cell. Once a 'solution' has been obtained we tested it to establish that θ_0 was indeed too large to satisfy equation (1.29), and then we reset $T = +1$. After this it is then possible to reduce the initial value of θ_0 by some value $\Delta\Theta$ (e.g. $\Delta\Theta \approx 1^\circ$). This process was repeated and, for as long as the resulting 'solution' is too large, we continue to reduce θ_0 by $\Delta\Theta$. Eventually this results in a 'solution' that tells us that θ_0 is too small to satisfy equation (1.29); when this happens we reset $T = -1$. When $T > 0$ we subtract $\Delta\Theta$ from θ_0 . However, $\Delta\Theta$ is added to θ_0 when $T < 0$. Every time there is a change in sign of T , between iterations, the size of $\Delta\Theta$ is halved. When equation (1.29) is satisfied we accept this solution and the process is stopped. This is shown schematically in figure (1.22).

1.8.3 Flow Diagram describing how the program is executed.

The computer program was executed on a UNIX workstation using ANSI C code written by the author. The details of the program may be found in Appendix J, however, the main features are shown in the flow chart below.

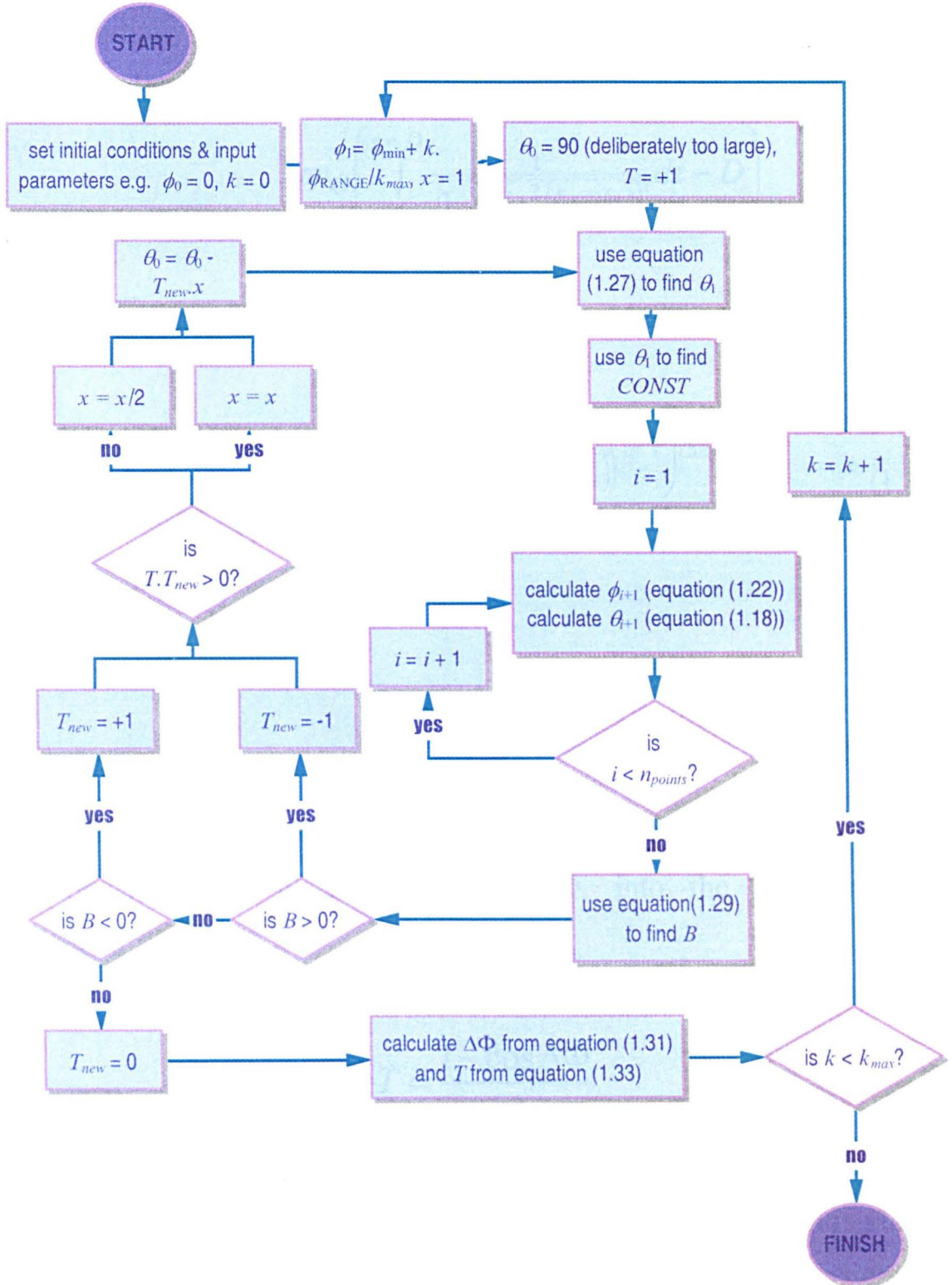


Figure 1.22: Shows the main features of the program used to solve the PDEs of § 1.7.

1.8.4 Phase Difference and Transmittance

Once we had obtained solutions for a range of applied voltages, we needed to convert this information into a transmittance versus applied voltage curve, as this was the form that the experimental data took. We achieved this by initially converting θ and ϕ data into phase differences, $\Delta\Phi$, for each applied voltage [31, 38], i.e.

$$\Delta\Phi = \frac{2\pi n_O \left(\int_{z=0}^{z=D} \frac{1}{\sqrt{1-R(\sin^2(\frac{\pi}{2}-\theta(z)))}} dz - D \right)}{\lambda}, \quad (1.30)$$

in finite difference notation this becomes:

$$\Delta\Phi = \frac{2\pi n_O \left(\sum_{i=0}^{i_{\max}} \frac{1}{\sqrt{1-R(\sin^2(\frac{\pi}{2}-\theta_i))}} - 1 \right) \Delta z}{\lambda}, \quad (1.31)$$

where λ is the wavelength of light and

$$R = \frac{n_E^2 - n_O^2}{n_E^2}. \quad (1.32)$$

with the ordinary refractive index n_O and the extraordinary refractive index n_E . Converting the phase difference, $\Delta\Phi$, into the light intensity transmitted¹³, T :

$$T = \frac{1 - \cos \Delta\Phi}{2} \quad (1.33)$$

which is expressed as a ratio of the light incident on the cell to the light that is transmitted (varying between zero and one), given that the cell is placed between crossed polarisers. As a consequence of the crossed polarisers: an

¹³ Also called the 'normal-incident transmission retardation measurement'[30]

even number of π phase differences results in darkness ($T = 0$), while an odd number of π phase differences results in maximum in light transmittance ($T = 1$). It is advantageous to plot the phase difference data as well as the transmittance curves. This is because the phase difference data is easier to analyse than the transmittance data, as very similar phase difference curves can result in seemingly totally different transmittance curves. The location of the turning point of the phase difference curves changes the shape of the central region of the transmittance curves.

There were two main motivating forces behind this work. The first was to see how individual continuum-model parameters could change the properties of the system and the second was to establish if this method could be used to reproduce experimental results. These are both dealt with in sections 1.9.1 and 1.9.2 respectively, of the Results and Discussion section.

1.9 Results and Discussion

This section is subdivided into two further sections, numbered § 1.9.1 and § 1.9.2. The first subsection is a theoretical examination of the system, involving varying input parameters to see what influence they exert upon the system. The second section then uses this information and understanding to assist in the simulating of experimental data. In the first section, by examining these effects, we can gain an understanding of *how* and *why* the parameters affect the system as they do. This knowledge can then be used to aid the design of future HAN cells, and enable recognition, in existing HAN cells, of the *fingerprints* of individual parameters. This assists in the modelling of real HAN cells in § 1.9.2, i.e. allowing 'educated guesses' to be made for the input parameters.

Section 1.9.1 starts by introducing the general input parameters, and specifies which are to be examined. Following this is an introduction to the different types of graph used in this section. The main body is then devoted to a systematic examination of numerous scenarios, with a running discussion alongside. The major findings are summarised in a table and there is a brief discussion at the end of the section.

Section 1.9.2, as previously stated, is an examination of experimental data with the express purpose of simulation. There are two purposes for this: it provides an opportunity to validate the model by seeing if it is possible to emulate the real systems; and the parameters used to achieve these simulations will reveal a great deal about those real systems. The experimental data used came from two sources: Takahashi et al. [1] and Bartle [30].

There are two main nematic liquid crystals that are of interest in this thesis. These are E7 and MBBA. Bartle [30] concentrated on the LC mixture E7 and 10% solutions of dopant molecules in E7, whereas Takahashi et al. [1] worked with MBBA. It is particularly interesting to look at both these systems as they have opposing signs of $\Delta\epsilon$ to one another. Generally, section 1.9.1 is preoccupied with examining MBBA systems. However, where it is deemed relevant and interesting, E7 systems (or MBBA with the sign of its $\Delta\epsilon$ changed) are also examined. Section 1.9.2 not only deals with the simulations but also demonstrates how sensitive these systems are to variations in input parameters.

1.9.1 Theory and Trends

In this, the first half of the results section, the effects of varying different continuum-model parameters are examined in order to obtain knowledge of *how* each affects the system. For MBBA systems the list of general input parameters used can be found in table (1.9.1), that is to say that, unless otherwise stipulated, these are the values used in the simulations performed throughout § 1.9.1. When E7 systems are examined, the default parameters contained in table (1.9.2) are used.

The parameters and scenarios investigated in this part are varying:

- Cell thickness, D
- Dielectric anisotropy, $(\Delta\varepsilon = \varepsilon_p - \varepsilon_n)$
- Elastic constants, K_{11} and K_{33}
- Angles of easy axes, at $z = 0$ and D , i.e. θ_{0easy} and θ_{Deasy} respectively
- Flexoelectric constant, $e = e_{11} + e_{33}$
- Homeotropic anchoring energy, A_{θ}
- Birefringence, $\Delta n = n_E - n_O$

Some of the parameters could be combined to produce some interesting properties; they therefore warranted further investigation. These included varying elastic constants when the flexoelectric coefficient, e , is either large or small. Various combinations of varying flexoelectric coefficient and homeotropic anchoring energy are a rich area of interest. The effects of changing the sign and magnitude of $\Delta\varepsilon$ are further complicated by changing e and/or A_{θ} , and so these are examined towards the end of this subsection. There, E7 is examined in similar detail to MBBA, thereby providing a comprehensive overview of HAN cell behaviour.

The effects of changing homogeneous anchoring energies are not shown here. The reason for this is that preliminary examination revealed that the computer program would only 'work' for relatively large values of $A_{\theta D}$, and within this range the effects of varying homogeneous anchoring energy were negligible.

Table 1.9.1: Shows the general input parameters used in § 1.9.1. Unless otherwise stipulated, the parameters and material constants used in the calculations, corresponding to MBBA, are shown below.

Angle of easy axis (at $z = 0$)	θ_{0easy}	=	90°	[1]
Angle of easy axis (at $z = D$)	θ_{Deasy}	=	2°	[1]
Cell thickness	D	=	$28.5 \mu\text{m}$	[1]
Elastic constant splay	K_{11}	=	$6.4 \times 10^{-12} \text{ N}$	[23]
Elastic constant bend	K_{33}	=	$8.2 \times 10^{-12} \text{ N}$	[23]
Anchoring energy (at $z = 0$)	$A_{\theta 0}$	=	$1.2 \times 10^{-5} \text{ J.m}^{-2}$	moderate ¹⁴
Anchoring energy (at $z = D$)	$A_{\theta D}$	=	$5.0 \times 10^{-2} \text{ J.m}^{-2}$	arbitrarily high
Relative permittivity normal	ϵ_n	=	5.4	[31]
Relative permittivity perpendicular	ϵ_p	=	4.7	[31]
Dielectric anisotropy	$\Delta\epsilon$	=	-0.7	[31]
Wavelength of light	λ	=	550 nm	[1]
Flexoelectric coefficient	E	=	$-5.0 \times 10^{-11} \text{ C.m}^{-1}$	arbitrary
Refractive index ordinary	n_o	=	1.57	[31]
Refractive index extraordinary	n_e	=	1.8	[31]
Birefringence	Δn	=	0.23	[31]

¹⁴ This is a moderate anchoring energy, and is of the same order of magnitude as is typical for polyimide homeotropic alignment layers.

Table 1.9.2: Shown below, unless otherwise stipulated, are the parameters and material constants used in the calculations for systems containing E7.

Angle of easy axis (at $z = 0$)	θ_{0easy}	=	90°	[30]
Angle of easy axis (at $z = D$)	θ_{Deasy}	=	2°	[30]
Cell thickness	D	=	$28.5 \mu\text{m}$	[1]
Elastic constant splay	K_{11}	=	$11.1 \times 10^{-12} \text{ N}$	[37]
Elastic constant bend	K_{33}	=	$17.1 \times 10^{-12} \text{ N}$	[37]
Anchoring energy (at $z = 0$)	A_ω	=	$1.2 \times 10^{-5} \text{ J.m}^{-2}$	moderate
Anchoring energy (at $z = D$)	$A_{\theta D}$	=	$5.0 \times 10^{-2} \text{ J.m}^{-2}$	arbitrarily high
Relative permittivity normal	ϵ_n	=	5.2	[37]
Relative permittivity perpendicular	ϵ_p	=	19	[37]
Dielectric anisotropy	$\Delta\epsilon$	=	+13.8	[37]
Wavelength of light	λ	=	633 nm	[31]
Flexoelectric coefficient	E	=	$-5.0 \times 10^{-11} \text{ C.m}^{-1}$	arbitrary
Refractive index ordinary	n_o	=	1.51821	[37]
Refractive index extraordinary	n_e	=	1.73283	[37]
Birefringence	Δn	=	0.21462	[17]

Before these different parameters are examined, it is necessary to introduce the various graphical forms in which the results are presented and the meaning of particular features within them. In experimental scenarios only transmittance data is available. However, here much more information is available due to the nature of the continuum modelling. It is important to know how this information can be used to aid understanding of a system's behaviour.

1.9.1.1 Introduction to figure types

These next two pages serve as an introduction to the five different figure types in which different graphs are used to demonstrate specific features of HAN cells. There are seven different graph types contained within five figure types, these figure types are:

Type 1 shows phase difference $\Delta\Phi$ (left) and transmittance (right) against voltage, where the key applies to both;

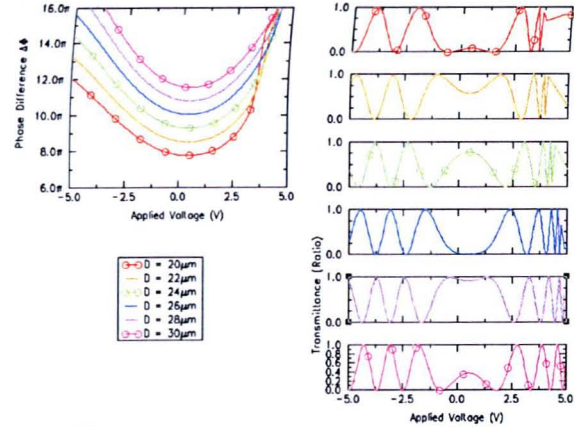
Type 2 shows the derivative (with respect to voltage) of the phase difference curve, i.e. $d(\Delta\Phi)/dV$, versus voltage;

Type 3 shows how the director, θ and the potential, ϕ , vary across the cell, i.e. with z , for three of the lines shown in figure types 1 and 2.

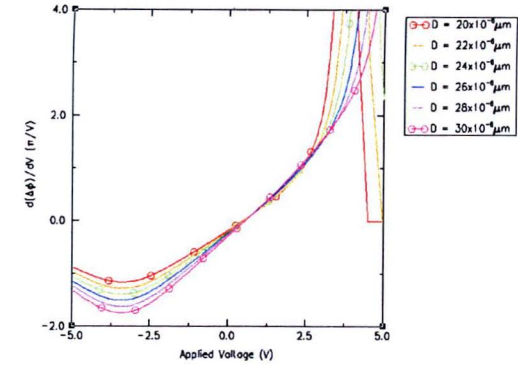
Type 4 shows how the voltage of the 'central feature' shifts with varying parameter.

Type 5 shows how the phase difference of the 'central feature' shifts with varying parameter.

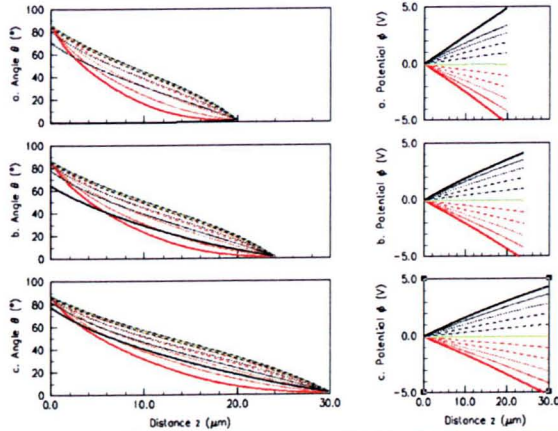
N.B. The definition of the central feature is defined on the next page.



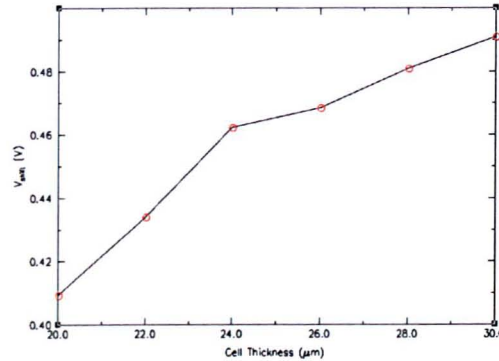
Type 1 Shows: on the right, the transmittance as a function of voltage, this information is available experimentally; and, on the left, the phase difference against voltage. The transmittance curves are the phase difference curves acted on by equation (1.33), i.e. $T = (1 - \cos \Delta\Phi)/2$



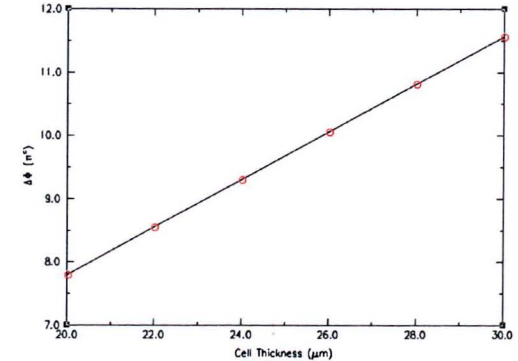
Type 2 Shows the gradient of the phase difference curves, left hand side of Type 1. This can be used to obtain a better appreciation of the asymmetry of the phase and transmittance curves.



Type 3 Shows what is happening inside the cells, both in terms of ϕ and θ , and can therefore lead to an understanding of why the observed trends occur.



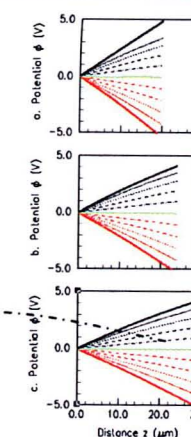
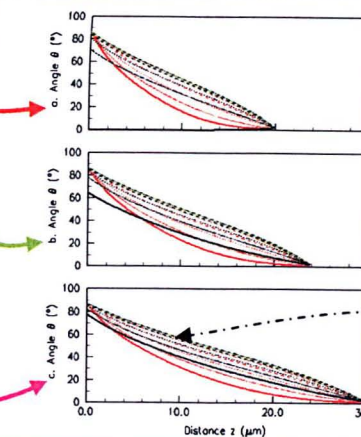
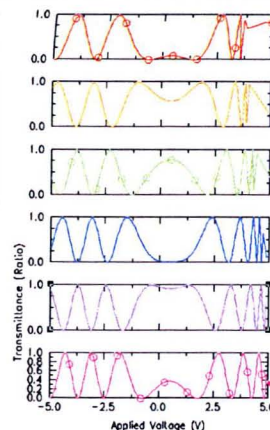
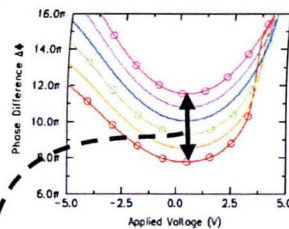
Type 4 Shows the voltage shift, also called the flexoelectric voltage shift, of the central feature as a function of the variable parameter. In so doing these graphs demonstrate that there are other parameters that can influence this voltage shift.



Type 5 Shows the phase shift of the central feature as a function of the variable parameter. Thus showing how varying a parameter changes the effective birefringence of the cell at the central feature.

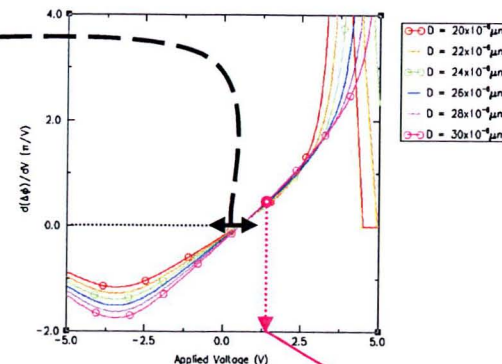
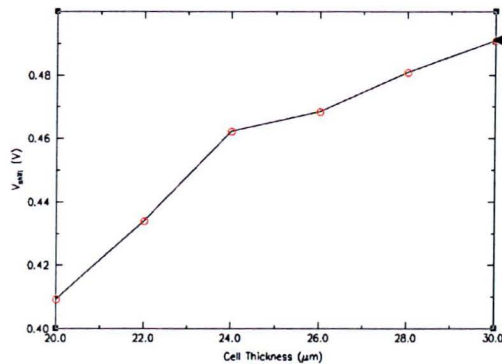
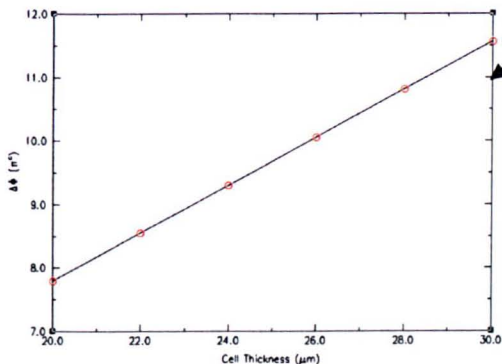
On this page, how the details of individual graphs and figures are inter-related is shown more clearly. This is shown by arrows pointing from one feature of a particular graph and how it is then transferred/depicted on another graph. (Note that the figures are no longer in the same order as on the previous page)

Type 1 is related to the amount that $\Delta\Phi$ of the central feature changes from one curve to the next (see key on type 1 to get x axis on type 5). Type 3 is related to the lines with circles on them, in types 1 and 2: the red lines of types 1 and 2 map to set (a), green to set (b), and cerise to (c). The individual circles in types 1 and 2 pertain to individual lines in type 3; these can be found by reading the voltage off the x axis in either type 1 or 2, then finding the line on the appropriate ϕ graph (according to line colour in types 1 and 2) whose ϕ value at $z = D$ is the same voltage; then the θ curve with the same colour and pattern corresponds to the same voltage.



Type 1 The director and potential profiles that resulted in these phase and transmission curves are shown in figure type 3.

Type 3 The three graphs on the left hand side are the director profiles for different voltages, and the graphs on the right are the corresponding potentials across the cells



Type 5 This shows the $\Delta\Phi$ shift of the central feature with changes in an input parameter (see black arrow in figure type 1)

Type 4 This shows the voltage shift of the central feature with changes in an input parameter (see black arrow on figure type 2). The voltages for this graph are taken by reading off when $d(\Delta\Phi)/dV=0$ in figure 2. N.B. The central feature is defined by the voltage at which $d(\Delta\Phi)/dV=0$.

Type 2 The most important feature here is the location of $d(\Delta\Phi)/dV=0$, as it defines the central feature: it is the voltage of the turning point in figure type 1. A second use for this graph (equally true for figure type 1); is demonstrated by example: the cerise arrow shows how particular circled points on these curves are related to an individual line in figure type 3.

1.9.1.2 Varying cell thickness, D

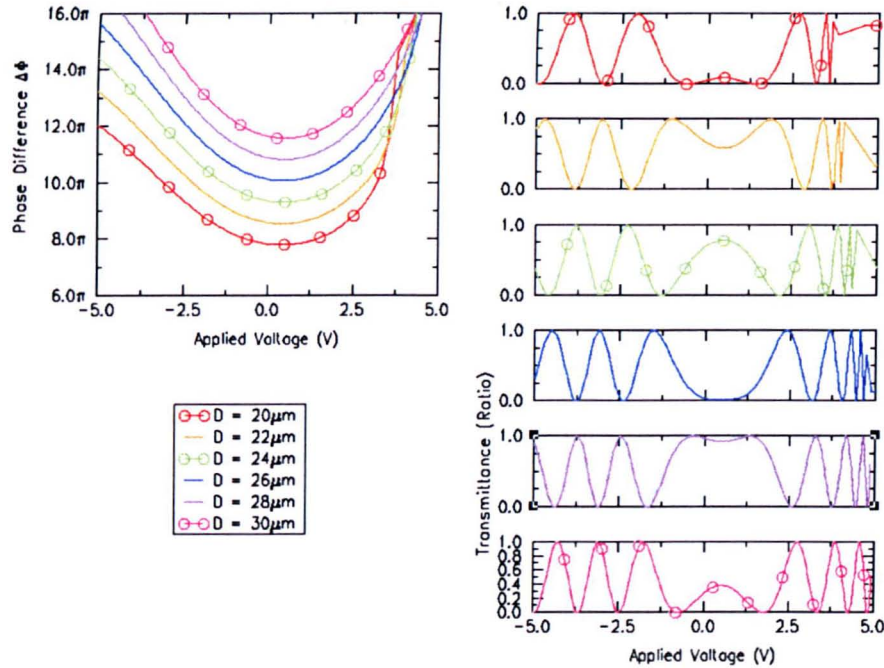


Figure (1.9.1.2.1) Transmittance and phase differences, $\Delta\Phi$, versus voltage for varying cell thickness, D .

Note that the trough of the blue $\Delta\Phi$ curve (left), $D = 26 \mu\text{m}$, corresponds to an even number of π ; we see this $\Delta\Phi$ corresponds to a minimum in transmittance (right). By contrast, the trough of the purple $\Delta\Phi$ curve ($D = 28 \mu\text{m}$) occurs at approximately an odd number of π , and so the magnitude of its transmittance in its central region is close to 1.

From the phase difference versus voltage curves, it can be seen that increasing cell thickness increases the phase difference for all voltages and that all the $\Delta\Phi$ curves appear to be roughly the same shape (c.f. the red $\Delta\Phi$ curve of $D = 20 \mu\text{m}$ with that of the cerise $\Delta\Phi$ curve of $D = 30 \mu\text{m}$). To find out more

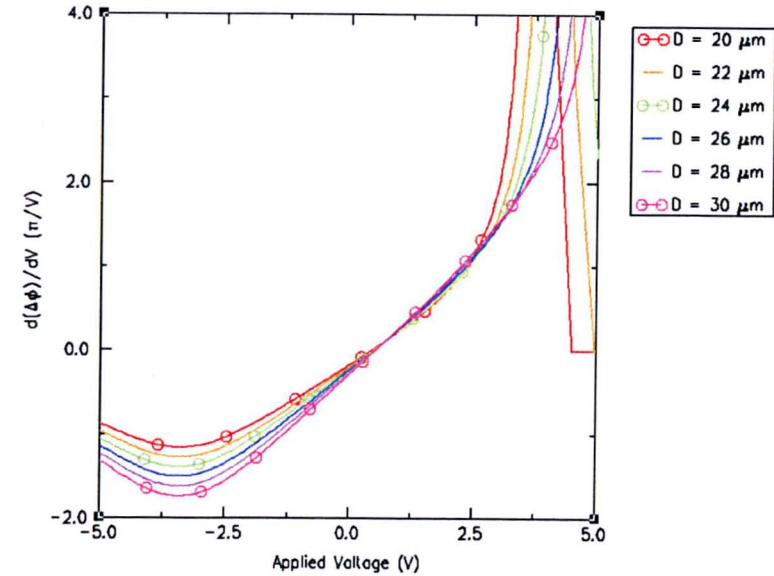


Figure (1.9.1.2.2) Rate of change of phase difference $\Delta\Phi$ against voltage for varying cell thickness, D .

It is seen here that the $d(\Delta\Phi)/dV$ curves are not identical for all cell thicknesses, D . While in the region -1 to $+3$ V the gradients of the curves are very similar, outside of this region varying cell thickness changes the gradient of the curves; we find that increasing D decreases the gradient of these $\Delta\Phi$ for positive voltages and increases it for negative voltages (c.f. red and cerise curves). In doing so, it appears that increasing cell thickness increases the rotational symmetry of these curves, and therefore the reflection symmetry of the phase and transmittance curves of the previous figure (1.9.1.2.1). For an example of this, compare the cerise transmittance curve for $D = 30 \mu\text{m}$ in Fig (1.9.1.2.1),

conclusively if the curves are the same shape, merely shifted by $\Delta\Phi$, it is constructive to examine the *gradient* of $\Delta\Phi$ curves, with respect to voltage, as if all the curves were the same shape $d(\Delta\Phi)/dV$ curves would all be identical.

$D = 20 \mu\text{m}$. To find an explanation for this trend examine the θ and ϕ curves shown in the figure (1.9.1.2.3).

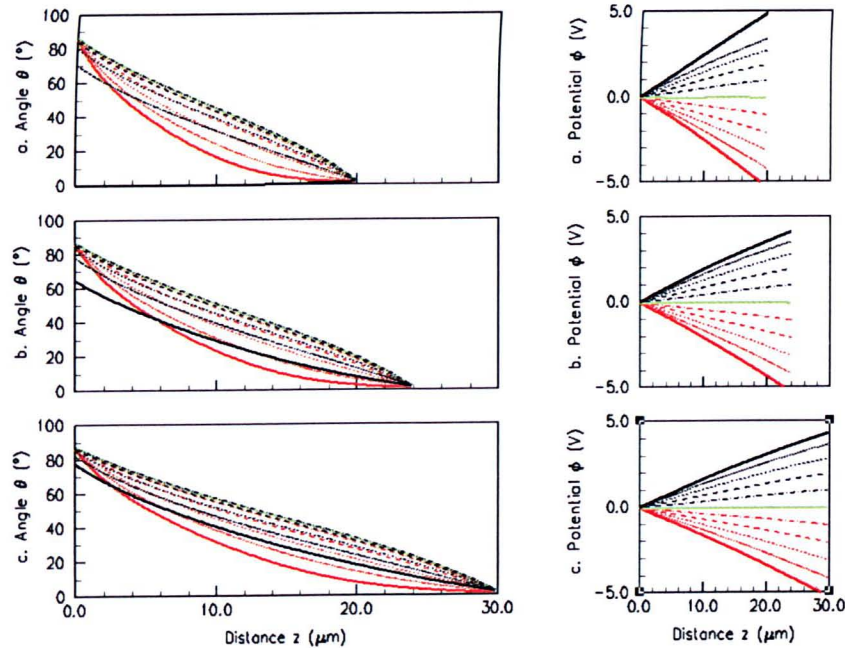


Figure (1.9.1.2.3) Shows director profile, θ , and electrical potential, ϕ , versus distance, z , for varying cell thickness, D :

- (a) $D = 20 \mu\text{m}$
- (b) $D = 24 \mu\text{m}$
- (c) $D = 30 \mu\text{m}$

The red lines of figures (1.9.1.2.1) and (1.9.1.2.2) correspond to the pair of (a) graphs in this figure; similarly green maps to (b) and cerise to (c). The first thing to note, which is obvious, is that the curves of set (a) stop at $z = 20 \mu\text{m}$; likewise, (b) terminates at $z = 24 \mu\text{m}$; and (c) at $z = 30 \mu\text{m}$, i.e. the θ curves terminate at $z = D$.

The reason for the steepening of the $\Delta\Phi$ curves for positive voltages, seen in figures (1.9.1.2.1) and (1.9.1.2.2), can be appreciated by comparing the black θ curves of graph (a) with those in graphs (b) and (c). In the θ graph of (c) the angle of the director at $z = 0 \mu\text{m}$ is fairly well behaved, remaining in the region 80 to 90°; however, this is not so for the thinner cells where the black curves (positive voltages) stray further from this region.

By contrast, the shallowing of the $\Delta\Phi$ curves for negative voltages are explained by examining what happens to the red curves (negative voltages) when D is reduced, then these negative voltage curves are more 'bowed' than their positive voltage counterparts; this trend is more marked as D is reduced.

Both of these trends contribute to the increasing asymmetry of the transmittance curves with decreasing cell thickness. It should also be noted that, while each ϕ graph has lines terminating at similar voltages to those in the other ϕ graphs, the gradients of the ϕ curves in (a) are greater than those in (c), i.e. the electric field strength within a thin cell is greater in the thinner cells than for a thicker cell with the same voltage across it.

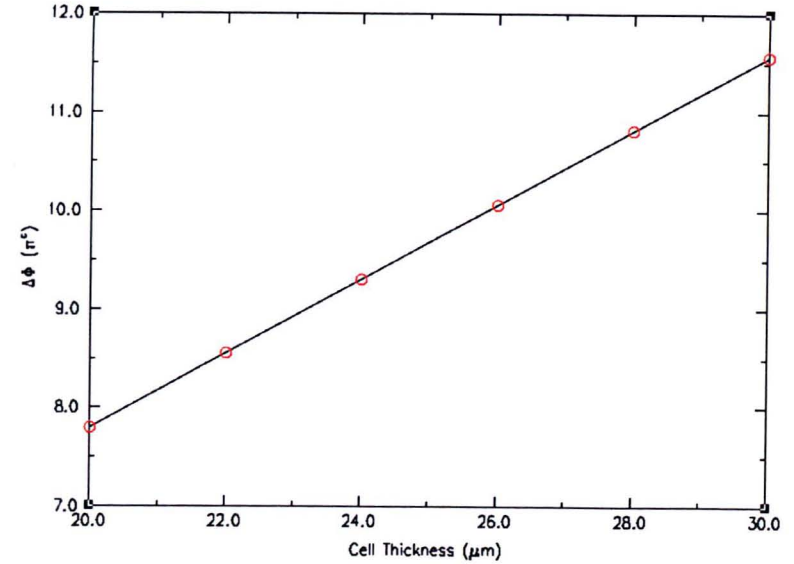
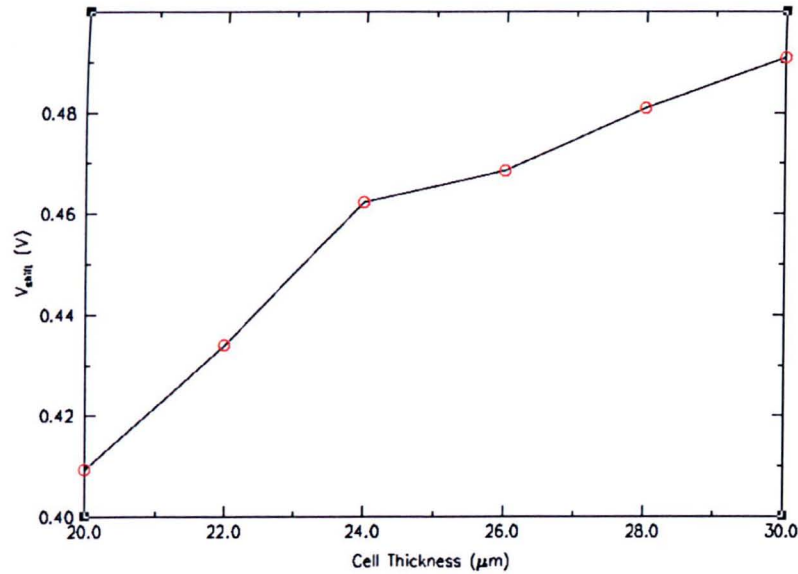


Figure (1.9.1.2.4) Shows voltage shift against cell thickness, D .

The voltage shift of the central feature increases slightly with increasing thickness. This increase is roughly +0.07 V per 10 μm , which is small. There is a 'kink', at $D = 24 \mu\text{m}$, which may be dismissed as insignificant as the y -axis is very sensitive.

Figure (1.9.1.2.5) Shows phase difference shift against cell thickness, D .

In contrast, the change in phase difference is much more marked, being roughly $3\frac{3}{4}\pi/10\mu\text{m}$. The explanation of this is simply that increasing the cell thickness increases the effective birefringence of the cell. Thus, by increasing the cell thickness, it is possible to cycle up through different wave plate values.

Summary of varying cell thickness, D

For the present system the voltage shift of the central feature is roughly +0.07 V per 10 μm and the shift in the phase difference of the central feature is roughly $3\frac{3}{4}\pi$ per 10 μm . More generally, increasing the cell thickness makes the cell's response more symmetrical.

1.9.1.3 Varying birefringence, Δn

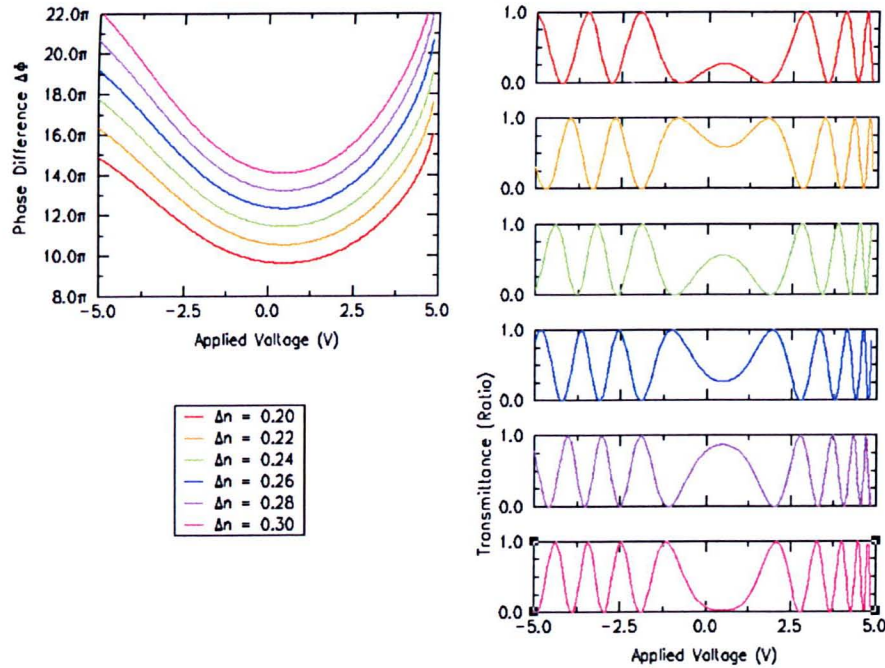


Figure (1.9.1.3.1) Shows transmittance and phase difference, $\Delta\Phi$, against voltage for varying birefringence, Δn

Here, almost exactly the same trends that were observed for increasing cell thickness are seen when the birefringence, Δn , is increased. This equivalence is due to a material's innate birefringence can be mimicked by a cell's effective birefringence as viewed externally, due to cell thickness: if the cell thickness is increased or the innate birefringence of the material is increased, then the effective birefringence of the cell will similarly grow. This is better exemplified in the following graph.

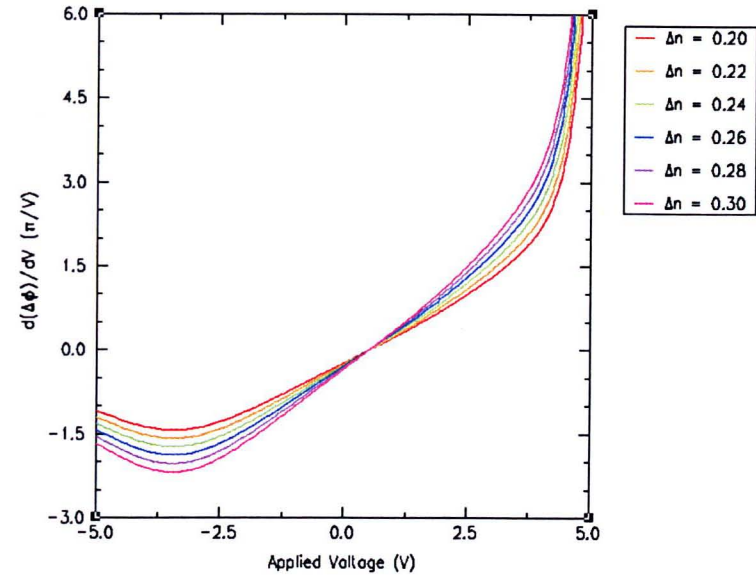


Figure (1.9.1.3.2) Shows the rate of change of phase difference, i.e. $d(\Delta\Phi)/dV$, against voltage for varying birefringence, Δn

All these curves are identical in shape, where the only changes are that they are scaled according to the size of Δn . This is because increasing Δn increases the rate of change of $\Delta\Phi$. The reason that this can be stated so categorically is the same reason why the graphs with the ϕ and θ curves for this system have not been included, i.e. the value of Δn is not instrumental in finding solutions for the PDEs, and therefore the ϕ and θ solution curves are unaffected by changes in Δn .

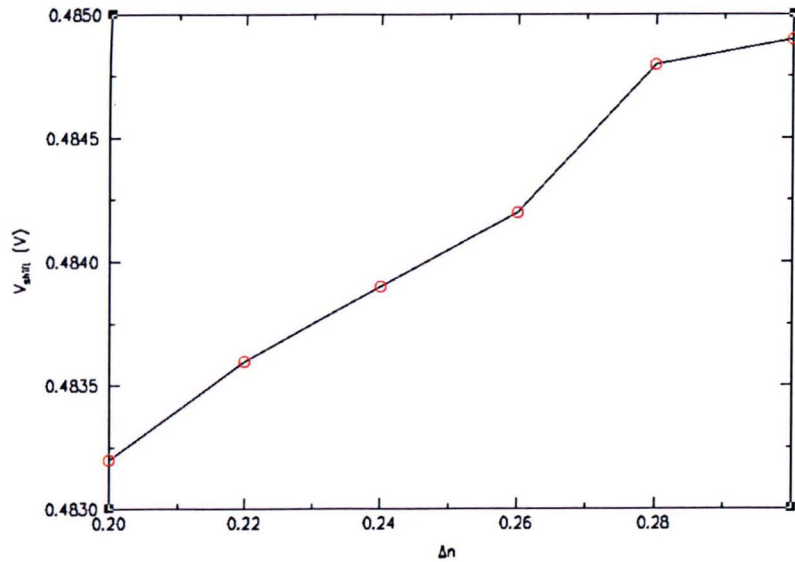


Figure (1.9.1.3.3) Shows voltage shift of the central feature against Δn .

The voltage shift of the central feature found from figure (1.9.1.3.2) and displayed here in figure (1.9.1.3.3) is 0.0016 V per 0.1 (change in Δn), which is miniscule.

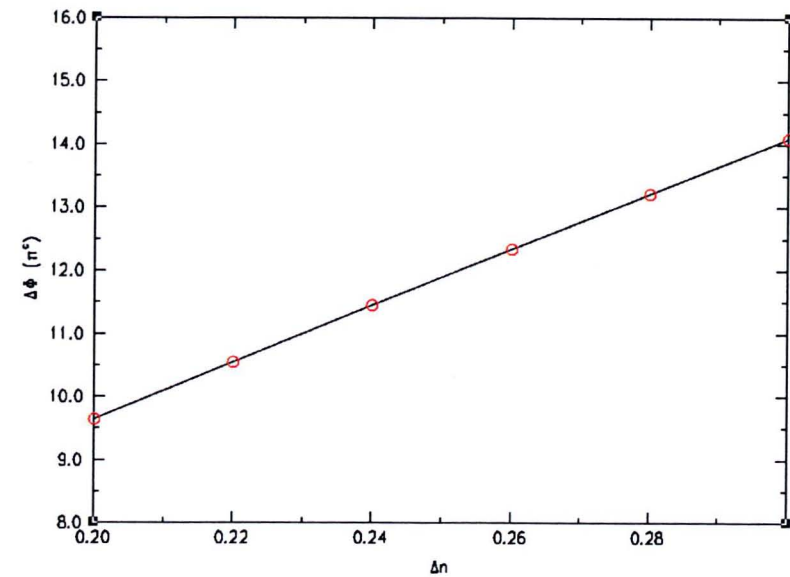


Figure (1.9.1.3.4) Shows $\Delta\Phi$ shift of the central feature against Δn .

The change in the phase difference, $\Delta\Phi$, of the central feature is $4\frac{1}{2}\pi$ per 0.1 (Δn), which is a significant increase: the effect due to a 0.1 change in Δn is greater than the effects seen when cell thickness was increased by 10 μm .

Summary of the effects of varying birefringence, Δn

Increasing Δn has similar effects to increasing the cell thickness. However, it does not change the director or electric field profiles and therefore is just a shifting and scaling of the $\Delta\Phi$ curves.

1.9.1.4 Varying elastic constants, K_{11} and/or K_{33} .

There are two elastic constants relevant to this system. These are the *splay* and *bend* coefficients K_{11} and K_{33} respectively. Here we look at three scenarios. We see how the cell behaves when: K_{11} is varied while K_{33} is held constant; K_{33} is varied while K_{11} is fixed; and K_{11} is made equal to K_{33} , and they are varied together. In addition, preliminary investigations showed that the responses of the system to these changes depended on the magnitude of e , and for that reason we carry out this process twice, i.e. for both large and small e (-5×10^{-11} C m $^{-1}$ and -1×10^{-11} C m $^{-1}$ respectively). Firstly, we examine the behaviour of the system when e is small.

1.9.1.4.1 Varying elastic constants, K_{11} and/or K_{33} when flexoelectric coefficient small, $e = -1 \times 10^{-11} \text{ C m}^{-1}$.

1.9.1.4.1.1 Varying the bend coefficient, K_{33} , while the splay coefficient is held constant, $K_{11} = 7 \times 10^{-12} \text{ N}$.

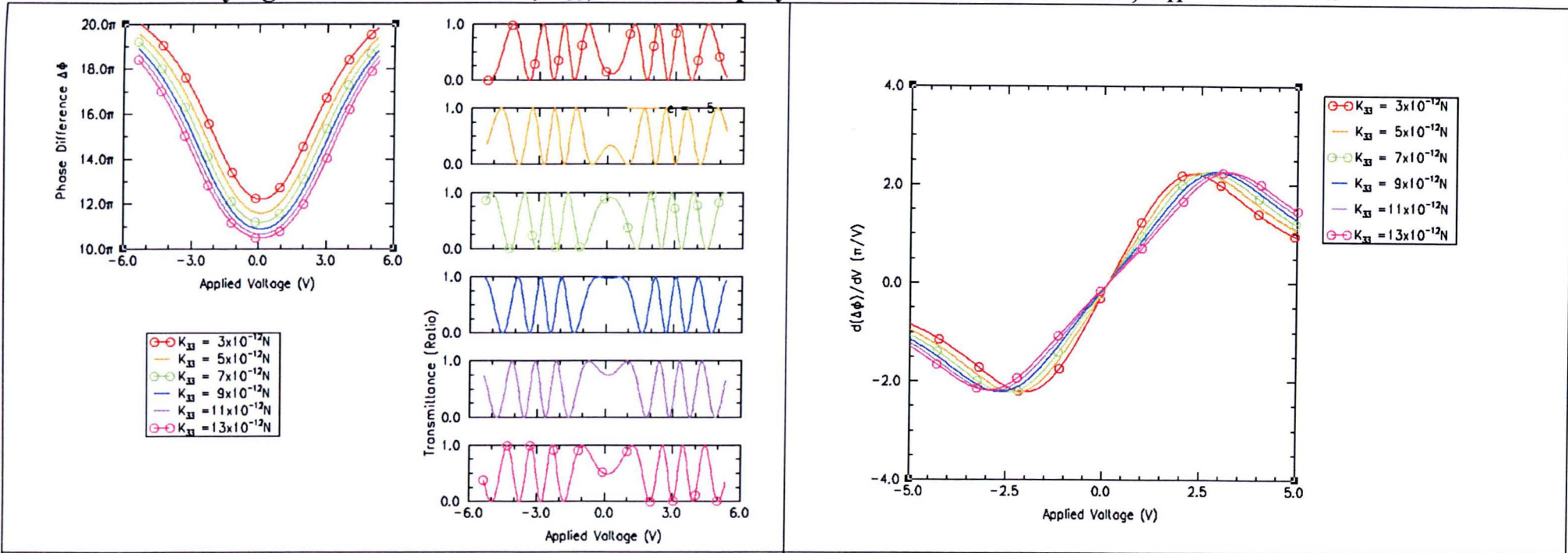
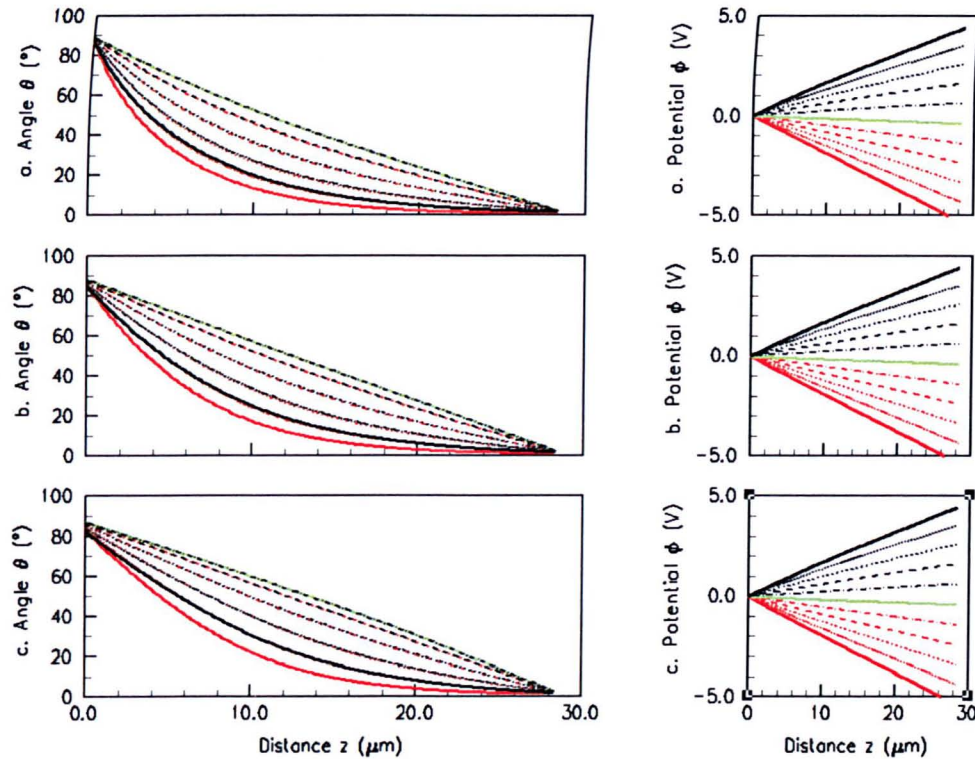


Figure (1.9.1.4.1.1) Shows transmittance and phase difference, $\Delta\Phi$, against voltage for varying K_{33} (while e is small)

From this phase difference graph (in figure (1.9.1.4.1.1)) two main points can be noted. Firstly, note that increasing K_{33} decreases the phase difference curve (for all voltage) but that this shift becomes less pronounced as K_{33} continues to increase. Secondly, the red curve's ($K_{33} = 3 \times 10^{-12} \text{ N}$) turning point (in the $\Delta\Phi$ graph) is sharper than for the other curves. This is borne out by the next graph (figure (1.9.1.4.1.2))

Figure (1.9.1.4.1.2) Shows the rate of change of phase difference, $\Delta\Phi$, against voltage for varying K_{33} (while e is small)

Between + and - 2 volts, i.e. in the central region, the red curve ($K_{33} = 3 \times 10^{-12} \text{ N}$) is steeper than the other curves ($K_{33} > 3 \times 10^{-12} \text{ N}$). Outside this voltage range, however, this trend in the gradient of $\Delta\Phi$ reverses. This combination results in a curious feature in figure (1.9.1.4.1.1), i.e. all the phase difference curves appear to be parallel to each other, never crossing one another.



Here we are able to see how varying the elastic constant K_{33} changes the director profile across the cell.

The top two panels (i.e. (a)) correspond to $K_{33} < K_{11}$ and the bottom two panels (i.e. (c)) show what happens when $K_{33} > K_{11}$. In graphs (b), where $K_{11} = K_{33}$, the zero voltage curve (green curve) in the θ graph is a straight line between 90° and 2° at $z = 0$ and $D \mu\text{m}$ respectively. However, when K_{33} is smaller than K_{11} , graph (a), the director profile follows a path where θ is generally smaller than had been the case when the K s had been equal. Whereas, when K_{11} is smaller than K_{33} , graph (c), the director profile follows a path for which $\theta(z)$ is generally greater than in graph (b).

Examining the θ curves near $z = 0 \mu\text{m}$ we see that, when K_{33} is small, θ varies more rapidly with respect to z than when K_{33} is large. The converse is also true for z close to D , although this trend is slightly less marked.

Figure (1.9.1.4.1.3) Shows how θ and ϕ vary with respect to z , for varying K_{33} (while e is small):

- (a) $K_{33} = 3 \times 10^{-12} \text{ N}$
- (b) $K_{33} = 7 \times 10^{-12} \text{ N}$
- (c) $K_{33} = 13 \times 10^{-12} \text{ N}$

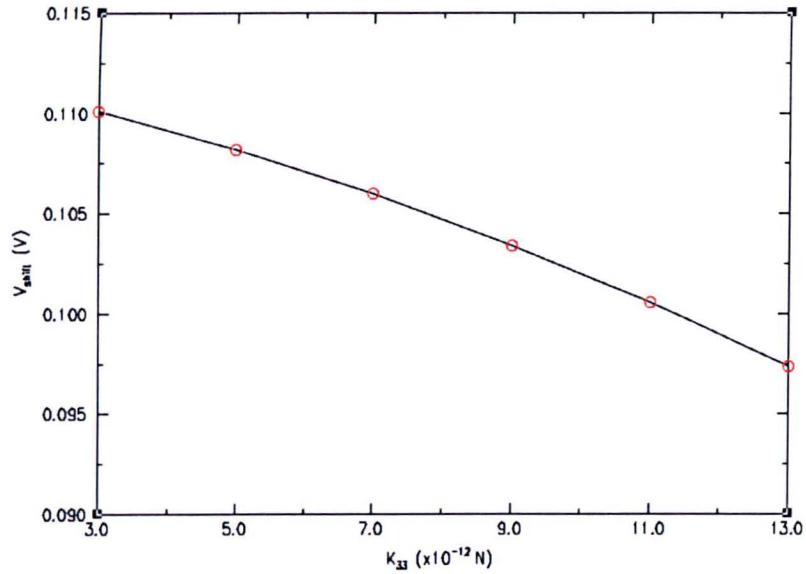


Figure (1.9.1.4.1.4) Shows voltage shift of the central feature against K_{33} (while e is small)

It is seen here that the changes in the observed voltage shift are small, only being roughly -0.015 V per 1.0×10^{-11} N. However, it should also be noted that this is not a straight-line relationship: the curve becomes gradually steeper as K_{33} increases.

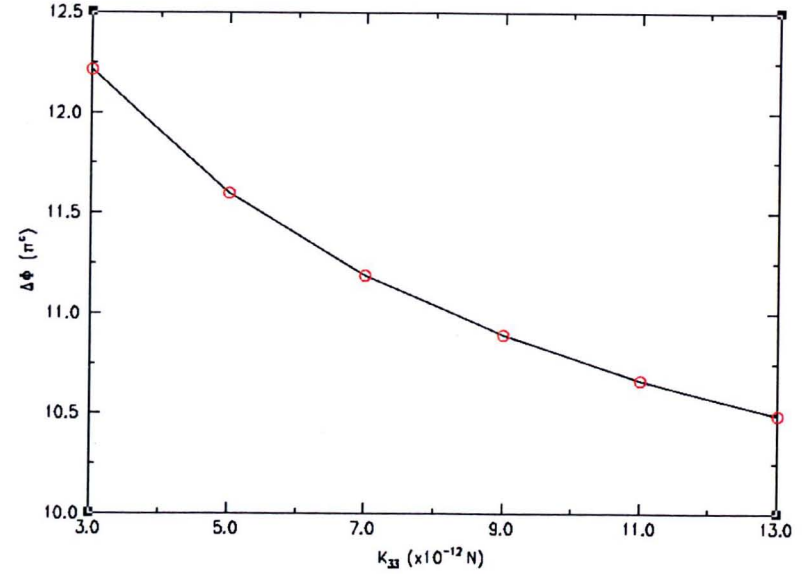


Figure (1.9.1.4.1.5) Shows $\Delta\Phi$ shift of the central feature against K_{33} (while e is small)

As with figure (1.9.1.4.1.4), this relationship is not linear but, in contrast to figure (1.9.1.4.1.4), this curve starts to level out as K_{33} increases. Over the range examined here, the change seen in $\Delta\Phi$ is -1.7π per 1.0×10^{-11} N, which is quite significant.

1.9.1.4.1.2 Varying the splay coefficient, K_{11} , while the bend coefficient is held constant, $K_{33} = 7 \times 10^{-12} \text{ N}$

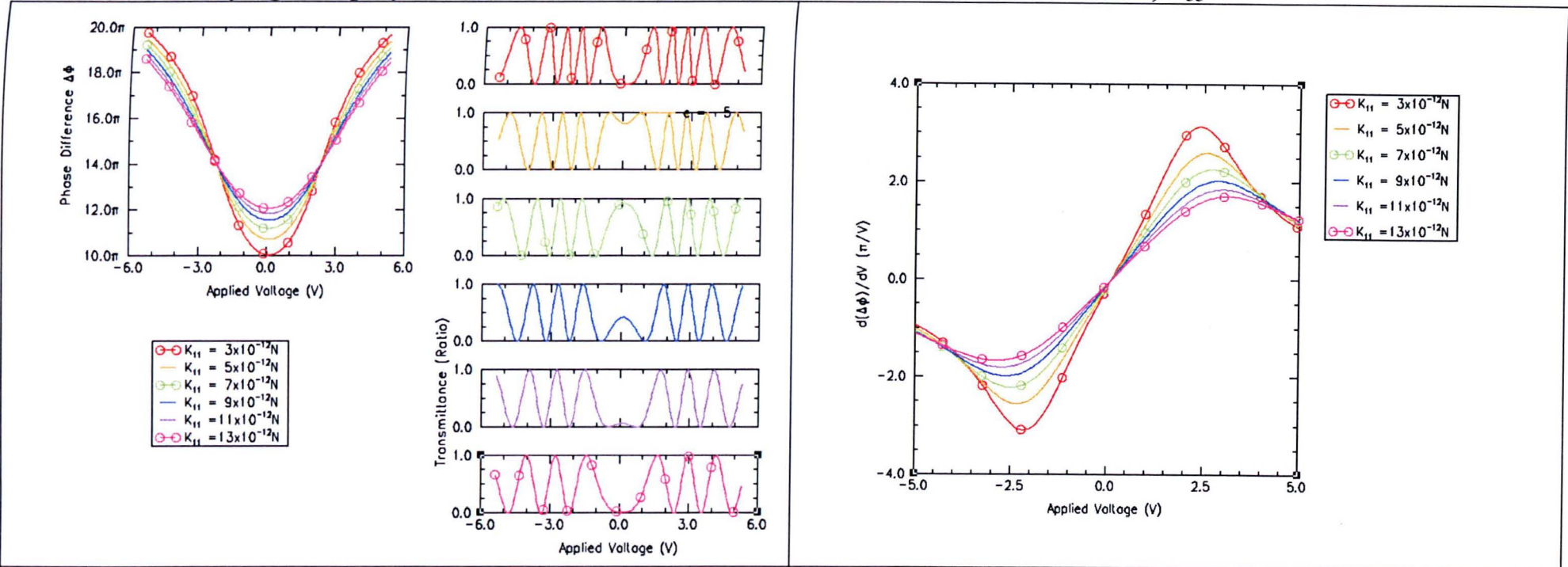


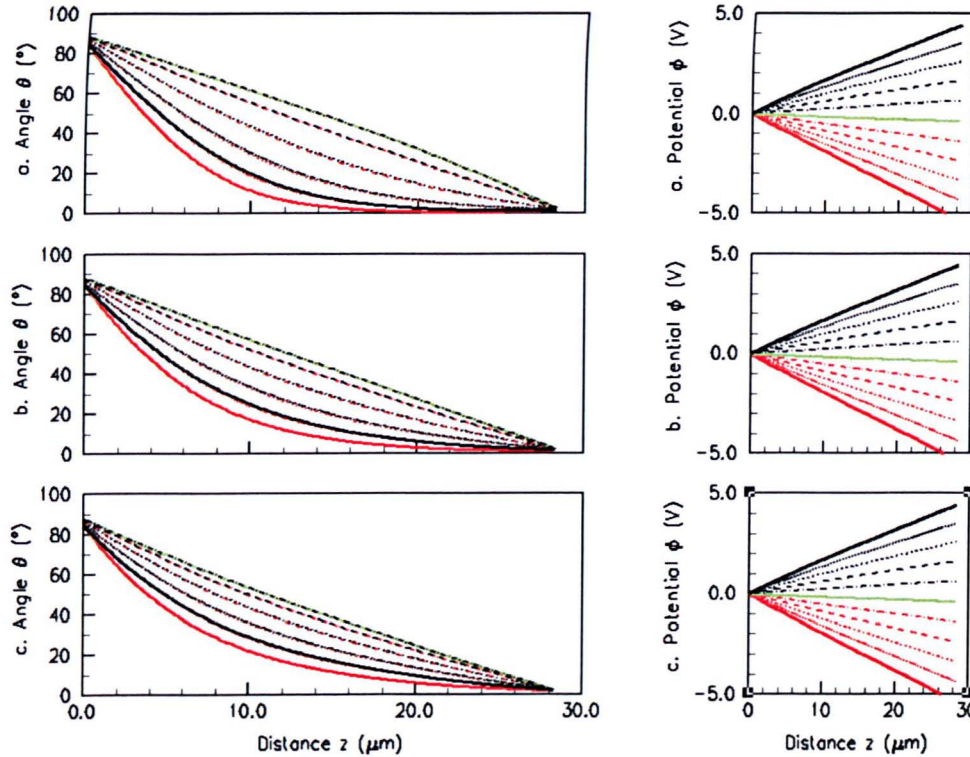
Figure (1.9.1.4.1.2.1) Shows transmittance and phase difference, $\Delta\Phi$, against voltage, for varying K_{11} (while e is small)

Again, it can be seen that an increase in an elastic coefficient results in a shallowing of the phase and transmittance curves. However, unlike when K_{33} is increased, increasing K_{11} increases the phase difference of the central feature. This combination of trends means that the phase difference curves actually cross one another (rather than being parallel, as was the case when K_{33} was varied instead). In fact, all this leads to the impression that varying K_{33} exerts greater influence on the system than K_{11} . This view is superficially confirmed when figure (1.9.1.4.1.2.2) is compared to figure (1.9.1.4.1.3.2) because outside of the central region of this figure (above) the transmittance curves look more alike (i.e. their

Figure (1.9.1.4.1.2.2) Shows the rate of change of phase difference, $\Delta\Phi$, against voltage, for varying K_{11} (while e is small)

We see in this figure that the observation of K_{33} 's apparent dominance in dictating the shape of the transmittance curves was an artefact of the location of where the phase difference curves cross one another in figure (1.9.1.4.1.2.1). However, we see here that changing K_{11} actually has a more significant effect on the rate of change of $\Delta\Phi$ than K_{33} had. Reducing K_{11} vastly changes the rate of change of $\Delta\Phi$, especially when this graph is compared with its parallel for varying K_{33} (i.e. figure (1.9.1.4.1.1.2)). This difference only subsides at voltages of larger magnitudes, i.e. $> | \pm 4 \text{ V} |$. The reason for this can be seen in the next set of graphs.

maxima and minima generally occur at similar voltages) than they did in figure (1.9.1.4.1.1.1) where the curves are markedly different across the whole voltage range.



While changing K_{11} changes the θ curve for zero volts (green curve), the most pronounced change in the θ graphs, between the three sets (a) to (c), occurs for larger positive and negative voltages. It is seen that increasing K_{11} has the effect of making the θ curves more tightly spaced, which corresponds to the shallowing of the $d(\Delta\Phi)/dV$ curve in figure (1.9.1.4.1.2.2). This can be seen in the (a) graphs (for $K_{11} = 3 \times 10^{-12} \text{ N}$) i.e. the separation between θ curves is greater than say for the $K_{11} = 13 \times 10^{-12} \text{ N}$ (i.e. the (c) graphs), that is to say that the system changes more rapidly when K_{11} is small.

Figure (1.9.1.4.1.2.3) Shows θ and ϕ against z for varying splay elastic constant, K_{11} (while e is small)

- (a) $K_{11} = 3 \times 10^{-12} \text{ N}$
- (b) $K_{11} = 7 \times 10^{-12} \text{ N}$
- (c) $K_{11} = 13 \times 10^{-12} \text{ N}$

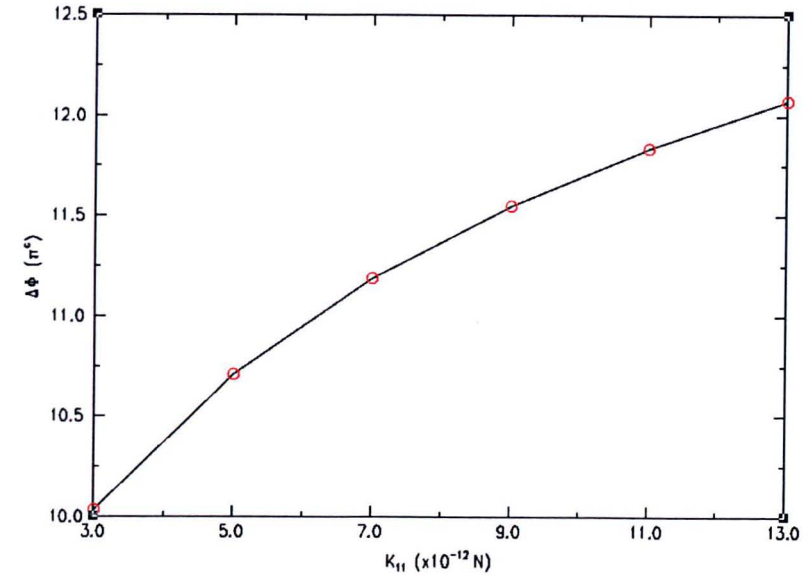
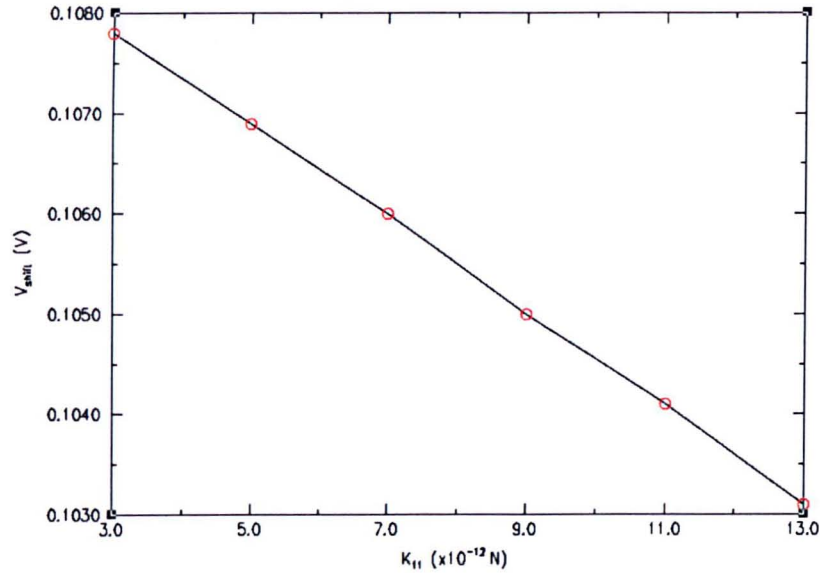


Figure (1.9.1.4.1.2.4) Shows voltage shift of the central feature against K_{11} (while e is small)

Increasing K_{11} has the effect of decreasing the magnitude of the flexoelectric voltage shift. The voltage shift of the central feature is very small, being only -0.005 V per 1×10^{-11} N. The response in this region is nearly a straight line

Figure (1.9.1.4.1.2.5) Shows $\Delta\Phi$ shift of central feature against K_{11} (while e is small)

The relationship between K_{11} and $\Delta\Phi$ is not a linear one but asymptotes as K_{11} increases. It should also be noted that, in contrast to the small changes in the voltage shift with varying K_{11} , the $\Delta\Phi$ of the central feature shifts a significant $2.1\pi/1 \times 10^{-11}$ N. As a result of this approximately 2π phase difference we see, if we return to figure (1.9.1.4.1.2.1), that the transmittance curves for $K_{11} = 3$ and 13×10^{-12} N (red and cerise respectively) exhibit the same shape for their central features.

1.9.1.4.1.3 Varying the splay and bend elastic coefficients such that $K_{11} = K_{33}$

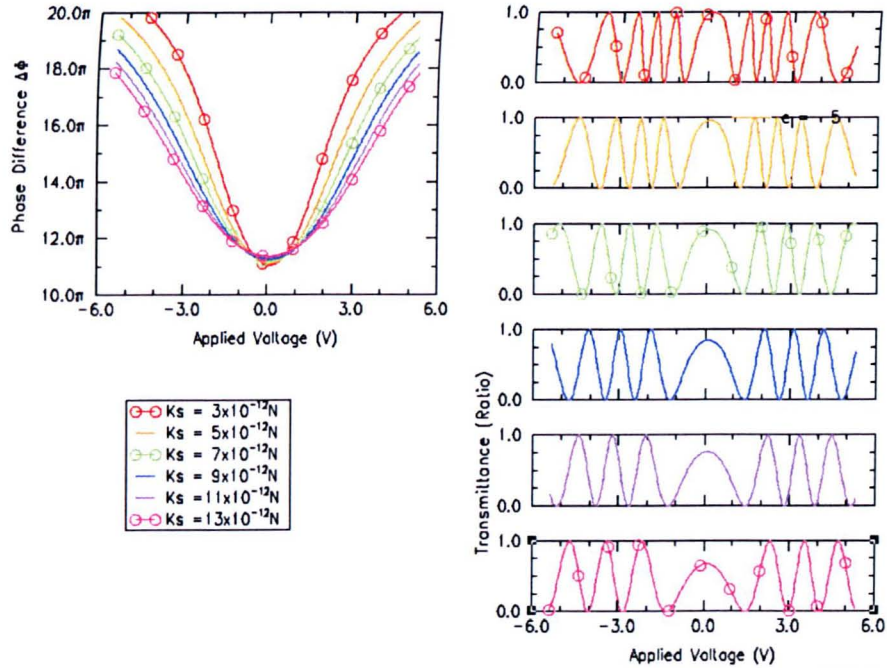


Figure (1.9.1.4.1.3.1) Shows transmittance and phase difference, $\Delta\Phi$, against voltage for varying K_{11} and K_{33} (while e is small)

A shallowing of all the phase difference curves is observed when the elastic constants are increased, c.f. the red curve of K_{11} and $K_{33} = 3 \times 10^{-12}$ N (which is steep), with the cerise curve of K_{11} and $K_{33} = 13 \times 10^{-12}$ N (which is comparatively shallow). However, keeping the two elastic constants equal appears to have the effect of keeping the phase difference of the central feature roughly constant.

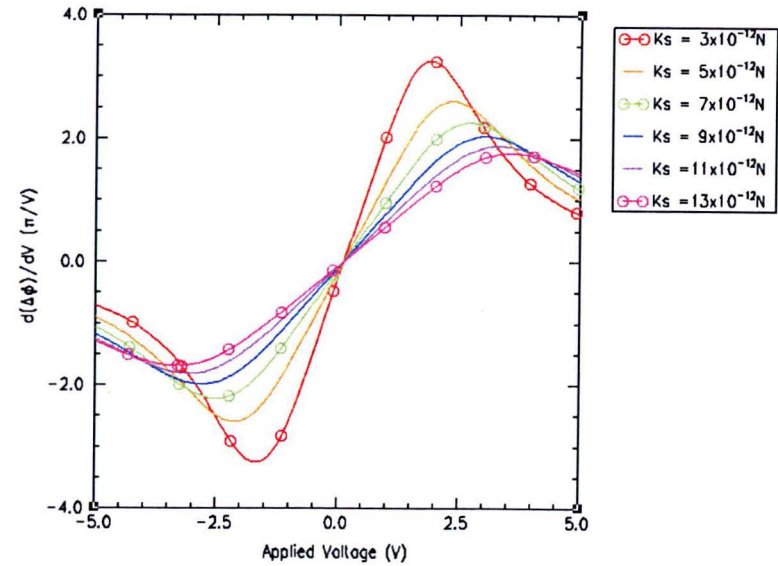
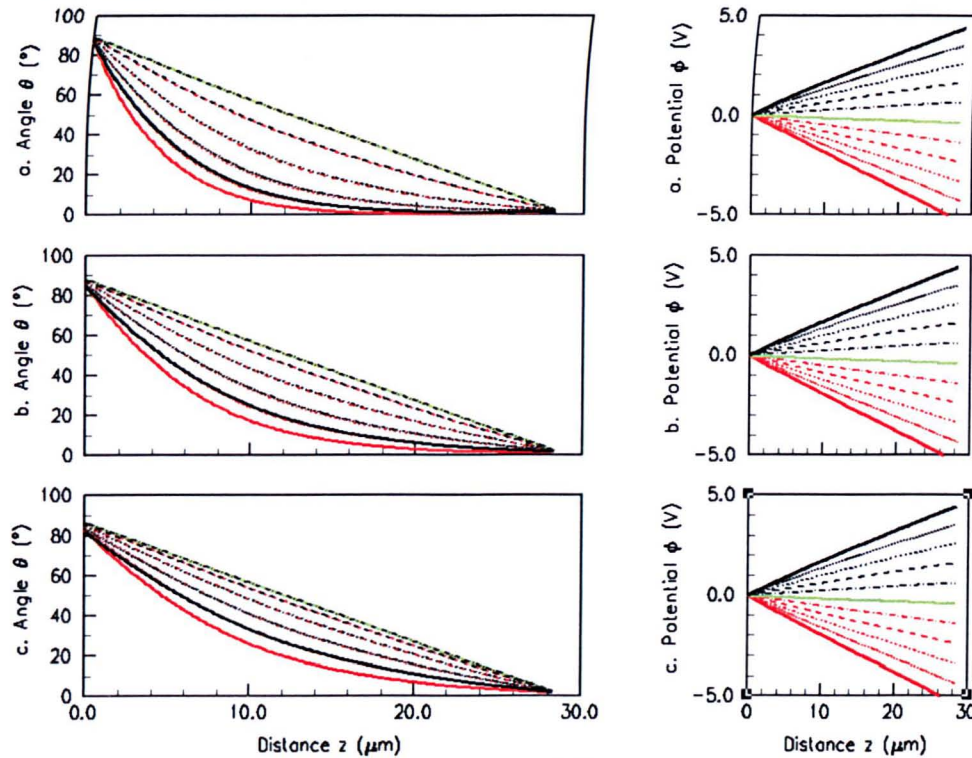


Figure (1.9.1.4.1.3.2) Shows the rate of change of phase difference $\Delta\Phi$ against voltage for varying K_{11} and K_{33} (while e is small)

It should be noted that these curves look remarkably similar to those of the K_{33} constant set (see figure (1.9.1.4.1.2.2)). This is further evidence that K_{11} is the dominant elastic constant parameter in dictating the *shape* of the phase difference curve, whereas K_{33} appears to be the more dominant of the two elastic constants with regards to the *location* of the curve (re: $\Delta\Phi$). However, the influence of K_{33} becomes more apparent when the magnitude of the voltage is greater than 3 V: the more pronounced crossing over of curves that had been observed in the K_{11} constant curves (see figure (1.9.1.4.1.2.2)) resurfaces here.



Here it can be seen that the zero voltage θ curves (solid green lines) for all three graphs look similar, all being roughly straight lines between $\theta(0)$ and $\theta(D)$. This explains why there is negligible change in the $\Delta\Phi$ of the central feature when the elastic constants are varied in this manner (c.f. the $\Delta\Phi$ s at the turning points of the red and cerise curves from graph (1.9.1.4.1.3.1)).

However, the θ curves for larger magnitude voltages become more closely spaced when the elastic constants are increased. This explains, once again, the shallowing observed in the phase difference curves, with increasing K_s , i.e. increasing the elastic constants increases the energy required to deform the system and therefore this reduces the effect an electric field will have.

Figure (1.9.1.4.1.3.3) Shows θ and ϕ against z for varying splay and bend elastic constants, $K_{11} = K_{33}$ (while e is small)

- (a) $K_s = 3 \times 10^{-12} \text{ N}$
- (b) $K_s = 7 \times 10^{-12} \text{ N}$
- (c) $K_s = 13 \times 10^{-12} \text{ N}$

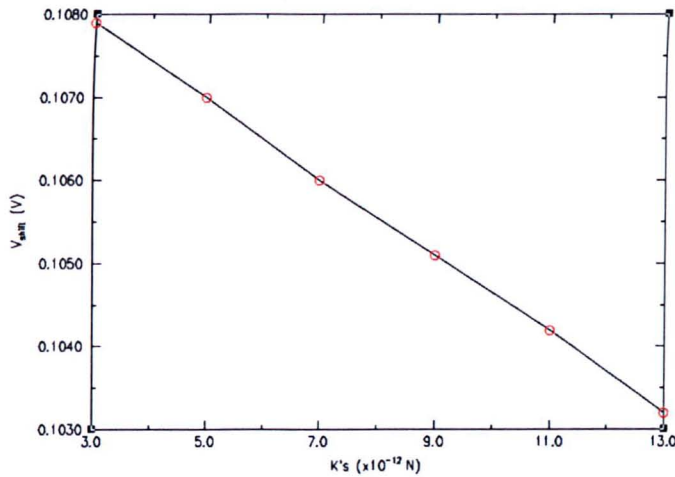


Figure (1.9.1.4.1.3.4) Shows voltage shift against elastic constants, $K_{11} = K_{33}$ (while e is small).

Once again, we see that changing the elastic constants causes only small changes in the voltage shift of the turning point of the phase difference curves (also referred to as 'the central feature'). The size of this shift is only -0.005 V per 1×10^{-11} N, and again, is a linear relationship.

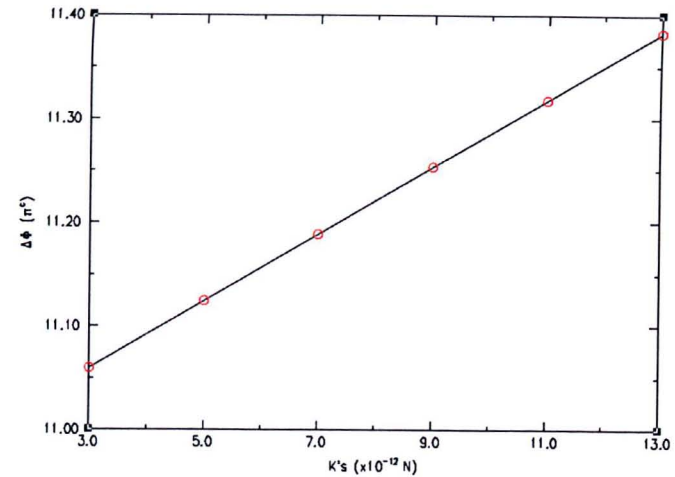


Figure (1.9.1.4.1.3.5) Shows $\Delta\Phi$ shift against elastic constants, $K_{11} = K_{33}$ (while e is small).

Here we see a small, but non-negligible, shift of 0.34π per 1×10^{-11} N in the $\Delta\Phi$ of the central feature of the curves.

Summary of varying elastic constants when flexoelectric coefficient, e , is small.

When the flexoelectric constant is small the transmittance, $\Delta\Phi$ and therefore the $d(\Delta\Phi)/dV$ curves all exhibit high degrees of symmetry and are relatively steep curves. The $d(\Delta\Phi)/dV$ curves for $K_{11} = K_{33}$ look remarkably similar to those of the K_{33} constant set (see figure (1.9.1.4.1.2.2)). This is evidence that K_{11} is the dominant elastic constant parameter in dictating the shape of the phase difference curve. It can be seen by comparing figures (1.9.1.4.1.1.5), (1.9.1.4.1.2.5) and (1.9.1.4.1.3.5) that K_{11} and K_{33} appear to exert roughly equal and opposite influences on the location of the central feature of the phase difference curves. However, the contribution from K_{11} is again slightly larger than that from K_{33} . That is to say that this system appears to be more sensitive to splay deformations than it is to bend deformations.

1.9.1.4.2 Varying the elastic constants when flexoelectric coefficient is large, $e = -5 \times 10^{-11} \text{ C m}^{-1}$

1.9.1.4.2.1 Varying the splay and bend elastic coefficients such that $K_{11} = K_{33}$

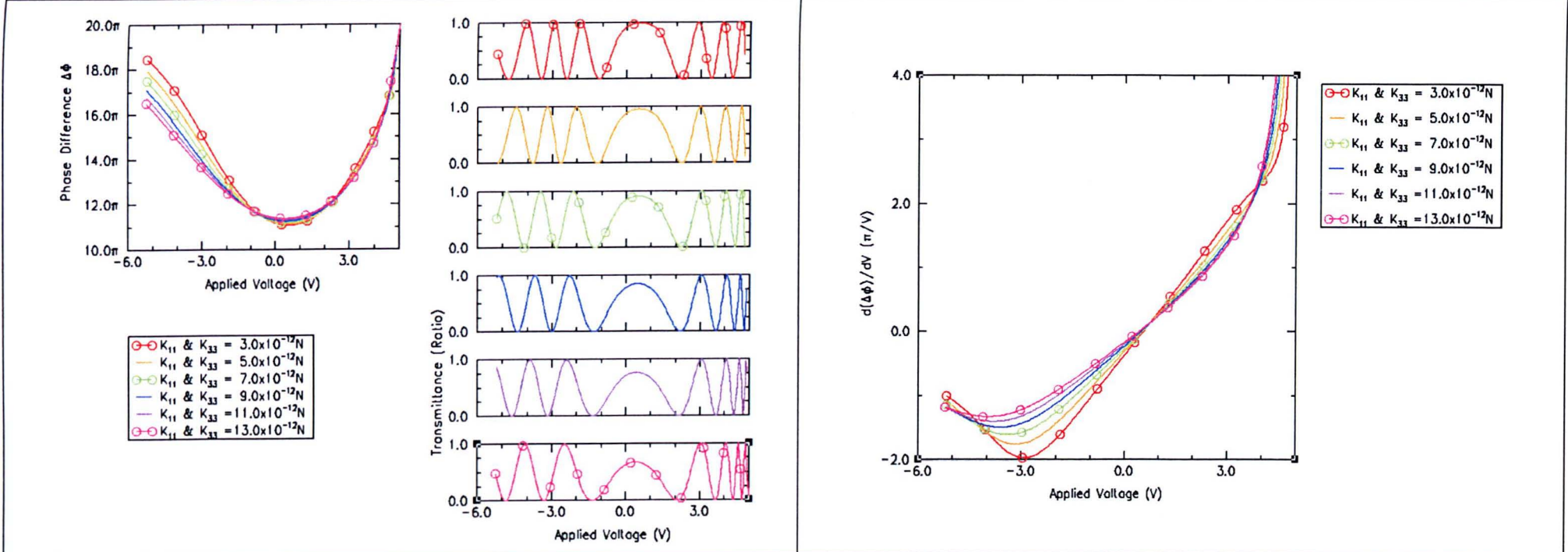


Figure (1.9.1.4.2.1) Shows transmittance and phase difference, $\Delta\Phi$, against voltage for varying elastic constants, K_s , for large e .

All the transmittance curves have roughly the same shape of the central feature. By examining the phase difference curves it is seen that, for zero and positive voltages, these curves are nearly indistinguishable. However, increasing the elastic constants decreases the phase difference for negative voltages. This can be seen in more detail in the figure (1.9.1.4.2.1.2).

Figure (1.9.1.4.2.2) Shows the rate of change of phase difference, $\Delta\Phi$, against voltage for varying elastic constants, K , for large e .

Generally, the effects of increasing the elastic constants is to decrease the rate of change of $\Delta\Phi$, for example the red curve of $K_s = 3 \times 10^{-12} \text{ N}$ is steeper than the cerise curve of $K_s = 13 \times 10^{-12} \text{ N}$. This effect is most marked between -3 and 0 V. This trend starts to reverse when the magnitude of the voltages becomes greater than $\pm 4 \text{ V}$, but this effect is not large.

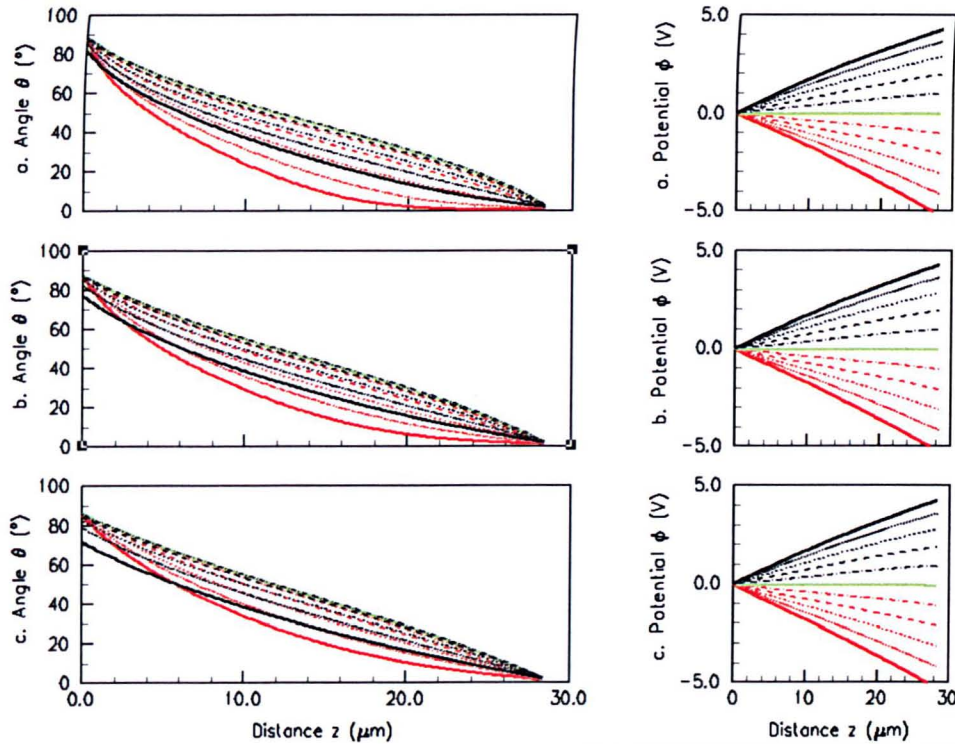


Figure (1.9.1.4.2.1.3) Shows θ and ϕ against z for varying elastic constants, K_s , for large e .

- (a) $K_s = 3 \times 10^{-12} \text{ N}$
- (b) $K_s = 7 \times 10^{-12} \text{ N}$
- (c) $K_s = 13 \times 10^{-12} \text{ N}$

The reason for the general (though small) shallowing of the $\Delta\Phi$ with increasing K_s in the previous two graphs appears to be that the θ curves in figure (1.9.1.4.2.1.3) deviate less from their zero voltage θ curve (green) when the elastic constants are increased. To see this, compare the θ curves in graph (a) with those of the θ curves in graph (c) of figure (1.9.1.4.2.1.3) and notice how, for the latter, these curves are much more closely spaced than when the elastic constants are small.

However, there is a small reversal of this trend at higher positive voltages, i.e. the trend of reduced changes in the θ curves, for the same voltages, when the elastic constants are increased. The reason for the reversal of this trend at higher voltages (despite the fact that the θ curves are still generally closely spaced) appears to be due to the anchoring energies becoming more relevant: note how the θ curves at $z = 0$ deviate away from θ_{easy} as the K_s increase (see the black curves, progressing from the θ graphs of (a) to (c)). The cumulative effect on the birefringence of this increased spacing of the θ curves at $z = 0$ compensates for the opposite effect due to the general closing of the θ curves across the cell. Hence we do not see the general shallowing in the $\Delta\Phi$ curves with increasing K_s that we had observed when the flexoelectric coefficient was small (see figure (1.9.1.4.1.3.2)).

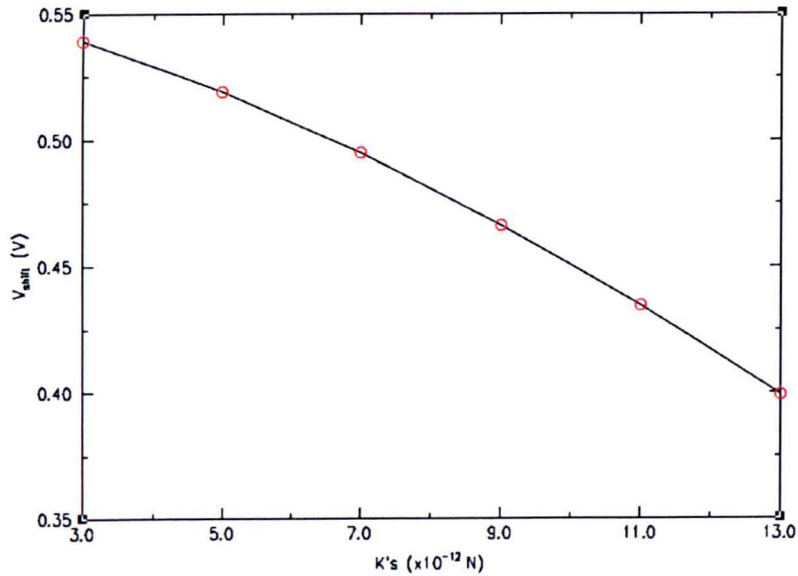


Figure (1.9.1.4.2.1.4) Shows voltage shift against elastic constants, K , for large flexoelectric constant, e .

Increasing K_{11} and K_{33} has the effect of decreasing the flexoelectric voltage shift. This shift is a reduction of 0.14 V over the range 3×10^{-12} N $\leq K \leq 13 \times 10^{-12}$ N. This relationship is not linear.

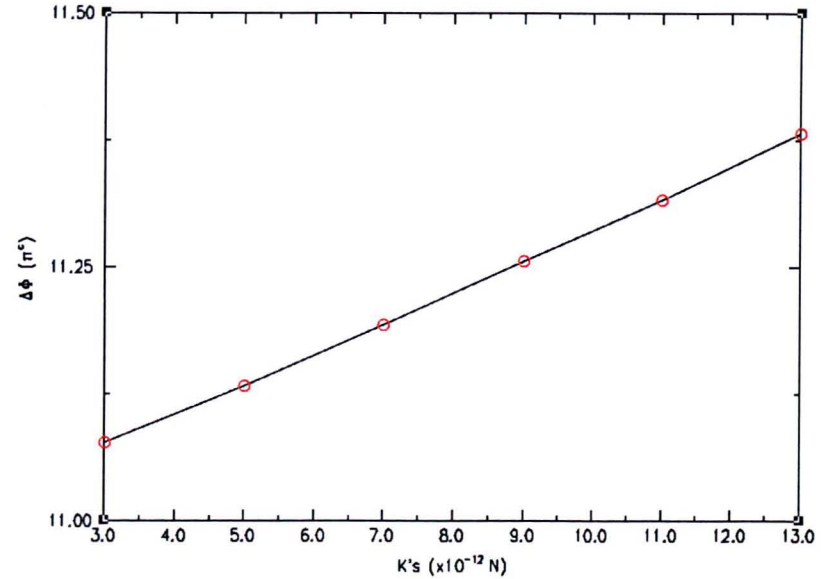


Figure (1.9.1.4.2.1.5) Shows $\Delta\Phi$ shift against elastic constants, K , for large flexoelectric constant, e .

Increasing the elastic constants K_{11} and K_{33} has the effect of increasing the phase difference of the central feature by 0.275π over the range 3×10^{-12} N $\leq K \leq 13 \times 10^{-12}$ N. This is a small effect.

1.9.1.4.2.2 Varying the splay coefficient, K_{11} , while the bend coefficient is held constant, $K_{33} = 7 \times 10^{-12} \text{ N}$

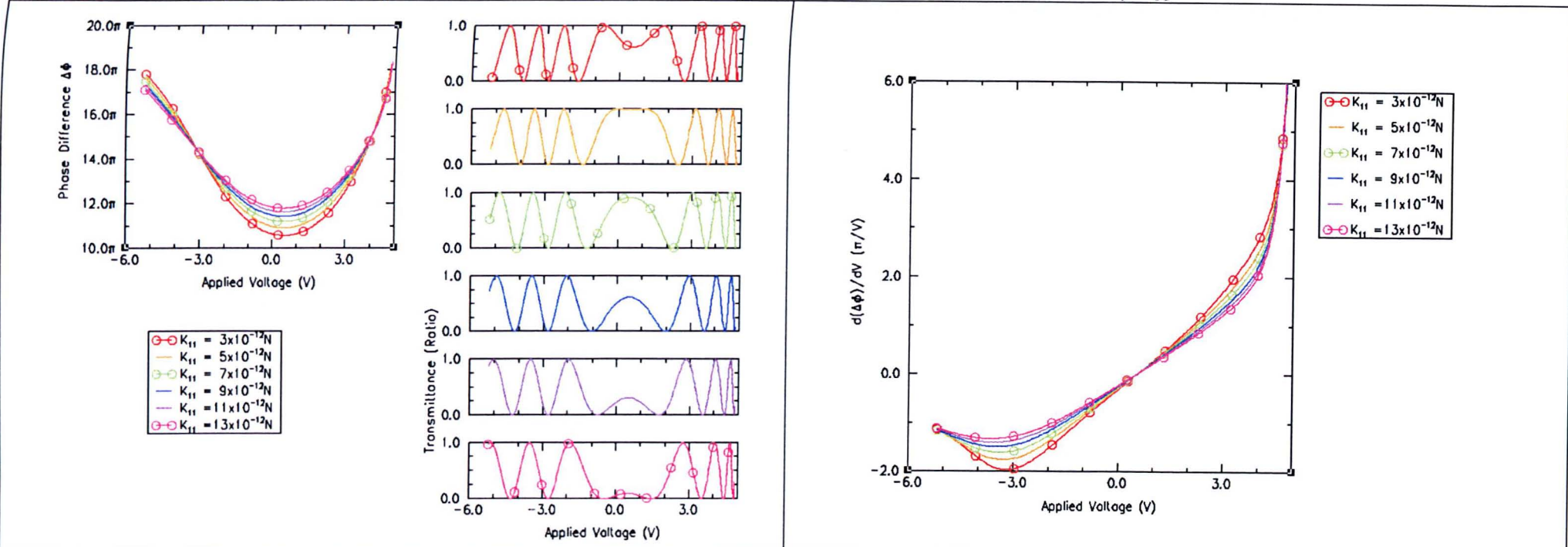


Figure (1.9.1.4.2.1) Shows transmittance and phase difference $\Delta\Phi$ against voltage for varying K_{11} while e is large.

At large voltages all the curves are similar. In the central region, however, increasing the splay elastic constant, K_{11} , increases the phase difference. To see this compare the red curve, of $K_{11} = 3 \times 10^{-12} \text{ N}$, with the cerise curve, of $K_{11} = 13 \times 10^{-12} \text{ N}$, in the central region in the phase difference graph, on the left hand side of figure (1.9.1.4.2.1).

Figure (1.9.1.4.2.2) Shows the rate of change of phase difference $\Delta\Phi$ against voltage for varying K_{11} while e is large.

Increasing K_{11} decreases the rate of change of $\Delta\Phi$ in the central region, but has little effect on it beyond $\pm 5 \text{ V}$. However, looking at figure (1.9.1.4.2.2.2.) it is seen that the effects of changing K_{11} are significantly reduced from when the flexoelectric coefficient was small, see figure (1.9.1.4.1.2.2).

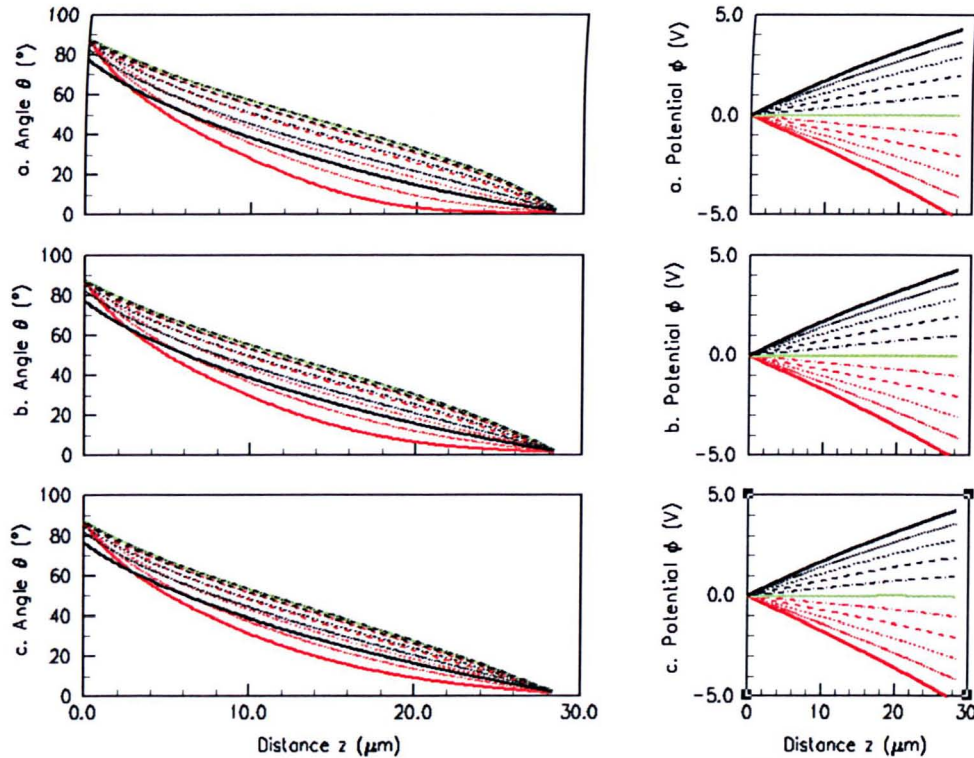


Figure (1.9.1.4.2.2.3) Shows how θ and ϕ vary with z for varying K_{11} while e is large.

- (a) $K_{11} = 3 \times 10^{-12} \text{ N}$
- (b) $K_{11} = 7 \times 10^{-12} \text{ N}$
- (c) $K_{11} = 13 \times 10^{-12} \text{ N}$

It can be seen from the solid black curves (approximately equal to +5 V) that all three θ graphs appear to be the same, as do the -3 V curves, red dotted curve (second after the solid red curve). The effects of this can be seen in figure (1.9.1.4.2.2.1), where the lines coalesce at -3 V and +5 V, whereas, the zero voltage θ curve gently veers towards smaller values of θ with increasing K_{11} (between the two relatively fixed end points), thus resulting in a $\Delta\Phi$ shift in the central region.

At $z = D$, however, the distortions are a combination of bend and splay; increasing either or both elastic constant will result in a 'tighter' formation of curves in the region of $z = D$, i.e. the system is more rigid in this region than before.

We also see that, particularly for large negative voltages (see solid red θ curves in graphs (a) to (c)), decreasing K_{11} increases how much the θ curves vary away from their zero voltage curves, i.e. when K_{11} is small, less energy is required to produce similar distortions from the zero voltage θ curve. This is similar to the trend observed when the flexoelectric coefficient was small although the effect is reduced.

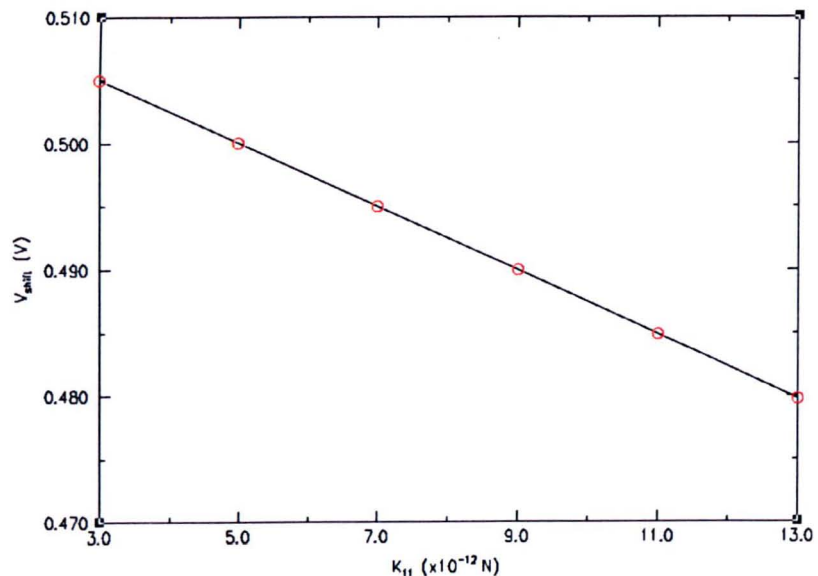


Figure (1.9.1.4.2.2.4) Shows voltage shift against splay elastic constant K_{11} when flexoelectric coefficient, e , is large.

Increasing K_{11} decreases the flexoelectric voltage shift by 0.025 V over the range $3 \times 10^{-12} \text{ N} \leq K \leq 13 \times 10^{-12} \text{ N}$.

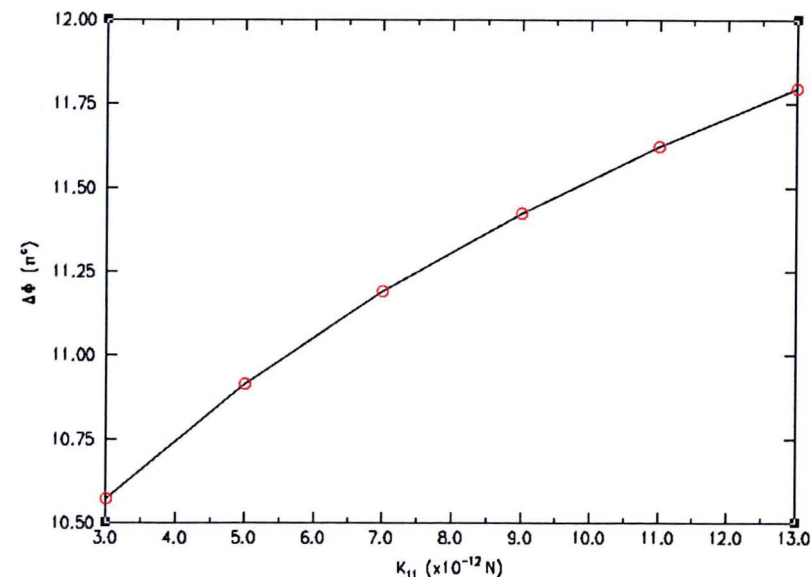


Figure (1.9.1.4.2.2.5) Shows $\Delta\Phi$ shift against splay elastic constant K_{11} when flexoelectric coefficient, e , is large.

Increasing K_{11} increases the phase difference of the central feature by 1.2π over the range $3 \times 10^{-12} \text{ N} \leq K \leq 13 \times 10^{-12} \text{ N}$. This change is not a linear relationship in this range, instead the rate of change decreases with increasing splay elastic constant.

1.9.1.4.2.3 Varying the bend coefficient, K_{33} , while the splay coefficient is held constant, $K_{11} = 7 \times 10^{-12}$ N.

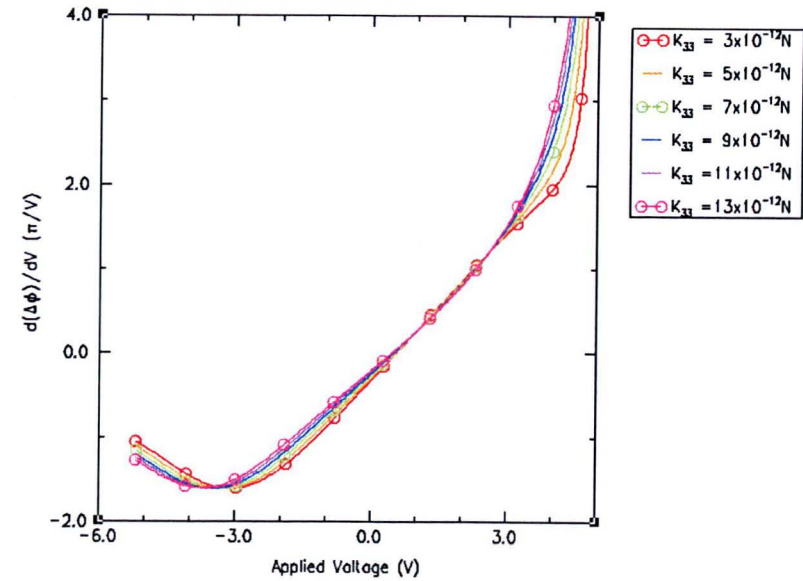
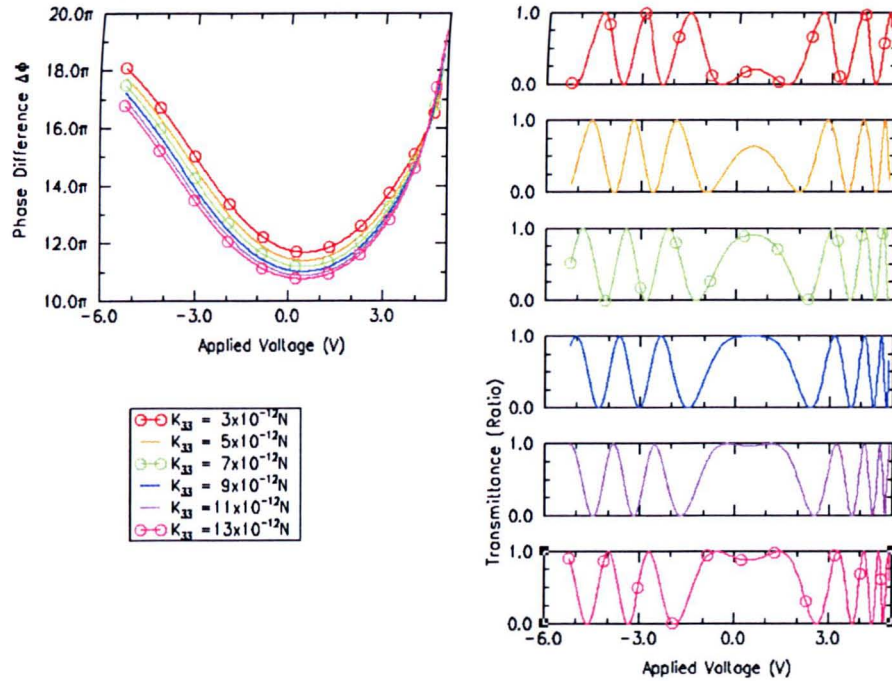
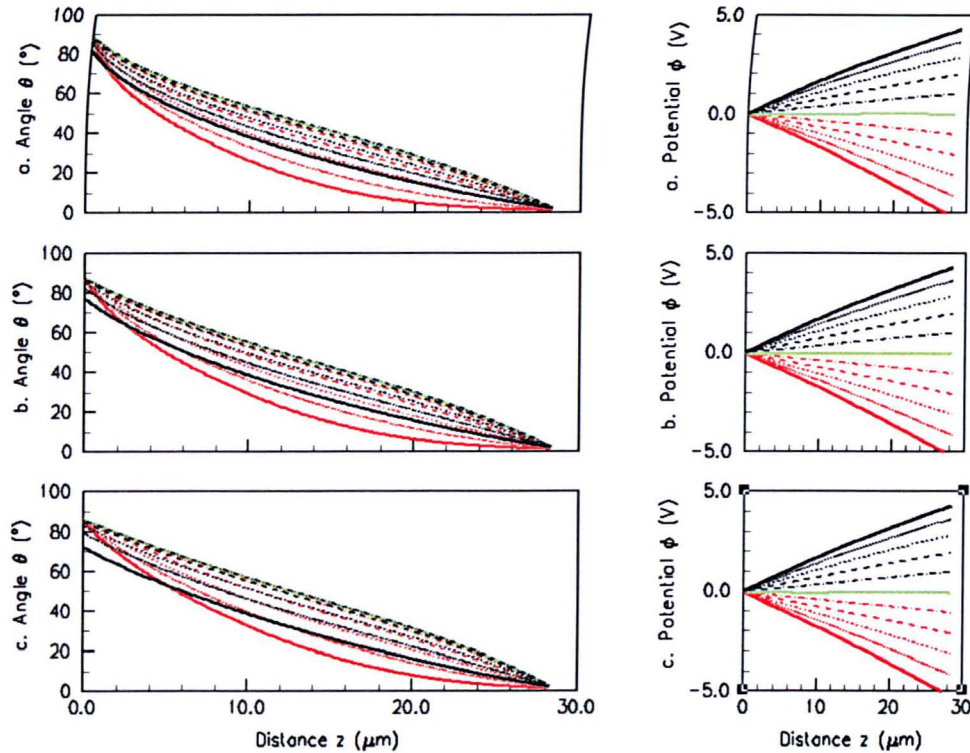


Figure (1.9.1.4.2.3.1) Shows transmittance and phase difference, $\Delta\Phi$, against voltage for varying bend elastic constant K_{33} when flexoelectric coefficient, e , is large.

Figure (1.9.1.4.2.3.2) Shows the rate of change of phase difference, $\Delta\Phi$, against voltage for varying bend elastic constant K_{33} when flexoelectric coefficient, e , is large.

Especially for the larger values of K_{33} , it can be seen that changes in K_{33} have little effect on the shape of the transmittance curves (right hand side). Comparing the blue, violet and cerise transmittance curves, (right hand side) where $K_{11} = 9, 11,$ and 13×10^{-12} N respectively, it can be seen that all these transmittance curves are roughly the same.

Between -2 and +3 V all these graphs have roughly the same gradient. Small changes from this occur most notably above $|+ \text{ and } -3 \text{ V}|$.



Here we see that increasing K_{33} reduces the bend deformations at the homeotropic alignment layer for positive applied voltages: the finite nature of the anchoring energy makes this possible. Notice that the value of θ at $z = 0$ for the solid black curve (+4.5 V) falls from 80° in (a) to *circa* 70° in (c).

Again, we see that at $z = D$ the distortions are a combination of bend and splay. This can be stated because increasing either or both elastic constant results in a 'tighter' formation of curves in the region of $z = D$, i.e. the system is noticeably more rigid in this region than before, when *either* elastic constant is increased.

Figure (1.9.1.4.2.3.3) Shows θ and ϕ against z for varying bend elastic constant K_{33} when flexoelectric coefficient, e , is large.

- (a) $K_{11} = 3 \times 10^{-12}$ N
- (b) $K_{11} = 7 \times 10^{-12}$ N
- (c) $K_{11} = 13 \times 10^{-12}$ N

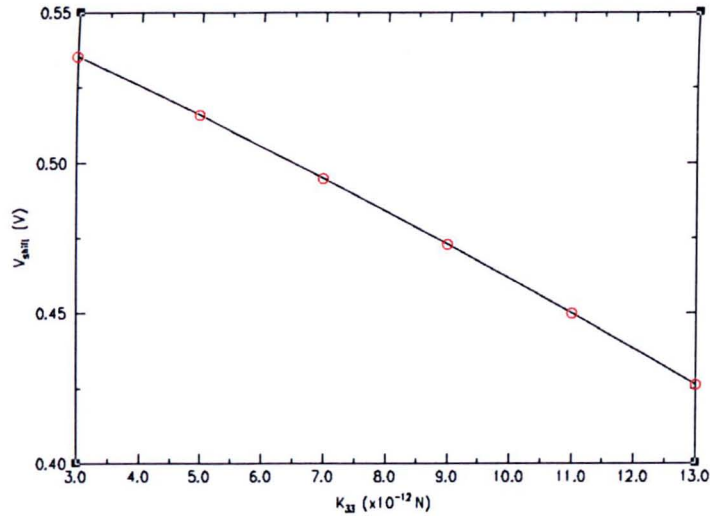


Figure (1.9.1.4.2.3.4) Shows voltage shift against bend elastic constant K_{33}

Increasing elastic constants makes the system more rigid, so the voltage shift is reduced. However, this is not a particularly large effect, being only -0.105 V over the range 3 to $13 \times 10^{-12} \text{ N}$.

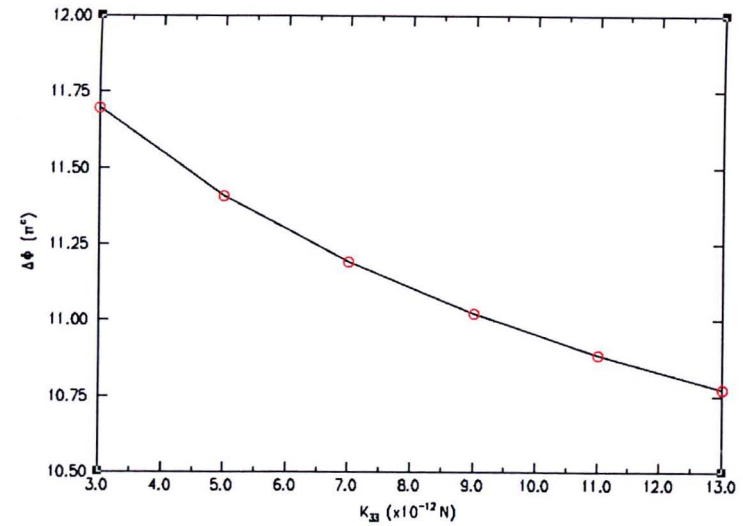


Figure (1.9.1.4.2.3.5) Shows $\Delta\Phi$ shift against bend elastic constant K_{33}

There is a change in the phase difference of -0.9π in the central feature over the same $1 \times 10^{-11} \text{ N}$ range. Further increases in the elastic constant have ever decreasing effects on the system. I.e. this is not a linear relationship but instead the curve starts to asymptote towards some value of $\Delta\Phi$ with increasing splay elastic constant.

Summarising the effects of varying the elastic constants, K_{11} and K_{33} , for high and low flexoelectric coefficient, e .

The first thing to note about all the curves in section 1.9.1.4.2 is how much wider they are than their smaller flexoelectric coefficient counterparts (section 1.9.1.4.1). The second thing to note, in addition to their increased voltage shift (from when $e = -1$ to $-5 \times 10^{-11} \text{ C m}^{-1}$), is the marked reduction in their symmetry. In section 1.9.1.4.1, when e was small, we saw that changing K s could change the phase difference curves profoundly, both in their shape and $\Delta\Phi$ of the central feature, depending upon whether K_{11} or K_{33} was varied. Here, however, that same trend is not observed, instead the flexoelectric effect dominates.

1.9.1.5 Varying angles of easy axes.

1.9.1.5.1 Homeotropic anchoring angle of easy axis, at $z = 0 \mu\text{m}$, θ_{easy} .

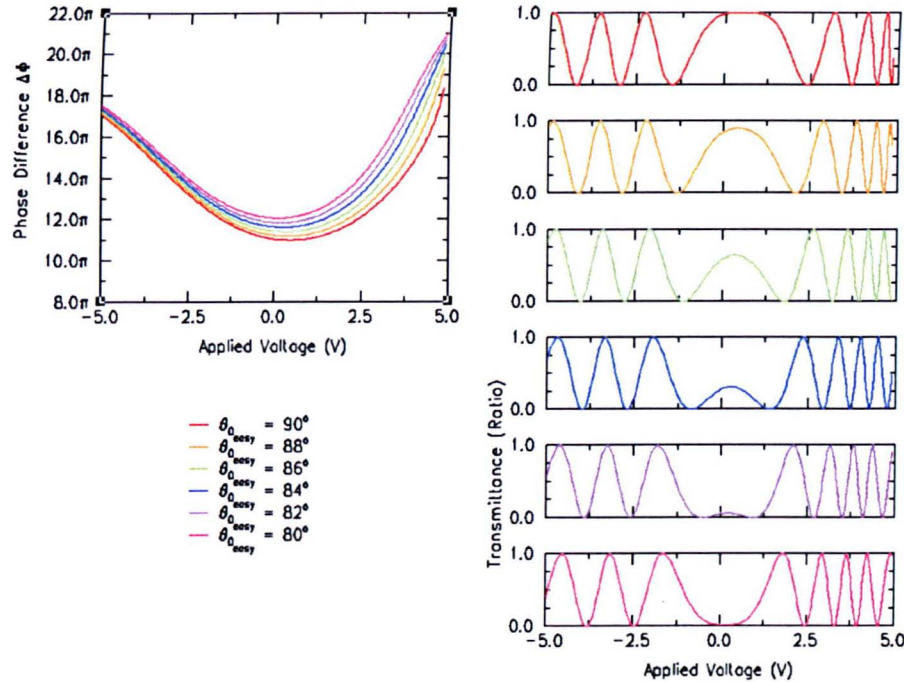


Figure (1.9.1.5.1) Shows transmittance and phase difference, $\Delta\Phi$, against voltage for varying θ_{easy}

While all the phase difference curves are similar, there are two main changes that decreasing θ_{easy} has: firstly, there is an increase in $\Delta\Phi$ of the central feature and, secondly, the central feature has moved towards negative voltages.

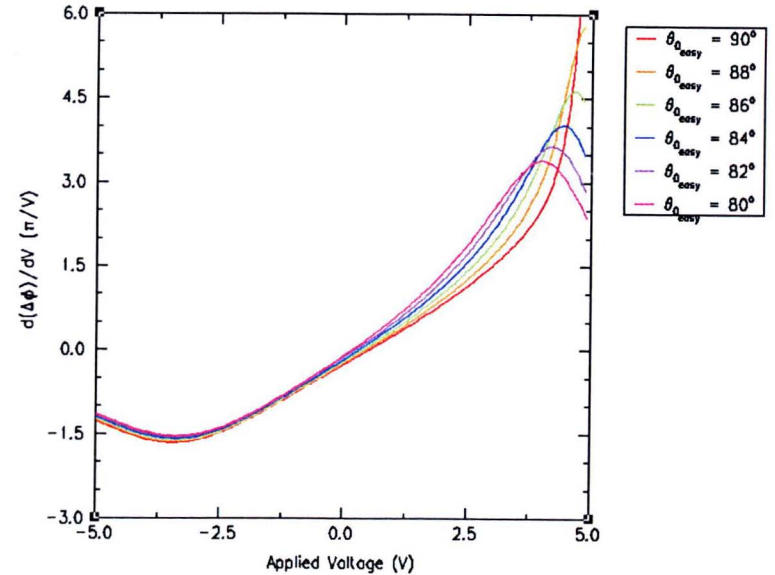


Figure (1.9.1.5.2) Shows the rate of change of phase difference, $\Delta\Phi$, against voltage for varying θ_{easy}

Note that the gradients are very similar up to circa +2 V. At around 4 V, the curves for smaller θ_{easy} reach a peak in their gradient, resulting in a slight levelling off in the phase difference graphs of figure (1.9.1.5.1). Note also that increases in the homeotropic angle of easy axis increases the level of asymmetry of these curves.

N.B. Because the changes in the θ and ϕ curves could be anticipated and considered trivial, figure type 3 (that shows this information) has not been included.

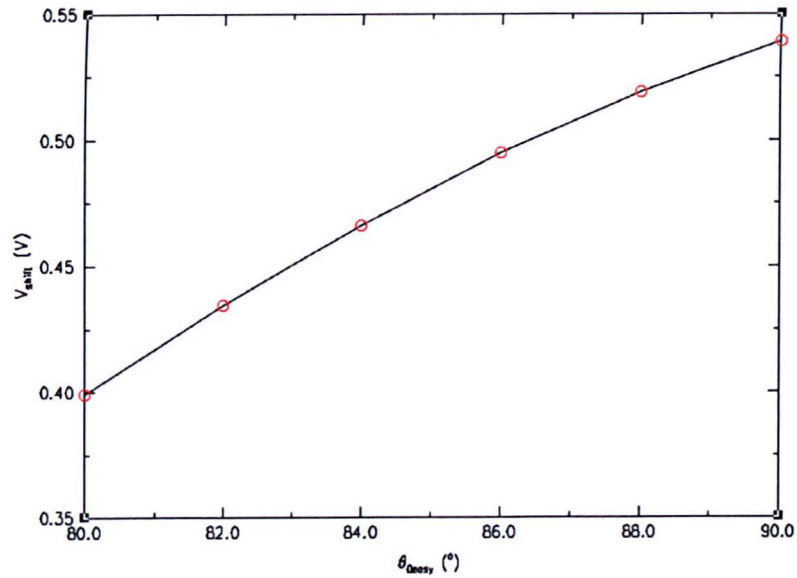


Figure (1.9.1.5.1.3) Shows voltage shift against homeotropic angle of easy axis, θ_{easy}

Decreasing θ_{easy} from 90° to 80° reduces the flexoelectric voltage shift by 0.14 V.

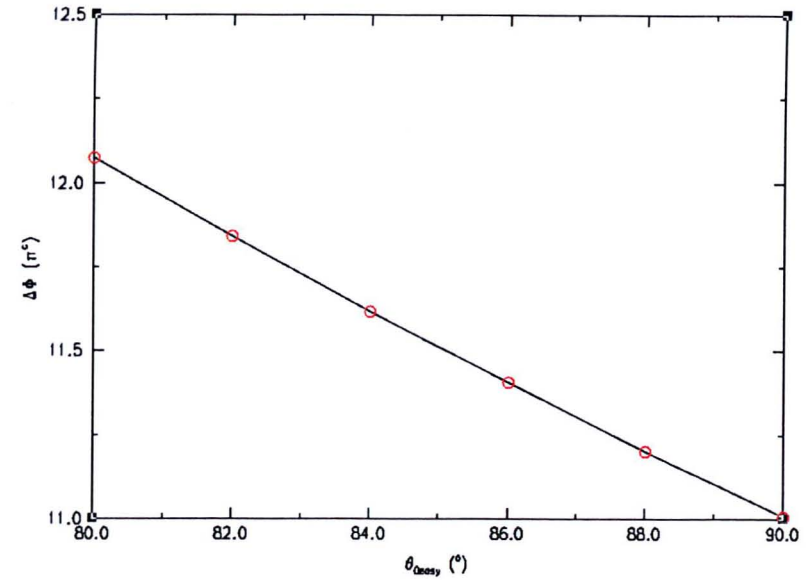


Figure (1.9.1.5.1.4) Shows $\Delta\Phi$ shift against homeotropic angle of easy axis, θ_{easy}

Decreasing θ_{easy} from 90° to 80° increases the phase difference of the central feature by 1.1π . This is why we see in figure (1.9.1.5.1.1) that, respectively, the transmittance curves of 90° and 80° have maxima and minima at their central features

1.9.1.5.2 Homogeneous anchoring angle of easy axis, at $z = D \mu\text{m}$, θ_{Deasy}

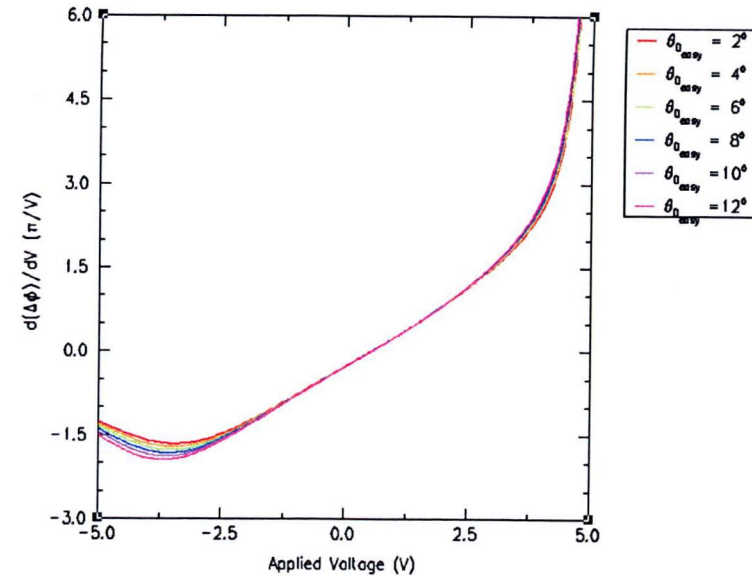
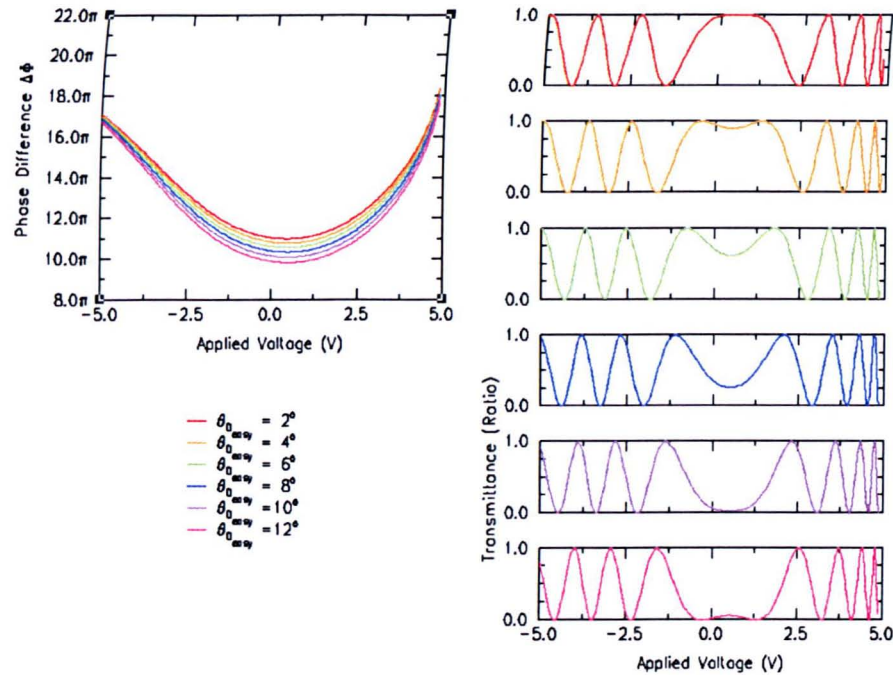


Figure (1.9.1.5.2.1) Shows transmittance and phase difference, $\Delta\Phi$, against voltage for varying homogeneous angle of easy axis, θ_{Deasy}

At large voltages, there are little variations in phase differences between the curves. At smaller voltages these differences between curves are greater: increasing θ_{Deasy} reduces the phase difference of the central region by roughly one wavelength: note how the transmittance at the central feature of the curve is roughly zero compared to, roughly, one for the red curve ($\theta_{Deasy} = 12^\circ$ and 2° respectively).

Figure (1.9.1.5.2.2) Shows the rate of change of phase difference, $\Delta\Phi$, against voltage for varying homogeneous angle of easy axis, θ_{Deasy}

In terms of their gradients, the central regions of these curves are almost indistinguishable. This ranges from circa -2 to +3 V.

N.B. Again, as differences between the θ curves did not reveal anything profound they have been excluded.

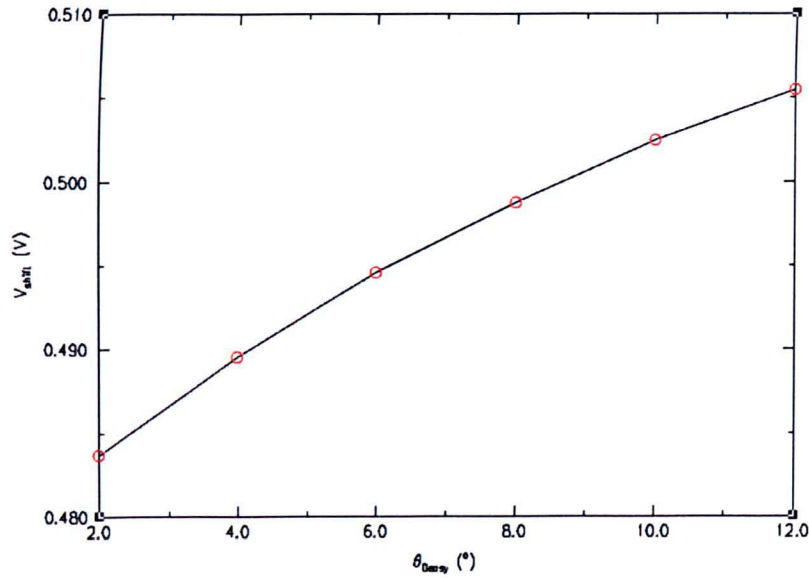


Figure (1.9.1.5.2.3) Shows voltage shift against homogeneous anchoring angle, θ_{Deasy}

Increasing the angle of easy axis at the homogeneous alignment layer increases the voltage shift of the central feature by 0.021 V over the range 2° and 12°, which is very small.

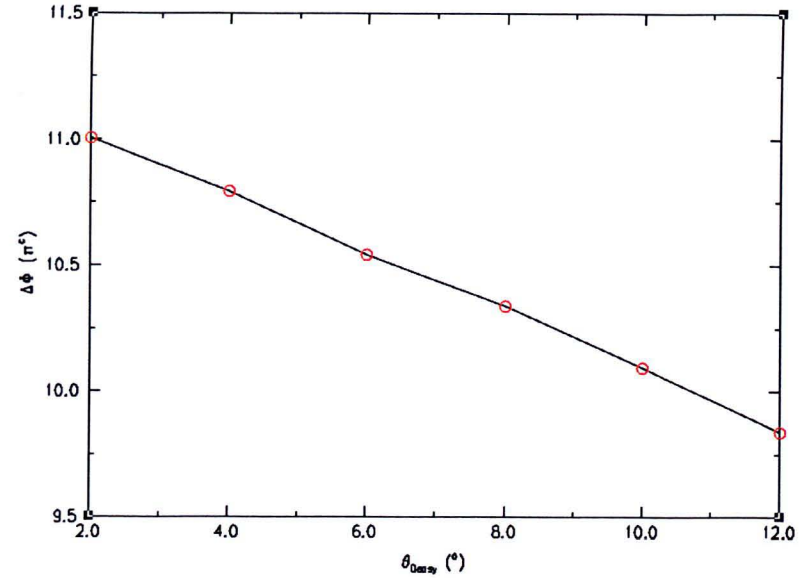


Figure (1.9.1.5.2.4) Shows $\Delta\Phi$ shift against homogeneous anchoring angle, θ_{Deasy}

Increasing the homogeneous angle of easy axis, θ_{Deasy} , from 2° to 12° decreases $\Delta\Phi$ of the central feature by 1.2π . It should be noted that if $\Delta\epsilon$ was of an opposite sign, the sign with increasing θ_{Deasy} of this $\Delta\Phi$ shift, would also be changed.

1.9.1.6 Varying flexoelectric coefficient, $e (= e_{11} + e_{33})$.

In this section the influences of changes in the flexoelectric coefficient, e , on HAN cells are investigated. However, the picture can be skewed by varying the magnitude of the homeotropic anchoring energy, A_{\varnothing} . For this reason three different homeotropic anchoring energies are investigated: firstly, large anchoring energy, $A_{\varnothing} = 1.2 \times 10^{-4} \text{ J m}^{-2}$; then, medium anchoring energy, $A_{\varnothing} = 1.2 \times 10^{-5} \text{ J m}^{-2}$; and finally, small anchoring energy, $A_{\varnothing} = 1.2 \times 10^{-6} \text{ J m}^{-2}$. By examining the combination of e and A_{\varnothing} in this order, it is possible to identify the contributions of each.

1.9.1.6.1 Varying flexoelectric coefficient, e , when homeotropic anchoring energy is large, $A_{\phi 0} = 1.2 \times 10^{-4} \text{ J m}^{-2}$.

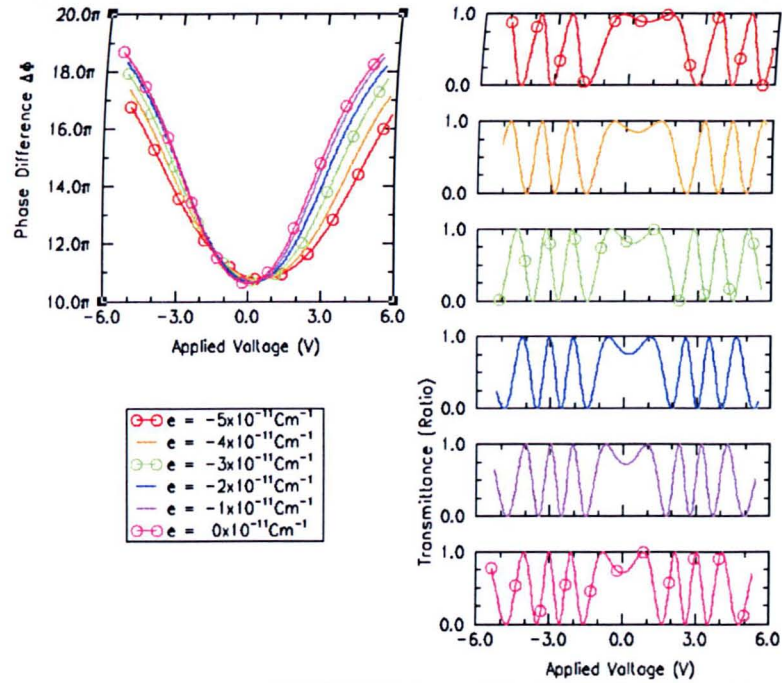


Figure (1.9.1.6.1) Shows transmittance and phase difference $\Delta\Phi$ against voltage for varying e when $A_{\phi 0}$ is large.

Here we see that the transmittance curves are symmetric. However, there is also a voltage shift when e is non-zero. This shift is of the opposite sign to that of e , c.f. the cerise curve of $e = 0 \text{ C m}^{-1}$ with the red curve of $e = -5 \times 10^{-11} \text{ C m}^{-1}$ to see all these effects. N.B. it should be noted that changing the sign of e reflects these curves about the 0 V axis.

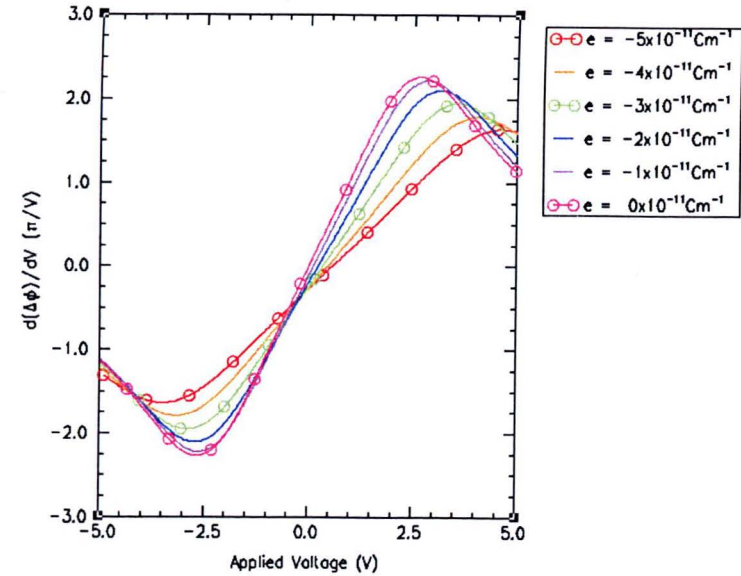


Figure (1.9.1.6.2) Shows the rate of change of phase difference $\Delta\Phi$ against voltage for varying e when $A_{\phi 0}$ is large.

Note also that, as the magnitude of e increases, the gradient of the phase difference curves decreases, c.f. the cerise curve of $e = 0 \text{ C m}^{-1}$ with the red curve of $e = -5 \times 10^{-11} \text{ C m}^{-1}$ to see all these effects. The $e = -5 \times 10^{-11} \text{ C m}^{-1}$ transmittance curve in figure (1.9.1.6.1) is wider than the $e = 0 \text{ C m}^{-1}$ transmittance curve.

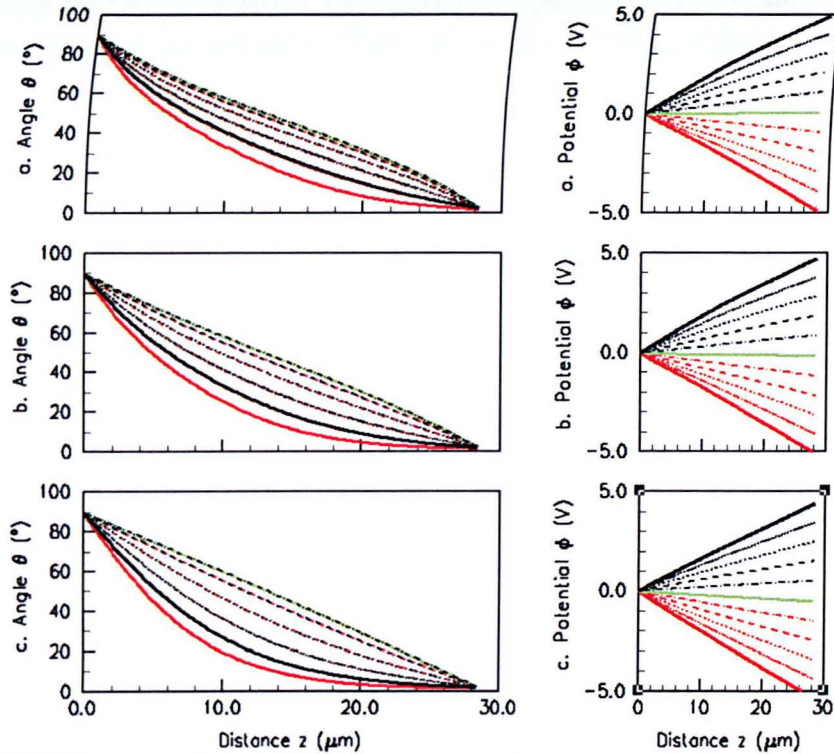


Figure (1.9.1.6.1.3) Shows θ and ϕ against z for varying e when $A_{\phi 0}$ is large

(a) $e = -5 \times 10^{-11} \text{ C m}^{-1}$

(b) $e = -3 \times 10^{-11} \text{ C m}^{-1}$

(c) $e = 0 \times 10^{-11} \text{ C m}^{-1}$

The reason for the decreasing gradient of the phase difference curves with increasing e can be seen in the θ curves of figure (1.9.1.6.1.3). The θ curves in (a) part of this graph (corresponding to $e = -5 \times 10^{-11} \text{ C m}^{-1}$) show comparatively little change with changing voltages (see (ϕ) for key), when compared to those in the (c) graph (corresponding to $e = 0 \text{ C m}^{-1}$).

It should be possible to examine the turning point of the previous two figures by examining the changes in the θ curves away from their zero voltage (green) θ curve. However, it should be noted that the ϕ separation between the curves shown here is slightly larger than the size of the flexoelectric voltage shift. This is therefore an inappropriate method for evaluating turning points on graphs of types 1 and 2.

While we did not include the curves for positive e in figures (1.9.1.6.1.1) to (1.9.1.6.1.3), because they were merely reflections about 0 V of their negative counterparts, here the voltage shift and phase shift data for both signs of e are now included.

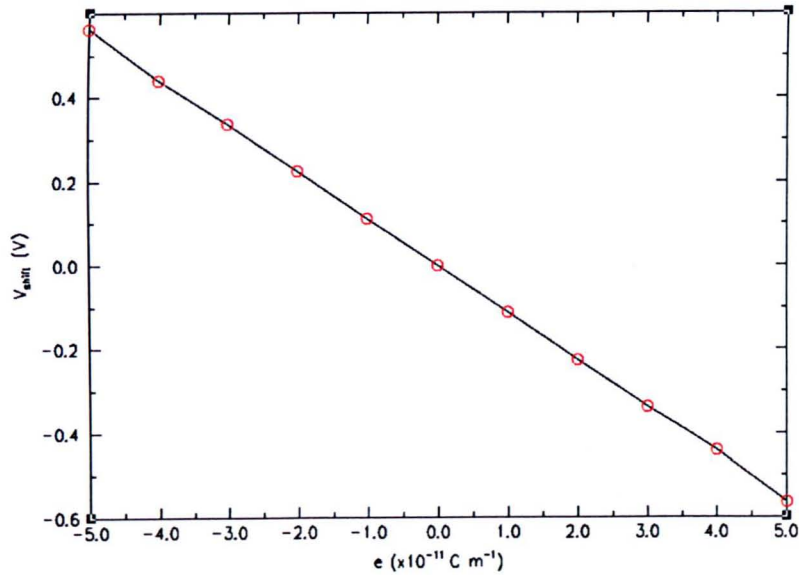


Figure (1.9.1.6.1.4) Shows voltage shift against flexoelectric coefficient, e , when $A_{\varphi 0}$ is large.

It can be seen that when $e = 0 \text{ C m}^{-1}$ the flexoelectric voltage shift is zero, whereas when e is non-zero the flexoelectric voltage shift is directly proportional to e : $V_{\text{shift}} = e \times (-1.1 \times 10^{10})$ in units of V.

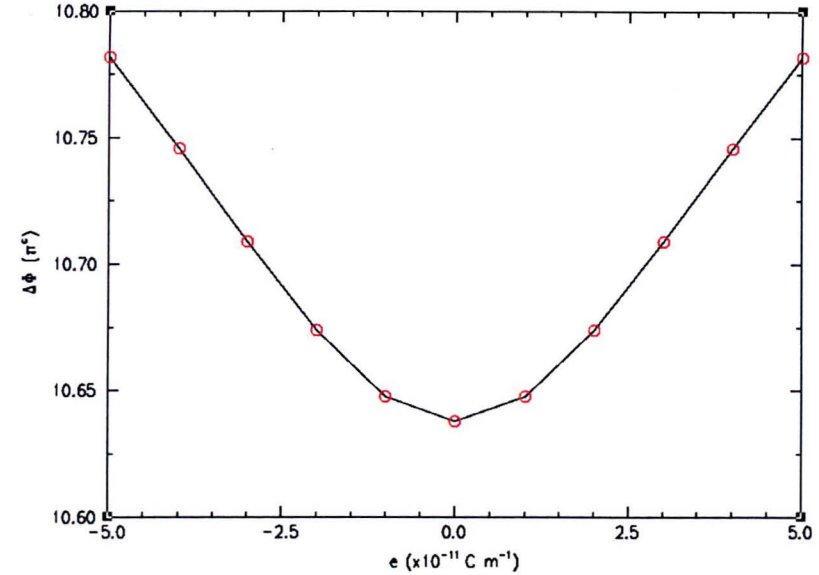


Figure (1.9.1.6.1.5) Shows $\Delta\Phi$ shift against flexoelectric coefficient, e , when $A_{\varphi 0}$ is large.

Here we see that the $\Delta\Phi$ of the central region reaches a minimum when $e = 0 \text{ C m}^{-1}$ and that increasing e 's magnitude by $5 \times 10^{-11} \text{ C m}^{-1}$ increases $\Delta\Phi$ by 0.15π . The size of the response is dependent on the magnitude and not on the sign of e , i.e. the response has reflection symmetry.

1.9.1.6.2 Varying flexoelectric coefficient, e , when homeotropic anchoring energy is medium, $A_{\theta 0} = 1.2 \times 10^{-5} \text{ J m}^{-2}$.

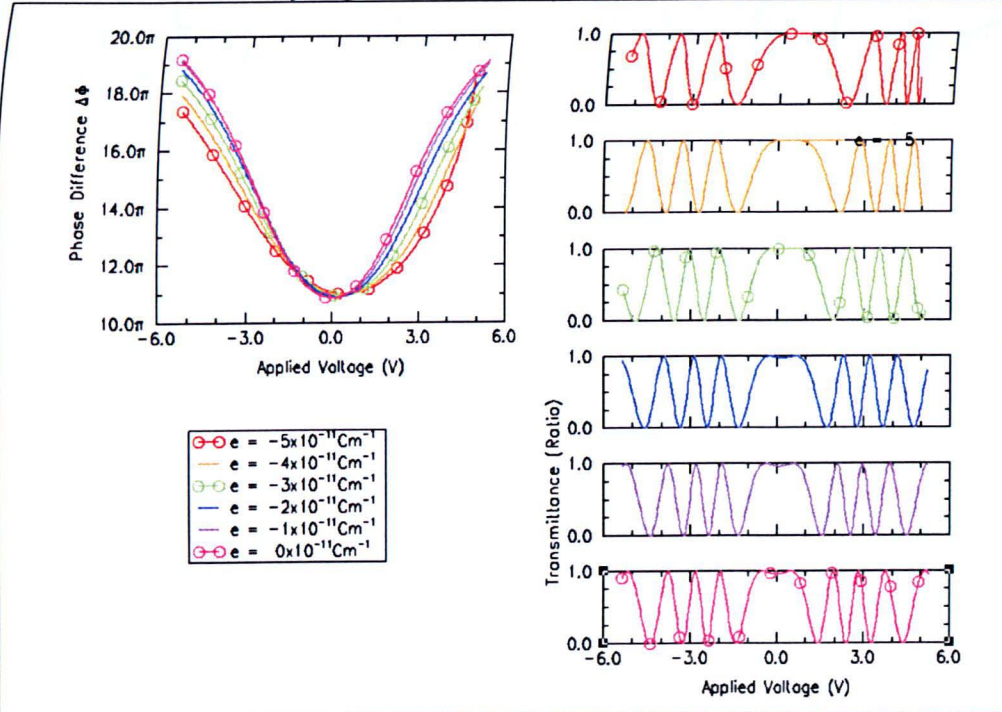


Figure (1.9.1.6.2.1) Shows transmittance and phase difference $\Delta\Phi$ against voltage for varying e when $A_{\theta 0}$ is medium.

It can be seen clearly from the transmittance curves that increasing the flexoelectric coefficient results in a voltage shift of the curve. As before, this shift takes the opposite sign to the flexoelectric coefficient. However, unlike before, what can also be seen for these curves is that increasing the flexoelectric coefficient also introduces an asymmetry that is not present when $e = 0 \text{ C m}^{-1}$, or when $A_{\theta 0}$ was large (see figure (1.9.1.6.1.1)).

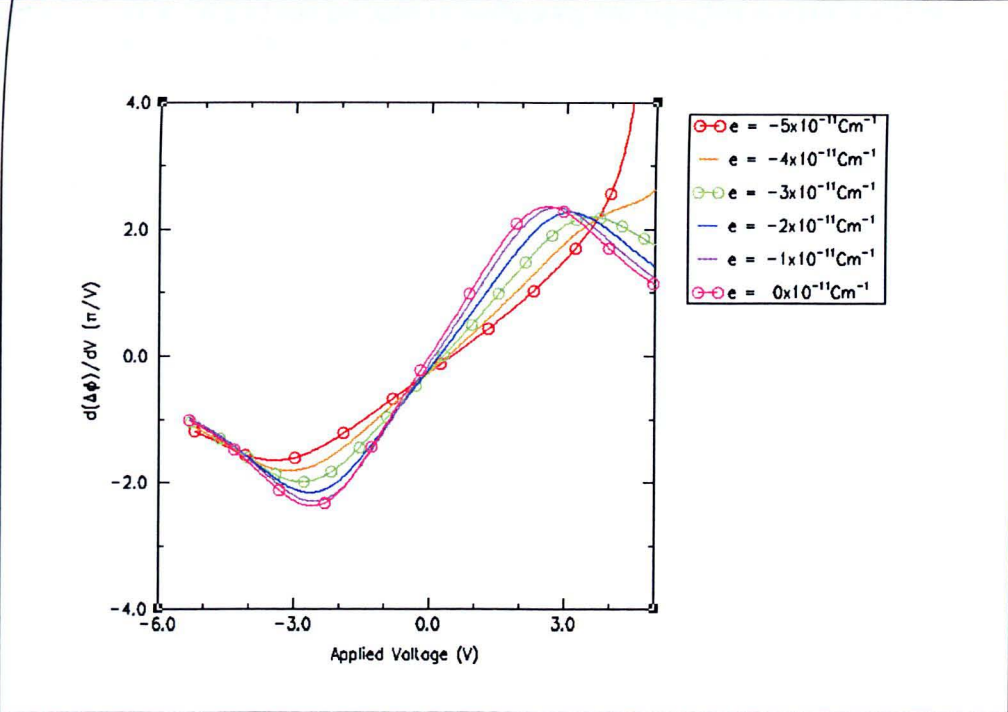


Figure (1.9.1.6.2.2) Shows the rate of change of phase difference $\Delta\Phi$ against voltage for varying e when $A_{\theta 0}$ is medium.

The asymmetry, due to changes in the flexoelectric coefficient, is further visible in these curves, where only the curve of $e = 0 \text{ C m}^{-1}$ has perfect rotational symmetry about voltage = 0 V. All the other curves demonstrate increasingly asymmetric $d(\Delta\Phi)/dV$ curves with increasing magnitudes of e . For example, when $e = -5 \times 10^{-11} \text{ C m}^{-1}$ the curve becomes very steep around +4 V; this is coupled with a complementary shallowing of the $d(\Delta\Phi)/dV$ curve for negative voltages. That is, these curves have become asymmetric.

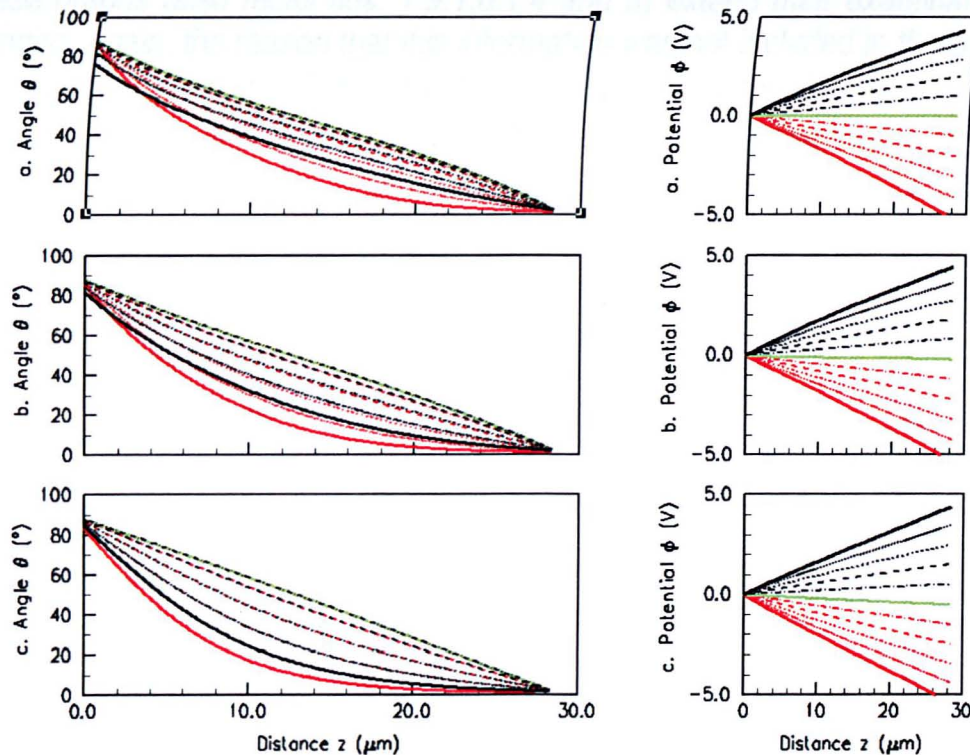


Figure (1.9.1.6.2.3) Shows θ and ϕ against z for varying flexoelectric coefficient, e , and $A_{\phi 0}$ medium.

- (a) $e = -5 \times 10^{-11} \text{ C m}^{-1}$
- (b) $e = -3 \times 10^{-11} \text{ C m}^{-1}$
- (c) $e = 0 \times 10^{-11} \text{ C m}^{-1}$

The reason for the asymmetries seen in figures (1.9.1.6.2.1) and (1.9.1.6.2.2) can be seen by comparing the θ graphs from (a) to (c) in this figure. The (a) graphs correspond to $e = -5 \times 10^{-11} \text{ C m}^{-1}$, whereas the (c) graphs correspond to $e = 0 \text{ C m}^{-1}$. In (c) we see that both positive and negative θ curves follow similar director paths (compare red and black curves). Whereas, in (a) we see that a small but significant change occurs at $z = 0 \mu\text{m}$ for the positive (black) voltage curves: it appears that decreasing the anchoring energy has meant that, under certain circumstances, θ is able to deviate from θ_{easy} with greater ease than previously (i.e. § 1.9.1.6.1).

As with § 1.9.1.6.1 we again see that increasing the magnitude of e decreases the spacing between θ curves. For example, notice how much closer the θ curves are to one another in (a) than they are in (c), in general across the cell (notable exception at $z = 0$ already discussed).

Here it has been demonstrated that the anchoring energy can become an important factor when it is sufficiently small and when e is non-zero. While it is not the source of the flexoelectric voltage shift, it combines with the flexoelectric effect to result in these asymmetries.

These graphs (also recall figs. 1.9.1.6.1.4 and 5) extend their examination to include the voltage shifts that occur when the sign of e is changed. Again, the reason that this information was not included in the previous three figure types is that a change in sign of e only reflects data about the 0 V axes of their graphs. For example, in the case of figure (1.9.1.6.2.3) the ϕ curves would be reflected about the 0 V axis thus changing the 'key' to the θ curves, which are otherwise unaltered.

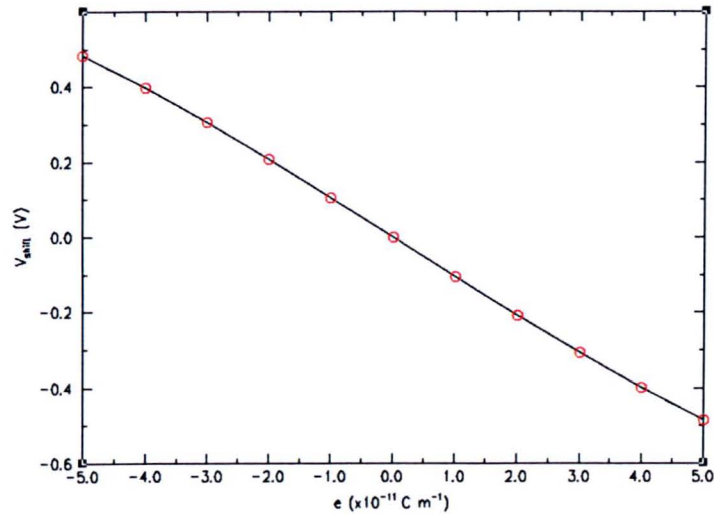


Figure (1.9.1.6.2.4) Shows voltage shift against flexoelectric coefficient, e , for $A_{\phi 0}$ medium.

The voltage shift across the range $e = -5 \times 10^{-11}$ C m $^{-1}$ to $+5 \times 10^{-11}$ C m $^{-1}$ is roughly -1 V, which is considerable but slightly smaller than when $A_{\phi 0}$ is large. It should also be noted that, while this graph still passes through zero when $e = 0$ C m $^{-1}$, the linearity of the relationship, seen when $A_{\phi 0}$ was large, is slightly reduced here: the curve is starting to shallow for large +/- voltages.

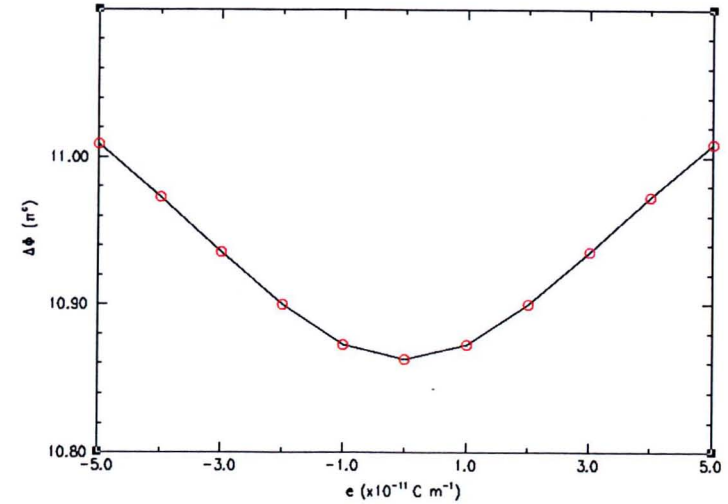


Figure (1.9.1.6.2.5) Shows $\Delta\Phi$ shift against flexoelectric coefficient, e , for $A_{\phi 0}$ medium.

Again, recalling figure (1.9.1.6.1.5), we see that there is reflection symmetry around the $e = 0$ C m $^{-1}$ axis and that $\Delta\Phi$ of the central feature reaches a minimum at that point. A change in e from 0 to $\pm 5 \times 10^{-11}$ C m $^{-1}$ produces a change in the phase difference of the central feature of 0.14π .

1.9.1.6.3 Varying flexoelectric coefficient, e , when homeotropic anchoring energy is small, $A_{\theta 0} = 1.2 \times 10^{-6} \text{ J m}^{-2}$.

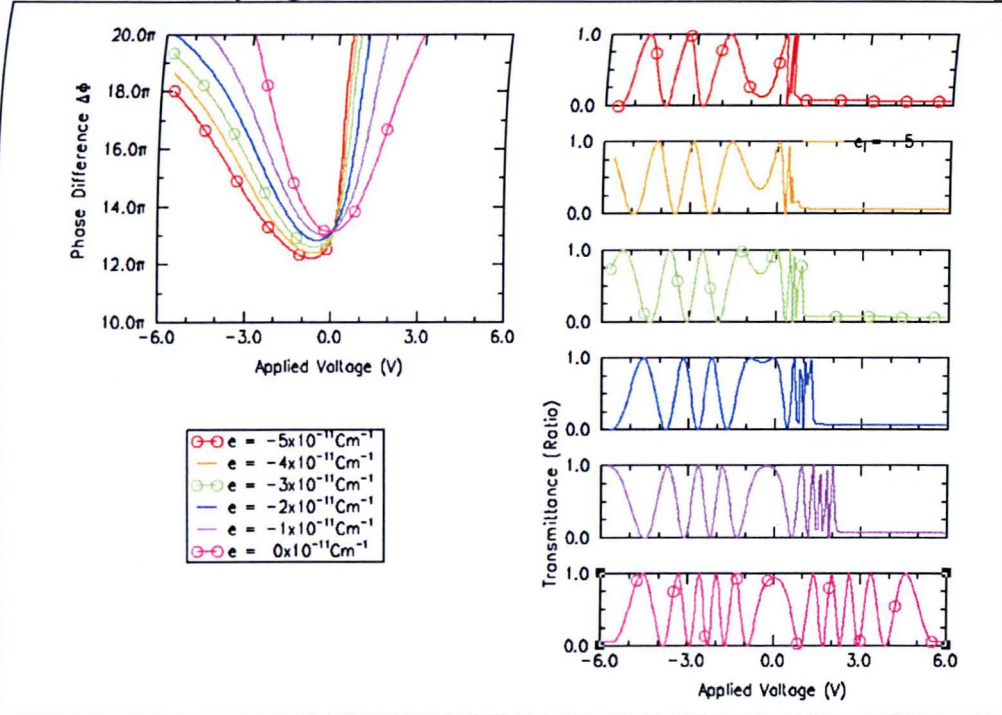


Figure (1.9.1.6.3.1) Shows transmittance and phase difference $\Delta\Phi$ against voltage for varying e when $A_{\theta 0}$ is low.

It can be seen clearly from the transmittance curves that increasing the flexoelectric coefficient results in a voltage shift of the curve. However, unlike in the case when the anchoring energy was higher, this shift takes the *same* sign as the flexoelectric coefficient. The asymmetry that was seen before (see section 1.9.1.6.2) has now grown massively and is responsible for the differing sign of the voltage shift. Again it can be seen that no asymmetry exists when $e = 0 \text{ C m}^{-1}$. When e is equal to zero the phase difference is considerably narrower than its equivalent in the graphs of higher $A_{\theta 0}$.

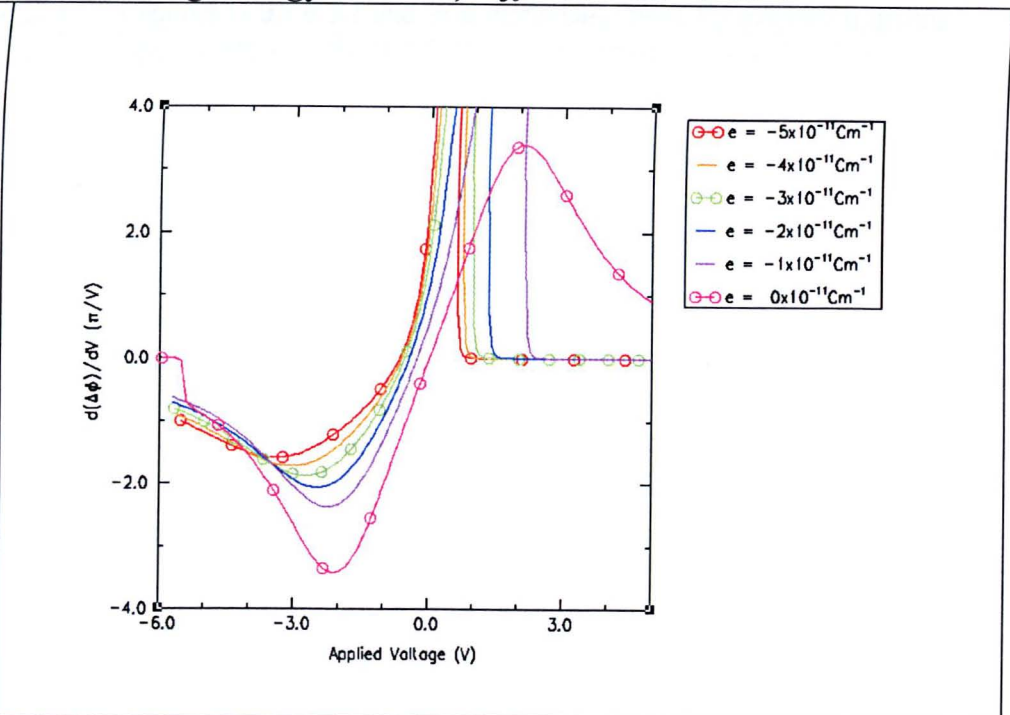
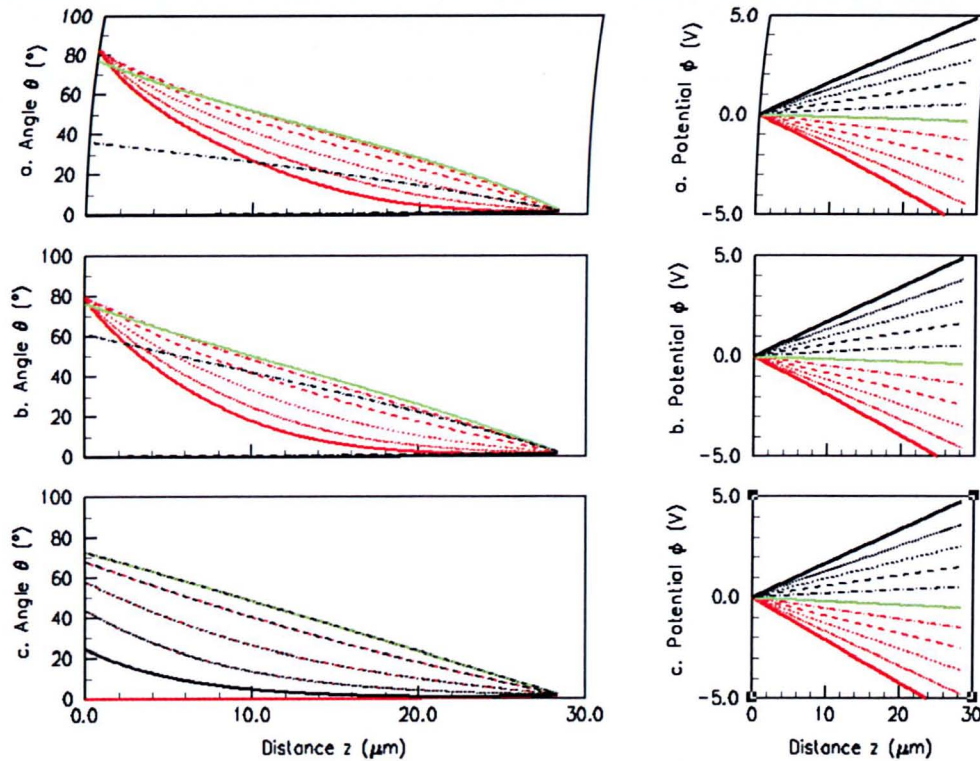


Figure (1.9.1.6.3.2) Shows the rate of change of phase difference $\Delta\Phi$ against voltage for varying e when $A_{\theta 0}$ is low.

The $e = 0 \text{ C m}^{-1}$ curve still possesses rotational symmetry as it has done for the previous two anchoring energy scenarios; however, the other curves do not, they all have very steep curves above 0 V which then falls again and the systems reach saturation for positive voltages of about +3 V. This is demonstrated in the next figure.



The reason for the saturation observed of the $e \neq 0 \text{ C m}^{-1}$ curves in figures (1.9.1.6.3.1 and 2) is made clear here. By examining graphs (a), where $e = -5 \times 10^{-11} \text{ C m}^{-1}$, to (b), where $e = -3 \times 10^{-11} \text{ C m}^{-1}$, we see that for positive voltages θ_0 is *not* equal to θ_{easy} . In fact, it is generally equal to 0° .

Also in figure (1.9.1.6.3.1), it can be seen that the $e = 0 \text{ C m}^{-1}$ curve was much narrower than it had been in figures (1.9.1.6.1.1) and (1.9.1.6.2.1), where the homeotropic anchoring energy was larger than it is here. This, too, can be attributed to the large movement of the director tilt angle at the homeotropic alignment layer: see the θ curves of graph (c) and how, unlike its higher $A_{\theta 0}$ counterparts, $\theta_0 \ll \theta_{\text{easy}}$ for all voltages. This allows the θ curves to be more widely spaced than before and so leads to the greater rate of changes observed in figures (1.9.1.6.3.1 and 2)

Figure (1.9.1.6.3.3) Shows θ and ϕ against z for varying flexoelectric coefficient, e , and $A_{\theta 0}$ small.

- (a) $e = -5 \times 10^{-11} \text{ C m}^{-1}$
- (b) $e = -3 \times 10^{-11} \text{ C m}^{-1}$
- (c) $e = 0 \times 10^{-11} \text{ C m}^{-1}$

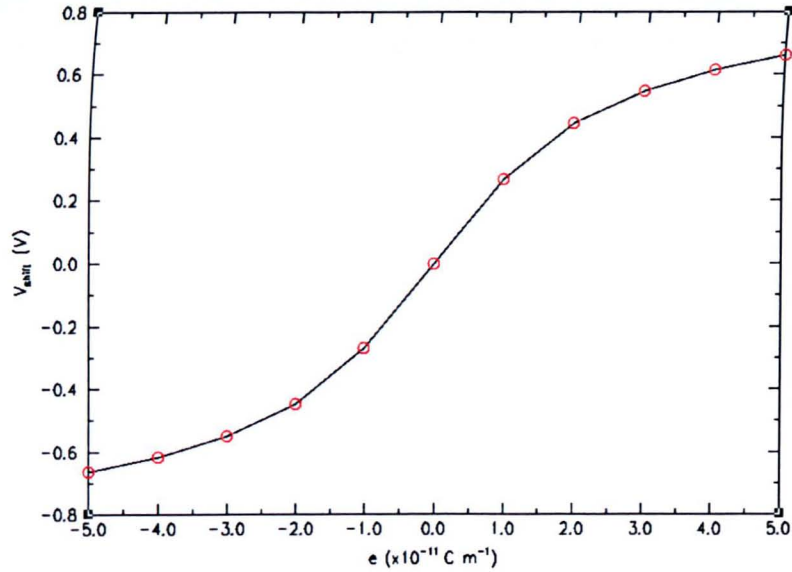


Figure (1.9.1.6.3.4) Shows voltage shift against flexoelectric coefficient, e , when A_{θ} is small.

Comparing with figures (1.9.1.6.1.4) and (1.9.1.6.2.4) we see that the gradient of this figure (above) has experienced a change in its sign with respect to its predecessors. This was due to the exaggerated response of θ at $z = 0$ for the voltage range -1 to +6 V, which has overcompensated, acting to move the flexoelectric voltage in the opposite direction from what it would usually be. While this curve still passes through zero for $e = 0 \text{ C m}^{-1}$, the range of flexoelectric voltage shifts are slightly larger than when A_{θ} was large (c.f. +1.3 V over $1 \times 10^{-10} \text{ C m}^{-1}$ for $A_{\theta} = 1.2 \times 10^{-6} \text{ J m}^{-2}$ with -1.1 V over $1 \times 10^{-10} \text{ C m}^{-1}$ for $A_{\theta} = 1.2 \times 10^{-5} \text{ J m}^{-2}$). Also this curve is significantly less linear than its predecessors. This trend is further investigated later in sections 1.9.1.8.

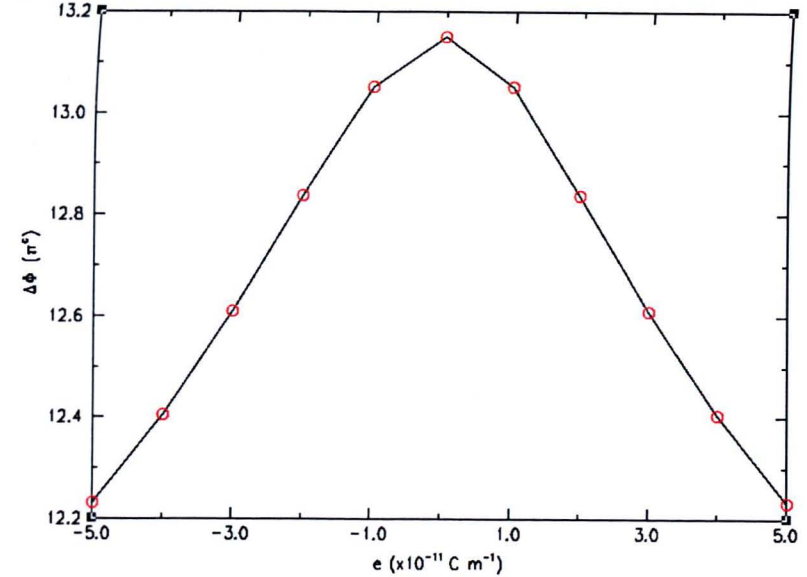


Figure (1.9.1.6.3.5) Shows $\Delta\Phi$ shift against flexoelectric coefficient, e , when A_{θ} is small.

Not only is there a change of sign of the gradient of the flexoelectric voltage shift there is also a change in the sign of the gradient of this graph with decreasing A_{θ} . While we still have symmetry, now, at $e = 0 \text{ C m}^{-1}$, there is a maximum instead of a minimum. Changing the flexoelectric coefficient from 0 to $\pm 5 \times 10^{-11} \text{ C m}^{-1}$ reduces the phase difference of the central feature by 0.91π .

Summarising the effects of varying the flexoelectric coefficient and the homeotropic anchoring energy.

When the anchoring energy is high the flexoelectric voltage shift is a linear function of the flexoelectric coefficient, e , and the transmittance curves are symmetric about their flexoelectric voltage shift. However, when the homeotropic anchoring energy is reduced the transmittance curves cease to be symmetric when $e \neq 0 \text{ C m}^{-1}$ and the linear relationship between e and V_{shift} is lost. In extreme cases, the sign of the flexoelectric voltage shift can be changed. However, the nature of the asymmetry (in $\Delta\varepsilon = \text{negative}$ systems) can be used to reveal the sign of e when A_{ϕ} is critically low.

1.9.1.7 Varying the homeotropic anchoring energy, $A_{\theta 0}$ (for constant e)

As has already been seen, reducing the homeotropic anchoring energy can have profound effects on the shape (among other things) of the transmittance curves. Also, examining the director profiles of the systems thus far raises the question *what would happen if the sign of $\Delta\varepsilon$ were changed?* Obviously, an electric field would not distort a positive $\Delta\varepsilon$ system the same way as it would a negative $\Delta\varepsilon$ system. It is also clear that the most interesting scenario for examining positive $\Delta\varepsilon$ systems will be for non-zero flexoelectricity and varying homeotropic anchoring energy. For these reasons, comparisons between such systems are of great interest. In this subsection we examine varying $A_{\theta 0}$, firstly for a negative $\Delta\varepsilon$ system (e.g. MBBA) with $e = -5 \times 10^{-11} \text{ C m}^{-1}$, then for the same system but changing the sign of $\Delta\varepsilon$.

Figure types four and five are not included here. However, figure type four is used to examine MBBA and E7 (i.e. opposing $\Delta\varepsilon$ systems) later on (in section 1.9.1.8.2) examining these systems more extensively, as the detail available at the current juncture does not reveal the true richness of this area.

1.9.1.7.1 Varying A_{θ} for MBBA, with $e = -5 \times 10^{-11} \text{ C m}^{-1}$ and $\Delta\epsilon$ negative.

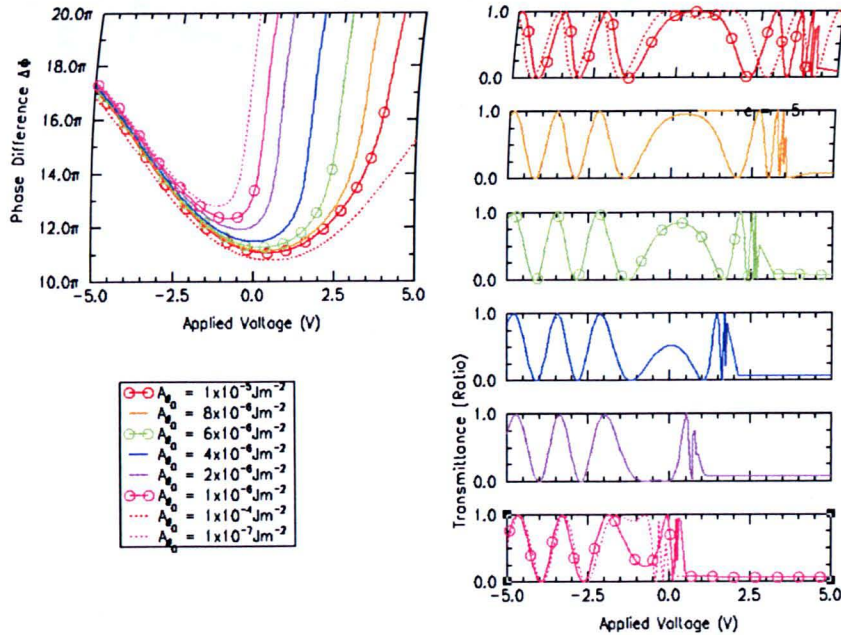


Figure (1.9.1.7.1) Shows transmittance and phase difference $\Delta\Phi$ against voltage for varying A_{θ} when $\Delta\epsilon$ is negative.

It can be seen that decreasing the anchoring energy from $1 \times 10^{-4} \text{ J m}^{-2}$ results in asymmetries in the transmittance and phase difference curves, in addition to moving the flexoelectric voltage shift of the central feature in the opposite direction than the flexoelectric coefficient moves it. For example, a *negative* flexoelectric coefficient produces a *positive* flexoelectric voltage shift when A_{θ} is large; *however*, reducing the homeotropic anchoring angle moves the voltage shift in the *same* direction as the sign of the flexoelectric coefficient. To see this compare the red dashed line (large A_{θ}) with the cerise dotted line (very low A_{θ}) and see how the intermediate curves behave.

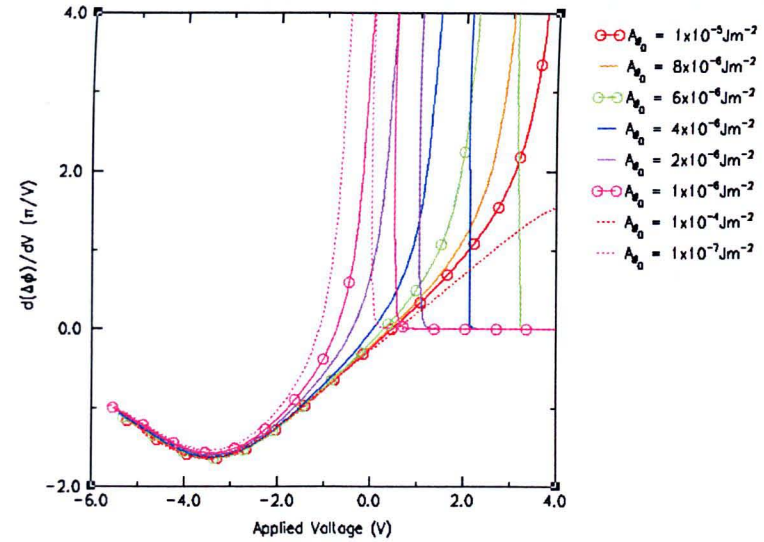


Figure (1.9.1.7.2) Shows the rate of change of phase difference $\Delta\Phi$ against voltage for varying A_{θ} when $\Delta\epsilon$ is negative.

When the anchoring energy is large, see the red dotted line of $A_{\theta} = 1 \times 10^{-5} \text{ J m}^{-2}$, the curve is symmetric (about the V_{shift}). Whereas, when the anchoring energy falls the right hand side of this graph becomes distorted, making these curves asymmetric and moving the voltage shift back towards zero and eventually beyond zero, when $A_{\theta} < 4 \times 10^{-6} \text{ J m}^{-2}$ (blue curve). Note that all the curves for voltages $< -2 \text{ V}$ are almost indistinguishable. Recall that these curves would be reflected about the 0 V axis if the sign of e were changed.

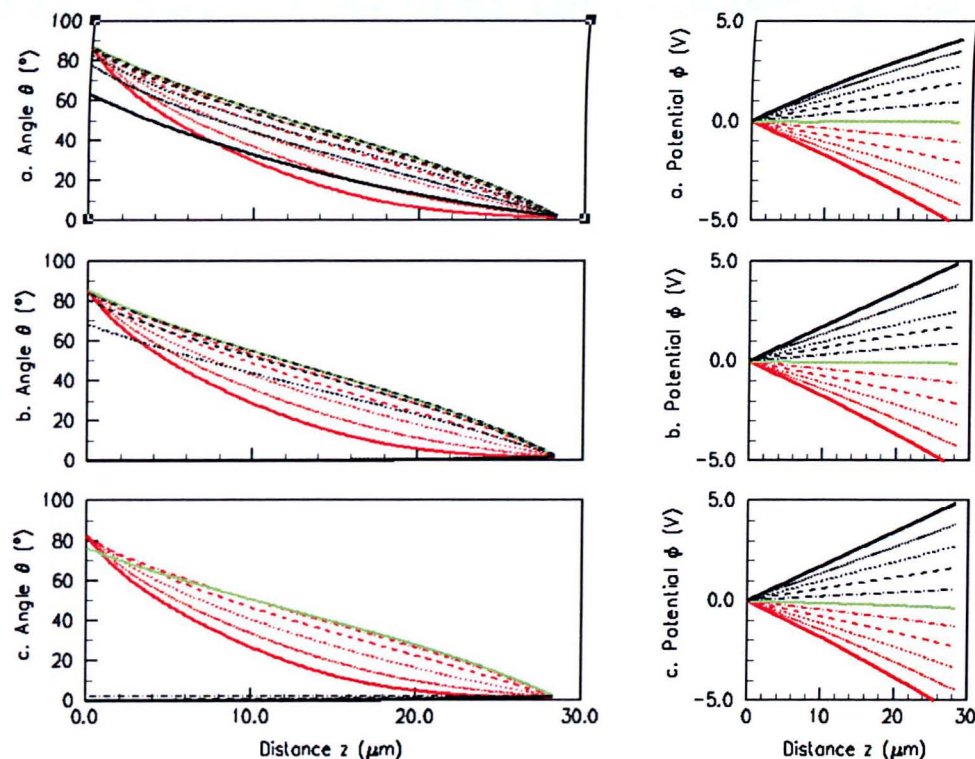


Figure (1.9.1.7.1.3) Shows θ and ϕ against z for varying $A_{\varphi 0}$ when $\Delta\epsilon$ is negative.

- (a) $A_{\varphi 0} = 1 \times 10^{-5} \text{ J m}^{-2}$
- (b) $A_{\varphi 0} = 6 \times 10^{-6} \text{ J m}^{-2}$
- (c) $A_{\varphi 0} = 1 \times 10^{-6} \text{ J m}^{-2}$

The reason for the changes in figures (1.9.1.7.1.1 and 2) for positive voltages, yet the lack of changes for negative voltages, become clearer by examining the graphs in this figure (left). To demonstrate the latter of these two points examine the red curves in the θ graphs. For each graph the curves of the negative voltages look almost identical: this is why the left hand sides of the graphs in figures (1.9.1.7.1.1 and 2) look so similar.

By contrast, and demonstrating the first point, the θ curves for positive voltage (black curves) look very different from graph (a) to (c). In (a), when $A_{\varphi 0}$ is moderate, θ at $z = 0$ deviates only slightly from θ_{easy} . However, in (c), when $A_{\varphi 0}$ is small, θ at $z = 0$ deviates significantly from θ_{easy} , instead being roughly equal to 0° .

1.9.1.7.2 Varying $A_{\theta 0}$ for MBBA, with $e = -5 \times 10^{-11} \text{ C m}^{-1}$ and $\Delta \epsilon$ positive.

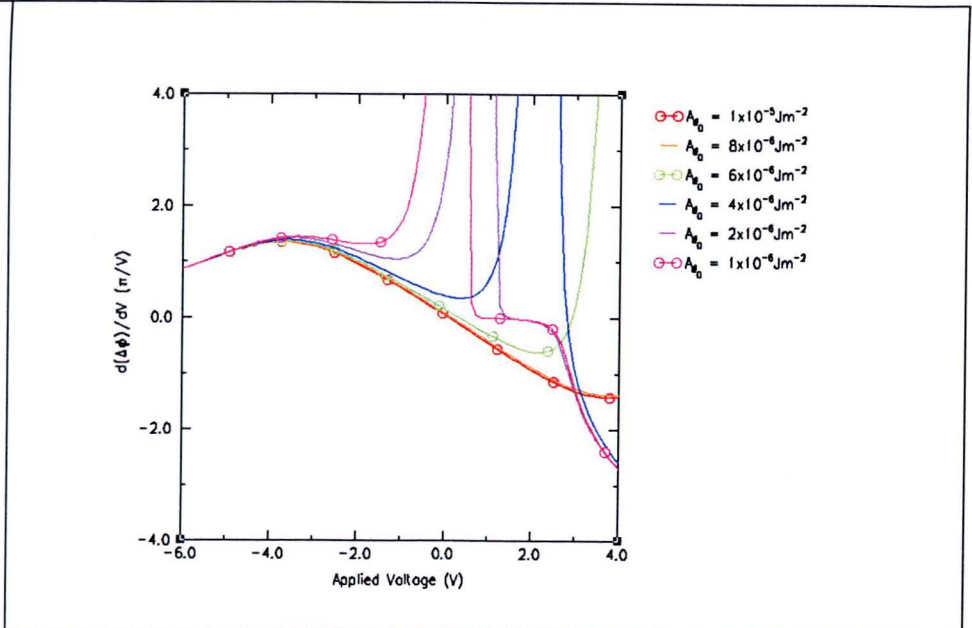
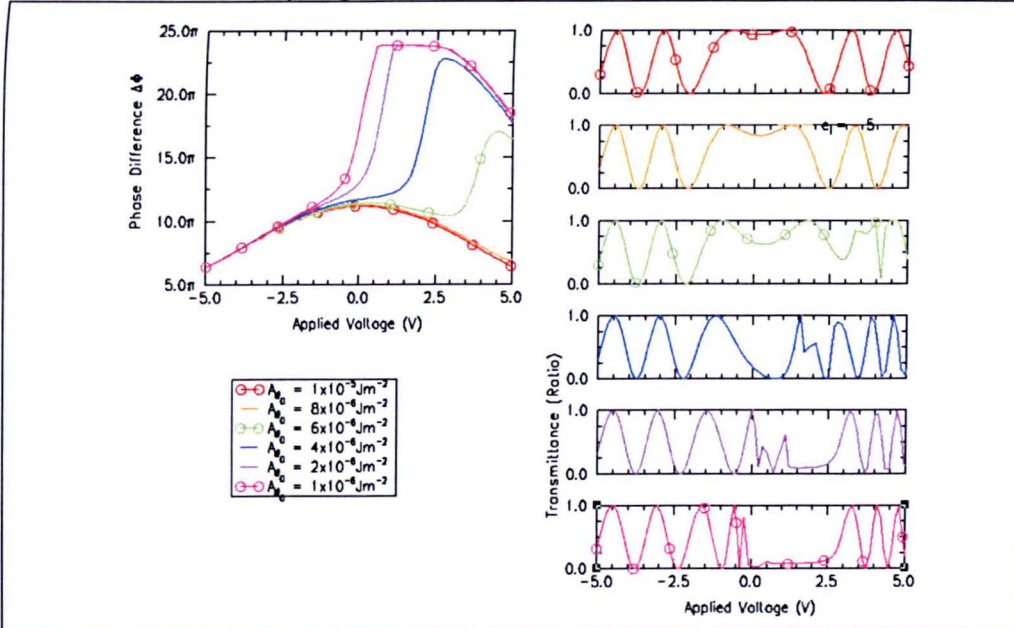


Figure (1.9.1.7.2.1) Shows transmittance and phase difference $\Delta\Phi$ against voltage for varying $A_{\theta 0}$ when $\Delta\epsilon$ is positive.

The first thing to be noted is that the phase difference curves are ‘the other way up’ from when $\Delta\epsilon$ was negative. The other thing to be noted is that decreasing the anchoring energy, while initially having next to no effect (compared with when $\Delta\epsilon$ was negative), can have devastating effects on the shape of the phase and transmittance curves once the anchoring energy has fallen. For example, once the anchoring energy falls to $4 \times 10^{-6} \text{ J m}^{-2}$ then the central turning point, which is referred to as the central feature, is lost. New turning points occur, however, these are distinctly separate from the central feature.

N.B. if the flexoelectric coefficient were smaller, then this picture would look different. This is touched upon in section 1.9.2, when examining E

Figure (1.9.1.7.2.2) Shows the rate of change of phase difference $\Delta\Phi$ against voltage for varying $A_{\theta 0}$ when $\Delta\epsilon$ is positive.

Reducing the anchoring energy initially has next to no effect, c.f. the red and orange curves of $A_{\theta 0} = 1 \times 10^{-5} \text{ J m}^{-2}$ and $A_{\theta 0} = 8 \times 10^{-6} \text{ J m}^{-2}$ respectively. However, when $A_{\theta 0} < 4 \times 10^{-6} \text{ J m}^{-2}$ (blue) the effects of reducing the anchoring energy have become alarming. While this system is initially slower to react to changing $A_{\theta 0}$ (i.e. slower to become noticeably asymmetric) it is interesting to note that the region where $A_{\theta 0}$ becomes critical is the same as it had been for negative $\Delta\epsilon$ system. Presumably, this is because the size of the contributions of the elastic, dielectric and flexoelectric terms remain of the same magnitude even if one changes sign

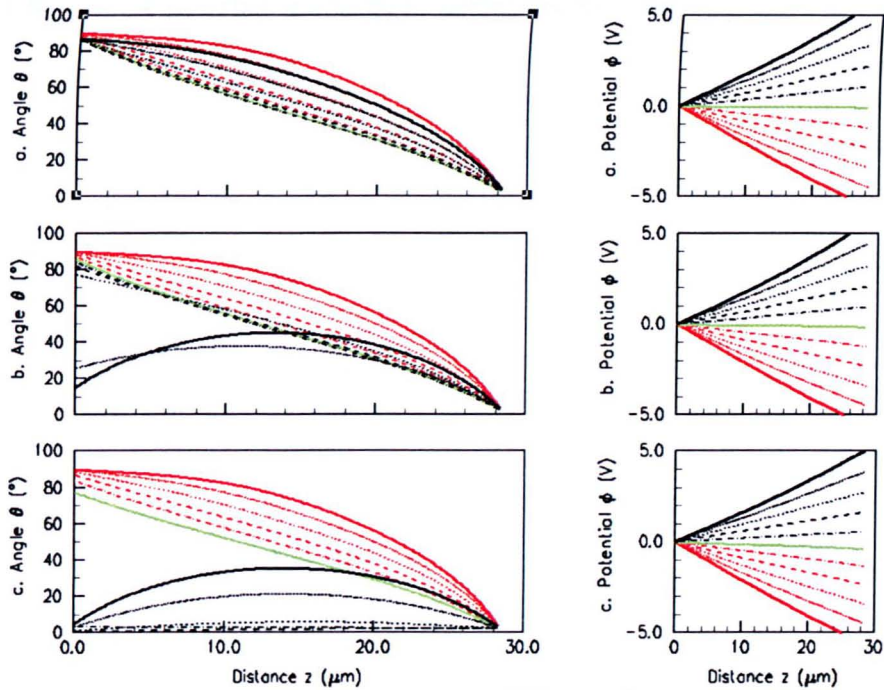


Figure (1.9.1.7.2.3) Shows θ and ϕ against z while varying $A_{\theta 0}$ when $\Delta\epsilon$ is positive

- (a) $A_{\theta 0} = 1 \times 10^{-5} \text{ J m}^{-2}$
- (b) $A_{\theta 0} = 6 \times 10^{-6} \text{ J m}^{-2}$
- (c) $A_{\theta 0} = 1 \times 10^{-6} \text{ J m}^{-2}$

The reason for the inversion of the phase curve is clear in the θ curves of this graph. By looking at the director profiles of (a) we see that the curves for positive and negative voltages follow paths where $\theta(z) > \theta(z)_{0V}$ (i.e. the green curve). Applying a voltage distorts the θ curves upwards instead of downwards, as had been the case when $\Delta\epsilon$ was of the opposite sign.

However, the reason why there are asymmetries observed once again when $A_{\theta 0}$ becomes small can be explained by examining the positive voltage θ curves in graphs (b) and (c) where $A_{\theta 0}$ is $6 \times 10^{-6} \text{ J m}^{-2}$ and $1 \times 10^{-6} \text{ J m}^{-2}$ respectively. There we see that the θ curves at $z = 0$ respond similarly to how they did when $\Delta\epsilon$ was negative (see figure (1.9.1.7.1.3)). This leads us to conclude that lowering the homeotropic anchoring energy can allow the flexoelectric contribution to exceed the dielectric contribution

1.9.1.8 Varying dielectric anisotropy, $\Delta\epsilon$

This section is subdivided slightly differently from what has generally been the trend. This is because figure type five is not of great interest compared with figure type four. Figure type four is of sufficiently great interest that we investigate it for a wider range of $\Delta\epsilon$ than is done in the next three figures (§ 1.9.1.8.1). Of particular interest is seeing how $\Delta\epsilon$ influences the flexoelectric voltage shift for MBBA and E7 systems (§ 1.9.1.8.2).

1.9.1.8.1 General effects of varying the dielectric anisotropy of a medium.

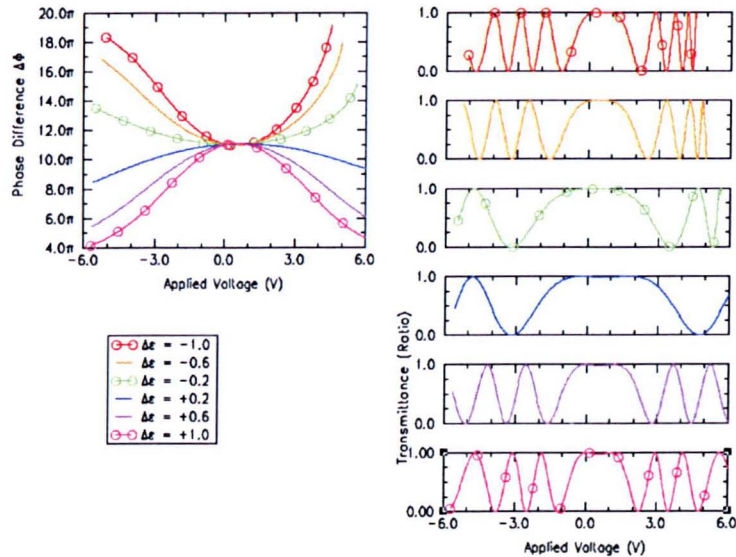


Figure (1.9.1.8.1.1) Shows transmittance and phase difference $\Delta\Phi$ against voltage with varying $\Delta\epsilon$

Here it can be seen that changing the sign of $\Delta\epsilon$ can result in very similar transmittance curves, certainly in the central region. An example of this can be seen by comparing the central features of the $\Delta\epsilon$ equal to + and -1 curves (cerise and red respectively). However, examining the phase difference curves (left) reveals that these transmittance curves are clearly the result of quite different

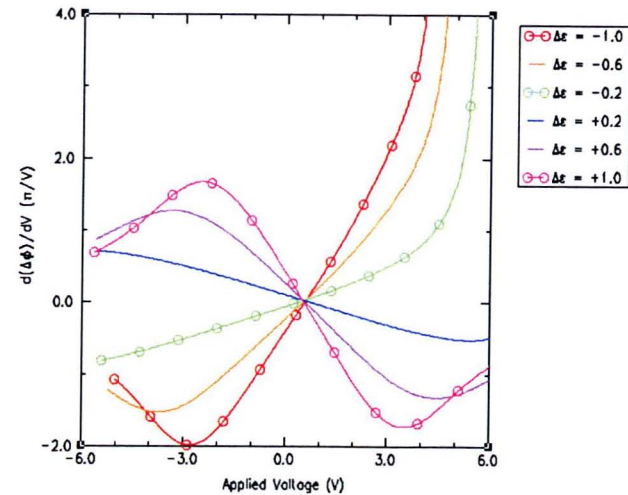


Figure (1.9.1.8.1.2) Shows the rate of change of phase difference $\Delta\Phi$ against voltage with varying $\Delta\epsilon$

It can be seen from this graph that the curves belonging to positive $\Delta\epsilon$ have rotational symmetry; therefore, these can be considered 'well behaved'. One aspect of what 'well behaved' means is that the flexoelectric voltage shift is proportional to the flexoelectric coefficient. As when discussing figure (1.9.1.8.1.1), the magnitude of the gradient of the $\Delta\epsilon$ curves is reduced when the magnitude of $\Delta\epsilon$ is reduced in

phase difference curves.

Another major feature to note is that decreasing $\Delta\epsilon$ results in a broadening of the curves: this can be seen as a shallowing of the gradient, depicted in the next graph.

the region -3 to +3 V. In this region the positive $\Delta\epsilon$ curves are almost exact reflections of their negative counterparts, reflected about the flexoelectric voltage shift of +0.5 V or about the $d(\Delta\Phi)/dV = 0$ axis. This accounts for the similarities between equal magnitude $\Delta\epsilon$ transmittance curves in figure (1.9.1.8.1.1).

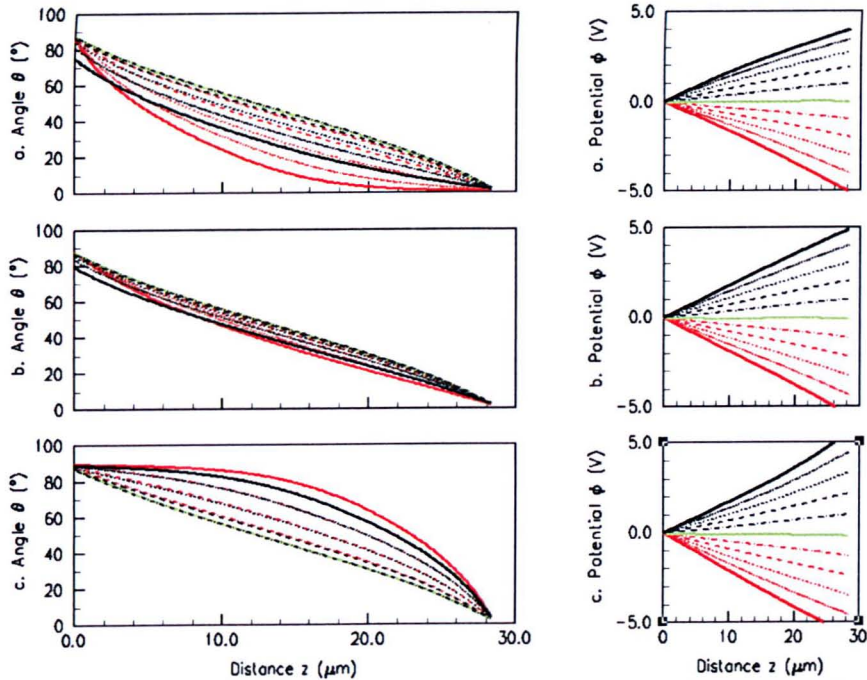


Figure (1.9.1.8.1.3) Shows θ and ϕ against z for varying dielectric anisotropy

- (a) $\Delta\epsilon = -1.0$
- (b) $\Delta\epsilon = -0.2$
- (c) $\Delta\epsilon = +1.0$

Here, the reasons for the differences observed in figures (1.9.1.8.1.1 and 2) due to both changing the sign of $\Delta\epsilon$ and changing the magnitude of $\Delta\epsilon$ are made clear.

The change due to changing the sign of $\Delta\epsilon$ was that the phase difference curves were (roughly) inverted about $\Delta\Phi$ of the central region. The reason for this is the different direction that voltages distort the θ curves when the sign is changed, c.f. graphs (a) and (c). The distortions are in the opposite direction but are of similar magnitudes, hence the differences between the phase difference curves yet the similarity between the transmittance curves (respectively)

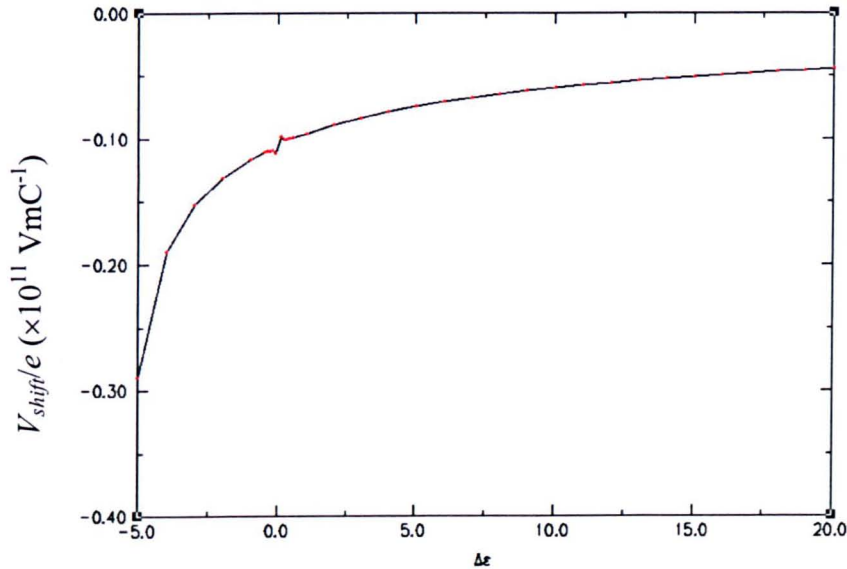
The second trend is due to the fact that when $\Delta\epsilon$ is smaller the distortions that the same voltage can produce are reduced. To see this, compare graphs (a) and (b), where $\Delta\epsilon$ has the same sign but different magnitudes. When $\Delta\epsilon$ is small the θ curves are more closely spaced than when $\Delta\epsilon$ is large, thus resulting in a decrease in the gradient of the $\Delta\Phi$ and transmittance curves in figure (1.9.1.8.1.1).

While it is of interest to look at the effects that this range of $\Delta\epsilon$ has on the voltage shift, it was considered more interesting to examine the situation for a much greater range, and to compare this with a similar graph obtained for E7. The results of this are shown on the next two pages.

1.9.1.8.2 The flexoelectric voltage shift for varying $\Delta\epsilon$ for an otherwise MBBA like material

$\Delta\epsilon$ and e are among the largest contributing factors to the magnitude of the voltage shift. It is the intention that the following two graphs be of some practical purpose: if $\Delta\epsilon$ is known and A_{θ} is large, these graphs and the flexoelectric voltage shift could be used in order to find the flexoelectric coefficient e ($= e_{11}+e_{33}$). The reader should note that these graphs were calculated for a flexoelectric coefficient of $e = -5 \times 10^{-11} \text{ C m}^{-1}$ and then expressed in units of $e = +1 \times 10^{-11} \text{ C m}^{-1}$; here the voltage shift is, to a very good approximation, linear in e .

1.9.1.8.2.1 Varying $\Delta\epsilon$ for MBBA



(Recall the default parameters for MBBA see table (1.9.1))

There are three main features to be noted here:

1. There is a singularity when $\Delta\epsilon = 0$.
2. When $\Delta\epsilon$ is large and positive the flexoelectric voltage shift changes gradually.
3. However, when $\Delta\epsilon$ is negative the flexoelectric voltage shift varies more rapidly with changes in $\Delta\epsilon$.

As MBBA's $\Delta\epsilon$ is negative, and homeotropic anchoring energies tend to be small, finding the flexoelectric coefficient e accurately would be more problematic than it would be for systems with positive $\Delta\epsilon$.

Figure (1.9.1.8.2.1) Shows voltage shift per e against changing dielectric anisotropy, $\Delta\epsilon$, for MBBA.

1.9.1.8.2.2 The flexoelectric voltage shift for varying $\Delta\epsilon$ for an otherwise E7 like material

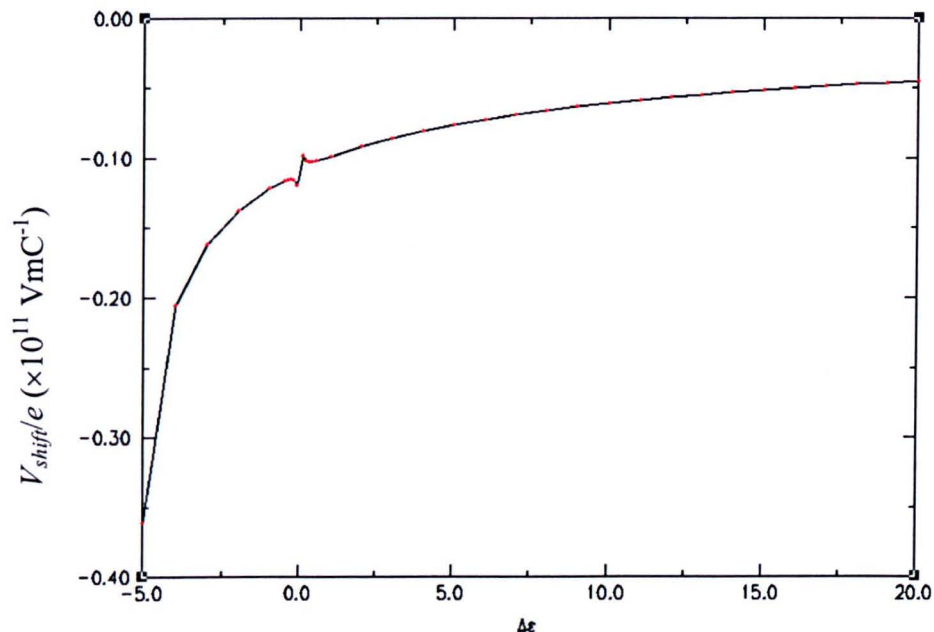


Figure (1.9.1.8.3.1) Shows V_{shift} per e against changing dielectric anisotropy, $\Delta\epsilon$, for E7.

(Recall the default parameters for E7 see table (1.9.2))

The same three things that could be noted about the same curve for MBBA are also the case for E7. In fact, these curves are almost identical. The only difference seems to be an increase in the steepness of the curve when $\Delta\epsilon$ is negative. This can be attributed to the smaller value of ϵ_N for E7 than for MBBA (5.2 and 5.4 respectively), therefore the ratio of $\Delta\epsilon$ to ϵ_N is smaller for E7 than for MBBA.

As E7's $\Delta\epsilon$ is positive, finding the flexoelectric coefficient e accurately will be easier than it would be for systems with negative dielectric anisotropy.

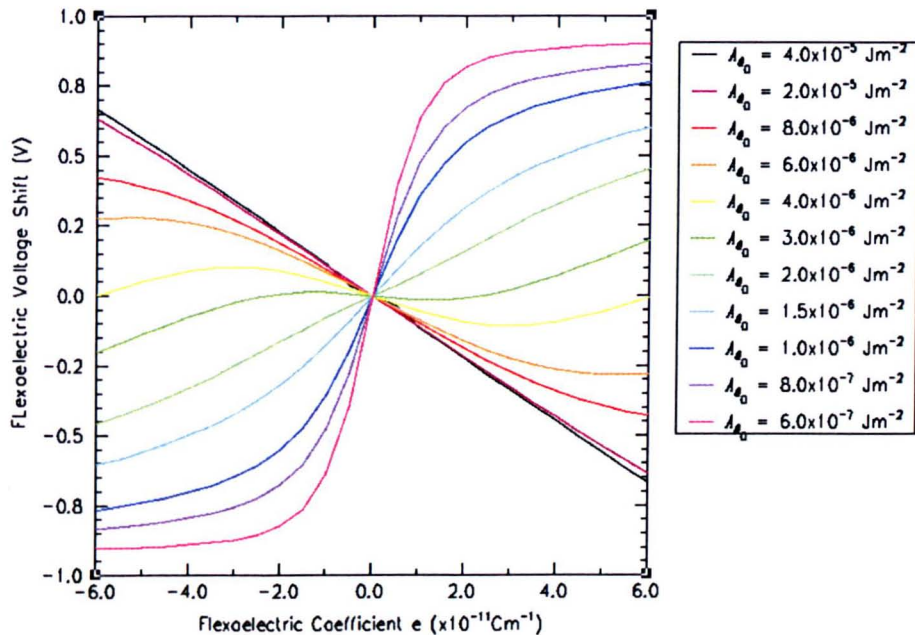
Summary of flexoelectric voltage shift for varying dielectric anisotropy for MBBA and E7

These curves (§ 1.9.1.8.2) are, in fact, so similar that they tell us that the flexoelectric voltage shift depends strongly on two factors: the size of e and the size of $\Delta\epsilon$. If the homeotropic anchoring energy is large, it may be possible that the flexoelectric coefficients could be found directly from these graphs and the experimental voltage shift. However, if the anchoring energy is not large this would become impractical. It will be seen in section 1.9.2 that this casts doubt on how Takahashi et al. [1] obtained their value of e for MBBA.

1.9.1.9 Varying homeotropic anchoring energy and flexoelectric coefficients.

Having previously not concluded our discussion in section 1.9.1.7 about the combined effects of varying homeotropic anchoring energy and flexoelectric coefficients on the size of the flexoelectric voltage shift, we propose to amend that now. Also, we have seen that the sign of $\Delta\varepsilon$ has profound effects on the behaviour of cells when combined with the two aforementioned parameters. For that reason we examine two systems with different $\Delta\varepsilon$ s here, i.e. MBBA and E7.

1.9.1.9.1 Varying homeotropic anchoring energy and flexoelectric coefficients for MBBA ($\Delta\varepsilon$ negative).



When A_{θ} is large the flexoelectric voltage shift is a linear function of e over the range examined. This can be seen by examining the black and maroon curves of $A_{\theta} = 4$ and $2 \times 10^{-5} \text{ J m}^{-2}$ respectively. However, when the anchoring energy is reduced this linearity is lost. In fact, for the range $A_{\theta} = 6 \times 10^{-6} \text{ J m}^{-2}$ to $A_{\theta} = 3 \times 10^{-6} \text{ J m}^{-2}$ there are voltage shift regions for which there are more than one flexoelectric coefficient that might be responsible. For example, when $A_{\theta} = 4 \times 10^{-6} \text{ J m}^{-2}$ (yellow curve) a flexoelectric voltage shift of $+0.04 \text{ V}$ could be due to a flexoelectric coefficient of circa $-5 \times 10^{-11} \text{ C m}^{-1}$ or $-1 \times 10^{-11} \text{ C m}^{-1}$. Alarmingly, extrapolating beyond the range of this graph, we see that e could also have been roughly equal to $+6 \times 10^{-11} \text{ C m}^{-1}$. Thus, when A_{θ} is sufficiently small, the sign of the flexoelectric voltage shift is no longer an adequate indicator of the sign (let alone the magnitude) of e . These *badly behaved* flexoelectric voltage curves are, however, accompanied by an asymmetry of the transmittance curves (recall section 1.9.1.7), therefore the *sign* of e can be established: if the positive arm (right hand side) of a transmittance curve is *badly behaved* then e is negative, and *vice versa*. Potentially, examining the extent of the asymmetry of the transmittance curves could be used to find which value of e is most likely to be correct.

Figure (1.9.1.9.1) Shows how the flexoelectric voltage shift varies for different homeotropic anchoring energies, A_{θ} , for MBBA.

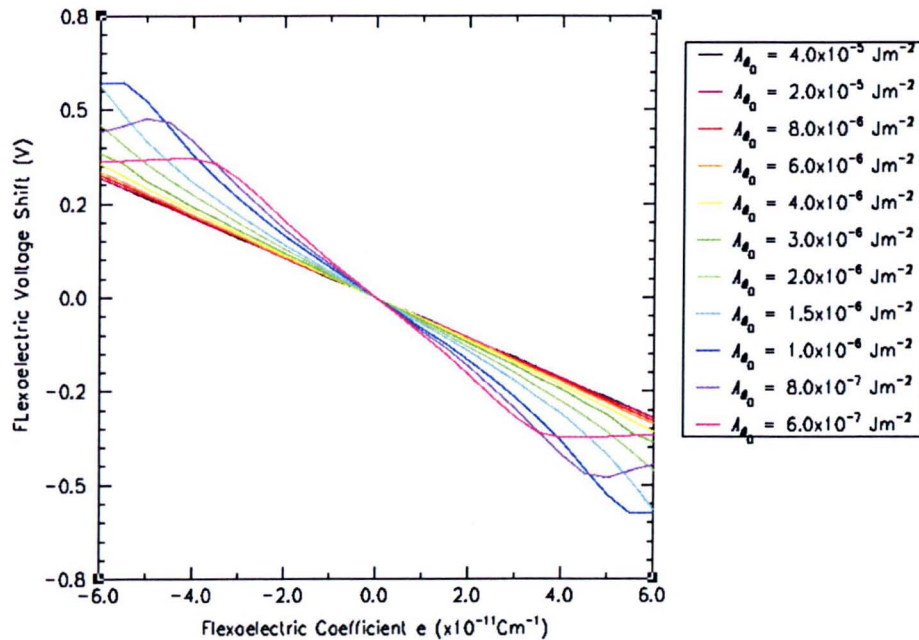
1.9.1.9.2 Varying homeotropic anchoring energy and flexoelectric coefficients for E7 ($\Delta\epsilon$ positive).

Figure (1.9.1.9.2) Shows how the flexoelectric voltage shift varies for different homeotropic anchoring energies, A_{e0} , for E7.

In comparison to figure (1.9.1.9.1), E7 is *well behaved* over the same A_{e0} range. Note for $A_{e0} = 4 \times 10^{-5}$ to 3×10^{-6} J m^{-2} (black to light-green) the flexoelectric voltage shift curves are nearly the same and, while the $A_{e0} = 8$ and 6×10^{-7} J m^{-2} curves are not exactly *well behaved*, they still result in the same sign of the flexoelectric voltage shift for a given e as when A_{e0} was larger.

1.9.1.10 Summary of Theoretical Findings and Conclusion

In table (1.9.3), below, some of the major findings from varying input parameters are summarised, including shifts in the voltage and $\Delta\Phi$ of the central features. This is followed by a brief discussion. However, the parameters e , A_{θ} and $\Delta\varepsilon$ combine to form more complex trends than other input parameters, so these are not summarised in this table but are discussed in greater detail after the other parameters.

Table 1.9.3: Summarises some of the main findings of the § 1.9.1.

PARAMETER	V_{shift}	$\Delta\Phi$ SHIFT	COMMENTS
Cell thickness, D	$+0.07 \text{ V} / 10 \mu\text{m}$	$+3.75 \pi / 10 \mu\text{m}$	Increasing D slightly increases the symmetry and steepness of the transmittance curve.
Birefringence, Δn	$+0.0016 \text{ V} / 0.1$	$+4.5 \pi / 0.1$	Increasing Δn slightly increases the steepness of the transmittance curve.
<i>Elastic constant</i>	<i>When e small</i>		K_{33} is more dominant in changing $d(\Delta\Phi)/dV$. Increasing elastic constant generally decreases $d(\Delta\Phi)/dV$. Also, these curves are steeper than they are when e is large.
$K_{11} = K_{33}$	$-0.005 \text{ V} / 1 \times 10^{-11} \text{ N}$	$+0.34 \pi / 1 \times 10^{-11} \text{ N}$	
Varying K_{11}	$-0.005 \text{ V} / 1 \times 10^{-11} \text{ N}$	$+2.1 \pi / 1 \times 10^{-11} \text{ N}$	
Varying K_{33}	$-0.015 \text{ V} / 1 \times 10^{-11} \text{ N}$	$-1.7 \pi / 1 \times 10^{-11} \text{ N}$	
<i>Elastic Constants</i>	<i>When e large</i>		K_{33} is slightly more dominant in changing $d(\Delta\Phi)/dV$. Increasing elastic constant generally decreases $d(\Delta\Phi)/dV$. Also, these curves are shallower than they are when e is small.
$K_{11} = K_{33}$	$-0.14 \text{ V} / 1 \times 10^{-11} \text{ N}$	$-0.275 \pi / 1 \times 10^{-11} \text{ N}$	
Varying K_{11}	$-0.025 \text{ V} / 1 \times 10^{-11} \text{ N}$	$+1.2 \pi / 1 \times 10^{-11} \text{ N}$	
Varying K_{33}	$-0.105 \text{ V} / 1 \times 10^{-11} \text{ N}$	$-0.9 \pi / 1 \times 10^{-11} \text{ N}$	
<i>Anchoring angle</i>			
Homeotropic θ_{easy}	$+0.13 \text{ V} / 10^\circ$	$-1.1 \pi / 10^\circ$	Decreasing θ_{easy} increases the symmetry of $\Delta\Phi$ curves.
Homogeneous θ_{Deasy}	$+0.021 \text{ V} / 10^\circ$	$-1.2 \pi / 10^\circ$	Varying θ_{Deasy} has little effect on the symmetry.
<i>Flexoelectric constant</i>			
When A_{θ} high	$-1.1 \text{ V} / 1 \times 10^{-10} \text{ Cm}^{-1}$	$+0.15 \pi / 5 \times 10^{-11} \text{ Cm}^{-1}$	Symmetric but shifted. Voltage shift is proportional to flexoelectric coefficient.
When A_{θ} medium	$-1.0 \text{ V} / 1 \times 10^{-10} \text{ Cm}^{-1}$	$+0.14 \pi / 5 \times 10^{-11} \text{ Cm}^{-1}$	Slightly asymmetric: Distortions occur for voltages of opposite sign to the flexoelectric coefficient. Voltage shift is roughly proportional to flexoelectric coefficient.
When A_{θ} low	$+1.35 \text{ V} / 1 \times 10^{-10} \text{ Cm}^{-1}$	$-0.91 \pi / 5 \times 10^{-11} \text{ Cm}^{-1}$	Very asymmetric: Distortions have continued and changed the sign of the voltage shift. Voltage shift is only proportional to flexoelectric coefficient when e is small.

***D* and Δn**

Varying either the cell thickness D , or the birefringence Δn , of a system has a comparable effect, i.e. increasing the net birefringence of a device. Increasing either of them increases the number of wavelength path differences between ordinary and extraordinary rays.

Elastic constants, K_{11} and K_{33} .

From the point of view of $\Delta\Phi$ of the central feature, the one-constant approximation is not appropriate irrespective of the size of the flexoelectric coefficient. The same is generally true of the flexoelectric voltage shift: over the range examined, the elastic constants could produce approximately a 10% change in the V_{shift} . However, we saw that the contributions to the flexoelectric voltage shift from both K s were not equal, as K_{33} appears to have a larger influence. Therefore, this leads us to conclude that, if a one-constant approximation is to be employed, it should be to make both K s roughly equal to K_{33} rather than the average of K_{11} and K_{33} .

Angles of easy axis, θ_{0easy} and θ_{Deasy}

Reducing the difference between θ_{0easy} and θ_{Deasy} reduces the cumulative path difference between ordinary and extraordinary components of the incident ray, i.e. the net birefringence of a cell. Reducing the homeotropic anchoring energy (θ_{0easy}) reduces the flexoelectric voltage shift significantly. Therefore, the importance of accurately knowing the value of θ_{0easy} has been demonstrated.

Homeotropic anchoring energy, flexoelectric coefficient and dielectric anisotropy, A_{θ} , e and $\Delta\varepsilon$ respectively.

These can all combine to contribute to some interesting properties. On their own they have the following effects:

- Reducing the homeotropic anchoring energy below a particular value increases the steepness of the transmittance curve.
- Increasing the flexoelectric coefficient increases the flexoelectric voltage shift.
- Changing the sign of $\Delta\varepsilon$ changes the direction that an applied electric field distorts the director profile, whereas changing the size of $\Delta\varepsilon$ changes the sensitivity of the cells to changes in the electric field.

However, some of the interesting properties that these parameters combine to produce are as follows, in particular when A_{θ} is small:

- The flexoelectric coefficient combined with low homeotropic anchoring energy produces asymmetries.
- When $\Delta\varepsilon$ is positive, even when A_{θ} is relatively small, the flexoelectric voltage shift of the cell is relatively *well behaved*, i.e. V_{shift} remains approximately proportional to e with roughly the same constant of proportionality for all A_{θ} s. Whereas, for negative $\Delta\varepsilon$, when A_{θ} falls the proportionality of V_{shift} to e is quickly lost: some curves do not have a uniquely defined e for a given V_{shift} ; and, for those curves that have a region of proportionality, the constant of proportionality may vary vastly from one A_{θ} to another.

In conclusion, as most homeotropic alignment layers have relatively weak anchoring energies, this last point casts doubt on the suitability of Takahashi's method for finding the flexoelectric coefficient of LC materials [1], especially when $\Delta\epsilon$ is negative as it is for MBBA. However if we examine the asymmetries of the transmittance curves at the same time as investigating the flexoelectric voltage shift, it may be possible to overcome this obstacle. This is examined in the next section, where the knowledge acquired here is applied to experimental systems.

1.9.2 Experimental Results

1.9.2.1 Introduction

The purpose of this section is to take the knowledge gained in the previous section and apply it to experimental data. There are two main materials under examination here which provide a good cross section of typical liquid crystal materials as these two materials have dielectric anisotropies $\Delta\epsilon$ of opposing sign. This parameter was found to exert the greatest influence on a cell's optical behaviour, and *how well* the cell 'behaves' when the homeotropic anchoring energy is low.

Seven sets of experimental results from HAN cells were obtained: one from Takahashi's paper [1], and six from experiments performed by Bartle (member of the Organophotonics Group, in conjunction with the Liquid Crystal Group at Hull University) [30]. The first of Bartle's systems was a HAN cell containing the liquid crystal mixture E7, and the remaining five were 10% solutions of different dopant liquid crystals dissolved in E7. Takahashi's experiments explored a different LC, i.e. working instead on a cell containing the nematic liquid crystal MBBA [1].

This section is further subdivided. Firstly, we introduce the seven different cells and explain how and why the experimental data was then normalized (with only one exception), before the simulations were undertaken. For this simulation process, the experimental results are then divided into three main sections. These are E7 (one set), 10% solutions (by weight) (five sets), and MBBA (one set). Their continuum-model input parameters are then introduced and which of these parameters are malleable is outlined (i.e. relatively unknown and therefore subject to large variations). After each subsection, these results are analysed and discussed. For Bartle's data we start by discussing which parameters are deemed variable as well as the

simulation process (in varying detail according to the system and its similarity to others). Calculations of the dipolar moments for the five dopant materials were also performed. The theoretical values of the dipole moments were then examined in the context of changes in the values obtained for $\Delta\epsilon$ with respect to that of E7. This was done to discover if there were any trends in how the dopant molecules cause changes in the properties of the systems.

While the Takahashi data is only one set, compared with the six data sets supplied by Bartle, it transpired that it poses greater challenges to the simulations than the Bartle data. For this reason a significantly more rigorously systematic method for finding a solution, or establishing if there is no solution, must be adopted.

Unlike in the previous section, where we could obtain a large amount of data about the cells, in this section the only experimental data available are the transmittance versus voltage curves. Each figure has been subdivided into a number of separate graphs in order to include the maximum amount of information while retaining clarity. For all the following results, the experimental data is shown in black and the simulations are coloured. Colour-coded keys are provided beneath the graphs.

E7 is a commercially available liquid-crystal mixture. The dopants were synthesised by the Organophotonics Group at the University of Hull [30] and their molecular structures are shown below in table (1.9.2.1).



IMAGING SERVICES NORTH

Boston Spa, Wetherby

West Yorkshire, LS23 7BQ

www.bl.uk

**PAGE NUMBERING AS
ORIGINAL**

fitting process (in varying detail according to the system and its similarity to others). Calculations of the dipolar moments for the five dopant materials were also performed. The theoretical values of the dipole moments were then examined in the context of changes in the values obtained for $\Delta\varepsilon$ with respect to that of E7. This was done to discover if there were any trends in how the dopant molecules cause changes in the properties of the systems.

While the Takahashi data is only one set, compared with the six data sets supplied by Bartle, it transpired that it poses greater challenges to curve fitting than the Bartle data. For this reason a significantly more rigorously systematic method for finding a solution, or establishing if there is no solution, must be adopted.

Unlike in the previous section, where we could obtain a large amount of data about the cells, in this section the only experimental data available are the transmittance versus voltage curves. Each figure has been subdivided into a number of separate graphs in order to include the maximum amount of information while retaining clarity. For all the following results, the experimental data is shown in black and the curve fits are coloured. Colour-coded keys are provided beneath the graphs.

The molecular information for the commercial liquid-crystal mixture E7 is not freely available. However, the dopants were synthesised by the Organophotonics Group at the University of Hull [30] and their molecular structures are shown below in table (1.9.2.1).

Table 1.9.2.1:

Shows molecular structures of the dopants dissolved (10% by weight) in E7.

Sample Code	Molecular Structure
JHW33	
JHW29	
JHW128	
JHW131	
JHW172	

1.9.2.2 Normalising Experimental Data

For the results obtained from the experiments, the transmittance T has arbitrary units (rather than being in the form of a ratio of transmitted light intensity to total light intensity). Therefore, if the intention is to simulate these data sets, then it is necessary for them to be normalised since both the computer program and the theory only predict transmittances in the form of ratios, i.e. between 0 and 1 (or 0 and 100%). With the possible exception of the central region of the transmittance-voltage curves, the theory dictates that maxima and minima correspond to 100% and 0% transmittances respectively, so (when normalising the experimental data curves) it is necessary to ensure that the troughs coincide with $T = 0$, and that the peaks coincide with $T = 1$. In order to achieve this several steps must be taken.

The first step is to find and note the voltages at which maxima occur and the magnitude of the transmittance there, and then repeat the process for the minima. The purpose of this is to establish a data set's envelope. Once the envelope is found, the data can be normalised: this is done by subtracting the minima function (i.e. the lower envelope), and then scaling the difference between the maxima and minima functions (i.e. upper and lower envelopes) to equal one.

The number of points on the minima and maxima curve (i.e. the envelopes) is limited, and is significantly smaller than the number of points within a transmittance-voltage curve. Therefore, to perform normalization, these curve fits should take the form of algebraic functions of the voltage: once an algebraic function is found, normalisation of each data point, and therefore the whole curve, is simple.

One method of obtaining curve fits in an algebraic form is to perform a polynomial regression on the maxima points, and to repeat the process for the minima points. In this particular instance, this was performed using a graphics package called XMGR, which is UNIX based. XMGR is capable of performing numerous different types of regressions, including polynomials up to 10th order.

These regressions are the second step in the curve fitting process. The order of regression is found by trial and error; the criterion being used for this decision was how well the experimental data, once operated on, fitted between 0 and 1 while trying to ensure that (with the possible exception of the central feature) the data oscillated between the full range of 0 to 1. The way in which these two regressions were used to normalise the curve was to subtract initially for each experimental data point the corresponding value of the minima regression curve, and then scale it by the difference between maxima and minima regression curves, i.e.

$$T_{normalized}(V_i) = (T_{experimental}(V_i) - \min(V_i)) / (\max(V_i) - \min(V_i)),$$

where $T_{experimental}(V_i)$ is the experimental transmittance, $T_{normalized}(V_i)$ is the normalized data, and the functions $\min(V_i)$ and $\max(V_i)$ are the polynomials used to curve fit the envelopes of the experimental data.

For some curves it was obvious that \max and/or \min curve fit functions needed to be composed exclusively of even functions or that they also needed some odd functions as well, and this helped in choosing the order of the regression polynomial $y(x)$, which took the general form

$$y = \frac{y - (a + bx + cx^2 + dx^3 + ex^4 + \dots)}{(A - a) + (B - b)x + (C - c)x^2 + (D - d)x^3 + (E - e)x^4 + \dots}$$

The experimental curves are shown below in figures (1.9.2.1) to (1.9.2.7). The experimental data before the numerical scaling, i.e. against an arbitrary transmittance scale, are shown on the left hand side of figures (1.9.2.1) to (1.9.2.6), followed by the results of the normalising process in the right hand panels. The sample containing JHW128 has been exempted from this (see below), just showing the pre-normalised data in figure (1.9.2.7). Otherwise, the polynomial fitting parameters used to normalise the experimental data can be found in Appendix I.

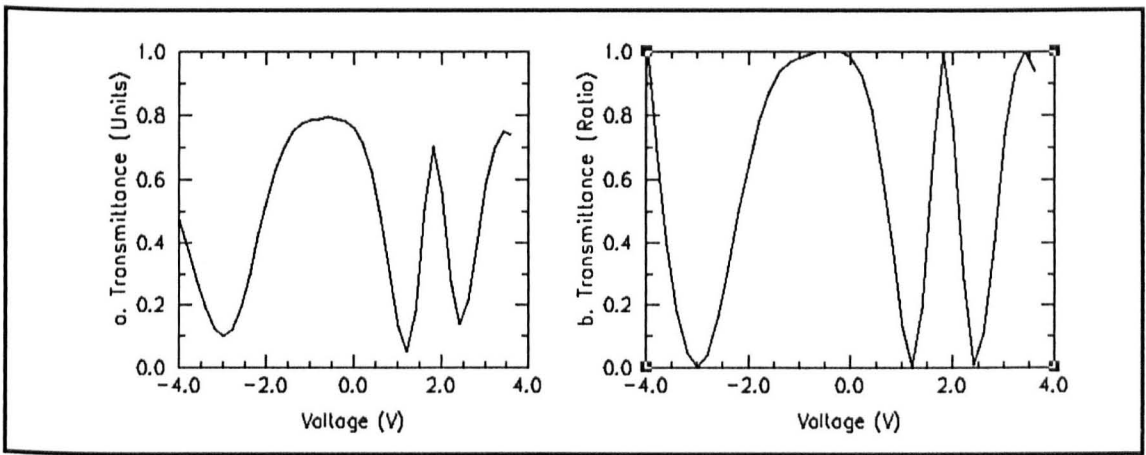


Figure 1.9.2.1: Shows the experimental data for the MBBA cell of Takahashi et al. [1].

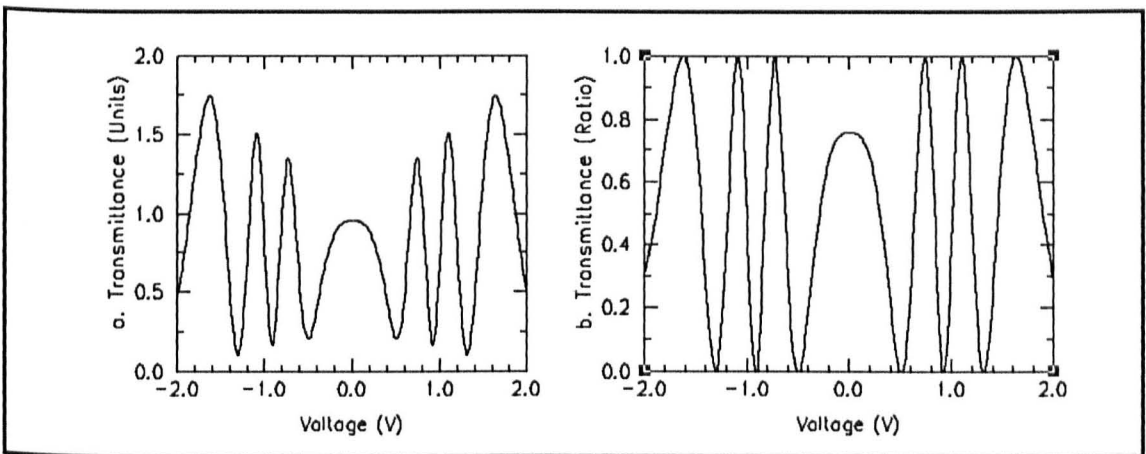


Figure 1.9.2.2: Shows the experimental data for the E7 cell of Bartle [30].

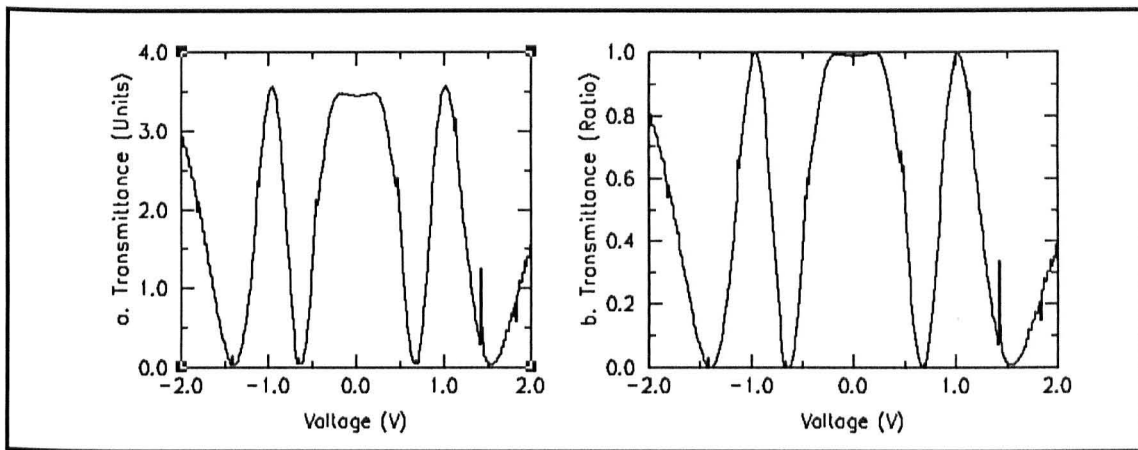


Figure 1.9.2.3: Shows the experimental data for the 10% JHW29 in E7 cell of Bartle [30].

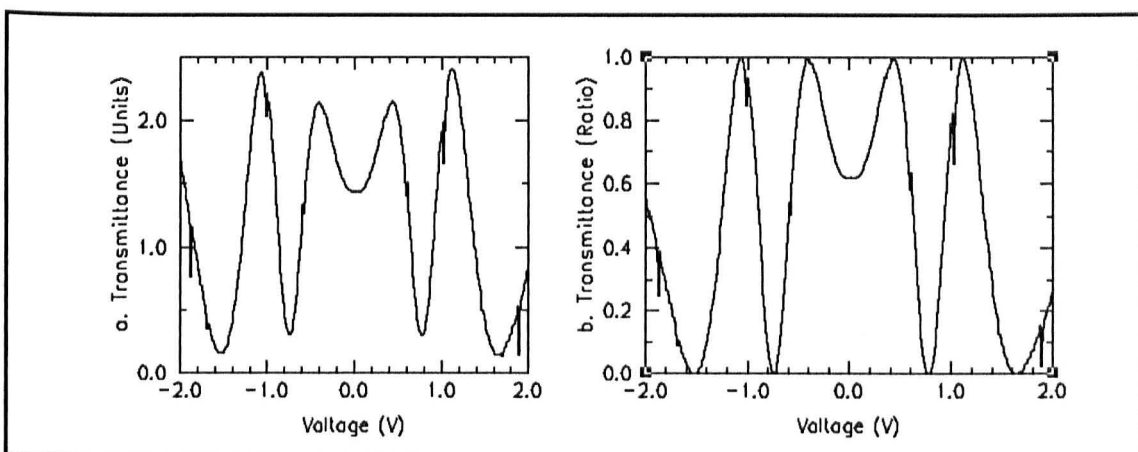


Figure 1.9.2.4: Shows the experimental data for the 10% JHW33 in E7 cell of Bartle [30].

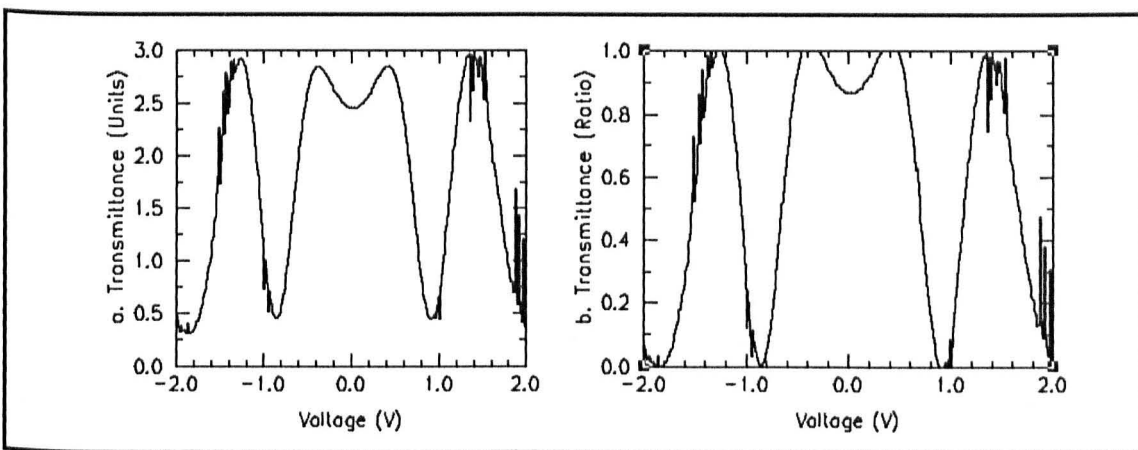


Figure 1.9.2.5: Shows the experimental data for the 10% JHW131 in E7 cell of Bartle [30].

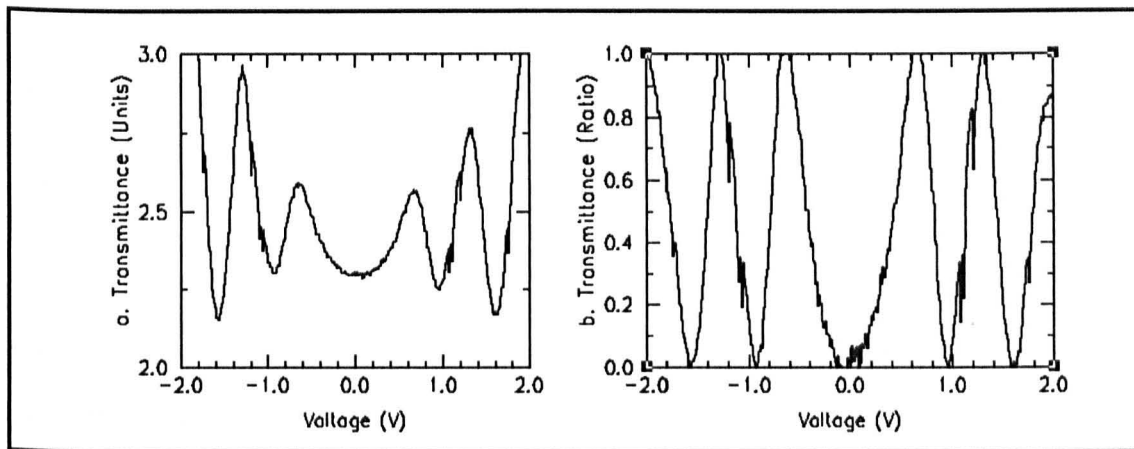


Figure 1.9.2.6: Shows the experimental data for the 10% JHW172 in E7 cell of Bartle [30].

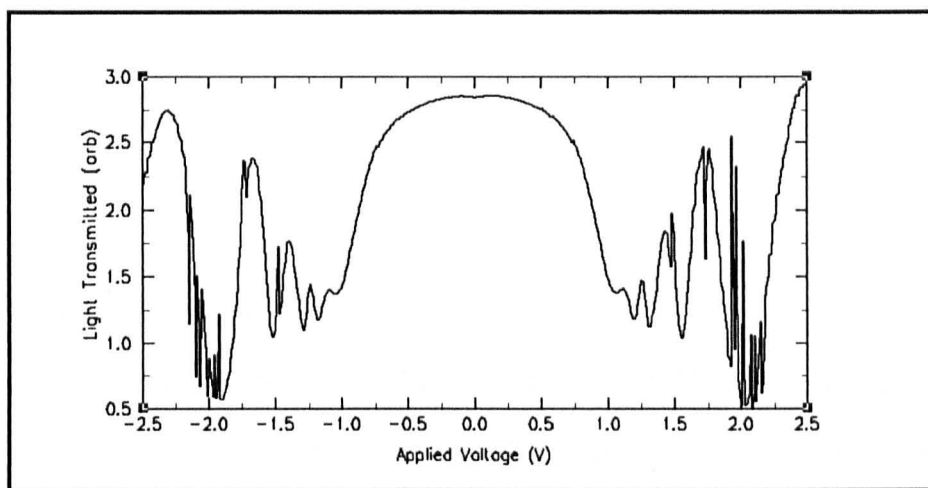


Figure 1.9.2.7: Shows only the experimental data for the 10% JHW128 in E7 cell of Bartle [30].

Unlike the other data sets, the one for JHW128 (figure (1.9.2.7)) was neither normalised nor simulated. The reason for this is that the fluctuations close to the central feature are unusually small and rapid: from the theory we expect the oscillations to toggle between the maximum and minimum of an enveloping function, whereas this is *clearly* not the case here. (Later, when examining E7, it will be seen that if this curve actually were to oscillate between 0 and 1 then its shape would be indicative of a very low anchoring energy for a system where $\Delta\varepsilon$ is positive.) Also, when there are such a large number of oscillations, it is usually difficult to discern one solution from another. Consequently, there is no confidence that a meaningful and distinguishable simulation to this data is obtainable.

1.9.2.3 Simulations

In what follows we are using the term “simulation” specifically to mean performing computer simulations to find data that is visually comparable with experimental data.

For the remaining six sets of data that shall be simulated here, we start with the E7 system and its four normalised 10% solutions systems, before going on to examine the MBBA system. For different systems, different input parameters are *malleable* and others are genuinely inflexible. For this reason, at the beginning of each of the three subsections (i.e. E7, 10% solutions in E7 and finally MBBA) a brief discussion about the variability of input parameters is given.

Aside for all E7 Systems:

With reference to which of the input parameters are malleable, the treatment of the two types of Bartle's curves (i.e. E7 and the 10% solutions) is different. Values of parameters such as $\Delta\varepsilon$ and Δn are well established for E7, therefore, for E7 these values are fixed. However, while the solutions contain 90% E7 (by weight), leading to similar behaviour and parameters for these cells being anticipated, the values of $\Delta\varepsilon$ and Δn for the mixtures are unknown. Consequently, these parameters are variable. Below, we shall discuss why we chose to keep Δn constant, and relate the values we obtain for $\Delta\varepsilon$ with the dopant molecules' dipolar moments.

Before starting the simulation process in earnest, and in the light of the uncertainty in the value of the cell thickness D , a preliminary examination of changing the cell thicknesses is undertaken. This is done in increments of 2 μm , over the range $D = 14$ to 32 μm . From the number of peaks and

the shape of the central region of the transmittance-voltage curves, we were able to estimate the actual thicknesses of the HAN cells. These compare favourably with the values obtained experimentally, see table (1.9.2.2) below, where the experimental values of D are taken from Bartle [30]. While the values obtained from the simulations are smaller than the experimental values, they appear to follow an approximate ratio of $D_{\text{experimental}} = 1.4 \times D_{\text{theory}}$. This suggests that either the experimental value is overestimated or that the theory has a scaling factor. However, this trend certainly is not a cause of major concern, given the uncertainty in both the theoretical and particularly the experimental values of the cell thickness. Thus, we conclude that there is reasonable agreement between the two sets of data, see table (1.9.2.2) below.

Table 1.9.2.2:

Shows how the experimentally determined cell thicknesses (in units of μm) correspond with the values obtained from the simulation process. The average ratio of $D_{(\text{exp})}/D_{(\text{sim})} = 1.4$.

LC	$D_{(\text{experimental})}$	$D_{(\text{sim})}$	Ratio $\text{EXP}/\text{C.F.}$
E7	30.2	27.5	1.10
JHW29	26.8	16.9	1.59
JHW33	24.9	18.0	1.38
JHW131	27.8	17.4	1.60
JHW172	35.4	26.6	1.33

Recall that, in section (1.9.1) we saw that varying Δn exhibited equivalence to varying D ; here, in table (1.9.2.2), we see that the theoretical value of D closest to its experimental value belongs to the one system whose Δn is most accurately known, i.e. E7. Whereas all the other cells have effective cell thicknesses more significantly reduced from their experimental values. This implies that when adding these dopant materials, all have similar effects on the effective birefringence of these cells, apparently decreasing it.

1.9.2.3.1 E7

E7 is a commercially available liquid crystal material. Most of its physical and optical properties are well documented. These properties were already summarized in table (1.9.2), section 1.9.1. Here we will limit the number of free parameters that are variable in order to focus the discussion on the main characteristics of the cell: the reader should note that the grey parameters in table (1.9.2.3) are not referred to throughout the remainder of this chapter. As mentioned above, there is some uncertainty in the actual thicknesses of the cells [30] and so these have been included among the variable parameters. For the E7 mixtures, the values used for their cell thicknesses in the simulations, are shown in the $D_{(sim)}$ column of table (1.9.2.2) and were found by trial and error.

Table 1.9.2.3: Shows the default parameters for E7 and MBBA

Parameter	E7	MBBA
θ_{Deasy}	90°	90°
θ_{Deasy}	2°	2°
D	30.2 μm	28.5 μm
K_{11}	$11.1 \times 10^{-12} \text{ N}$	$6.4 \times 10^{-12} \text{ N}$
K_{33}	$17.1 \times 10^{-12} \text{ N}$	$8.2 \times 10^{-12} \text{ N}$
A_{θ}	$1.2 \times 10^{-5} \text{ J.m}^{-2}$	$1.2 \times 10^{-5} \text{ J.m}^{-2}$
$A_{\theta\theta}$	$5.0 \times 10^{-2} \text{ J.m}^{-2}$	$5.0 \times 10^{-2} \text{ J.m}^{-2}$
ε_n	5.2	5.4
ε_p	19.0 ¹⁵	4.7
$\Delta\varepsilon$	+13.8	-0.7
λ	633 nm	550 nm
E	$-5.0 \times 10^{-11} \text{ C.m}^{-1}$	$-5.0 \times 10^{-11} \text{ C.m}^{-1}$
n_o	1.51821	1.57
n_E	1.73283	1.8
Δn	0.21462	0.23

For these two materials E7 and MBBA, $\Delta\varepsilon$ and Δn are very well established experimentally. However, parameters such as anchoring energies, specifically the homeotropic anchoring energy, A_{θ} , and the

¹⁵ While this value is not malleable for the E7 system, it becomes so for the 10% solutions of dopant in E7, hence its inclusion here

flexoelectric coefficient e are not well known. As has already been mentioned above, there is also some uncertainty in the actual thicknesses of the cells [30]. Having established that at least three of the input parameters are malleable (i.e. $A_{\theta 0}$, e and D) and that two are not (Δn and $\Delta \epsilon$), it is now possible to start seeking appropriate simulations for these two systems.

There are two circumstances in which more of the input parameters are varied. The elastic constants are among the parameters that are not accurately known from experiment [40]. However, as it is desirable to limit the number of parameters that are varied, this fact is only employed for the MBBA system (where it was considered necessary; further, these results of varying K_s and D were found to be interesting); whereas, for the systems containing 90% E7, $\Delta \epsilon_s$ are no longer known so we choose to vary ϵ_N , thus changing $\Delta \epsilon$ in these cases. As a result, while the study of E7 is limited to only changing D , e and $A_{\theta 0}$, for reference only, a graph showing how sensitive the system would be to changes in $\Delta \epsilon$ is also included. This sensitivity becomes relevant in the next section, where the $\Delta \epsilon$ is unknown, let alone fixed, for the 10% solutions.

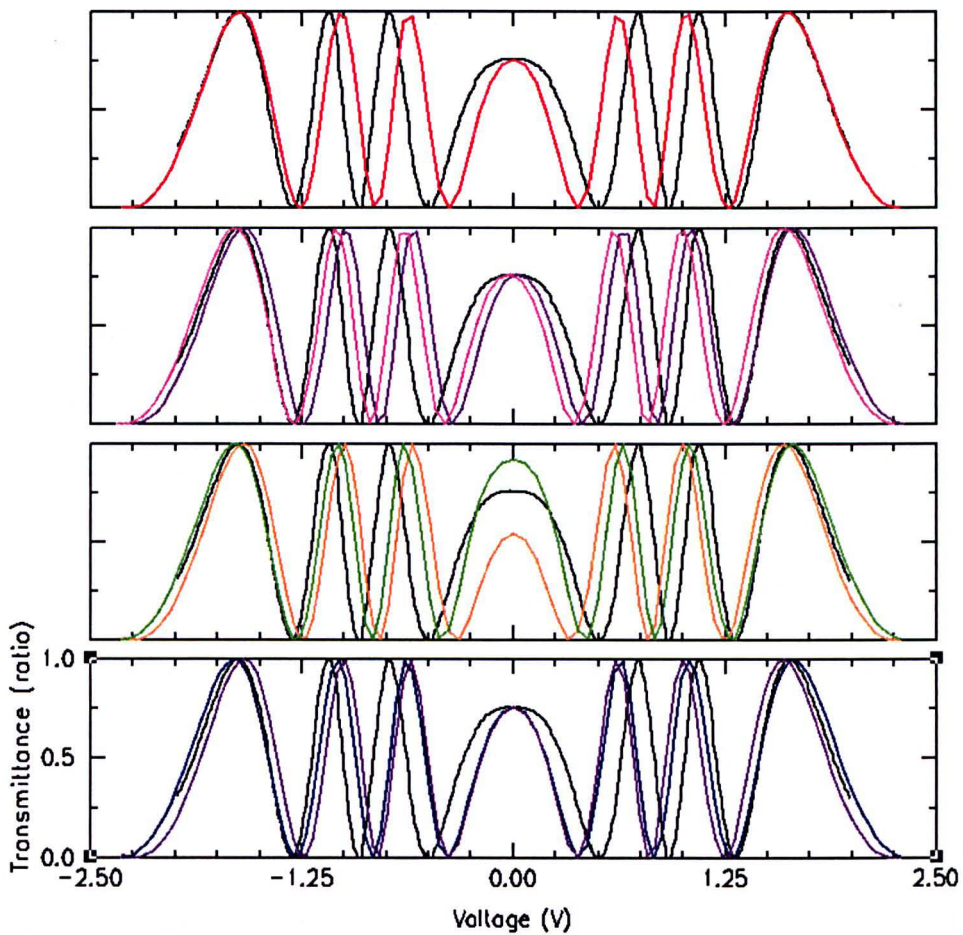


Figure 1.9.2.8: Shows simulations (coloured curves, see key) for E7 cell (black curve)

Colour	D μm	$\Delta\epsilon$	e $\times 10^{-11} \text{ Cm}^{-1}$	A_{∞} $\times 10^{-6} \text{ Jm}^{-2}$
KEY: Red	27.5	13.8	0.0	9.00
Violet	27.5	13.8	-0.5	9.00
Cerise	27.5	13.8	0.5	9.00
Orange	27.0	13.8	0.0	9.00
Green	28.0	13.8	0.0	9.00
Blue	27.5	13.3	0.0	9.00
Purple	27.5	14.3	0.0	9.00

A best fit (red curve) to the experimental data (black curve) for the E7 cell is shown in the first panel of figure (1.9.2.8). While it has roughly the correct shape and has a central feature of the correct magnitude, only three out of the seven peaks coincide with the peaks of the experimental data. The theoretical curves in this figure are colour-coded according to the key underneath the figure, where altered input parameters are denoted in bold

font. The bottom three panels are included to demonstrate the sensitivity of the simulations.

Changing e (the flexoelectric coefficient) does not improve matters overall (see second panel): while it may improve matters for two peaks (e.g. near 0.75 and 1.0 V *or* -0.75 and -1.0 V), the effects on all the other peaks and troughs is to the detriment of the simulations (see the violet and cerise curves). The degree of symmetry here suggests that the flexoelectric coefficient is very small if not zero. This is significantly smaller than the value of $(1.5 \pm 0.2) \times 10^{-11}$ C m as determined by Yang *et al.* [39]. The reason for this is currently unclear but may be due to the relatively large experimental uncertainties.

In the next panel, with the green and orange curves, we see the effects of changing the cell thickness. These changes affect the whole of the curve rather than just the central area, which is actually the region of concern. From this it is deduced that the value of $D = 27.5 \mu\text{m}$ is appropriate, and that varying D from this value will not lead to a better simulation. (N.B. this was performed for all the 90% E7 cells to obtain the values shown in table (1.9.2.3)). However, that process is not shown here as it was discussed in detail for MBBA in section 1.9.1.1 and reiterating it here will add nothing beyond the trivial to the current discussion.

Despite the fact that $\Delta\epsilon$ is well established experimentally, we are curious to see how sensitive the system would be to errors in this parameter. This is shown in the final panel of figure (1.9.2.8). Decreasing $\Delta\epsilon$ has the effect of broadening the curves. This effect is uniform across the curves, so even if this parameter were flexible it could not provide the simulation sought.

Earlier, the lack of accuracy with which $A_{\theta 0}$ is known was mentioned so this parameter was also varied. However, the results were far more interesting than those shown in figure (1.9.2.8). Consequently, we pause here to examine these effects in greater detail and the results of this are shown below in figure (1.9.2.9).

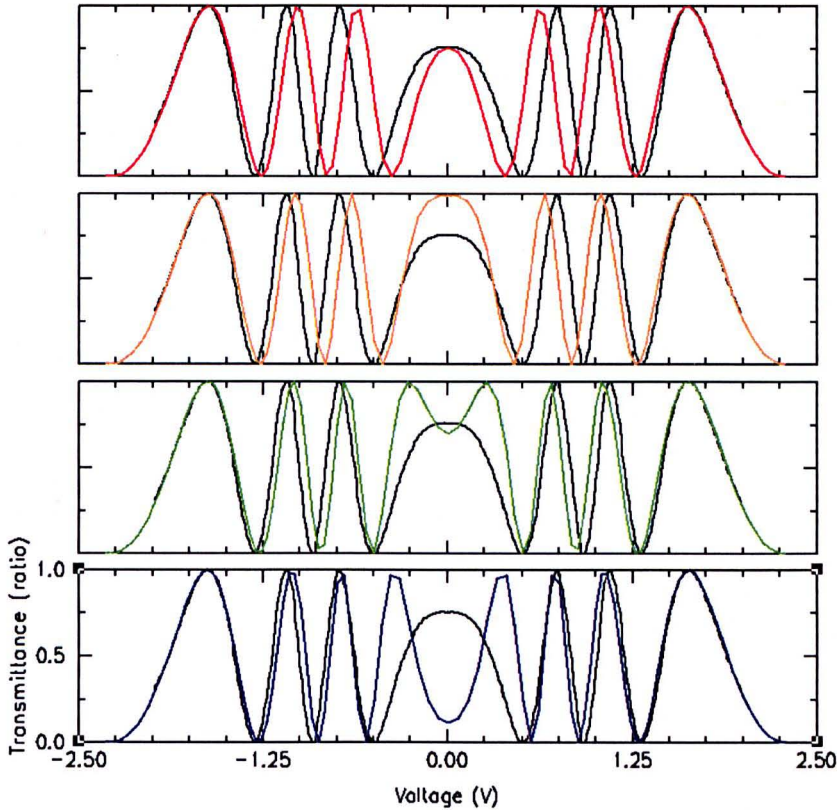


Figure 1.9.2.9: Shows the effects of varying $A_{\theta 0}$ for the E7 cell.

Colour	D μm	$\Delta\epsilon$	$\times 10^{-11} \text{ e Cm}^{-1}$	$A_{\theta 0}$ $\times 10^{-6} \text{ Jm}^{-2}$
Red	27.5	13.8	0.0	9.00
Orange	27.5	13.8	0.0	6.00
Green	27.5	13.8	0.0	4.00
Blue	27.5	13.8	0.0	3.00

It is seen here in figure (1.9.2.9), that lowering the homeotropic anchoring energy, while having negligible effect on the curve shape for large positive and negative voltages, has a profound effect on the central region. For the moderate voltages regions (larger than $\pm 0.5 \text{ V}$) we see that reducing this anchoring energy actually improves the quality of the simulation.

If ion impurities were present in the cell, they would act to screen the electric field across the cell at lower voltages and their effect on the optical transmittance would become absent at higher voltages, because they would be removed from the system. This could go some way towards explaining these experimental observations (black curve) in figure (1.9.2.9). The screening due to ion impurities could be acting to reduce the responsiveness of the cell at low voltages and would give rise to large errors in the anchoring energies determined by the fitting procedure. While the cell thickness appears to determine the shape of the transmittance-voltage curve at large voltages relatively strictly (see figure (1.9.2.8)), this knowledge of how anchoring energies affect the central region could lead to an effective method for finding the anchoring energy (as long as the influence of ion impurities is small). Admittedly, the issues presented by ion impurities are still relevant here and mean that the value obtainable for A_{∞} could potentially include large errors.

1.9.2.3.2 Simulations and Discussion for the 10% Solutions

For the 10% solutions fewer of the input parameters are readily known. However, all systems contain 90% E7 (by weight). It is therefore reasonable (and desirable) to keep as many of the parameters as possible equal to those of E7. Amongst the parameters that we either know or suspect could differ from our E7 system are D , e , $\Delta\epsilon$ and Δn . Later we wish to relate the theoretical dipole moments of the dopant molecules with the birefringence obtained from our simulations for the 10% solutions; this comparison might become more opaque if *both* $\Delta\epsilon$ and Δn are altered. For this reason, we avoid tampering with Δn , concentrating our examination on varying $\Delta\epsilon$ instead. Thus we are limiting our investigation to varying only three of the above parameters (of which cell thicknesses have already been approximated, see table (1.9.2.3) at the beginning of the simulation section), and A_{∞} (which was not conclusively established for E7). How sensitive the optical properties of HAN cells are to variations in these continuum-model parameters in the vicinity of their best-fit values shall also be examined.

Firstly, we examine the two systems that contain the larger-sized dopant molecules JHW29 and JHW33. Then we examine the systems containing the smaller dopant molecules JHW131 and JHW172 (recalling that the data set for JHW128 was not normalised, hence its omission).

JHW29:

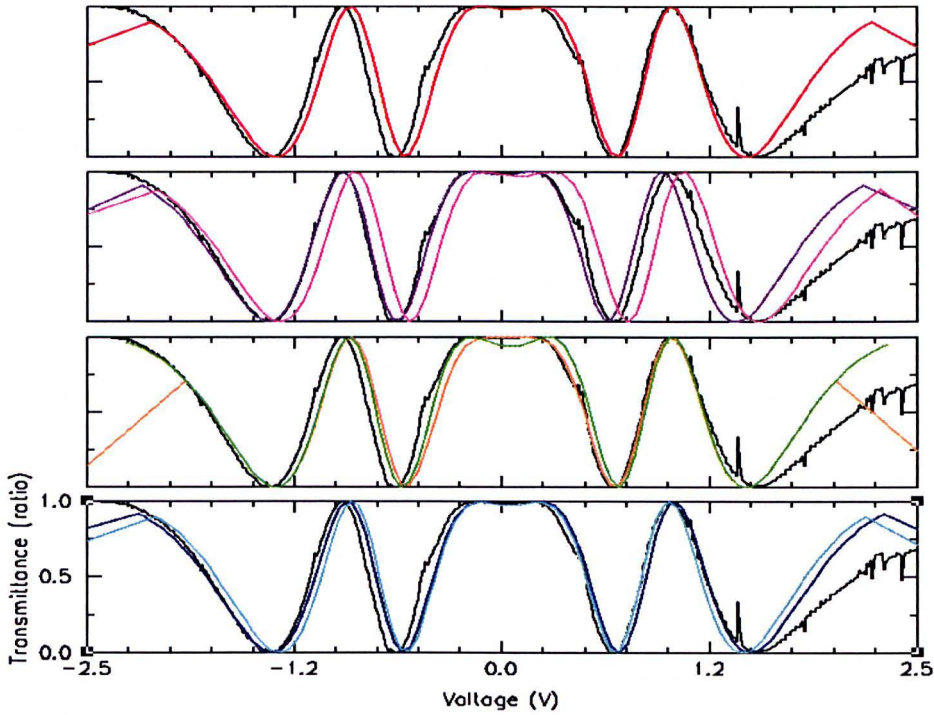


Figure 1.9.2.10: Shows simulations obtained for JHW29

Colour	D (μm)	$\Delta\epsilon$	e ($\times 10^{-11} \text{ Cm}^{-1}$)	A_{∞} ($\times 10^{-5} \text{ Jm}^{-2}$)
Red	16.9	15.8	-1	5.00
Violet	16.9	15.8	0	5.00
Cerise	16.9	15.8	-2	5.00
Orange	16.9	15.8	-1	10.00
Green	16.9	15.8	-1	3.00
Blue	16.9	15.3	-1	5.00
Turquoise	16.9	16.4	-1	5.00

The red curve of the top panel of figure (1.9.2.10) is the “best fit” simulation for JHW29. As can be seen, except for large positive voltages, the calculated emulates the experimental observations reasonably well (the kinks and straight lines in the calculated curves are artefacts of the calculations and should be ignored). However, the curves in the subsequent panels show how sensitive the system is to changes in the three variable parameters (shown in bold font in the key, beneath figure (1.9.2.10)). Some of these curves achieve better fits in certain regions than the red curve. For

example in the second panel the effects of varying e are examined. Here, the central region and negative voltages are better described by $e = 0$ than $-1 \times 10^{-11} \text{ C m}^{-1}$, whereas the cerise curve of $e = -2 \times 10^{-11} \text{ C m}^{-1}$ is better for large positive voltages but represents a poor fit for voltages below $+1 \text{ V}$.

In the next panel (with the orange and green curves) we see that changing the anchoring energy reduces the quality of the simulation. Note how, around the central feature, the location of peaks are adversely affected by changes made to the value of the homeotropic anchoring energy away from $A_{\theta 0} = 5 \times 10^{-5} \text{ J m}^{-2}$.

Unlike for the 100% E7 system, we do not have an experimental value for $\Delta\varepsilon$ for the 10% solutions. Thus, having found a best-fit curve (red, top panel), in the final (bottom) panel we examine how sensitive the system is to this parameter's influence. In certain regions (e.g. $+0.75$ to 1.0 V) increasing $\Delta\varepsilon$ improves the simulation (turquoise), whereas in other regions (e.g. $|V| > 1.5 \text{ V}$) decreasing $\Delta\varepsilon$ has the desired effect.

JHW33

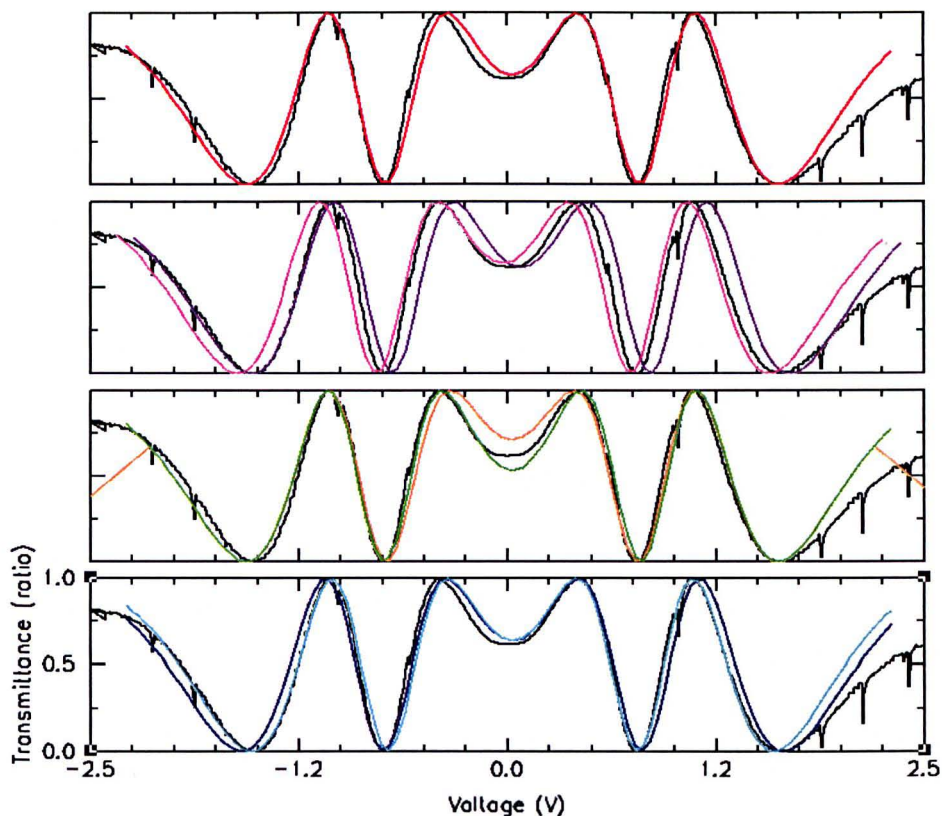


Figure 1.9.2.11: Shows simulatons obtained for JHW33

Colour	D (μm)	$\Delta\epsilon$	e ($\times 10^{-11} \text{ C m}^{-1}$)	A_{∞} ($\times 10^{-5} \text{ J m}^{-2}$)
Red	18	13.8	-0.5	5.00
Violet	18	13.8	-1.5	5.00
Cerise	18	13.8	0.5	5.00
Orange	18	13.8	-0.5	10.00
Green	18	13.8	-0.5	3.00
Blue	18	13.3	-0.5	5.00
Turquoise	18	14.3	-0.5	5.00

Again, the red curve in the first (top) panel shows our best simulation. It shows a slight discrepancy both for the central region and for voltages of magnitude larger than +1.5 V but, apart from that, it provides an excellent fit.

In the second panel the effects of varying the flexoelectric coefficient are shown; subtracting $1 \times 10^{-11} \text{ C m}^{-1}$ from e , thus increasing e 's magnitude

(violet curve), generally reduces the quality of the simulation, however, in the region below -1 V it actually improves it. When $1 \times 10^{-11} \text{ C m}^{-1}$ is added to e the overall quality of the simulation deteriorates.

In the next panel of figure (1.9.2.11), we see the influences of changing the homeotropic anchoring energy. Once again, we see that varying this parameter changes the shape of the central feature to the detriment of the simulation. However, it appears to have next to no influence on the shape of the simulations for large positive and negative voltages.

In the final (bottom) panel of figure (1.9.2.11) we see that increasing $\Delta\epsilon$ by 0.5 (turquoise curve) marginally improves the simulation for voltages less than +1.5 V. Whereas, an improvement in the quality of the simulation above +1.5 V can be obtained by decreasing $\Delta\epsilon$ (blue curve), but the rest of the curve suffers.

JHW128

As discussed above, we were not able to normalise this curve, consequently it has not been simulated. However, recalling the trend that was demonstrated in figure (1.9.2.9), we found that significantly decreasing the anchoring energy had little effect on the transmittance-voltage curve for large voltages but, effectively, 'squeezed' more peaks and troughs into the intermediate space. If it is assumed here that the peaks and troughs adjacent to the central feature should oscillate between 0 and 1, this would suggest that the anchoring energy is particularly low for this cell. We can also assume that the flexoelectric coefficient is small as, if it were not, we could expect to see features more akin to those observed in figure (1.9.1.7.2.1) of the theory results section.

JHW131

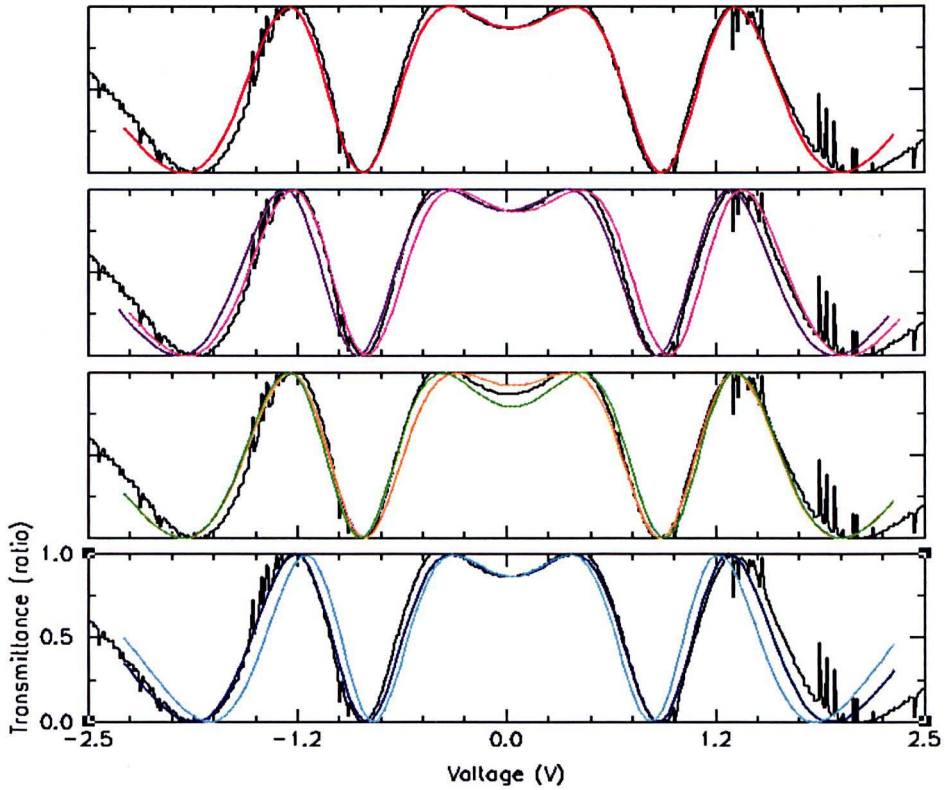


Figure 1.9.2.12: Shows simulations obtained for JHW131

colour	D (μm)	$\Delta\epsilon$	e ($\times 10^{-11} \text{ Cm}^{-1}$)	A_∞ ($\times 10^{-5} \text{ Jm}^{-2}$)
red	17.4	8.8	-0.5	5.00
violet	17.4	8.8	0	5.00
cerise	17.4	8.8	-1	5.00
orange	17.4	8.8	-0.5	1.00
green	17.4	8.8	-0.5	3.00
blue	17.4	8.3	-0.5	5.00
turquoise	17.4	9.3	-0.5	5.00

The red curve in the top panel of figure (1.9.2.12) is our best fit for the 10% solution of JHW131 in E7. It has a slightly negative flexoelectric coefficient of $e = -0.5 \times 10^{-11} \text{ C m}^{-1}$. The second panel shows the effects of reducing (violet) and increasing (cerise) the flexoelectric coefficient. For most voltages the experimental curve lies between these two fitting curves. However, when the magnitude of the voltage exceeds 1.75 V, all of the simulations start to deviate from the experimental curve. Following the

trend seen in the previous graphs, changing the anchoring energy has no effect on the quality of the simulation for large voltages. It has also not resulted in an improvement in the quality of the simulation in the central region. In the final (bottom) panel of figure (1.9.2.12), we see that decreasing $\Delta\varepsilon$ improves the simulation's quality for large negative voltages. However, this change in $\Delta\varepsilon$ produces a concurrent worsening of the quality of the simulation for large positive voltages.

JHW172

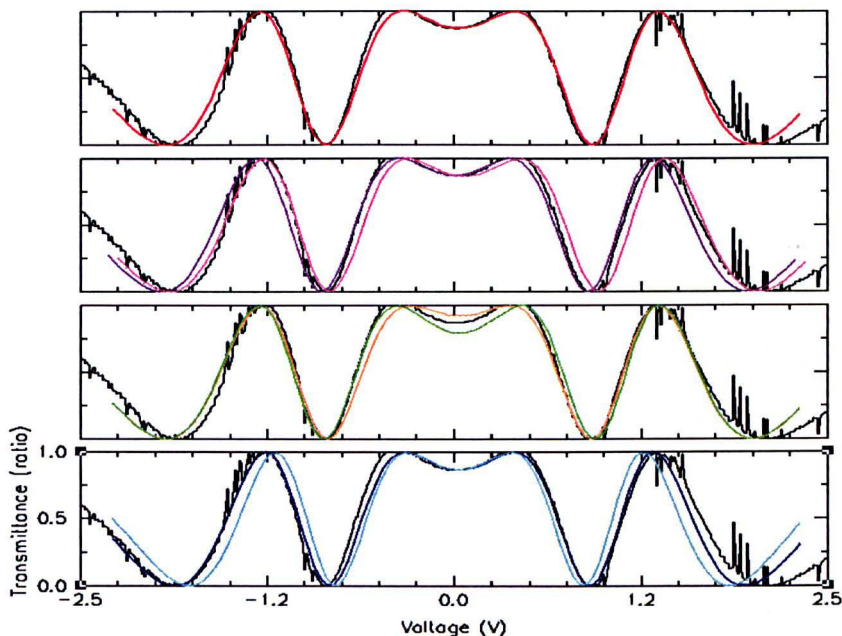


Figure 1.9.2.13: Shows simulations obtained for JHW172

KEY:	Colour	D (μm)	$\Delta\epsilon$	e ($\times 10^{-11} \text{ C m}^{-1}$)	A_{∞} ($\times 10^{-5} \text{ J m}^{-2}$)
	Red	26.6	7.8	0	5.00
1	Violet	26.6	7.8	-0.5	5.00
	Cerise	26.6	7.8	0.5	5.00
2	Orange	26.6	7.8	0	1.00
	Green	26.6	7.8	0	3.00
3	Blue	26.6	7.3	0	5.00
	Turquoise	26.6	8.3	0	5.00

Turning to our last 10% solution (i.e. JHW172 in E7), our best simulation (red, top panel) has e equal to zero. While we see that this is a good quality simulation, it does not reproduce the small asymmetry seen in the experimental data. However, in the next panel we see that increasing or decreasing e improves the simulation in different ways. The cerise curve with a value of $e = -0.5 \times 10^{-11} \text{ C m}^{-1}$ improves the simulation considerably for larger voltages, whereas the violet curve of $e = +0.5 \times 10^{-11} \text{ C m}^{-1}$ improves the curve fit considerably in the central region. Therefore, there is not only ambiguity about the magnitude of e for this particular system but also its sign.

Once more, in the third panel of figure (1.9.2.13), we see the effects of changing the anchoring energy; i.e. changing the shape of the central feature while otherwise exerting very little effect.

Finally, in the fourth (bottom) panel we see that increasing $\Delta\epsilon$ (turquoise) reduces the quality of the curve fit. While decreasing $\Delta\epsilon$ (blue) is generally also detrimental to the curve fit, it does, however, improve the curve fit for negative voltages.

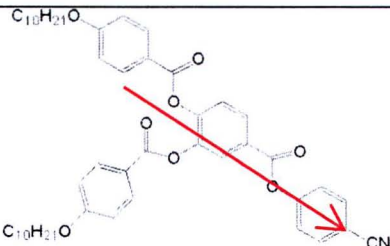
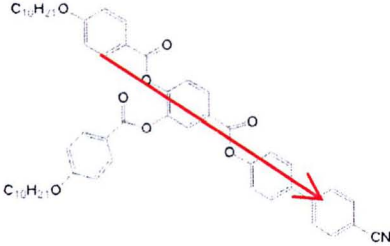
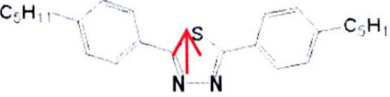
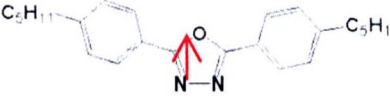
In order to gain additional information from these curve fits it is necessary to analyse them in conjunction with a molecular modelling of the dopant molecules. This is done in the next section.

Molecular Modelling

As was stated earlier, it is desirable to relate the values that we obtained for $\Delta\epsilon$ from our curve fits for the various 10% mixtures to the molecular dipoles of the dopant molecules. To do this, we now consider the molecular structures of the dopants in more detail. This was carried out using molecular modelling of the LC molecules JHW33, JHW29, JHW131, JHW172 and JHW128 using the AM1 parameter set within the MOPAC simulation package [41]. The molecules were first energy-minimised and the electric dipole moments, μ , were then calculated. The results of these calculations are summarized in table (1.9.2.4).

Also shown in this table are the values of $\Delta\epsilon$ obtained from the continuum-model fitting procedure. As can be seen from table (1.9.2.4), there is a good correlation between the calculated dipole moments of the molecules and the dielectric anisotropies of the liquid crystals. This is in agreement with the theoretical predictions of Maier and Meier [42], i.e. large molecular dipole moments along the molecular long axis give rise to large dielectric anisotropies, whereas, dipole moments across the molecular long axis give rise to a reduction in the dielectric anisotropy of the medium. This theory [42] goes on to predict that the ratio of $\Delta\epsilon$ to μ^2 is proportional to the order parameter S . We have calculated this ratio and the resulting values are shown in the penultimate column of table (1.9.2.4).

Table 1.9.2.4: Shows the dipole moments, μ (in Debye), calculated using a semi-empirical Hamiltonian (SEH) [41], the dipole orientation with respect to the molecules (red arrows), the solutions' dielectric anisotropy, $\Delta\epsilon$, found from the continuum model, and the parameter $\Delta\epsilon\mu^2$ ($1/D^2$), which is related to the order parameter [42]. As the solutions are 10% by weight, molecular mass (grams per mole) has also been included. The blank entries correspond to the 10% solution for which we were unable to achieve a curve fit (i.e. JHW128). $\Delta\epsilon = 13.8$ for the E7 host.

		$\mu(D)$	$\Delta\epsilon$	$\Delta\epsilon\mu^2$ ($1/D^2$)	mol mass
JHW33 ¹⁷		10.8	13.8	0.12	757
JHW29 ¹⁷		10.3	15.8	0.15	833
JHW131		3.5	8.8	0.72	362
JHW172		3	7.8	0.87	372
JHW128		3.6	-	-	378.1

If all liquid crystal solutions had the same *molar* concentration of dopant then we would be able to compare these order parameters directly. Instead, however, these solutions are 10% *by weight*. Having said this, JHW33 and JHW29 have comparable structures and are of similar weights as are JHW131 and JHW172. Therefore, molar concentrations within these pairs are comparable. Furthermore, we see that the values of $\Delta\epsilon/\mu^2$ are also

¹⁷ We note that when these molecules' energy is minimised the ester groups of the two R groups (i.e. the groups without the cyano-group) re-orientate so that they counter one another. This is why the dipole moment of the molecule is predominantly oriented along the long axis of the molecule.

similar among these pairs, and that $\Delta\epsilon/\mu^2$ is larger for the smaller molecules JHW131 and JHW172 (i.e. higher molar concentrations) than it is for the larger molecules JHW33 and JHW29 (i.e. lower molar concentrations). This appears to be due to similarities in the molecular structures within these pairs (see column two of the table) and therefore gives rise to similar values of the dipole moments, the dielectric anisotropy and the order parameter.

However, the order parameter is larger, by a factor of about two, than the mass ratios between these two pairs would have led us to expect. This can be seen from the last column of table (1.9.2.5) which displays the product of $\Delta\epsilon/\mu^2$ and the molecular mass. From this we conclude that having C_{2v} symmetry, as the two molecules JHW131 and JHW172 do, gives rise to a larger value of the order parameter compared with molecules that have no such symmetry, e.g. JHW33 and JHW29.

Table 1.9.2.5: Shows the Molecular Mass (grams per mole) multiplied by $(\Delta\epsilon/\mu^2)$ in order to compare the order parameters of different molar concentrations.

	$\Delta\epsilon/\mu^2$	Mol Mass	Mol Mass. $\Delta\epsilon/\mu^2$
JHW33	0.12	757	91
JHW29	0.15	833	125
JHW131	0.72	362	261
JHW172	0.87	372	324

Recalling that the dielectric anisotropy of E7 is 13.8, we see from table (1.9.2.5) that the molecules with their dipole moment vector predominantly along the long axis of the molecule (i.e. JHW33 and JHW29) act to increase the net dielectric anisotropy of the medium, whereas those molecules with their dipole moment vector across the molecules (i.e. JHW131 and JHW172) act to reduce the net dielectric anisotropy of the medium. While this effect was eminently predictable, we also notice that the magnitude of

this effect is greater for the smaller molecules. This can be seen from the greater size of $\Delta\varepsilon/\mu^2$ for the smaller molecules in table (1.9.2.5). However, this is to be expected as the mixtures are 10% by weight, i.e. the JHW131 and JHW172 solutions are higher molar concentrations than the JHW29 and JHW33 solutions (see Appendix H). It would be interesting to know how these cells would compare if they contained 10% *molar* concentrations. This would make comparisons between cells easier and mean that more could be deduced about how each of these dopant materials affects the order parameter in the system. Unfortunately, this information is not available at this juncture, however, we recommend that this be amended in future works in this field.

1.9.2.3.3 Parameter Fitting for MBBA and Discussion.

Having accumulated relevant knowledge about how different parameters affect the optical properties of HAN cells in the first half of the results section, we need to apply a robustly systematic approach for obtaining a curve fit for the MBBA system of Takahashi et al. [1]. This is because there are features in the transmittance curves of MBBA data that may be due to numerous combinations of the input parameters, much more so than was the case for the E7 systems. Firstly, note that the experimental curve for MBBA in figure (1.9.2.1), in addition to having an asymmetry, exhibits a voltage shift of the central feature. The magnitude of the voltage shift is -0.45 V, see Ref. [1]. In addition, the asymmetry of the curve is considerable. The fact that the asymmetry is so pronounced would indicate that the homeotropic anchoring energy is rather small. There are consequences of this low anchoring energy when it comes to choosing e and $A_{\theta 0}$: recall the graph from the theory section, i.e.

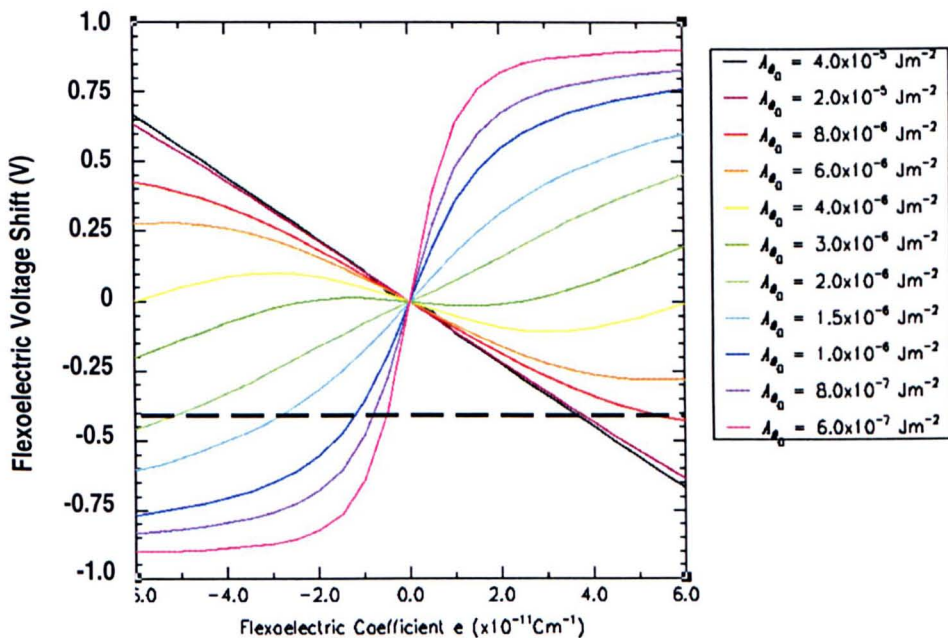


Figure 1.9.2.14: Shows figure (1.9.1.9.1) with a dashed line cutting across at a flexoelectric voltage shift of -0.45V. The value of e at which the dashed line cuts a coloured line tells us the flexoelectric coefficient for that anchoring energy that will result in a voltage shift of -0.45 V.

For each anchoring energy, the e that would lead to a flexoelectric voltage shift of -0.45 V can be found from the intersection of the calculated voltage shift versus e curves with the black horizontal dashed line (denoting the observed voltage shift of -0.45 V [1]). Table (1.9.2.6) below shows the values for e thus obtained from figure (1.9.2.14).

Table 1.9.2.6: Shows the flexoelectric coefficient for each anchoring energy that results in a voltage shift of -0.45 V. The final column is included to show that there is a correlation between the preceding two columns. The entries in black denote those anchoring energies that would result in the right type of asymmetry accompanying the voltage shift, whereas, the grey entry (last row) would not. Note that the black and maroon curves have been excluded as such high anchoring energies would not result in any asymmetry.

colour	A_{∞} (10^{-6} J m $^{-2}$)	e (10^{-11} C m $^{-1}$)	$e/(A_{\infty}^2)$ (C m 3 J $^{-2}$)
green	2.00	-5.90	-14.8
turquoise	1.50	-3.34	-14.8
Blue	1.00	-1.40	-14.0
violet	0.80	-0.93	-14.5
cerise	0.60	-0.62	-17.2
(red)	4.00	4.03	2.52

From table (1.9.2.6) we can see that there is an approximate empirical relationship (in this region) between A_{∞} and e giving rise to the same voltage shift; this relationship is $e/A_{\infty}^2 \approx \text{constant} \approx 15$. In theory, this could be a useful tool with which to pursue a solution. However, we are alerted to an additional problem when we turn to the curves that resulted from the parameters in table (1.9.2.6), see figure (1.9.2.15) below.

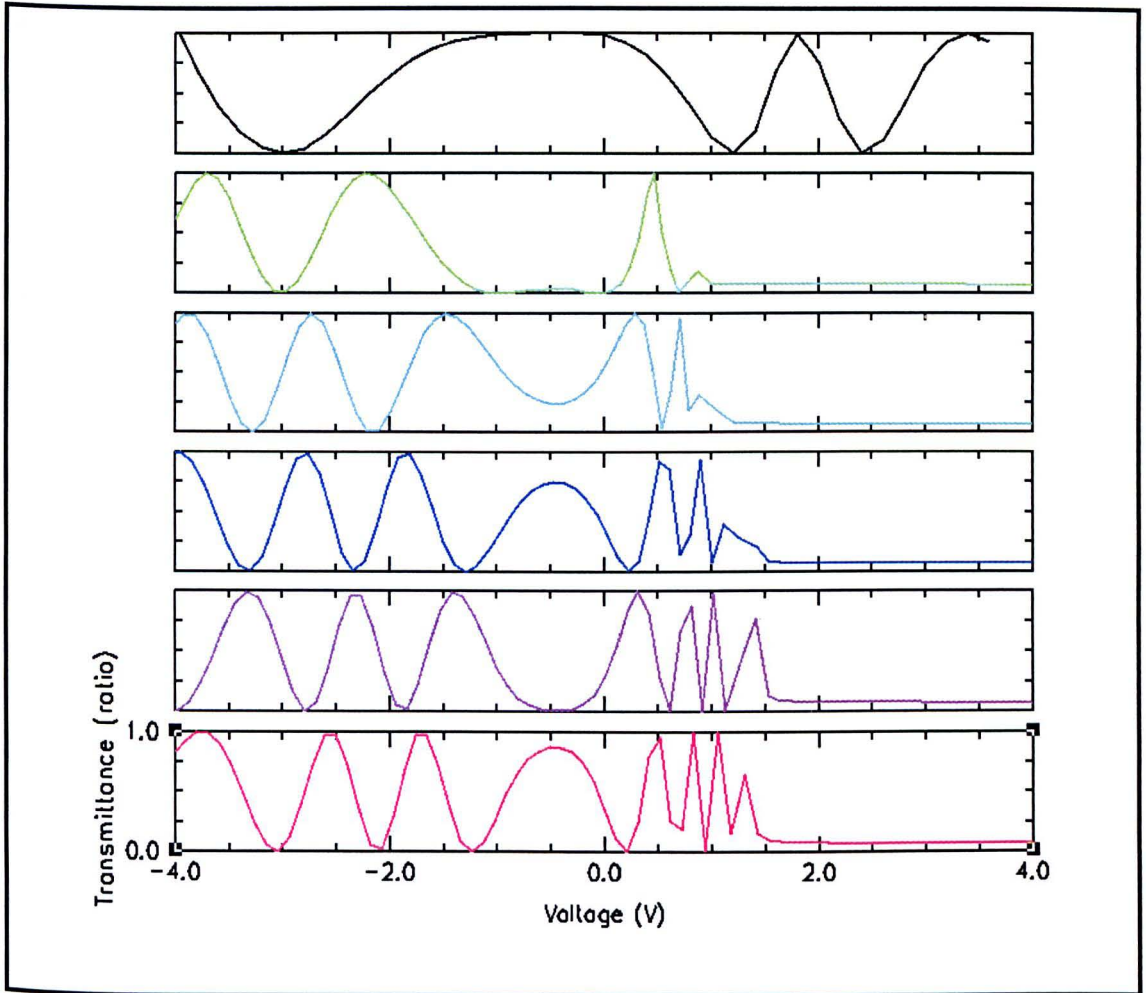


Figure 1.9.2.15: The top panel shows the experimental data of Takahashi et al. [1]. Then, using the A_{∞} and e data from table (1.9.2.6), and the theoretical model, we obtain the coloured curves (for key see table 1.9.2.6)

Obviously, the coloured curves in figure (1.9.2.15) are much narrower than Takahashi’s experimental data (black curve). This narrowness is so significant that it is too soon to be overly concerned about the *shape* of the central feature. However, we can still examine these curves. We find that they all have the ‘right type’ of asymmetry, which seems to confirm our choice of a negative flexoelectric constant.

However, if we are comparing the asymmetries for different widths of transmittance curves, we see that while the green curve ($e = -5.90 \times 10^{-11} \text{ C m}^{-1}$ and $A_{\infty} = 2.00 \times 10^{-6} \text{ J m}^{-2}$) is the widest, it is also the

most asymmetric. Notice how the green and turquoise curves have reached their asymptotes by +1 V, whereas the cerise curve ($e = -6.20 \times 10^{-12} \text{ C m}^{-1}$ and $A_{\infty} = 6.00 \times 10^{-7} \text{ J m}^{-2}$) is sufficiently asymmetric, but is too narrow. The cerise curve also has the right shape of central feature (compared with the central feature of the black experimental curve) but we are currently so far away from a solution that no significance should be attributed to this coincidence.

These observations alert us to the fact that these two parameters, A_{∞} and e , cannot alone be altered such as to result in a curve fit to this HAN cell. From the theoretical results section we know that there are a number of alternative parameters that can be used to broaden a curve, the obvious one being Δn . Decreasing Δn would certainly broaden the curves; however, Δn is one of the parameters that is accurately obtainable from experiments, so it would be an inappropriate choice of variable parameter.

By contrast, the elastic constants are not so well defined; therefore, they could be used to broaden the curves. Here, we chose to keep the ratio of K_{11} to K_{33} constant so that we retain some of the integrity of the experimentally obtained parameters. The problem with changing the elastic constants is that they do not simply change the width of the curves but also change the shape of the central feature. Compensating for this can be achieved by simultaneously changing the cell thickness, D . The graphs below, in figure (1.9.2.16), show curves that result from simultaneously changing D and multiplying the K s by a constant, so that they can give rise to the same shape of central feature. We wish to see if these can be used to obtain the desired broadening.

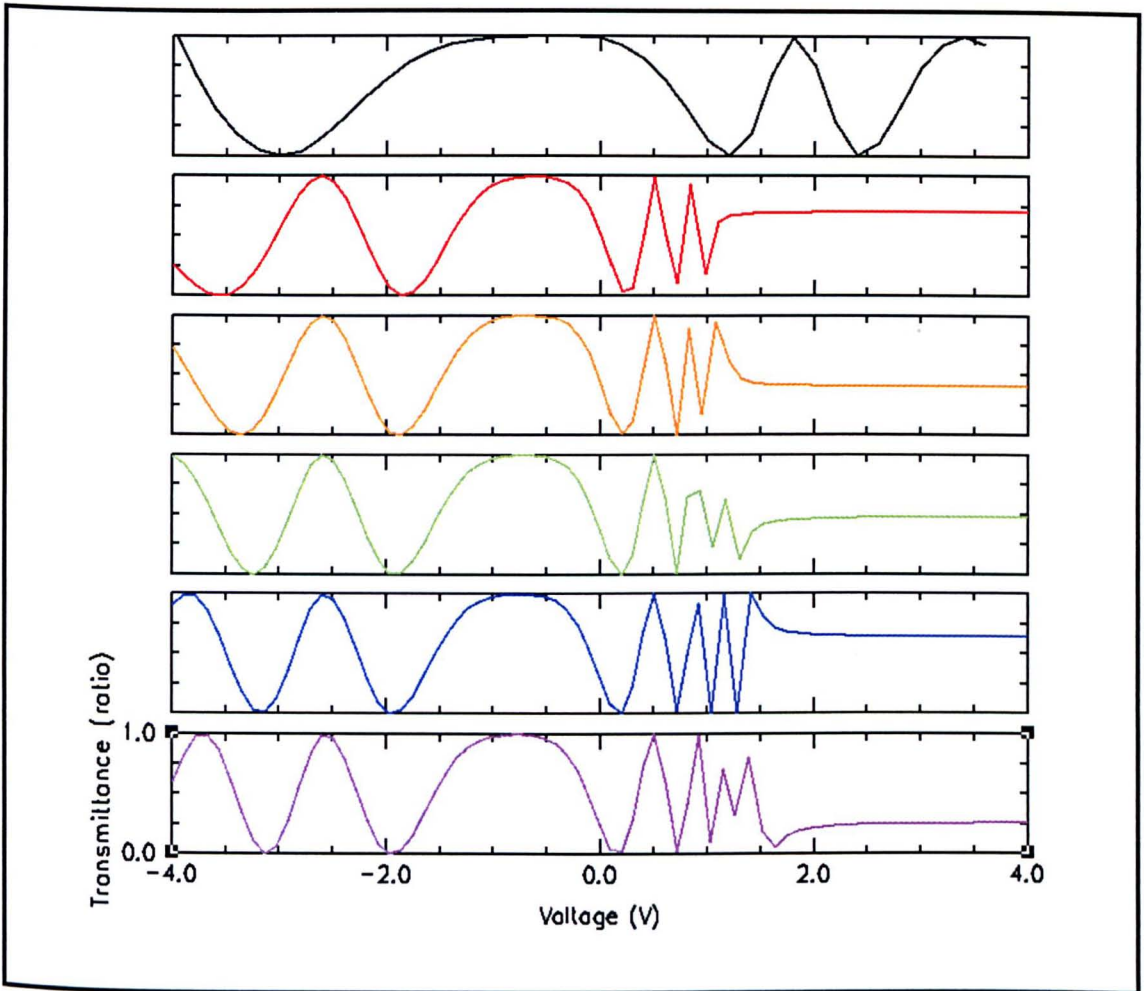


Figure 1.9.2.16: Shows numerous examples of curves, with similar central regions, obtained by varying D and K_s together (see key). Note that we have chosen $A_{\infty} = 1 \times 10^{-6} \text{ J m}^{-2}$ and $e = -1 \times 10^{-11} \text{ C m}^{-1}$ because these appear to be in the general vicinity of a likely solution.

Key:

colour	K_s Multiplied	D (μm)
Red	1.00	17.5
Orange	1.25	21.0
Green	1.50	24.5
Blue	1.75	28.0
Violet	2.00	31.5

As had been stated when we were introducing which input parameters were malleable, we see here, in figure (1.9.2.16), that varying K_s and D results in an interesting trend in as much as they appear to compensate for one another. Most of the peaks and troughs do not move significantly considering the sizes of the changes we have implemented in K_s and D . In fact the main observations are that increasing D and K_s in this fashion has

resulted in a marginally narrower transmittance curve and (note in the region +1 to +2 V) that it has also resulted in more peaks and troughs being *squeezed* in, without changing $\Delta\Phi$ of the central feature.

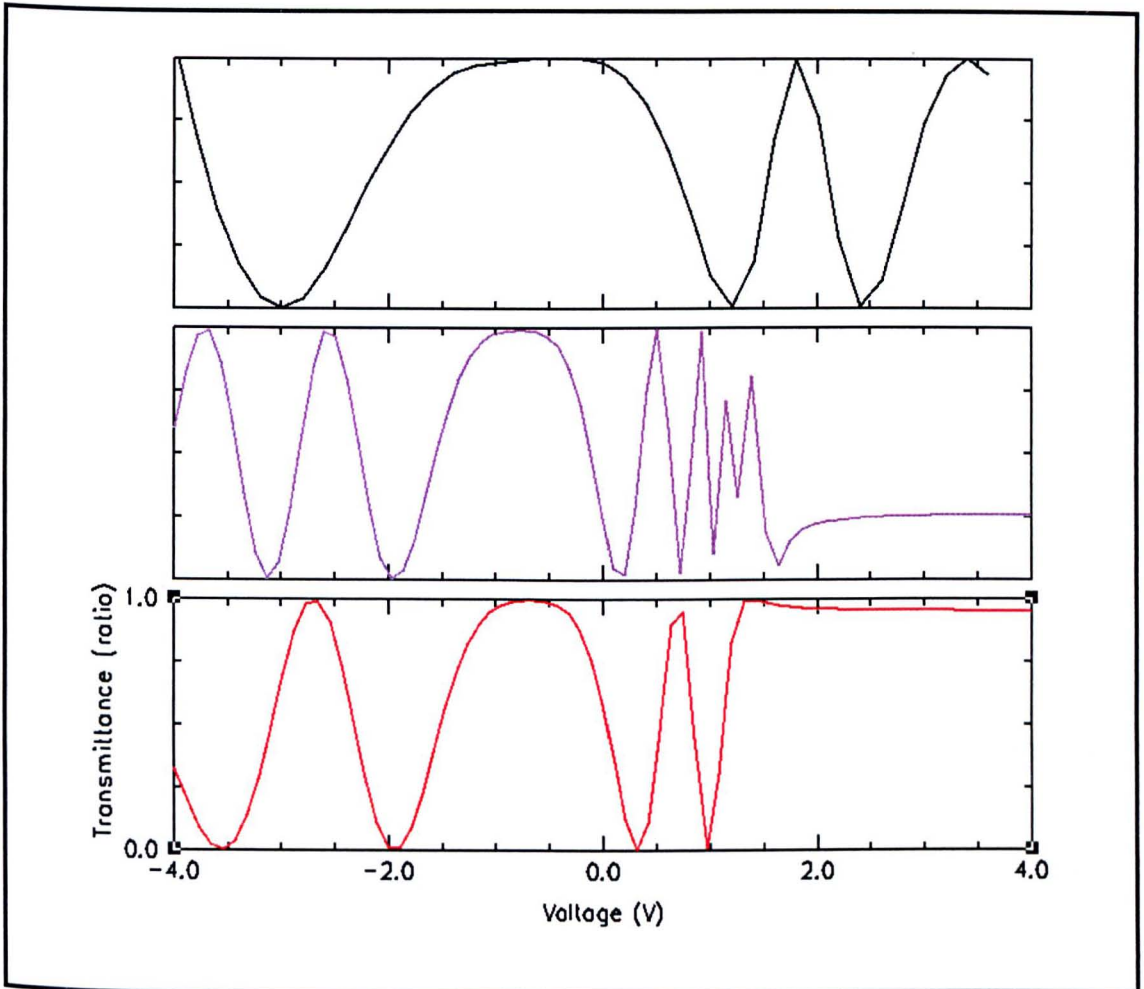


Figure 1.9.2.17: Shows the effects of reducing the cell thickness from $D = 31.5 \mu\text{m}$ (violet) to $D = 20.5 \mu\text{m}$ (red) in order to broaden the curve and reduce the number of peaks and troughs, having previously increased this number by increasing the elastic constants (by twofold) and cell thickness (see figure (1.9.2.16)). The violet curve corresponds to the same colour curve from figure (1.9.2.16). The red curve is for a cell of thickness of $D = 20.5 \mu\text{m}$ but is otherwise identical to the violet curve.

Figure (1.9.2.17) shows how we can partially “back track” from figure (1.9.2.16). In figure (1.9.2.16) we saw that increasing K s and D in such a way that we were following a path for which the shape of the central feature was fixed (i.e. $\Delta\Phi$ of the central feature is kept constant). We saw that these two parameters almost entirely countered one another and no significant

change in the width of the transmittance curve was observed. However, what was seen in figure (1.9.2.16) was that increasing K_s and D in this fashion resulted in a larger number of peaks and troughs in the transmittance curves at larger voltages. As a result we can decrease $\Delta\Phi$ of the central feature by multiples of 2π in order to retain the same shaped central feature but reduce the number of peaks and troughs at larger voltages. In doing so, we increase the width of the transmittance curve. This was done and is shown in the red curve of figure (1.9.2.17), where K_s are twice their experimental values and the cell thickness has been reduced from $D = 31.5 \mu\text{m}$ (violet) to $D = 20.5 \mu\text{m}$.

Clearly, from these graphs, figure (1.9.2.17), we could continue to significantly increase the value of the elastic constants and then vary the cell thickness D (so that the correct shape of the central feature was obtained) and then we could vary the flexoelectric constant and homeotropic anchoring energy (until the right voltage shift and asymmetry were obtained). I.e. while there may be a solution that provides a virtually perfect curve fit, one has to be careful in ascribing physical significance to the fitting parameters obtained. It is, therefore, appropriate to discontinue the search at this point. However, it may be worthwhile to briefly discuss further what the implications are for the data obtained by Takahashi et al. [1].

These observations may be due, once again, to such factors as ion impurities. However, without more detail about Takahashi et al.'s [1] experimental procedures and set-up, this is just speculation. Although, on the other hand, what can be taken from these simulations is that the flexoelectric coefficient, e , is negative. We have also seen that the homeotropic anchoring energy is critically small so that the flexoelectric

voltage shift is of the opposite sign to what it would be if $A_{\theta 0}$ were large enough. This point is of significant interest and so it is discussed in more detail in the conclusion. We have also seen that, when the anchoring energy is this small, even very small flexoelectric constants can result in significant flexoelectric voltage shifts and deceptively large asymmetries. Therefore, we conclude that both e and $A_{\theta 0}$ are small for this system.

1.9.2.4 Conclusion to Experimental Curve Fitting

Here, we briefly summarize our findings for all the experimental systems. Firstly, we examine the most recent one, i.e. the MBBA system, before concluding our results for the E7 systems.

We were able to find various curves with the right magnitude of the flexoelectric voltage shift for the MBBA data of Takahashi et al. [1]. In addition, we have seen that this model is able to reproduce the *shape* of this transmittance curve and so this particular objective of the present work has been fulfilled.

We have also found out information about the significant importance of particular parameters. This has included finding that, when the dielectric anisotropy is negative and the homeotropic anchoring energy is low (i.e. there is some asymmetry in addition to a flexoelectric voltage shift), it is particularly beneficial to perform simulations in order to gain a graph like figure (1.9.1.9.1) below for the MBBA system, i.e.

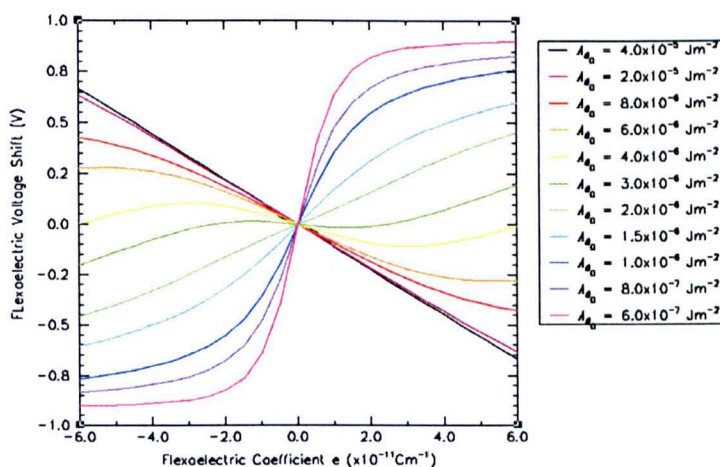


Figure (1.9.1.9.1) Shows the flexoelectric voltage shift as a function of e for different homeotropic anchoring energies, for MBBA.

in order to find the flexoelectric coefficient, e , and the homeotropic

anchoring energy for such systems.

However, when the anchoring energies are high, the flexoelectric voltage shift is, roughly, a function of $\Delta\varepsilon$ and e : recall figures (1.9.1.8.2.1 and 2)

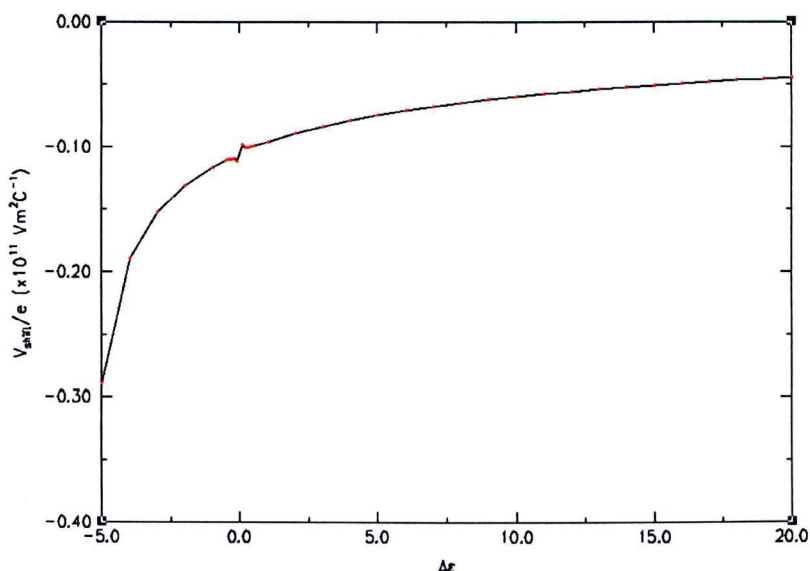


Figure (1.9.1.8.2.1) Showing the flexoelectric voltage shift as a function of $\Delta\varepsilon$ for MBBA (recalling that the figure for E7 was almost identical)

We have, however, found that errors in the value of the cell thickness can be compensated for by varying the elastic constants¹⁸ (which are also prone to experimental errors). Furthermore, we experimented with varying the cell thickness and the elastic constants in order to see if these parameters could be used to both select the shape and broaden the transmittance curves. We found K s and D approximately compensated one another to the point where multiplying the K s by a constant factor (coupled with the corresponding increase in D) would have relatively little effect on the width of a transmittance curve (though this effect was to *reduce* rather than increase the width of the transmittance curves). So we are able to conclude that this

¹⁸ While maintaining the ratio $K_{11} : K_{33}$ found experimentally.

is not an appropriate method of increasing the width of the central feature *unless* we choose D so as to decrease $\Delta\Phi$ by some multiple of 2π instead.

We learned that A_∞ , e , D and K s cannot alone be used to curve fit this MBBA data, but that it would also be necessary to vary $\Delta\varepsilon$. As this parameter is established accurately this was a cause for concern: the most feasible reason why a cell may have an effective $\Delta\varepsilon$ smaller than usual (as obtained from a continuum model) would be ion impurities being responsible for a significant screening of the electric field.

We saw from the Takahashi curve fit (of MBBA) that we were able to recreate the basic shape of the transmittance curves. From this we were able to conclude that the homeotropic anchoring energy was very low and that the flexoelectric coefficient was *probably* small but *definitely* negative.

For the E7 systems rather more success was had. Curve fitting Bartle's data [30], we were able to estimate the cell thickness and the size of the homeotropic anchoring energy for the E7 cell and reproduce, reasonably, the experimental curves. For the 10% solutions in E7 we were able to find values of the dielectric anisotropies, cell thicknesses, homeotropic anchoring energies and flexoelectric coefficients. We saw that, for all these E7 cells, the flexoelectricity was small but the occurrence of asymmetries in the transmittance curves confirmed its presence. The table below, (1.9.2.7), shows the fitting parameters used, and the estimated accuracies of them are included in the form of errors.

Table 1.9.2.7: Shows the curve fitting parameters used for the E7 systems.

	D μm	$\Delta\epsilon$	A_{∞} $\times 10^{-6} \text{Jm}^{-2}$	e $\times 10^{-11} \text{Cm}^{-1}$
E7	27.5 ± 0.5	13.8	9.0 $3.0 < A_{\infty} < 9.0$	0.0 ± 0.5
JHW29	16.9 ± 0.5	15.8 ± 0.5	5.0 $3.0 < A_{\infty} < 10.0$	-1.0 ± 1.0
JHW33	18.0 ± 0.5	13.8 ± 0.5	5.0 $3.0 < A_{\infty} < 10.0$	-0.5 ± 1.0
JHW131	17.4 ± 0.5	8.8 ± 0.5	5.0 $3.0 < A_{\infty} < 10.0$	-0.5 ± 0.5
JHW172	26.6 ± 0.5	7.8 ± 0.5	5.0 $3.0 < A_{\infty} < 10.0$	0.0 ± 0.5

In addition, the cell thickness is typically being either experimentally overestimated by a factor of about 1.4 from the values used in our simulations or *underestimated* by the theory, see table (1.9.2.2). However, we also found that the ratio between experimental cell thickness and theoretical thickness was closer for the E7 data than the systems containing dopants. The direction of this shift leads us to conclude that these dopants act to reduce the system's order parameter.

This model is able to reproduce the shapes, asymmetries, and voltage shifts seen experimentally. However, until more work is performed to increase the magnitude of the anchoring energies, using this method (i.e. calculating the flexoelectric coefficient from the flexoelectric voltage shift as proposed by Takahashi et al. [1]), is fraught with difficulties. We have shown that it is possible to make educated estimates for the values of e and A_{∞} using the whole of a transmittance curve, but this was simply not addressed in Takahashi's work in which the preference was to concentrate solely on the flexoelectric voltage shift. We have also shown that this method is *particularly* inappropriate for finding the flexoelectric coefficient for systems with low homeotropic anchoring energy and a *negative* dielectric anisotropy (such as is the case for MBBA).

1.10 Conclusion

Our objectives were to: devise a continuum modelling method that would produce physically meaningful solutions to the PDEs (unlike the self consistent method); find out how different continuum modelling parameters affect the behaviour of HAN cells, thus gaining an understanding of why they caused these behaviours; to be able to reproduce experimental curves; and, more specifically, obtain meaningful curve fits for experimental data. It is our belief that these objectives have been, for the main part, satisfied.

We started this work with a particular interest in the behaviour of HAN cells due to the flexoelectric coefficient; we have reached the end of this study with a much richer view of how flexoelectricity interacts with other properties of such cells. The contribution due to low homeotropic anchoring energy has raised the possibility that values of flexoelectric coefficients may be overestimated or even have their sign wrongly diagnosed. This certainly goes a long way towards explaining why there are such large fluctuations in the values reported in the literature for given material, some of which are shown in the table below:

Table 1.9.2.8: Values of e for MBBA from the literature [1].

$e_{11} + e_{33}$ (Cm ⁻¹)	Experimentalists
-5.4×10^{-11}	Takahashi et al [1]
-0.33×10^{-11}	Dovov et al [43]
-2.48×10^{-11}	Madhusudana and Durand [44]
-2.31×10^{-11}	Valenti et al [45]
$+0.99 \times 10^{-11}$	Blinov et al [46]
$+8.8 \times 10^{-11}$	Ponti et al [31]

There are two major theory findings of this work. Firstly, when the homeotropic anchoring energy is low the flexoelectric voltage shift is better 'behaved' if the system has positive dielectric anisotropy than if $\Delta\epsilon$ is negative. That is, the flexoelectric voltage shift retains a high degree of proportionality and the constant of proportionality does not vary vastly with

A_{θ} when $\Delta\varepsilon$ is positive. However, this is not so when $\Delta\varepsilon$ is negative. Secondly, the distortions of the transmittance curves (when A_{θ} is small) are of the opposite sign to that of the flexoelectric coefficient, e .

1.11 Further work

It would be beneficial to adjust the model so that we can investigate the effects of varying the homogeneous anchoring energy thoroughly: from the trend seen in the work on changing signs of $\Delta\varepsilon$ and the magnitudes of A_{∞} for $e \neq 0 \text{ C m}^{-1}$ systems, we predict that some of the asymmetries in the positive $\Delta\varepsilon$ experimental systems may be due to a lowering of the *homogeneous* anchoring energies instead of the *homeotropic* anchoring energies.

Due to the new nature of the way in which we find solutions for the PDEs that describe this system, we have yet to find a way to incorporate ion impurities into the model. It would be of great interest if we could address this omission.

Furthermore, it would be desirable to work on both systems (i.e. positive and negative dielectric anisotropies) with higher anchoring energies and/or (in the case of the systems containing E7) exhibiting greater asymmetries and/or voltage shifts than those investigated here. It would also be of great interest to examine other MBBA cells to see if the experimental results obtained by Takahashi et al. [1] were typical of MBBA systems.

Bibliography

- [1] T. Takahashi, S. Hashidate, H. Nishijou, M. Kimura and T. Akahane, *Jpn. J. Appl. Phys.* **37**, 1865 (1998).
- [2] S. R. Warriar and N. V. Madsudana, *J. Phys II France* **7**, 1789 (1997).
- [3] <http://www.eng.ox.ac.uk/lc/research/what#what> [Accessed 12 Aug 2003]
- [4] P.G. de Gennes and J. Prost, *The Physics of Liquid Crystals*, 2nd Ed, (Oxford, Clarendon Press, 1993).
- [5] Petrov, Alexander G. *The Lyotropic state of matter: molecular physics and living matter physics*. (Gordon & Breach, Amsterdam, 1998)
- [6] <http://reynolds.ph.man.ac.uk/~dierking/gallery/gallery1.html> [Accessed 18 Jan 2004]
- [7] <http://www.lci.kent.edu/defect.html> [Accessed 18 Jan 2004]
- [8] P.G. de Gennes and J. Prost, *see reference* [4]
- [9] Collings, P. J. Hird, M. “*Introduction to liquid crystals*” (London : Taylor & Francis, 1997)
- [10] Y. Takanishi, K. Hiraoka, V. K. Agrawal, et al. *Jpn J Appl Phys* **1**, **30**, 9a, pp 2023 (1991)
- [11] M. Yoshida, N. Seo, K. Hori, H. Toriumi, *Mol. Cryst. Liquid Cryst.* **365**, pp 1769 (2001).
- [12] S. Chandrasekhar, “*Liquid Crystals*” (Cambridge, Cambridge University Press, 1977).
- [13] C. W. Oseen, *Trans. Faraday Soc.* **29**, 883 (1933), F. C. Frank, *Disc. Trans. Faraday Soc.* **25**, 19 (1958)
- [14] G. Durand, *Mol. Cryst. Liq. Cryst.* **113**, 237, (1984).
- [15] R. B. Meyer, *Phys. Rev. Lett.* **22**, 918 (1969).
- [16] P. Rudquist, L. Komitov, S. T. Lagerwall, *Phys. Rev. E*, **50**, 6, pp 4735 (1994)

- [17] Per Rudquist, S. T. Lagerwall, *Liq. Cryst.* **23**, 503 (1997)
- [18] W. T. Welford, "*Optics*" (London, Oxford University Press, 1976).
- [19] <http://www.laserphysics.kth.se/nlopt/nlo2003.pdf> [Accessed 18 Jan 2004]
- [20] http://www.itp.physik.tu-berlin.de/muschik/liquid_crystals/lc_intro.html [Accessed 18 Jan 2004]
- [21] R. P. Feynman, R. B. Leighton, M. Sands *The Feynman Lectures in Physics: Volume I* (Addison-Wesley Publishing Company, 1963)
- [22] E. Lueder, "*Liquid Crystal Displays: Addressing Schemes and Electro-optical Effects*" (John Wiley & Sons, 2001).
- [23] T. Takahashi, S. Hashidate, M. Kimura and T. Akahane, *Mol. Cryst. Liq. Cryst.* **302**, 133, (1987).
- [24] L. M. Blinov, A. YU. Kabayenkov, A. A. Sonin, *Liq. Cryst.* **5**, 2, pp 645 (1989)
- [25] P. Hindmarsh, G. J. Owen, S. M. Kelly, P. O. Jackson, M. O'Neill, R. Karapinar, *Mol. Cryst. Liq. Cryst. Sci. Technol. Sect. A-Mol. Cryst. Liq. Cryst.* **332**, pp 2949 (1999)
- [26] A. Contoret, PhD Thesis (University of Hull, Hull, 2002)
- [27] S. Chandrasekhar, *Liquid Crystals*, (Cambridge University Press, Cambridge, 1977)
- [28] P. Yeh, C. Gu, *Optics of Liquid Crystal Displays*, (New York : Wiley, 1999); N. A. Clark, S. T. Lagerwall, *Ferroelectrics* **58**, 345 (1984); R. B. Meyer, *Mol. Cryst. Liq. Cryst.* **40**, 33 (1977).
- [29] Chigrinov, V. G., *Liquid crystal devices : physics and applications*, (Boston, Mass : Artech House, 1999). T. J. Scheffer, J. Nehring, *Appl. Phys. Lett.* **45**, 1021 (1984).
- [30] K. Bartle, PhD Thesis (Hull University, Hull, 2003).
- [31] S. Ponti, P. Zihlerl, C. Ferrero and S. Žumer, *Liquid Crystals* **26**, 1171 (1999).
- [32] G. Barbero, G. Durand, *J. Appl. Phys.* **68**, 11, pp 5549 (1990)

- [33] G. Barbero, G. Skačej, A. L. Alexe-Ionescu, S. Žumer, *Phys. Rev. E*, **60**, 1, pp 628 (1999)
- [34] P. R. Maheswara-Murthy, V. A. Ragunathan, N. V. Madhusudana, *Liq. Cryst.* **14**, 2, pp 483 (1993).
- [35] G. Barbero, P. Taverna Valabrega, R. Bartolino, B. Valenti, *Liq. Cryst.* **1**, 5, pp 483 (1986).
- [36] <http://tardis.union.edu/~andersoa/postm/liquidcrystals.html> [Accessed 18 Jan 2004]
- [37] Licristal®, E,Merck, Darmstadt Germany, (1999); Kevin Bartle, PhD Thesis (Hull University, Hull, 2003).
- [38] G. Barbero and L. R. Evangelista, *An elementary course on the continuum theory for nematic liquid crystals*, (World Scientific, Singapore, 2001)
- [39] F. Yang, L. Ruan and J. R. Sambles, *J. Appl. Phys.* **88**, 6175 (2000).
- [40] S. Singh, *Liq. Cryst.* **20**, 797 (1996)
- [41] Cerius², Molecular Modelling Software, Molecular Simulations Inc., 230/250 The Quorum, Barnwell Road, Cambridge CB5 8RE, UK (<http://www.msi.com/>).
- [42] W. Maier and G. Meier, *Z. Naturforsch.* **16a**, 262, (1961); L. M. Blinov and V. G. Chigrinov, *Electrooptic effects in liquid crystal materials*, (Springer, New York, 1994), p. 53.
- [43] I. Dozov. Ph Martinot-Lagarde and G. Durand, *J. Physique Lett.* **43**, 365, (1982).
- [44] N. V. Madsudana and G. Durand, *J. Physique Lett.* **46**, L195 (1985).
- [45] B. Valenti. C. Bertoni. G. Barbero, P. Taverna-Valabrega and R. Bartolino, *Mol. Cryst. Liq. Cryst.* **146**, 307, (1987).
- [46] L. M. Blinov. G. Durand and S. V. Yablonsky, *J. Physique Lett II*, **2**, 1287 (1992).

Chapter 2

A New Method for Investigating Surface Tension of Liquid Droplets from Molecular Dynamics Simulations.

2.1 Introduction

At present, there is considerable interest in the determination of surface tension of liquid droplets of sub-microscopic size, with a view to controlling their surface properties [1, 2, 3, 4 and 5]. Examining sub-microscopic droplets provides the opportunity to explore potential applications, ranging from ink-jet printers, and aerosols (including antiperspirant sprays and insecticides), to metal soldering and gas arc welding, etc. [6]. Increasing our understanding of these sub-microscopic droplets increases our ability to understand, design and control such

systems. This chapter, for these same reasons, proposes a method that will provide a new tool and insight into modelling and examining these systems.

Surface tension is measured in either force/length, hence the name *surface tension*, or energy/area, which has more thermodynamic connotations. Recalling that force *is* energy/length, it can be seen that these are equivalent.

Despite this, defining surface tension is not entirely straightforward: it is a macroscopic phenomenon with microscopic origins [7, 8]. The macroscopic phenomenon can be observed when a pin, which is denser than water, is rested upon the water's surface, appearing to be suspended by an invisible film. The microscopic origin of this phenomenon can be attributed to the inter-molecular forces, e.g. between water molecules. However, at the microscopic level there is no 'film'. Thus, one of the problems faced when defining surface tension occurs when relating the macroscopic to the microscopic, and vice versa, while obtaining a definition that is physically meaningful at both ends of this scale [9]. In the present chapter we put forward a method that aims to bridge this gap.

The microscopic origins of surface tension are the inter-particle forces. In the surface region the inter-particle distances are such that a net attraction between the particles occurs. In a liquid's bulk, however, the particle separations are typically slightly less than the equilibrium separation, giving rise to an, on average, repulsive force between particles. The mean particle separations are maintained at less than equilibrium distances by an inward pressure exerted by the surface region, i.e. the region responsible for surface tension. Thus the whole system is kept in equilibrium by these

two opposing forces. Figure (2.1) below shows some of these features schematically.

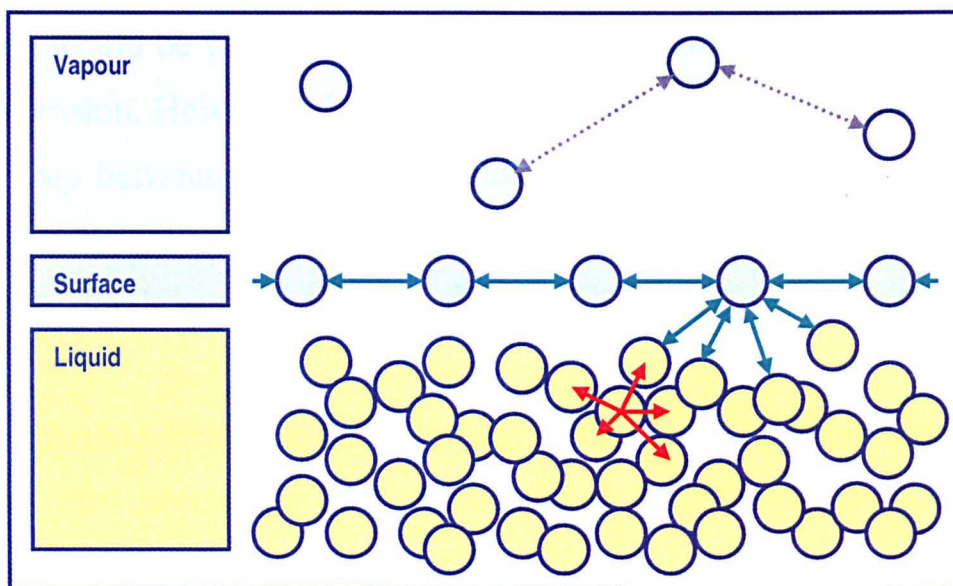


Figure 2.1: Shows how the different spacings between molecules in the three regions vary. In the liquid (yellow) region we see that the particles are on average very closely spaced and experience repulsive forces¹⁸ (red arrows). The particles in the vapour (blue region) experience small attractive forces (blue dotted arrows) as they are widely dispersed. However, in the surface (green) region the particles generally experience attractive forces towards each other and the molecules in the bulk liquid phase (green arrows).

If appropriate approximations for given force fields are used, molecular dynamic (MD) simulations, performed on computer, can emulate physical systems. By performing MD simulations upon a system of particles, at a given temperature and allowing the system to evolve through time, the general equilibrium distribution of particles will reveal much about the system [10]. For instance, Kopolik et al [11] employed MD simulations to investigate the coalescence, solidification and evaporation of nanometer-sized Lennard-Jones liquid droplet. Similarly, Huang et al [12] and Kinma et al [13] studied the spreading and nucleation behaviour of liquid drops on a rough solid surface by means of the MD method. The positional data of the particles enables the calculation of local densities, particle energies and forces.

¹⁸ N.B. For a spherical droplet the net average repulsive force tends toward zero as radius, r , tends towards ∞ , i.e. for planar surface.

The output information from MD simulations is inherently microscopic in nature. Having a definition of surface tension in terms of the information available would be valuable: particle energies and forces *are* the origins of surface tension. However, there is a distinct lack of any direct, formalized, relationship between positional data and surface tension in the literature. Consequently, a method by which this information can be used to *calculate* surface tension is proposed here.

As inter particle forces are the origins of surface tension, so too should they facilitate the calculation of surface tension directly. If an adequately accurate approximation to inter-particle force fields is employed, subsequent molecular dynamic simulations can meaningfully describe real systems. Therefore, in equilibrated states, the positional data and inter-particle force fields will assist the examination of the phenomenon of 'surface tension' at a molecular level, comparable with surface tension in the macroscopic realm. As a consequence, the practical implications of this new model / method can be realized. These include examining microscopic droplets.

To do this, initially some spherical droplets, of varying sizes, must be created on the computer. Then MD simulations are performed over a range of temperatures. Firstly, for reasons of comparison with data in the literature, we shall curve fit these droplets' density profiles (as a function of radius). Secondly, we shall use the positional data to calculate energy and force profiles (again as functions of R). Our new method involves using this data to calculate the surface tension; it also allows us to meaningfully define and locate the surface region. Due to the statistical fluctuations inherent to the MD method, averaging methods have to be employed in order to smooth over the noise.

This chapter limits its examination of surface tension to spherical droplets of monatomic material in which the particles interact in accordance with a Lennard-Jones 12-6 pair potential. This pair potential is mathematically simple and a fairly accurate approximation to the Van der Waals' interaction. However, the theory proposed here is more general and could be applied to systems with other geometries, using more intricate force fields, describing interactions between several different constituent molecules. Before anything so ambitious is undertaken, we should test the new method's validity by examining simple systems and then compare our results with other work available in the literature.

Here the Lennard-Jones pair potential is chosen to mimic Argon – Argon interactions. This allows comparisons to be made both with other theories and simulations [7, 9, 14, 15, 16, 17 and 18]. These can then be compared with the experimentally obtained macroscopic values of surface tension for Argon [19]. Obviously, a direct comparison would be inappropriate as the droplets being examined here are on the scale of nanometres; accurately obtaining surface tension of such miniscule droplets is currently beyond the reach of experimental techniques. Nevertheless, comparisons between the surface tensions gained from existing simulations, theories (covering the large range of possible systems sizes) or experimental values (for macroscopic systems) and our new method are still of interest.

While it is desirable to be able to make such comparisons between our droplets and those obtained by others, not all researchers working on Lennard-Jones droplets have parameterised them so that they would emulate Argon. However, the variation of a Lennard-Jones droplets' density profile in the surface region is fairly well behaved; with appropriate

scaling, comparisons between different Lennard-Jones droplets can be made independent of input parameters. This is achieved by finding the parameters that can be used to curve fit these density profiles with a *tanh* function [15]. Before comparing the values for surface tension obtained by our new method with those gained by other methods, we need to establish that the droplets created by our simulation are physically similar to those studied by others.

Before the new method is explained, it is important to lay out the historical background and thus set it into context. By doing so, we hope to demonstrate the need for a new method. At the same time we provide arguments as to why our method can bridge the gap between microscopic simulations and macroscopic observations.

2.2 Historical background

Historically there have been many different approaches to the problem that the interface between two phases presents, and subsequently in defining surface tension [7]. In order to gain a general overview an examination of the works of scientists, such as Laplace, Gibbs and Van der Waals, will be presented here. Their methods ranged from molecular mechanical to quasi-thermodynamic approaches. Some researchers approached this problem by trying to rigidly define the surface, typically as an idealised film of zero thickness. Others have tried to tackle it by describing the thermodynamic properties of the bulk phases on either side of the surface region, and to then treat the surface as though it were a third bulk phase. Some theories tried to define surface tension in terms of the thermodynamic properties of the whole system, without focussing on the exact location of the surface region. All of these approaches had a macroscopic angle to them. In contrast, statistical mechanics attempts to provide local definitions of thermodynamic properties, which is a more microscopic approach. As this is also of interest, an exploration of this will follow, providing a brief outline of the pressure tensor and direct correlation functions [7 and 20].

2.2.1 Thermo-dynamical Theories

Thermodynamics considers macroscopic (average) properties of a system. Despite the fact that Daniel Bernoulli's theories¹⁹ provided a better understanding of what was happening in a system, his theories on this

¹⁹ He believed the origin of pressure was collisions between molecules in a fluid and the walls of a system [7]. Putting this into a historical context (due to the similarities), it is interesting to note that Daniel Bernoulli died 62 years before Boltzmann was born [29] as even in Boltzmann's lifetime the opposition to a statistical mechanics approach was great. Regrettably, Boltzmann committed suicide shortly before his theories were validated and more than a hundred years after Bernoulli had himself 'shuffled off this mortal coil'.

matter were almost universally ignored in favour of the works of Dupré, Rayleigh and Laplace. Only Laplace's theory will be examined here.

Laplace believed that the surface could be idealised as a perfect film, assuming that there was a step in the density profile separating liquid and vapour phases. He treated the surface as an infinitely thin region between two phases [7] and defined the surface tension, σ , of a spherical droplet to be

$$\sigma = \frac{\Delta p \cdot r_s}{2} \quad (2.1)$$

where Δp is the pressure difference between the two bulk phases (i.e. liquid and vapour) and r_s is the radius of the surface of tension.

It must be noted that r_s is defined such that Equation (2.1) gives agreement with the experimental values for the surface tension. This definition does not help in the calculation of the surface tension from MD simulations because, as yet, we do not have a definition of r_s or local pressure. This problem is compounded by our inability to perform experiments on sub-microscopic droplets. Therefore, the Laplace equation falls short of being able to provide sufficient information to help us find surface tension from the MD simulations we performed.

Alternatively, there is the Kelvin equation, i.e.

$$\frac{P_R}{P_\infty} = \exp \frac{2\sigma}{R\rho_N kT}$$

where P_R is the pressure of the vapour in equilibrium with a droplet of radius R , P_∞ is the conventional pressure of the vapour and ρ_N is the number density of the liquid well inside the drop. This equation has been

utilised in MD simulations to evaluate the surface tension [15]. However, the validity of thermodynamic-type equations, such as the Kelvin equation, for very small droplets is highly questionable. This is because these equations are derived from macroscopic arguments, specifically *for* macroscopic systems.

Also, there is the Tolman equation for the variation of the surface tension with drop size, i.e.

$$\frac{\sigma}{\sigma_{\infty}} = 1 - \frac{2\delta}{r_s} + \dots$$

where σ_{∞} is the surface tension for a planar interface and $\delta = r_e - r_s$, where r_e is the radius for the equimolar surface, which has been employed in MD simulations [21 and 22]. In particular, Koga et al. [23] showed that the Tolman equation is only applicable for systems containing more than approximately 10^6 particles. Because these equations have their origin in thermodynamics, all of them fail for sufficiently small drops.

2.2.2 Quasi-Thermodynamical Theories

2.2.2.1 Gibbs' Theory

In contrast, Gibbs [7] opted for combining bulk thermodynamic properties with the concept of an idealized surface film as a third bulk phase. He achieved this by initially employing a continuous density profile to describe the interface between two phases. The properties of a bulk phase, at equilibrium with its surroundings, are well defined by the theory of thermodynamics. However, the surface region does not constitute a bulk phase and so thermodynamics, in its existing form, is not ideally suited to describe this region.

The approach Gibbs employed to amend this was to calculate the additional energy that a smooth system possesses over that of a stepped system²⁰, separating the two bulk phases with a hypothetical ‘skin membrane’. This additional energy is called the *surface free energy* or the *Helmholtz surface energy* [7]. The Helmholtz surface energy divided by the surface area gives the surface tension.

The problem Gibbs now faced was that he needed a definition that would enable him to find the surface area reliably and consistently. He called this dividing line the equimolar surface, r_e , also called the Gibbs dividing surface. At its simplest, the Gibbs dividing surface is defined as the surface for which the two areas A and B (see figure (2.2)), encased between the step function and the continuous curve, are equal (see Appendix I for the thermodynamics underlying the equimolar surface).

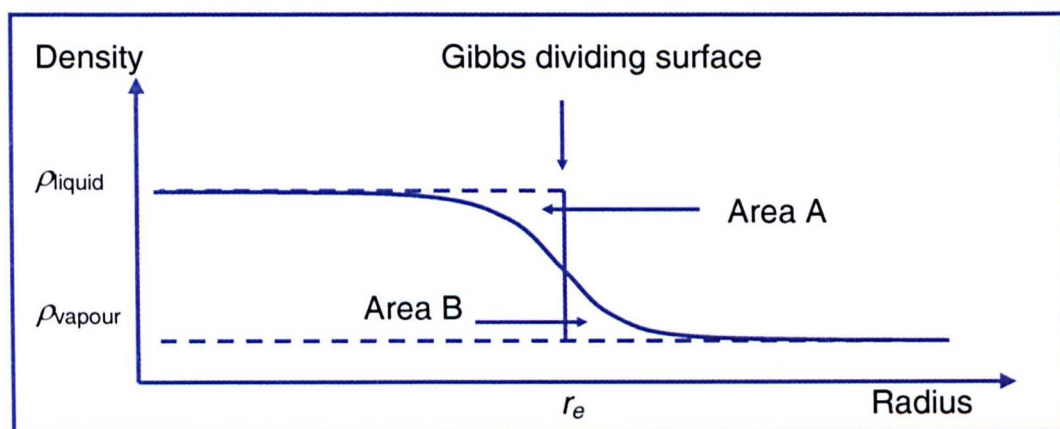


Figure 2.2: Shows the density profile of a liquid to vapour transition, where ρ_{liquid} is the density in the liquid bulk and ρ_{vapour} is the density in bulk vapour phase. The Gibbs dividing surface is defined such that $\text{Area A} = \text{Area B}$.

The way in which Gibbs then used this to define the surface tension was to divide the Helmholtz energy, F_s , by the area, A , of the equimolar surface, i.e.

²⁰ As employed by Laplace

$$\sigma = \frac{F_s}{A}$$

In the case of a sphere, A can be defined in terms of r_e , recall figure (2.2).

2.2.2.2 Van der Waals' Theory

Similarly, using Van der Waals' theory, it has been shown [7] that the surface tension can be calculated from any of the following formulae:

$$\begin{aligned} \sigma &= \int_{-\infty}^{\infty} \Psi(z) dz \\ &= \int_{-\infty}^{\infty} m[\rho(z)] \rho'(z)^2 dz \\ &= -2 \int_{-\infty}^{\infty} W[\rho(z)] dz \\ &= \int_{\rho^\alpha}^{\rho^\beta} [-2m(\rho)W(\rho)]^{\frac{1}{2}} d\rho \end{aligned} \tag{2.2}$$

where $\Psi(z)$ is the free energy density excess due to the inhomogeneity in the interface region, and m and W are two functions which depend on the density profile $\rho(z)$. Equations (2.2) imply that the density profile can be utilised to determine the surface tension. However, in the absence of an explicit functional form for $W(\rho)$ and $m(\rho)$ we are unable to evaluate equation (2.2). Although the density profiles are examined²¹, the direct link between density profiles and surface tension is not transparent. It should also be noted that equations (2.2) apply to flat surfaces and would have to be modified to be applicable to spherical droplets.

There were numerous problems facing these original attempts to define surface tension. As Laplace did not possess the computational power to perform molecular dynamic simulations, how was he to correlate the molecular force-fields and the density profiles with the surface tension?

²¹ Density profiles, at different points in time, can be employed to establish if a droplet has reached equilibrium. They are also of interest because they can show where in the droplet certain features (seen in the energy and force profiles) occur.

Gibbs, despite employing a quasi-thermodynamical method, experienced similar problems. Even Van der Waals, whose method was also quasi-thermodynamical, faced similar difficulties. For all three models, the direct link between inter-particle forces or energies and surface tension appears severed; statistical mechanics attempts to provide a solution to this dilemma by marrying thermodynamics and molecular dynamics [14] and this is described in the following section.

2.2.3 Statistical Thermodynamics

In contrast with classical mechanics, which examines individual particles, statistical mechanics describes systems in terms of statistical distributions of the values of given properties. In so doing, it bridges the intuitive gap between systems composed of discrete particles and the thermodynamics of a bulk. This is accomplished, for a given property, by using distribution functions to ascribe a probability of a particle having a value in a particular range. An example of this is the Boltzmann distribution which describes the distribution of molecules' momenta. This approach is particularly useful for describing large homogenous systems. However, there have been numerous reasonably successful attempts at applying statistical mechanics to inhomogeneous systems, such as systems containing two phases. Some of these are introduced below.

The starting point from which this success is built is the statistical mechanics approach to the topic of surface tension: it employs some of the results from thermodynamics and it aspires to find and locally define the thermodynamical properties that would otherwise be unknown. Before looking at how statistical mechanics achieves this we should examine the thermodynamics it utilises. Thermodynamics relates surface tension to the

Helmholtz free energy²², F , or the grand potential, Ω . The grand potential is defined as $\Omega = F - \boldsymbol{\mu} \cdot \mathbf{n}$, where $\boldsymbol{\mu} \cdot \mathbf{n}$ is $\sum_{i=1}^c \mu_i n_i$, μ_i is the chemical potential and n_i is the molar concentration of species i . The theory defines surface tension, σ , to be the Helmholtz free energy or the grand potential differentiated with respect to the surface area [7 and 8], i.e.

$$\sigma = (\partial F / \partial A)_{T,V,\mathbf{n}} \text{ or } \sigma = (\partial \Omega / \partial A)_{T,V,\boldsymbol{\mu}}$$

where T is temperature and V is volume; the fact that \mathbf{n} and $\boldsymbol{\mu}$ are in bold is to denote that these are to be held constant.

Thermodynamics relates pressure and surface tension to the Helmholtz free energy, F ,

$$dF = -p(dV)_T + \sigma(dA)_T$$

$$p = -(\partial F / \partial V)_{T,A,\mathbf{n}} \text{ and } \sigma = (\partial F / \partial A)_{T,V,\mathbf{n}}$$

or to the internal energy, U ,

$$dU = -p(dV)_S + \sigma(dA)_S$$

$$p = -(\partial U / \partial V)_{S,A,\mathbf{n}} \text{ and } \sigma = (\partial U / \partial A)_{S,V,\mathbf{n}}$$

In statistical mechanics, as Bernoulli believed, pressure $\mathbf{p}(r)$ is related to density $\rho(r)$ and particle velocities $\mathbf{v}(r)$, i.e.

$$\nabla \cdot \mathbf{p}(\mathbf{r}) = -\rho(\mathbf{r})\nabla \mathbf{v}(\mathbf{r})$$

Further tools in the statistical armoury include correlation functions [8]. These are conditional probabilities of pairs of atoms or molecules occurring (in large numbers) at specific places. The purpose they serve is to provide the probability of a molecule being present in the vicinity of another molecule: for example in Monte Carlo simulations it is clear that, if a

²² This is a canonical ensemble.

molecule is present in a particular location, it would influence the probability of a second, third etc, molecule also being present. These functions are invaluable in helping to describe complex systems.

With distribution and correlation functions it should be possible to describe a system, including the interface between liquid and gas phases. However, the correlation functions used to describe liquid and gas phases are different, and the form they should take in the surface region is unclear [8]. The total correlation function $h(\mathbf{r}_1, \mathbf{r}_2)$ is defined [7] as $\rho^{(2)}(\mathbf{r}_1, \mathbf{r}_2) - \rho(\mathbf{r}_1)\rho(\mathbf{r}_2) = \rho(\mathbf{r}_1)\rho(\mathbf{r}_2)h(\mathbf{r}_1, \mathbf{r}_2)$, where $\rho(\mathbf{r}_1)$ and $\rho(\mathbf{r}_2)$ are the single particle density profiles for particles 1 and 2 respectively, e.g. liquid and gas, and $\rho^{(2)}(\mathbf{r}_1, \mathbf{r}_2)$ is the two particle density distribution, i.e. a density correlation function. According to theory, $\rho^{(2)}(\mathbf{r}_1, \mathbf{r}_2)$ is well defined for a planar surface.

Employing the generalized Ornstein - Zernike equation, the surface tension, σ , may be written in terms of polar coordinates [8] as

$$\sigma = \frac{\pi}{2k} \int_{-\infty}^{\infty} dz_1 \cdot \rho(z_1) \int_{-\infty}^{\infty} dz_2 \cdot \rho(z_2) \int_{|z_{12}|}^{\infty} g^{(2)}(z_1, r_{12}) \times \frac{d\Phi(r_{12})}{dr_{12}} (r_{12}^2 - 3z_{12}^2) dr_{12}$$

where $g^{(2)}(z_1, r_{12}) = h(z_1, r_{12}) + 1$ is the two particle configurational distribution function for particle 1 and 2, and $\Phi(r_{12})$ is the pair potential between particles 1 and 2.

Leng et al. [24] utilized a mean-field approximation to investigate the surface tension by using this approach and demonstrated an analytical equivalence to a similar formalism developed by Lovett et al. [25]. Fundamentally, however, any meaningful comparison with experiments not only hinges on the applicability of mean-field theory (which is highly

questionable for small droplets) but also on an explicit knowledge of the density and pair correlation functions.

An alternative method, which circumvents many of the above mentioned drawbacks, employs the pressure tensor to evaluate the surface tension, i.e.

$$\sigma = \int [p_N(z) - p_T(z)] dz$$

where p_N (p_T) is the normal (transverse) component of the pressure tensor [14, 15 and 16]. For pairwise additive potentials, Schofield and Henderson [26] demonstrated that the pressure tensor can be written in the form

$$p_{\alpha\beta}(\mathbf{r}) = kT \cdot \rho(\mathbf{r}) \delta_{\alpha\beta} - \frac{1}{2} \sum_{i \neq j} \sum \left\langle r_{ij}^{\alpha} \frac{1}{r_{ij}} \frac{du(r_{ij})}{dr_{ij}} \int_{C_{ij}} dl^{\beta} \delta(\mathbf{r} - \mathbf{l}) \right\rangle \quad (2.3)$$

where C_{ij} is any contour joining r_i and r_j , r_i is the location of molecule i , $\delta_{\alpha\beta}$ is the Kronecker delta, $u(r_{ij})$ is the intermolecular potential and $\delta(\mathbf{r} - \mathbf{l})$ is the Dirac delta function. As can be seen from equation (2.3), this formalism is readily amenable to computer simulations using, e.g., the molecular dynamics method. However, it can also be seen from this equation that there is no mechanical route (i.e. via the pressure tensor) to the surface tension of a spherical droplet that is invariant to the choice of contour of integration (i.e. independent of the choice of integral C_{ij}) [14]. The Irving-Kirkwood and the Harasima pressure tensor [14] are just two possible choices employed in the literature for this purpose. For instance, Rusanov and Brodskaya [16] employ the Irving-Kirkwood form in their MD simulations (with up to $N = 256$ Lennard-Jones particles) and obtained a decrease in the surface tension with decreasing radius of the surface of tension. Similarly, Thompson et al. [14] investigated a liquid droplet containing up to $N = 2048$ Lennard-Jones particles. These authors also found a reduction in the surface tension with decreasing drop radius and with increasing temperature by utilizing both the Irving-Kirkwood and the

Harasima form of the pressure tensor. However, a comparison between the two sets of theoretical results is impeded by the large uncertainties in the surface tension values arising from the poor statistics of the Harasima pressure tensor [14]. Also, an experimental verification of either of these choices of contour of integration is difficult because measurements of surface tension for sub-micrometer size droplets are fraught with difficulties.

In addition to this inability to unambiguously define the pressure tensor, the main problem facing statistical mechanics is that the correlation functions are not well defined in regions of phase transitions and therefore they are less than adequate to describe the surface region and subsequently the surface tension [7].

So, instead of defining surface tension in terms of ambiguous and ill defined expressions, we will utilize the output of molecular dynamic simulations directly. These simulations can provide information about molecular distributions throughout the system including the surface region. From this it should be possible to define surface tension in terms of this distribution. We put forward a theory in the next section that enables such a definition.

2.3 New Theoretical Method

In what follows, a new method for the determination of surface tension is proposed. We will limit the scope of this study to spherical droplets composed entirely of one type of particle. However, it should be noted that this method is equally applicable to multi-component systems and other surface geometries. This method uses a direct route from MD simulation results (via intuitive and physical arguments) to surface tension. Thus it avoids the problems of the thermodynamical and/or statistical mechanical theories described above.

The method we propose to find surface tension (described in more detail in the following section) is briefly summarized as follows:

- Choose an appropriate force field to perform MD simulations, e.g. Lennard-Jones 12-6 pair potential, etc.
- Equilibrate the system for a given temperature,
- Use the positional data of the particles (combined with the force field) to calculate the forces exerted on the particles. These will be repulsive in the bulk and attractive in the surface region
- Find where the attraction between the particles is a maximum and define this to be the surface of tension. This is needed both because it is used to identify the corresponding region in the energy profiles and it enables the surface area to be calculated. Both are required to calculate the surface tension (see below).
- Use the force field to calculate the energies of each particle.
- Viewing the droplet as a potential well, we find the energy required to remove a particle from the surface region to infinity. This is achieved by finding the average energy of the particles in the region corresponding to the surface of tension of the energy profile, as identified by the force

curves (shown in more detail in figure (2.5) below).

- This value is then divided by the surface area to give the average potential energy of the particles at the surface divided by the surface area. This gives a measure of surface tension and has units of J m^{-2} or N m^{-1} .

The method for evaluating the surface tension proposed here is a close analogy to experimental techniques, such as the du Noüy ring tensiometer, involving the mechanism of ‘meniscus breaking’ [7].

2.4 Computer Simulation Details

2.4.1 The System.

We applied the method, described in § 2.3, to spherical droplets containing N particles (where $N = 500, 1000, 2000$ and 4000). Simulations were performed for a range of different temperatures. We did this to see how the predictions of our model would compare with the predictions made by previous theories [7, 15]. The droplets were created and modelled using Cerius², a molecular modelling and visualisation package written by MSI [27]. The reasons for choosing spherical droplets were their practical significance and the simplification that their geometry allows. However, it should be noted that this model is easily adaptable to other geometries and choices of coordinate systems.

2.4.2 The Pair Potential.

For the MD simulations a Lennard-Jones 12-6 pair potential was chosen, both because of its simplicity and because it approximates the Van der Waals' interaction particularly well. The Lennard-Jones 12-6 pair potential employed has the form

$$u(r) = \varepsilon \left[\left(\frac{r_m}{r} \right)^{12} - 2 \left(\frac{r_m}{r} \right)^6 \right] \quad (2.3)$$

where r is the inter-particle spacing and ε is the depth of the potential well ($\varepsilon/k = 93.16$ K) which occurs at $r = r_m$ ($r_m = 0.3868$ nm) see figure (2.3). The significance of these parameters is that they can be used to approximate the Van der Waals' argon-argon interaction [27].

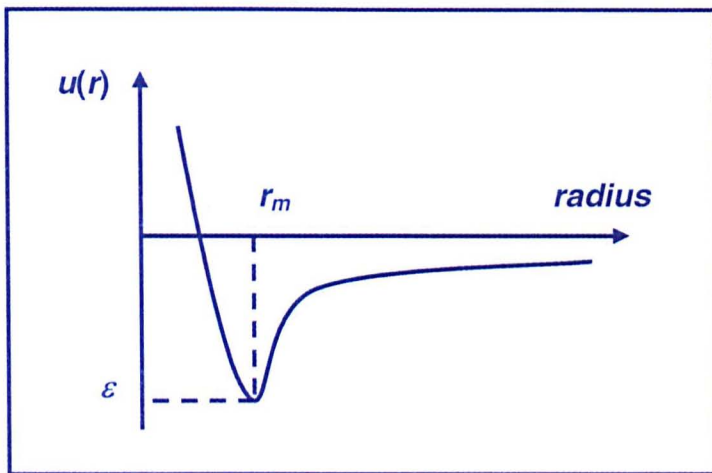


Figure 2.3: Shows the general shape of the potential energy of the Lennard-Jones 12-6 pair potential, where r_m is the radius at which the maximum depth, ε , of the potential well occurs.

The forces acting on the particles can be calculated by using the derivative of equation (2.3) to give equation (2.4), i.e.

$$F(r) = 12\varepsilon \left[\left(\frac{r_m^6}{r^7} \right) - \left(\frac{r_m^{12}}{r^{13}} \right) \right] \quad (2.4)$$

2.4.2.1 Creating Spherical Droplets.

Initially it is necessary to produce an appropriate proto-droplet. There are two reasons for this. Firstly, having a suitable initial droplet reduces the time taken to reach equilibrium and, secondly, an inappropriate choice of molecular distributions within a system could preclude any meaningful equilibrium from ever being attainable. For these reasons particular care was taken when creating the proto-droplets. The spherical droplets were created in the Cerius² visualisation window and this was done by a combination of copying and pasting, followed by repeated energy minimizations and low-temperature MD simulations²³ until droplets containing the desired number of particles and having the required shape (i.e. spherical) were obtained.

2.4.2.2 Running the Molecular Dynamic Simulations.

Once an initial droplet (a 'proto-drop') had been obtained, the MD simulations began. Certain aspects of these simulations were established prior to the MD run, e.g. the temperature was set, the time step was chosen to be 0.01 ps, and the simulation type was set to 'constant NVT' (i.e. the number of particles, volume and temperature were all kept constant). In addition, a potential cut-off radius of 1.4 nm ($= 3.6 r_m$) was employed in the calculations, in order to reduce CPU time.

The proto-drop was then equilibrated over several hundred picoseconds until fluctuations in the energies and the temperature were deemed acceptable (± 0.4 K in the case of temperature). For the 4,000 particle

²³ These were performed for short periods of time and at sufficiently low temperatures so that evaporation would not occur, but also at *high enough* temperatures, and for *long enough* times, so that *some* thermal movement could occur.

droplets this process typically took between ten and twenty hours. Subsequently, the number of steps was set to 1,000 and, for each droplet and given temperature, ten consecutive simulations were performed. This was done so that time averages could be performed (see below). For the 4,000 particle droplet the CPU time required to perform a thousand steps was approximately one hour.

2.4.2.3 Analysing the Droplets.

Once ten output files (for each temperature and droplet) had been obtained, the data generated by Cerius² could be analysed. It was necessary to have a method to process this considerable amount of data. This was provided by computer programs, written by the author in the programming language C, and utilising the mathematical formalism described below. Further to the mathematics used, the program 'DIAtimes10.c' which was used to perform these tasks can be found in Appendix M.

The start of this process began with an examination of the input data from Cerius² before analysis was undertaken. The output files from Cerius² were in Cartesian co-ordinates. For most of our needs this was ideal, allowing particle positions and separations to be calculated easily (using Pythagoras' theorem).

However, for some of our other needs, Cartesian co-ordinates (see below) with an arbitrarily located origin, were less than comprehensive. Instead, the geometry of the system lends itself to spherical polar co-ordinates with the origin coinciding with the centre of the droplet. It is a reasonable assumption that for a roughly spherical droplet the centre of mass should coincide with the centre of its geometry. The origin was reset by using the

following (given in x , y and z directions)

$$(x_{cm}, y_{cm}, z_{cm}) = \left(\sum_{j=1}^N \frac{x_j}{N}, \sum_{j=1}^N \frac{y_j}{N}, \sum_{j=1}^N \frac{z_j}{N} \right)$$

where the system has N particles, subscript cm denotes the centre of mass, and j is the particle number (an arbitrary name). The centre of mass co-ordinate was subtracted from each particle's co-ordinate, i.e.

$$(x_i, y_i, z_i) = (x_j, y_j, z_j) - (x_{cm}, y_{cm}, z_{cm})$$

thus resetting the origin where i is the particle number (same as j but allowing us to distinguish between before and after the droplet's origin has been reset).

In a spherically symmetric system, to which these droplets roughly correspond, we can reduce the number of co-ordinates against which we plot the data from three (x , y and z) to one, r . For each particle r_i is given by

$$r_i = \sqrt{x_i^2 + y_i^2 + z_i^2}.$$

If spherical symmetry is assumed, or taken as an appropriate approximation, then the spherical polar co-ordinates θ and ϕ can be discarded; however, the newly centred x , y , and z co-ordinates will still be required, as will be seen below.

2.4.2.4 Calculating Density Profiles.

Depending on the geometry of a system, decisions must be made about how to divide a system in order to facilitate its analysis. To calculate density, it is necessary to know the number and masses of particles within a given volume. With a suitable choice of volume, the geometry of this system can be exploited. In this case, by dividing the droplet into radial shells and using the radial co-ordinate of each particle, it is possible to find

the number of particles, $n(r_1, r_2)$, that are contained within the shell enclosed by the two radii r_1 and r_2 (where $r_1 < r_2$). Given the particle mass, m , and a calculation of the volume of that shell, we were able to calculate each droplet's density as a function of the two radii, i.e.

$$\rho(r_1, r_2) = \frac{3 \cdot n(r_1, r_2) \cdot m}{4\pi(r_2^3 - r_1^3)}$$

If we used sufficiently small shells we could approximate

$$\rho(r_1, r_2) = \rho\left(\frac{r_1+r_2}{2}\right) \approx \rho(r_1) \approx \rho(r_2).$$

However, because we needed to balance the accuracy with which $\rho(r)$ and r were defined, the approximation $\rho(r_1, r_2) = \rho\left(\frac{r_1+r_2}{2}\right)$ was chosen.

2.4.2.5 Calculating Forces and Energies

Next, it was vital to determine how forces and energies of the particles vary as a function of distance, r , from the centre of the droplet. From the positional data, the potential energies and forces were evaluated for each particle using modified versions of equations (2.3) and (2.4). These equations now took the forms

$$u(r_i) = \frac{1}{2} \varepsilon \sum_{j=1, j \neq i}^N \left[\left(\frac{r_m}{r_{ij}} \right)^{12} - 2 \left(\frac{r_m}{r_{ij}} \right)^6 \right] \quad (2.5)$$

and

$$F(r_i) = \frac{1}{2} 12 \varepsilon \sum_{j=1, j \neq i}^N \left[\frac{r_m^6}{r_{ij}^7} - \frac{r_m^{12}}{r_{ij}^{13}} \right] \quad (2.6)$$

for the energy and force, respectively. The factors of $\frac{1}{2}$ were introduced to compensate for double counting.

2.4.2.6 Calculating Radial Averages.

Given that there was a Boltzmann distribution of particle velocities in the system, we could expect there to be a distribution of the potential energies of the particles. Thus, a technique to smooth over these statistical fluctuations was called for. For the density profiles, spatial averaging had already been performed. However, this still needed to be done for the energy and force profiles. Again, using the high degree of spherical symmetry, we were able to achieve this by dividing the droplet into radial shells²⁴ and finding particle averages within individual shells. For the energy this reads

$$\overline{E\left(\frac{r_1+r_2}{2}\right)} = \frac{\sum_{r_1}^{r_2} E_i(r)}{n(r_1, r_2)}$$

and for the force

$$\overline{F\left(\frac{r_1+r_2}{2}\right)} = \frac{\sum_{r_1}^{r_2} F_i(r)}{n(r_1, r_2)}$$

where $\sum_{r_1}^{r_2} E_i(r)$ is the total potential energy of all the particles within the shell between r_1 and r_2 , and $\overline{E\left(\frac{r_1+r_2}{2}\right)}$ is the average of this (likewise for F).

Computationally, problems arose with this definition as some of the shells were empty. For these we assigned the value of 'integer 0' to \overline{E} and \overline{F} so that these could be distinguished from energies and forces equal to 'real 0.0'. In this way, empty cells could be noted as such and their data not written to file; as a result, the spatial average curves are not subject to artificial fluctuations that they would otherwise have suffered. This was done so that, in addition to not skewing the spatial averages, empty shells would not skew the time averages either. Next, using the spatial averages, the temporal averages were calculated.

²⁴ We chose to use a shell thickness of $d = 0.1$ nm

2.4.2.7 Calculating Temporal Averages.

We had ten data sets for each temperature and droplet, evolving over some time period, typically 90 ps²⁵. For the time averaged density profile we added the ten $\rho(r)$ curves together and divided each element by ten. For the energy (and force) time average(s) we added the ten sets of data together and then divided each element by the number of non-empty sets at that radius. Thus, for each function (F , E and ρ), we had meaningful temporally and spatially averaged curves. By doing this we significantly reduced the statistical fluctuations inherent in the data.

2.4.2.8 Implementation on Computer: The Program

Initially, several programs were written, each to perform specific tasks, i.e. calculating: density; forces and energies; spatial averages; and finally, temporal averages. Once these programs had been verified as working, they were amalgamated into one program carrying out the whole sequence of calculations for each grouping of ten data sets, DIAtimes10.c (see Appendix M). The basic components of the program are shown below in figure (2.4):

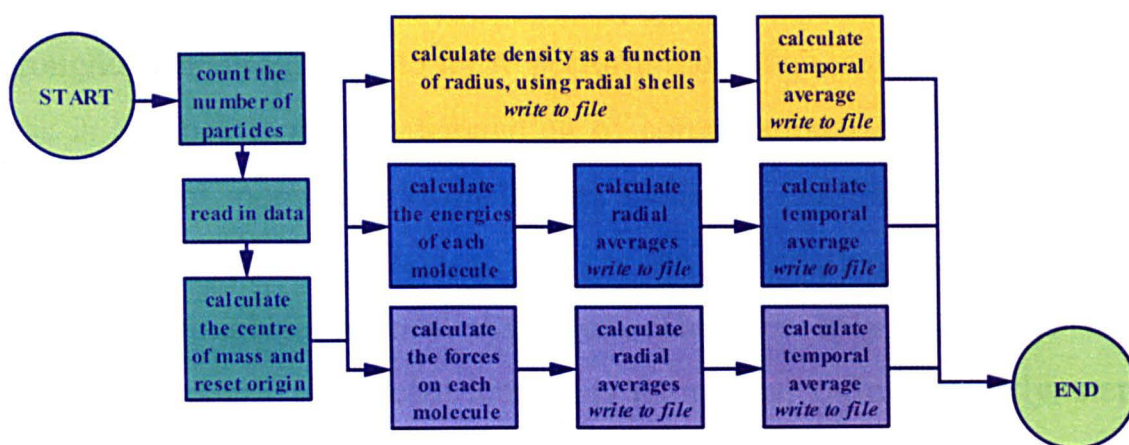


Figure 2.4: Shows the basic components of the program DIAtimes10.c (see Appendix M)

²⁵ Snapshots were taken at intervals of 10 ps.

In addition to the basics of the model described above, certain practicalities had to be taken into consideration when converting the raw data into something meaningful. For this purpose the following procedures were put into practice.

Firstly, it is important to know how many particles are in a system. When we are examining a droplet we do so at a particular temperature and at ten different points in time. Because all ten of these sets are for the same droplet and since particles are unable to leave the system, we know that the number of particles N , is the same for all ten data sets. While this is a fairly trivial detail to point out, it means that, to obtain this number, it is only necessary to count the number of particles in one out of ten sets. Once this number has been found, the program can allocate an appropriate amount of memory. With this dynamic memory available, the positional data is read in. The detail of how to do this is included in Appendix M.

In the process of reading in all the data, the individual sums of all the x , y and z components are obtained for each droplet. From this the centre of mass is calculated for each droplet, see § 2.4.2.3. A recurring theme throughout the program is to try to perform more than one task in one loop. This is because loops are demanding of computational time, so reducing the number of loops is a desirable aim. Once the droplets' origins are re-centred, the geometry of how to process the information becomes simple due to the roughly spherical symmetry. Thus the only coordinate with which there is any significant interest is the radius, r . Subsequently, steps are taken in order that the positional data of all the particles can be expressed in terms of x , y , z and r , relative to the centre of mass.

Density

Now the calculation of density is relatively straightforward. A shell thickness, dr , is chosen. This should be sufficiently small so that enough detail is available in the surface region but not so much that a fairly smooth profile is lost: in extreme cases this could be due to there being a significant number of shells containing no particles. Then the density, ρ , is simply described by:

$$\rho(r_i, r_{i+1}) = \frac{n(r_i, r_{i+1}) \cdot m_{molar}}{(V(r_{i+1}) - V(r_i)) \cdot A_v}$$

where $n(r_i, r_{i+1})$ is the number of particles in a shell which extends from r_i to r_{i+1} , m_{molar} is the molar mass of that given material, A_v is Avogadro's number, and $V(r_i)$ and $V(r_{i+1})$ are the volumes of the spheres respectively, i.e. $\frac{4}{3} \pi r^3$.

Energies and Forces

Having calculated the energies and forces, using equations (2.4) and (2.5), enormous fluctuations are observed, thus it is necessary to calculate both spatial and temporal averages.

Spatial averaging

By its very nature, density is a spatial average; in their current form the same is certainly not true of the energy and force data. Therefore, finding spatial averages for the energies and forces is subject to more pitfalls than was the case for density. This is because spatial averaging of energies or forces does not involve division by volume but by the *number* of particles within that volume. If shells are sufficiently thin, close to the origin or outside the droplet, then this number can be zero; as division by zero is undefined, appropriate allowances need to be made in order to avoid skewing the results. This is relevant to both the spatial and, later on, the

temporal averages.

Initially the molecules are stored in an arbitrary order; sorting the particles according to radial position eases the calculation of spatial averages. This works as a 'two part' histogram. In each shell there is a specific number of particles; this is part one of the histogram. It is easier to find this number when the particles are stored in ascending order of radial position. The second part of the histogram is to obtain the sum of these particles' energies or forces. From these two parts it is then simply a case of dividing the total energy or force of the particles in a shell by the number of particles in that shell, thus providing a spatial average.

The only problem with this is that the number of particles within a cell can be zero. While zero divided by zero is, in this case, clearly equal to zero, computationally it is ambiguous. Also, from the point of view of having a physically meaningful graph, it is appropriate to exclude such data points: they might mislead the reader into believing that the energy or force curves fluctuate more than they do. It would also have implications for temporal averaging.

The solution to this was to employ a method that identified empty cells and dealt with them accordingly. This was achieved by defining the entries of empty energy- and force- shells to be INTEGER 0; the shells, defined as INTEGER 0, were not written to file, thus avoiding misleading zig-zagging of the curves.

However, noting which radial cells are empty is still required in order to calculate temporal averages. If, when making this calculation, it was assumed that all the radial shells have particles in them, the temporal

average would be the sum (of energies or forces) divided by the *total number of data sets* (in this particular case ten) rather than the said sum divided by the number of occupied shells. Obviously, if only one out of ten of the radial shells contained molecules (from all the ten data sets), then dividing that single shell's energy or force by ten (rather than by one) would be nonsensical. To avoid this pitfall, the program counts how many shells have entries that are not equal to INTEGER 0; this value is then used in the temporal averaging instead.

Again there is the possibility that all the shells for the ten droplets are empty, and so the method of ascribing the value 'Integer 0' is revisited for temporal averages. This is so that, when writing to file, these shells can be omitted; again, avoiding artificial fluctuations in the resultant curves. The program, see Appendix M, performed all these calculations in slightly less than five minutes on a 1GHz Pentium PC for each set of ten droplets when containing 4,000 particles; correspondingly, the smaller droplets took less time.

From the output files, we were able to calculate the surface tension. How this is done is shown in the next section, with some examples of output files. This aspect of calculating the surface tension was performed manually.

2.4.2.9 Calculating Surface Tension.

In section 2.3 a general definition of how to find surface tension was proposed. This model has been applied to monatomic systems with a high degree of spherical symmetry. At this point, we use this system to demonstrate, by example, how to apply this theory in practice prior to

discussing the actual results. This is achieved by examining the output data obtained from the calculations above and then proceeding to use them in order to calculate surface tension.

Firstly, let us examine the form of the output data. Figure (2.5) shows an example of a force (middle panel) and potential energy profile (bottom panel) obtained from performing the program on a set of ten droplets. The corresponding density profile of this droplet (top panel) has also been included in this figure in order to illustrate where the surface region occurs with respect to density. This region is characterised by attractive (negative) inter-particle forces, which occur for radii beyond the vertical blue dashed line in figure (2.5). The radius r_s at which the maximum inter-particle attraction occurs is also indicated in figure (2.5) by the vertical (red) dotted line. This is the radius at which we extract the surface energy E_s . The surface tension of the droplet can now be calculated as:

$$\sigma = \frac{E_s}{4\pi r_s^2} \quad (2.7)$$

It is interesting to note that the region responsible for surface tension (i.e. the region around the red vertical dotted line, at $r = r_s$) occurs at relatively low densities.

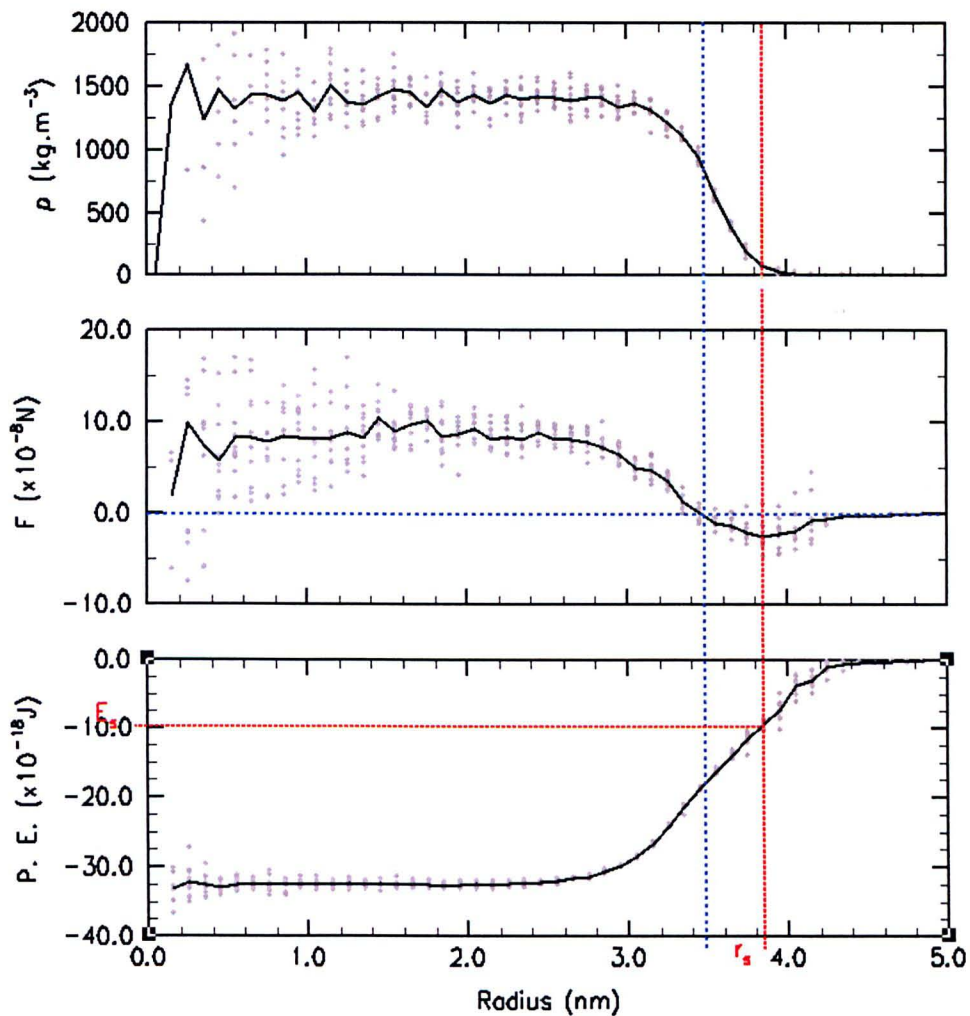


Figure 2.5: Shows typical examples of density, force, and potential energy profiles as functions of radius, r . The features of the force curve allow us to define where the surface region begins (see the vertical blue dashed line, which is the radius at which the force curve becomes negative). We define the surface to be typified by the maximum attractive force; this occurs at a radius, r_s (shown by the vertical red dotted line), which allows us to find the surface energy E_s (shown by the horizontal red dotted line). This example is for the 4000 particle droplet at 60 K. (N.B. the grey dots that can be seen on these graphs belong to the contributing ten data sets, for which the black lines represent their averages).

2.4.2.10 Density Profile Fitting (tanh-Fitting)

It is appropriate here to address the important issue of how our droplets compare with those from other researchers' simulations of Lennard-Jones droplets. This must be done before we can compare the resulting surface tensions; if the droplets are dissimilar then comparing surface tensions would be futile. To do this the density profiles for our droplets are examined, with a view towards curve fitting them using a *tanh* function.

This technique will enable a direct comparison between our simulations and those performed by others. If our simulations yield similar results, then we can confidently commence with making comparisons between our results for surface tensions, calculated using our new and different method, with those obtained using 'established' methods.

It is standard in the literature [15] to approximate the density profiles $\rho(r)$ by the following empirical expression:

$$\rho(r) = \frac{1}{2}(\rho_{liquid} + \rho_{vapour}) - \frac{1}{2}(\rho_{liquid} - \rho_{vapour}) \tanh\left(2\frac{r-r_0}{D}\right) \quad (2.8)$$

where ρ_{liquid} (ρ_{vapour}) denotes the density of the liquid (vapour), and r_0 and D are two fitting parameters which describe the location and thickness of the surface region respectively. We used this curve fit on the droplets containing 4000 argon atoms, for each temperature, to investigate the density profiles as a function of temperature. One example of such a curve fit is shown in figure (2.6) and the tanh-fitting parameters obtained for various temperatures are summarized in table (2.1).

As we can see from table (2.1), the thickness D of the surface increases monotonically with increasing temperature. However, the radius r_0 of the droplet increases first with increasing temperature (for $T \leq 60$ K) and then decreases as the droplet starts to evaporate. We also note that the calculated density at the interior of the 4000 particle droplet agrees reasonably well with experimental data, i.e. comparing the density of our liquid droplet (at 40 K) of 1590 kg m^{-3} with that obtained experimentally for bulk liquid argon of 1656 kg m^{-3} [19].

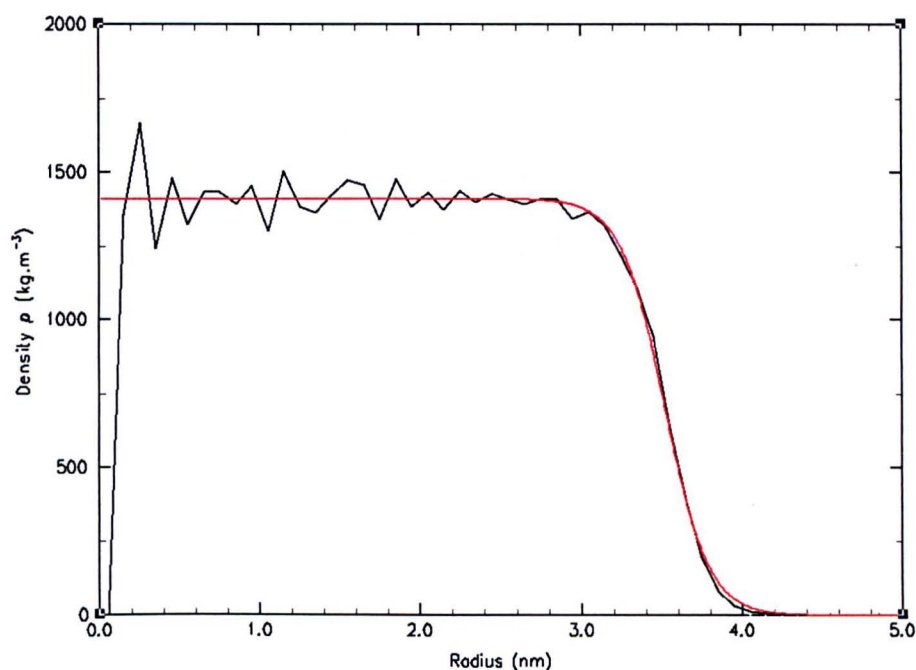


Figure 2.6: Shows an example of a density profile (for the 4000 particle droplet at 60 K) and the tanh-curve fit used to approximate it.

Table 2.1: Shows the tanh-curve fitting parameters used for the 4000 particle droplet for different temperatures (see equation (2.8)).

Temp	ρ_{liquid}	ρ_{vapour}	D	r_0
20K	1660 kg m ⁻³	0 kg m ⁻³	0.23 nm	3.35 nm
30K	1600 kg m ⁻³	0 kg m ⁻³	0.24 nm	3.39 nm
40K	1590 kg m ⁻³	0 kg m ⁻³	0.4 nm	3.41 nm
50K	1475 kg m ⁻³	0 kg m ⁻³	0.45 nm	3.48 nm
60K	1420 kg m ⁻³	1 kg m ⁻³	0.5 nm	3.51 nm
70K	1335 kg m ⁻³	5 kg m ⁻³	0.7 nm	3.48 nm
72.5K	1330 kg m ⁻³	4 kg m ⁻³	0.75 nm	3.45 nm
75K	1300 kg m ⁻³	5 kg m ⁻³	0.9 nm	3.41 nm
77.5K	1270 kg m ⁻³	7 kg m ⁻³	0.85 nm	3.4 nm
80K	1245 kg m ⁻³	8 kg m ⁻³	0.85 nm	3.38 nm
82.5K	1245 kg m ⁻³	8 kg m ⁻³	1.15 nm	3.28 nm
85K	1190 kg m ⁻³	10 kg m ⁻³	1.15 nm	3.3 nm
87.5K	1190 kg m ⁻³	11 kg m ⁻³	1.2 nm	3.2 nm

Having performed the tanh-curve fits (see table (2.1)) for our Lennard-Jones fluid, we are now able to compare our results with those obtained by Powles et al. for a similar Lennard Jones fluid [15]. This is done in a parameter independent form, where D/r_m is calculated (recall that $D = \text{skin}$

thickness [see equation (2.8)] and r_m is the radius of the largest negative potential in the Lennard–Jones model, recall equation (2.3)). This is a dimensionless quantity; by plotting it against kT/ε (recall that ε is the potential well depth in equation (2.3)) it is possible to compare these droplets directly with other MD simulations (also performed on droplets comprising of Lennard-Jones particles).

This comparison is shown in figure (2.7), where the red crosses with error bars are our values of D/r_m obtained for the 4000 particle droplet. The solid black line is an empirical fit to similar MD calculations performed by Powles and co-workers [15] for a range of droplet sizes, containing between 260 and 1,300 particles. The sizes of these droplets relative to ours should be noted as ours range from 500 to 4,000. We can see that, within statistical errors, our data shows good agreement with the data of Powles et al. . For the purpose of illustration only, we have extrapolated the empirical expression of Powles et al. [15] to lower temperatures (i.e. the dashed line in figure (2.7)) in an attempt to bring out the characteristic features of our low-temperature results.

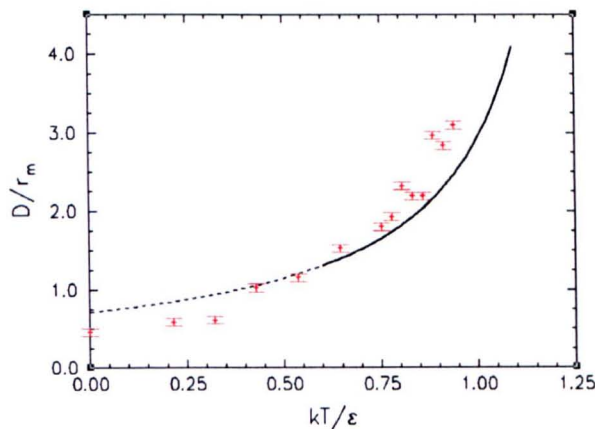


Figure 2.7: Shows D/r_m against kT/ε , and allows us to compare Lennard-Jones droplets directly. The black crosses, with error bars, represent the results from our 4000 particle droplet at various temperatures. The full black line was taken from Powles et al. [15] obtained by virial theorem (the dashed line is an extrapolation of the solid line).

It can also be seen, from a comparison with the extrapolated curve (the dashed line in figure (2.7)), that our droplet exhibits a solid-to-liquid phase transition at $kT/\varepsilon \approx 0.38$. Such a phase transition was also observed in the MD simulations performed by Rusanov and Brodskaya [16]. These authors obtained a transition point of 0.32 (38 K) for a system of 256 Lennard-Jones argon particles and ascribed the lower melting temperature of the droplet compared with a macroscopic crystal of argon (of 84 K) to the smaller size of the crystallite. It could be argued that a liquid-to-vapour phase transition is also visible in figure (2.7) (at $kT/\varepsilon \approx 0.87$). However, this result is inconclusive due to the statistical fluctuations in the MD simulation data.

From figure (2.7) we conclude that our simulations have yielded similar droplets to those of Powles et al. [15]. Therefore, we can assume that we are applying our theory to droplets similar to those obtained by other groups working in this field. Consequently, we are now in a position to evaluate the surface tension of the droplets. This is addressed in the section that follows.

2.5 Results and Discussion

2.5.1 Surface Tension in Relation to Temperature and N .

Figure (2.8) shows the values of surface tension obtained from equation (2.7) for the various droplets, as a function of temperature. The calculated values are represented by the data points with error bars, where the solid coloured lines are the result of exponential regression and provided as a guide for the eyes. The fitting parameters used to curve fit these data are included in Appendix L. The dashed red curve is also an exponential regression but certain data points have been excluded; this line is *purely* a guide to the eye and its inclusion is justified only by the intuitive argument that some of the points at higher temperatures are questionable.

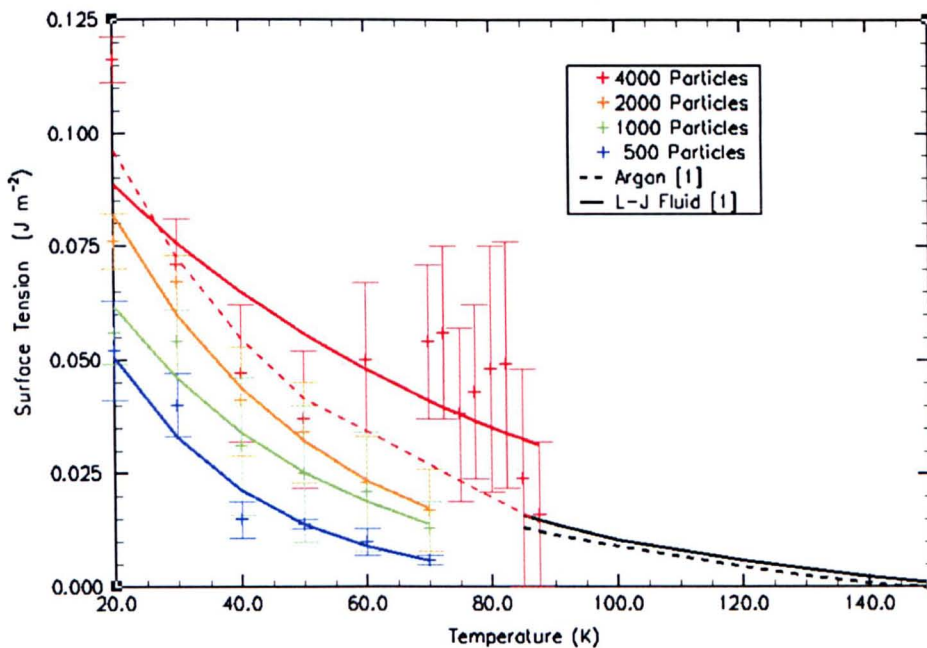


Figure 2.8: Shows surface tension as a function of temperature for the four different droplet sizes. The solid lines coloured: red, orange, green and blue, are exponential regressions (see Appendix L) of the data for the droplets containing 4000, 2000, 1000 and 500 particles respectively. Note that a dotted red line has also been included as an aid to the eye. (This is also an exponential regression for the 4,000 particle droplet, but performed only on the points at 20, 30, 40, 50 and 87.5 K as, purely on an intuitive basis, the other points seem incongruous.) Also included are experimental surface tension values for argon (black dashed line), and the theoretical results obtained for a Lennard-Jones 12-6 planar argon surface (solid black line) [7]

The question as to the large fluctuations in the data points for the 4,000 particle droplet in the temperature region 60 to 87.5 K; may be due to the absence of a boundary box (thus leading to evaporation of the droplets at larger temperatures) and/or, the increased “slowness” with which the larger droplet appears to change with time, thus detrimentally affecting our ability to distinguish between pre-equilibrated droplets and those at equilibrium.

Examining the 500, 1000, and 2000 particle curves in figure (2.8), we see that with increasing temperature, the surface tension decreases. This can also be seen for the temperature range $20 \text{ K} < T < 50 \text{ K}$ for the 4000 particle droplet. Over the temperature range $50 \text{ K} < T < 87.5 \text{ K}$ (for the 4000 particle droplet) the general trend is continued. However, within this range the statistical fluctuations are large, which we mainly attribute to the difficulty in establishing when equilibrium has been reached, i.e. the comparatively small changes in the density profile for this droplet with respect to time which, in turn, introduces further uncertainty in the value of the obtained surface tension. It is interesting to note that ‘pre-equilibrium’ surface tensions are higher than equilibrium surface tensions. Notwithstanding, the general conclusion we can make from these results is that surface tension decreases with increasing temperature; this is in good qualitative agreement with the predictions of thermodynamical theories [16].

If it is the intention to use these graphs in order to accurately calculate surface tension then, currently, the sizes of these error bars are prohibitively large. However, at this point the main intention of this work was to find trends and to see if this method could provide a new alternative to those put forward in section 2.2. To that end, this method fulfils these criteria; reducing the errors can be achieved by increasing the number of data sets, which can be done at a later date.

For reasons of comparison between our results and those of other researchers, there are included in figure (2.8) two additional sets of data, taken from Rowlinson and Widom [7], corresponding to experimental data and Lennard-Jones MD simulations of a planar argon surface over a temperature range of 85 K to 150 K (the full and dashed black lines). If we compare the curves of exponential regressions used to curve fit our data with the values of surface tension obtained by Rowlinson and Widom [7] (i.e. the two black lines; the dashed line is the experimental value of the surface tension of a planar argon surface and the solid line is the surface tension calculated for a planar Lennard-Jones argon surface [7]), we see that, while they do not apply to the same temperature range as our simulations, they appear to be very acceptable extrapolations to our data. In particular, the 4000 particle droplet appears to be already a good approximation of a flat surface. This is further evidence of the validity of this new method. This also provides anecdotal evidence that our droplets are of a sufficiently large size for calculations of surface tension to be physically meaningful. Therefore, pursuing further work to reduce statistical fluctuation would appear to have merit.

In addition, on further examination of figure (2.8) we see that, for all temperatures, increasing the droplet size has the effect of increasing the surface tension. This is demonstrated by comparing the data for the smallest droplet containing 500 particles (blue curve) with those of the 1000 particle (green curve), the 2000 particle (orange curve) and finally the 4000 particle curve (red); each has slightly larger surface tension values than the previous droplet. From this we can conclude that surface tension increases with increasing droplet size. This behaviour is in good qualitative agreement with the predictions of thermodynamical theories [14].

2.5.2 Surface Tension in Relation to Temperature and Surface of Tension, r_s .

While figure (2.8) shows how surface tension varies with respect to temperature, here we examine how surface tension varies as a function of droplet radius. In the previous graph (i.e. figure (2.8)) this was done for droplets containing specific numbers of particles, however, here we examine the situation for different temperatures. This is shown in figure (2.9).

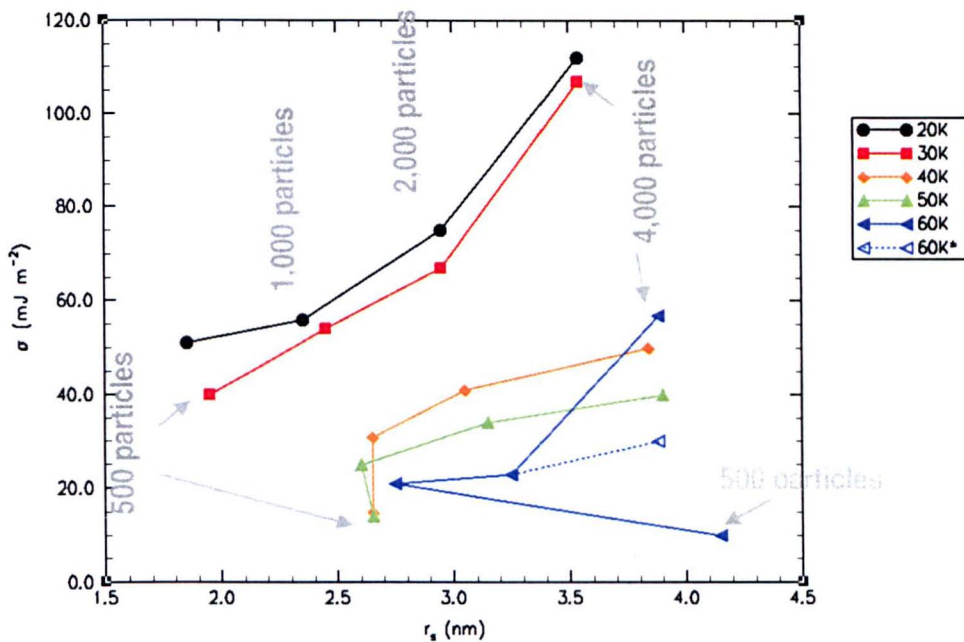


Figure 2.9: Shows the surface tension as a function of the radius r_s of the droplets at temperatures 30, 40, 50 and 60 K. Here the 60K* data point was obtained from the dashed red σ -curve in figure (2.8). For each of the curves in this figure (i.e. 2.9) the smallest surface tension corresponds to the 500 particle droplet, and the largest value of surface tension on each curve corresponds to the 4000 particle droplet. The adjoining lines are drawn purely to guide the eye in order of increasing particle numbers.

There are several observations that can be made from this graph, the first of these is temperature related. As was seen from figure (2.8), the surface tension decreases with increasing temperature, i.e. going from the black curve to the blue curve. Second (which was already suspected from figure

(2.7)), there is a definite phase change occurring between 30 and 40 K (the red and orange curves). It can also be seen that the surface tension generally²⁶ increases with decreasing curvature of the droplets and, for the *liquid* droplets (i.e. $T > 30$ K), eventually saturates as it approaches the planar limit. This behaviour confirms findings [16], obtained from a pressure tensor analysis of the MD simulations of Lennard-Jones liquid droplets, where it was found that the surface tension decreased with decreasing droplet size. The present results are also in good qualitative agreement with the thermodynamic formalism developed by Tolman [9] and the statistical mechanical approach of Kirkwood and Buff [17, 18], which both predict a decrease in surface tension with decreasing droplet size.

The second and more interesting array of things to be noted from figure 2.9 is concerned with the relationship between the number of particles within a droplet and the radii of the droplets. While this relationship differs for different temperatures, the way in which it changes is intriguing. For the lower temperature droplets (20 and 30 K) we see something fairly expected, i.e. that the surface tension increases with increasing radii. However, for larger temperatures, while this general trend is continued, what is observed for very small droplets is that the surface tension is sufficiently small for the droplet to expand significantly, i.e. r_s becomes much larger than it would for a droplet with, say, twice as many particles (c.f. $r_s = 2.75$ nm for the 1000 particle droplet at 60 K with 4.15 nm for the 500 particle droplet at 60 K, coupled with a halving of the surface tension from the former to the latter). This appears to support the idea that evaporating smaller droplets is much easier than larger droplets.

²⁶ For very small droplets at temperatures above 40 K we see that the radii tend to be larger than the radii of more massive droplets, see the blue curve in figure (2.9).

The values of the radii r_s and the energies E_s for various droplets, obtained from the method described in the previous section are summarized in table (2.2) together with the calculated values of surface tension, σ .

Table 2.2: Summarizes the values of r_s and E_s obtained from the MD simulations for all the droplets.

Droplet	Temperature (K)	r_s (nm)	E_s ($\times 10^{-18}$ J)	σ (mJm $^{-2}$)
500	20	1.85	-2.23	52
	30	1.95	-1.9	40
	40	2.65	-1.3	15
	50	2.65	-1.2	13
	60	4.15	-2.1	10
	70	5.6	-2.41	6
1000	20	2.35	-3.9	56
	30	2.45	-4.0	53
	40	2.65	-2.7	31
	50	2.6	-2.0	25
	60	2.75	-2.0	21
	70	3.8	-2.35	13
2000	20	2.95	-8.26	76
	30	2.95	-7.3	67
	40	3.05	-4.8	41
	50	3.15	-4.3	34
	60	3.25	-3.1	23
	70	3.65	-2.8	17
4000	20	3.54	-17.7	112
	30	3.54	-16.9	107
	40	3.84	-9.3	50
	50	3.9	-7.6	40
	60	3.88	-10.7	57
	70	3.9	-8.2	43
	72.5	3.8	-10.6	58
	75	3.9	-10.2	53
	77.5	4.14	-5.1	24
	80	3.72	-10.1	58
	82.5	4.08	-10	48
	85	4.02	-5.7	28
	87.5	4.2	-3.6	16

Comparing Radii for Different Sized Droplets:

Table 2.3: Shows the ratios of radii for the different droplets at different temperatures, where r_{s500} denotes the radius of the 500 particle droplet, etc.

	20K	30K	40K	50K	60K	70K	Average
r_{s1000}/r_{s500}	1.270	1.256	1	0.981	0.663	0.679	0.975
r_{s2000}/r_{s1000}	1.255	1.204	1.151	1.212	1.182	0.961	1.161
r_{s4000}/r_{s2000}	1.2	1.2	1.302	1.279	1.194	1.069	1.207

If the droplets were perfectly scaled versions of one another, we would expect that doubling the number of particles (and therefore volume) would increase the radius of a droplet by a factor of $1.2599 = \sqrt[3]{2}$. Indeed, this is the kind of ratio that is seen (see table (2.3)) at lower temperatures. At higher temperatures, however, we see that the smaller droplets expand more rapidly than the larger droplets (i.e. giving rise to smaller ratios) and therefore have lower densities. This is evidence of the greater ease with which smaller droplets evaporate.

Comparing Surface Energies for Different Sized Droplets:

Table 2.4: Shows the ratios of surface energies for each droplet at different temperatures, where E_{s500} denotes the surface energy of the 500 particle droplet, etc.

	20K	30K	40K	50K	60K	70K	Average
E_{s1000}/E_{s500}	1.749	2.105	2.077	2	0.852	0.977	1.643
E_{s2000}/E_{s1000}	2.118	1.825	2.15	1.433	1.55	1.192	1.711
E_{s4000}/E_{s2000}	2.143	2.315	1.938	1.767	3.452	2.929	2.424

In table (2.4) we see that there is a general trend of increasing surface energy with increasing droplet size (c.f. the average energy ratios in the last column), i.e. in terms of the potential-well interpretation of surface tension, the droplets become deeper as they become more massive. This makes intuitive sense, so this is additionally encouraging that it is substantiated by the simulation results.

2.6 Conclusions

Here, we have proposed a new method to calculate surface tension. The intention was for this model to overcome many of the drawbacks faced by thermodynamical theories [15, 17 and 28] and the non-invariance with respect to the choice of the pressure tensor form in the case of mechanical statistical approaches [14]. It is our conclusion that this model is effective in this aim as it eliminates these problems by being a microscopic theory that considers the liquid droplet as a 'potential well' and simply uses the inter-particle forces to characterise the surface region. Having applied this method to several Lennard-Jones liquid droplets it was found that the surface tension decreases with increasing temperature and that surface tension increases with increasing droplet size. These observations are in good qualitative agreement with the predictions of thermodynamics [7].

2.7 Further Work

The present method can be applied to numerous different areas. For example, it could be applied to multiple components systems, i.e. systems with more than one type of atom or molecule present. This would mean that we could investigate the properties of systems with impurities, or colloidal systems. As this model also allows us to define, at a mesoscopic level, the location of the surface region, we could apply this model to different geometries, including investigating interactions between solids and liquids, e.g. contact angles, wetting and waterproofing.

By employing appropriate boundary conditions, we could investigate flat surfaces and pressure dependent phenomena, such as droplet formation. Performing simulations using a MD simulating program with access to the source code would mean that we would have more control over the force

fields, so that we could investigate more complex molecules (in particular water, and its solutions). This model could be applied to problems such as ink jet printers, wetting and waterproofing materials, electrical contacts in the case of soldering, gas arc welding, etc. and is therefore a subject for future investigations.

However, work also needs to be done in order to reduce the errors intrinsic to this definition of surface tension for it to be of more than merely theoretical use. This could be achieved by increasing the number of data sets until the standard deviations of the error bars are of acceptable magnitudes. For now, we believe that we have shown that this method both provides a valid definition of surface tension and that it is capable of reproducing trends observed experimentally and predicted by theoretical models, such as thermodynamics and statistical mechanics.

Bibliography

- [1] N. Mourougou-Candoni, B. Prunet-Fock, F. Legay, M. Vigned-Adler and K. Wong, *J. Colloid Interface Sci.* **192**, 129 (1997)
- [2] M. Rein, *Fluid Dyn. Res.* **12**, 61, (1993)
- [3] D. Richard and D. Quéré, *Europhy. Lett.* **50**, 769 (2000)
- [4] X. G. Zhang and O. A. Bazaran, *J. Colloid Interface Sci.* **187**, 166 (1997)
- [5] V. Bergeron, D. Bonn, J. Y. Martin and Vovelle, *Nature* **405**, 772 (2000)
- [6] S. Subramaniam, D. R. White, D.J. Scholl, and Weber, *J. Phys. D. Appl. Phys.* **31**, 1963 (1998)
- [7] J. S. Rowlinson and B. Widom, *Molecular theory of capillarity*, (Clarendon Press, Oxford, 1982).
- [8] C. A. Croxton, *Statistical mechanics of the liquid state*, John Wiley, Bath, (1980).
- [9] R. C. Tolman, *J. Chem. Phys.* **17**, 333 (1949).
- [10] M. P. Allen and D. J. Tildesley, *Computer simulations of liquids*, (Clarendon Press, Oxford, 1992).
- [11] J. Kopolik, S. Pal, J. R. Banavor *Phys. Rev E* **65**, 021504 (2002)
- [12] C. C. Huang, Y. R. Jeng, Y. L. Hsu, J. G. Chang *J. Phys Soc. Jpn.* **70**, 2626 (2001)
- [13] T. Kinma, S. Maruyama *Microscale Therm. Eng.* **6**, 3 (2002)
- [14] S. M. Thompson, K. E. Gubbins, J. P. R. B. Walton, R. A. R. Chantry, and J. S. Rowlinson, *J. Chem. Phys.* **81**, 530 (1984).
- [15] J. G. Powles, R. F. Fowler, and W. A. B. Evans, *Phys. Letters* **98A**, 421 (1983).
- [16] A. I. Rusanov and E. N. Brodskaya, *J. Colloid and Interface Science* **62**, 542 (1977).

- [17] J. G. Kirkwood and F. P. Buff, *J. Chem. Phys.* **17**, 338 (1949).
- [18] F. P. Buff, *J. Chem. Phys.* **19**, 1591 (1951).
- [19] G. W. C. Kaye and T. H. Laby, *Tables of physical and chemical constants*, 16th edition. (Harlow Longman, 1995).
- [20] H. T. Davis, *Statistical mechanics of phases, interfaces, and thin films*. (Wiley-VCH, Inc. New York, 1996).
- [21] V. I. Kalikmanov *Phys. Rev. E* **55**, 3068 (1997)
- [22] M. J. P. Nijmeijer, C. Bruin, A. B. Van Leuwen *J. Chem. Phys.* **96**, 565 (1992)
- [23] K. Koga, X. C. Zeus, A. K. Shchekin *J. Chem Phys.* **109**, 4063 (1998)
- [24] C. A. Leng, J. S. Rowlinson and S.M. Thompson, *Proc. Roy. Soc. A*, **358**, 267 (1977)
- [25] R. Lovett, P. W. De Haven, J. J. Viecelli, and F. P. Buff, *J. Chem. Phys.* **58**, 1880 (1973)
- [26] P. Schofield, J. R. Henderson *Proc. Roy. Soc. London A* **379**, 231 (1982)
- [27] Cerius², Molecular Modelling Software, Molecular Simulations Inc., 230/250 The Quorum, Barnwell Road, Cambridge CB5 8RE, UK (<http://www.msi.com/>).
- [28] F. O. Koenig, *J. Chem. Phys.* **18**, 449 (1950).
- [29] <http://www-gap.dcs.st-and.ac.uk/~history/Mathematicians/Boltzmann.html>; [Accessed 18 Jan 2004]
- [30] http://www-gap.dcs.st-and.ac.uk/~history/Mathematicians/Bernoulli_Daniel.html [Accessed 18 Jan 2004]

Appendix A: The Frank Energy Density

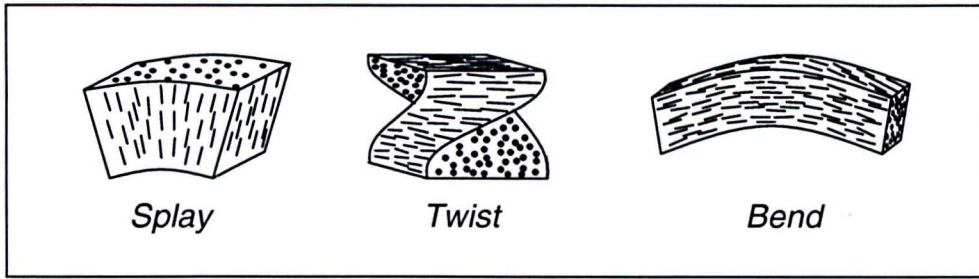


Figure A.1: Shows different types of deformation possible

The Frank expression for the elastic energy density of a deformed nematic LC can be written as [Barbero].

$$f_{Frank} = \frac{1}{2}K_{11}(\nabla \cdot \vec{n})^2 + \frac{1}{2}K_{22}(\vec{n} \cdot \nabla \times \vec{n})^2 + \frac{1}{2}K_{33}(\vec{n} \times \nabla \times \vec{n})^2 \tag{A.1}^{27}$$

where the three terms represent the splay, twist and bend deformation of the director field \vec{n} respectively.

Geometry

in spherical polars $\vec{n} = \begin{pmatrix} \cos\theta \cdot \cos\phi \\ \cos\theta \cdot \sin\phi \\ \sin\theta \end{pmatrix}$ and $|\vec{n}| = 1$

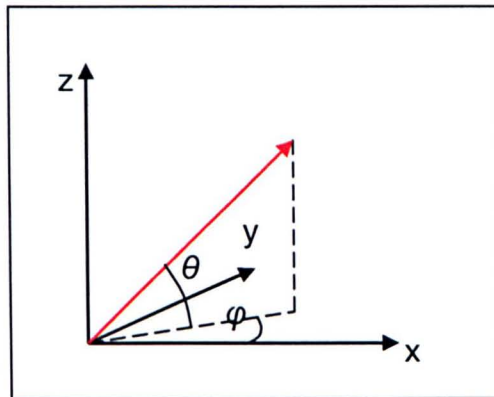


Figure A.2: Co-ordinate System

²⁷ If we use the one-constant approximation ($K_{11} = K_{22} = K_{33} = K$) then equation (A.1) becomes $F_d = \frac{1}{2}K[(\nabla \cdot \vec{n})^2 + (\nabla \times \vec{n})^2]$.

In general:

$$\vec{n} = \begin{pmatrix} \cos \theta \cos \phi \\ \sin \phi \\ \sin \theta \cos \phi \end{pmatrix}$$

however we can assume $\phi = 0 = \text{const} \cdot f(z)$ so

$$\Rightarrow F_{Frank} = \frac{1}{2} f_{elas}(\theta) \left(\frac{\partial \theta}{\partial z} \right)^2 \quad (\text{A.2})$$

$$\text{i.e. } \frac{\partial}{\partial x} \equiv 0 \text{ and } \frac{\partial}{\partial y} \equiv 0$$

thus

$$\vec{n} = \begin{pmatrix} \cos \theta \\ 0 \\ \sin \theta \end{pmatrix}$$

with

$$\theta = \theta(z)$$

A.1 Splay:

$$\begin{aligned} \nabla \cdot \vec{n} &= \frac{\partial u_x}{\partial x} + \frac{\partial u_y}{\partial y} + \frac{\partial u_z}{\partial z} \\ &= \frac{\partial u_z}{\partial z} = \frac{\partial}{\partial z} \sin \theta \\ &= \cos \theta \frac{\partial \theta}{\partial z} \end{aligned} \quad (\text{A.3})$$

A.2 Twist:
using

$$\begin{aligned}\nabla \times \vec{n} &= \begin{vmatrix} \hat{i} & \hat{j} & \hat{k} \\ \frac{\partial}{\partial x} & \frac{\partial}{\partial y} & \frac{\partial}{\partial z} \\ u_x & u_y & u_z \end{vmatrix} = \begin{vmatrix} \hat{i} & \hat{j} & \hat{k} \\ 0 & 0 & \frac{\partial}{\partial z} \\ \cos \theta & 0 & \sin \theta \end{vmatrix} \\ &= \hat{j} \frac{\partial}{\partial z} \cos \theta = -\hat{j} \sin \theta \frac{\partial \theta}{\partial z} \\ &= \begin{pmatrix} 0 \\ -\sin \theta \frac{\partial \theta}{\partial z} \\ 0 \end{pmatrix}\end{aligned}$$

we find that the twist term is:

$$\begin{aligned}\vec{n} \cdot \nabla \times \vec{n} &= \begin{pmatrix} \cos \theta \\ 0 \\ \sin \theta \end{pmatrix} \cdot \begin{pmatrix} 0 \\ -\sin \theta \frac{\partial \theta}{\partial z} \\ 0 \end{pmatrix} \\ &= 0\end{aligned}\tag{A.4}$$

i.e. there is no contribution due to twist.

A.3 Bend:
again using

$$\begin{aligned}\nabla \times \vec{n} &= \begin{vmatrix} \hat{i} & \hat{j} & \hat{k} \\ \frac{\partial}{\partial x} & \frac{\partial}{\partial y} & \frac{\partial}{\partial z} \\ u_x & u_y & u_z \end{vmatrix} = \begin{vmatrix} \hat{i} & \hat{j} & \hat{k} \\ 0 & 0 & \frac{\partial}{\partial z} \\ \cos \theta & 0 & \sin \theta \end{vmatrix} \\ &= \hat{j} \frac{\partial}{\partial z} \cos \theta = -\hat{j} \sin \theta \frac{\partial \theta}{\partial z} \\ &= \begin{pmatrix} 0 \\ -\sin \theta \frac{\partial \theta}{\partial z} \\ 0 \end{pmatrix}\end{aligned}$$

we find that the bend term is:

$$\begin{aligned}
 \vec{n} \times \nabla \times \vec{n} &= \begin{pmatrix} \cos \theta \\ 0 \\ \sin \theta \end{pmatrix} \times \begin{pmatrix} 0 \\ -\sin \theta \frac{\partial \theta}{\partial z} \\ 0 \end{pmatrix} \\
 &= \begin{pmatrix} \sin^2 \theta \frac{\partial \theta}{\partial z} \\ 0 \\ -\sin \theta \cos \theta \frac{\partial \theta}{\partial z} \end{pmatrix} \\
 &= -\sin \theta \cos \theta \frac{\partial \theta}{\partial z} \hat{k} + \sin^2 \theta \frac{\partial \theta}{\partial z} \hat{i}
 \end{aligned} \tag{A.4}$$

we substitute equations (A.2), (A.3) and (A.4) into (A.1) to get

$$\begin{aligned}
 F_{Frank} &= \frac{1}{2} f_{elas}(\theta) \left(\frac{\partial \theta}{\partial z} \right)^2 \\
 &= \frac{1}{2} K_{11} \left(\cos \theta \frac{\partial \theta}{\partial z} \right)^2 + \frac{1}{2} K_{33} \left(-\sin \theta \cos \theta \frac{\partial \theta}{\partial z} \hat{k} + \sin^2 \theta \frac{\partial \theta}{\partial z} \hat{i} \right)^2
 \end{aligned} \tag{A.5}$$

where

$$f_{elas}(\theta) = K_{11} \cos^2 \theta + K_{33} \sin^2 \theta .$$

[Barbero] G. Barbero and L. R. Evangelista, *An elementary course on the continuum theory for nematic liquid crystals*, (World Scientific, Singapore, 2001), p. 63

Appendix B: Derivation of the Free Energy Density for the HAN Cell

B.1 Elastic FE term ($F_{elas} = F_{Frank}$ from Appendix A)

From equation (A.6):

$$\begin{aligned}
 F_{elas} &= \frac{1}{2} K_{11} \left(\cos \theta \frac{\partial \theta}{\partial z} \right)^2 + \frac{1}{2} K_{33} \left(-\sin \theta \cos \theta \frac{\partial \theta}{\partial z} \hat{k} + \sin^2 \theta \frac{\partial \theta}{\partial z} \hat{i} \right)^2 \\
 &= \frac{1}{2} K_{11} \cos^2 \theta \left(\frac{\partial \theta}{\partial z} \right)^2 + \frac{1}{2} K_{33} \left(\sin^2 \theta \cos^2 \theta + \sin^2 \theta \sin^2 \theta \right) \left(\frac{\partial \theta}{\partial z} \right)^2 \\
 &= \frac{1}{2} K_{11} \cos^2 \theta \left(\frac{\partial \theta}{\partial z} \right)^2 + \frac{1}{2} K_{33} \sin^2 \theta \left(\frac{\partial \theta}{\partial z} \right)^2 \\
 &= \frac{1}{2} f_{elas}(\theta) \left(\frac{\partial \theta}{\partial z} \right)^2
 \end{aligned} \tag{B.1}$$

where

$$f_{elas}(\theta) = K_{11} \cos^2 \theta + K_{33} \sin^2 \theta$$

B.2 Dielectric FE Term

$$\vec{D} = \epsilon'_n \cdot \vec{E} + (\epsilon'_n - \epsilon'_n) \cdot (\vec{n} \cdot \vec{E}) \cdot \vec{n}$$

[de Gennes & Prost]

$$\begin{aligned}
 F_{diel} &= -\frac{1}{2} \vec{D} \cdot \vec{E} \\
 &= -\frac{1}{2} \left[\epsilon'_n \cdot E^2 + (\epsilon'_n - \epsilon'_n) \cdot (\vec{n} \cdot \vec{E})^2 \right] \\
 &= -\frac{1}{2} \left[\epsilon'_n \cdot E^2 + \Delta \epsilon' \cdot E^2 \cdot \cos^2 (\vec{n} \cdot \vec{E}) \right] \\
 &= -\frac{1}{2} \epsilon_0 \left(\epsilon_n + \Delta \epsilon \cdot \sin^2 \theta \right) \cdot E^2 \\
 &= -\frac{1}{2} \cdot f_{diel}(\theta) \cdot \left(\frac{\partial \phi}{\partial z} \right)^2
 \end{aligned} \tag{B.2}$$

where

$$f_{diel}(\theta) = \varepsilon_0 (\varepsilon_n + \Delta\varepsilon \cdot \sin^2 \theta)$$

and where we have used

$$E = \frac{\partial \phi}{\partial z}$$

B.3 Flexoelectric FE Term

$$F_{flex} = -\vec{P} \cdot \vec{E}$$

$$\vec{P} = e_{11}(\nabla \cdot \vec{n}) \cdot \vec{n} + e_{33}(\nabla \times \vec{n}) \times \vec{n}$$

$$\vec{n} = \begin{pmatrix} \cos \theta \\ 0 \\ \sin \theta \end{pmatrix} \quad \text{and} \quad \vec{E} = \begin{pmatrix} 0 \\ 0 \\ E \end{pmatrix}$$

$$\begin{aligned} F_{flex} &= e_{11} \cos \theta \frac{\partial \theta}{\partial z} \vec{n} \cdot \vec{E} + e_{33} \left(-\sin^2 \theta \frac{\partial \theta}{\partial z} \hat{i} + \sin \theta \cos \theta \frac{\partial \theta}{\partial z} \hat{k} \right) \vec{E} \\ &= e_{11} \cos \theta \frac{\partial \theta}{\partial z} \vec{E} \sin \theta + e_{33} \sin \theta \cos \theta \frac{\partial \theta}{\partial z} \vec{E} \\ &= (e_{11} + e_{33}) \sin \theta \cos \theta \frac{\partial \theta}{\partial z} \vec{E} \\ &= f_{flex}(\theta) \frac{\partial \theta}{\partial z} \frac{\partial \phi}{\partial z} \end{aligned}$$

(B.3)

where

$$f_{flex}(\theta) = (e_{11} + e_{33}) \sin \theta \cos \theta$$

and where we have used

$$E = \frac{\partial \phi}{\partial z}$$

Thus the Free Energy Density is given by

$$\Rightarrow f_z = \frac{1}{2} f_{elas}(\theta) \left(\frac{\partial \theta}{\partial z} \right)^2 - \frac{1}{2} f_{diel}(\theta) \left(\frac{\partial \phi}{\partial z} \right)^2 + f_{flex}(\theta) \frac{\partial \theta}{\partial z} \frac{\partial \phi}{\partial z}$$

(B.4)

(from equations (B.1) (B.2) and (B.3)).

[de Gennes & Prost] P.G. de Gennes and J. Prost, *The Physics of Liquid Crystals*, 2nd Ed, (Oxford, Clarendon Press, 1993).

Appendix C: Energy Minimising the Laplacian

C.1 Minimize f_z with respect to θ

$$f_z = \frac{1}{2} f_{elas}(\theta) \left(\frac{\partial \theta}{\partial z} \right)^2 - \frac{1}{2} f_{diel}(\theta) \left(\frac{\partial \phi}{\partial z} \right)^2 + f_{flex}(\theta) \frac{\partial \theta}{\partial z} \frac{\partial \phi}{\partial z} \quad (\text{B.6})$$

C.1.1 Elastic Energy Term:

using variational calculus

$$\frac{1}{2} \left(\frac{\partial f_{elas}(\theta)}{\partial \theta} \right) \left(\frac{\partial \theta}{\partial z} \right)^2 + f_{elas}(\theta) \frac{\partial \theta}{\partial z} \frac{\partial}{\partial z} \delta \theta$$

integrate 2nd term of RHS by parts

$$f_{elas}(\theta) \frac{\partial \theta}{\partial z} \delta \theta - \int \frac{\partial}{\partial z} \left(f_{elas}(\theta) \frac{\partial \theta}{\partial z} \right) \delta \theta$$

differentiating

$$- \frac{\partial}{\partial z} \left(f_{elas}(\theta) \frac{\partial \theta}{\partial z} \right)$$

resulting in:

$$\begin{aligned} &= \frac{1}{2} \frac{\partial f_{elas}(\theta)}{\partial \theta} \left(\frac{\partial \theta}{\partial z} \right)^2 - \frac{\partial f_{elas}(\theta)}{\partial z} \frac{\partial \theta}{\partial z} - f_{elas}(\theta) \frac{\partial^2 \theta}{\partial z^2} \\ &= \frac{1}{2} \frac{\partial f_{elas}(\theta)}{\partial \theta} \left(\frac{\partial \theta}{\partial z} \right)^2 - \frac{\partial f_{elas}(\theta)}{\partial \theta} \left(\frac{\partial \theta}{\partial z} \right)^2 - f_{elas}(\theta) \frac{\partial^2 \theta}{\partial z^2} \\ &= -\frac{1}{2} \frac{\partial f_{elas}(\theta)}{\partial \theta} \left(\frac{\partial \theta}{\partial z} \right)^2 - f_{elas}(\theta) \frac{\partial^2 \theta}{\partial z^2} \\ &= -\frac{1}{2} f'_{elas}(\theta) \left(\frac{\partial \theta}{\partial z} \right)^2 - f_{elas}(\theta) \frac{\partial^2 \theta}{\partial z^2} \end{aligned} \quad (\text{C.1})$$

This (last line) corresponds to the Euler-Lagrange equation, [Barbero]

C.1.2 Dielectric Energy Term:

$$\frac{\partial}{\partial \theta} \left(-\frac{1}{2} f_{diel}(\theta) \left(\frac{\partial \phi}{\partial z} \right)^2 \right) = -\frac{1}{2} \frac{\partial f_{diel}(\theta)}{\partial \theta} \left(\frac{\partial \phi}{\partial z} \right)^2 = -\frac{1}{2} f'_{diel}(\theta) \left(\frac{\partial \phi}{\partial z} \right)^2 \quad (C.2)$$

C.1.3 Flexoelectric Energy Term:

using variational calculus

$$\frac{\partial f_{flex}(\theta)}{\partial \theta} \frac{\partial \theta}{\partial z} \frac{\partial \phi}{\partial z} + f_{flex}(\theta) \frac{\partial \phi}{\partial z} \frac{\partial}{\partial z} \delta \theta$$

integrate the second term by parts

$$f_{flex}(\theta) \frac{\partial \phi}{\partial z} \delta \theta - \int \frac{\partial}{\partial z} \left(f_{flex}(\theta) \frac{\partial \phi}{\partial z} \right) \delta \theta$$

differentiating

$$-\frac{\partial}{\partial z} \left(f_{flex}(\theta) \frac{\partial \phi}{\partial z} \right)$$

resulting in:

$$\begin{aligned} & \frac{\partial f_{flex}(\theta)}{\partial \theta} \frac{\partial \theta}{\partial z} \frac{\partial \phi}{\partial z} - \frac{\partial f_{flex}(\theta)}{\partial z} \frac{\partial \phi}{\partial z} - f_{flex}(\theta) \frac{\partial^2 \phi}{\partial z^2} \\ &= \frac{\partial f_{flex}(\theta)}{\partial \theta} \frac{\partial \theta}{\partial z} \frac{\partial \phi}{\partial z} - \frac{\partial f_{flex}(\theta)}{\partial \theta} \frac{\partial \theta}{\partial z} \frac{\partial \phi}{\partial z} - f_{flex}(\theta) \frac{\partial^2 \phi}{\partial z^2} \\ &= -f_{flex}(\theta) \frac{\partial^2 \phi}{\partial z^2} \end{aligned} \quad (C.3)$$

f_z minimized with respect to θ becomes:

$$-\frac{1}{2} f'_{diel}(\theta) \left(\frac{\partial \phi}{\partial z} \right)^2 - \frac{1}{2} f'_{elas}(\theta) \left(\frac{\partial \theta}{\partial z} \right)^2 - f_{elas}(\theta) \frac{\partial^2 \theta}{\partial z^2} - f_{flex}(\theta) \frac{\partial^2 \phi}{\partial z^2} = 0 \quad (C.4)$$

C.2 Minimize f_z With Respect to ϕ

$$f_z = \frac{1}{2} f_{elas}(\theta) \left(\frac{\partial \theta}{\partial z} \right)^2 - \frac{1}{2} f_{diel}(\theta) \left(\frac{\partial \phi}{\partial z} \right)^2 + f_{flex}(\theta) \frac{\partial \theta}{\partial z} \frac{\partial \phi}{\partial z} \quad (B.6)$$

C.2.1 Dielectric Energy Term

using variational calculus

$$- f_{diel}(\theta) \frac{\partial \phi}{\partial z} \frac{\partial}{\partial z} \delta \phi$$

integrate by parts

$$- f_{diel}(\theta) \frac{\partial \phi}{\partial z} \delta \phi + \int \frac{\partial}{\partial z} \left(f_{diel}(\theta) \frac{\partial \phi}{\partial z} \right) \delta \phi$$

differentiating

$$\frac{\partial}{\partial z} \left(f_{diel}(\theta) \frac{\partial \phi}{\partial z} \right)$$

resulting in:

$$\frac{\partial f_{diel}(\theta)}{\partial \theta} \frac{\partial \theta}{dz} \frac{\partial \phi}{dz} + f_{diel}(\theta) \frac{\partial^2 \phi}{dz^2} \quad (C.5)$$

C.2.2 Flexoelectric Energy Term

using variational calculus

$$f_{flex}(\theta) \frac{\partial \theta}{\partial z} \frac{\partial}{\partial z} \delta \phi$$

integrate by parts

$$f_{flex}(\theta) \frac{\partial \theta}{\partial z} \delta \phi - \int \frac{\partial}{\partial z} \left(f_{flex}(\theta) \frac{\partial \theta}{\partial z} \right) \delta \phi$$

differentiate

$$-\frac{\partial}{\partial z} \left(f_{flex}(\theta) \frac{\partial \theta}{\partial z} \right) = -\frac{\partial f_{flex}(\theta)}{\partial \theta} \left(\frac{\partial \theta}{\partial z} \right)^2 - f_{flex}(\theta) \frac{\partial^2 \theta}{\partial z^2} \quad (C.6)$$

f_z Minimized With Respect to ϕ Becomes:

From equations (C.5) and (C.6) we get:

$$\frac{\partial f_{diel}(\theta)}{\partial \theta} \frac{\partial \phi}{\partial z} \frac{\partial \theta}{\partial z} + f_{diel}(\theta) \frac{\partial^2 \phi}{\partial z^2} - \frac{\partial f_{flex}(\theta)}{\partial \theta} \left(\frac{\partial \theta}{\partial z} \right)^2 - f_{flex}(\theta) \frac{\partial^2 \theta}{\partial z^2} = 0$$

which can be written as

$$\frac{\partial}{\partial z} \left(f_{diel}(\theta) \frac{\partial \phi}{\partial z} - f_{flex}(\theta) \frac{\partial \theta}{\partial z} \right) = 0$$

$$\therefore f_{diel}(\theta) \frac{\partial \phi}{\partial z} - f_{flex}(\theta) \frac{\partial \theta}{\partial z} = Const \quad (C.7)$$

[Barbero] G. Barbero and L. R. Evangelista, *An elementary course on the continuum theory for nematic liquid crystals*, (World Scientific, Singapore, 2001), p. 4 equation 1.13

Appendix D: Anchoring Energies

Anchoring Energy Terms

Minimizing the Functional (solution $\tilde{\theta}(z)$)

$$F[\theta(z)] = \int_0^D f[\theta(z), \theta'(z); z] dz$$

choose

$$\theta(z) = \tilde{\theta}(z) + \alpha \cdot v(z)$$

$$F[\theta(z)] = \int_0^D f[\tilde{\theta}(z) + \alpha \cdot v(z), \tilde{\theta}'(z) + \alpha \cdot v'(z); z] dz$$

$$\left\{ \frac{d}{d\alpha} \int_0^D f[\dots] dz \right\}_{\alpha=0} = 0$$

$$\Rightarrow \int_0^D \left[\frac{\partial f}{\partial \theta} \frac{\partial \theta}{\partial \alpha} + \frac{\partial f}{\partial \theta'} \frac{\partial \theta'}{\partial \alpha} \right]_{\alpha=0} dz = 0$$

$$\Rightarrow \int_0^D \left[\frac{\partial f}{\partial \tilde{\theta}} + \frac{d}{dz} \frac{\partial f}{\partial \tilde{\theta}'} \right] v(z) dz + \left[\frac{\partial f}{\partial \tilde{\theta}'} v(z) \right]_0^D = 0$$

bulk term

surface terms

Bulk Term

Euler-Lagrange equation

$$\frac{\partial f}{\partial \theta} + \frac{d}{dz} \frac{\partial f}{\partial \theta'} = 0$$

$$f = \frac{1}{2} f_{elas}(\theta) \left(\frac{\partial \theta}{\partial z} \right)^2 - \frac{1}{2} f_{diel}(\theta) \left(\frac{\partial \phi}{\partial z} \right)^2 + f_{flex}(\theta) \left(\frac{\partial \theta}{\partial z} \right) \left(\frac{\partial \phi}{\partial z} \right)$$

$$\frac{\partial f}{\partial \theta} = \frac{1}{2} f'_{elas}(\theta) \left(\frac{\partial \theta}{\partial z} \right)^2 - \frac{1}{2} f'_{diel}(\theta) \left(\frac{\partial \phi}{\partial z} \right)^2 + f'_{flex}(\theta) \left(\frac{\partial \theta}{\partial z} \right) \left(\frac{\partial \phi}{\partial z} \right)$$

$$\frac{\partial f}{\partial \theta'} = f_{elas}(\theta) \left(\frac{\partial \theta}{\partial z} \right) + f_{flex}(\theta) \left(\frac{\partial \phi}{\partial z} \right)$$

$$\frac{d}{dz} \frac{\partial f}{\partial \theta'} = f'_{elas}(\theta) \left(\frac{\partial \theta}{\partial z} \right)^2 + f_{elas}(\theta) \left(\frac{\partial^2 \theta}{\partial z^2} \right) + f'_{flex}(\theta) \left(\frac{\partial \theta}{\partial z} \right) \left(\frac{\partial \phi}{\partial z} \right) + f_{flex}(\theta) \left(\frac{\partial^2 \phi}{\partial z^2} \right)$$

$$\begin{aligned} \frac{\partial f}{\partial \theta} - \frac{d}{dz} \frac{\partial f}{\partial \theta'} &= -\frac{1}{2} f'_{elas}(\theta) \left(\frac{\partial \theta}{\partial z} \right)^2 - f_{elas}(\theta) \left(\frac{\partial^2 \theta}{\partial z^2} \right) - \frac{1}{2} f'_{flex}(\theta) \left(\frac{\partial \theta}{\partial z} \right) \left(\frac{\partial \phi}{\partial z} \right) - f_{flex}(\theta) \left(\frac{\partial^2 \phi}{\partial z^2} \right) = 0 \\ &= f'_{elas}(\theta) \left(\frac{\partial \theta}{\partial z} \right)^2 + 2f_{elas}(\theta) \left(\frac{\partial^2 \theta}{\partial z^2} \right) + f'_{flex}(\theta) \left(\frac{\partial \theta}{\partial z} \right) \left(\frac{\partial \phi}{\partial z} \right) + 2f_{flex}(\theta) \left(\frac{\partial^2 \phi}{\partial z^2} \right) = 0 \end{aligned}$$

Bulk Term

$$\frac{\partial f}{\partial \phi} - \frac{d}{dz} \frac{\partial f}{\partial \phi'} = 0$$

$$\frac{\partial f}{\partial \phi} = 0$$

$$\frac{\partial f}{\partial \phi'} = -f_{diel}(\theta) \frac{\partial \phi}{\partial z} + f_{flex}(\theta) \frac{\partial \theta}{\partial z}$$

$$\frac{d}{dz} \frac{\partial f}{\partial \phi'} = -f'_{diel}(\theta) \frac{\partial \theta}{\partial z} \frac{\partial \phi}{\partial z} - f_{diel}(\theta) \frac{\partial^2 \phi}{\partial z^2} + f'_{flex}(\theta) \left(\frac{\partial \theta}{\partial z} \right)^2 + f_{flex}(\theta) \frac{\partial^2 \theta}{\partial z^2}$$

$$\begin{aligned} \frac{\partial f}{\partial \phi} - \frac{d}{dz} \frac{\partial f}{\partial \phi'} &= f'_{diel}(\theta) \frac{\partial \theta}{\partial z} \frac{\partial \phi}{\partial z} + f_{diel}(\theta) \frac{\partial^2 \phi}{\partial z^2} - f'_{flex}(\theta) \left(\frac{\partial \theta}{\partial z} \right)^2 - f_{flex}(\theta) \frac{\partial^2 \theta}{\partial z^2} \\ &= \frac{d}{dz} \left[f_{diel}(\theta) \frac{\partial \phi}{\partial z} - f_{flex}(\theta) \frac{\partial \theta}{\partial z} \right] = 0 \end{aligned}$$

Surface Term

$$\begin{aligned} \left[\frac{dF}{d\alpha} \right]_{\alpha=0} &= \left\{ \frac{d}{d\alpha} \int_0^D f[\theta(z)\theta'(z); z] dz + \frac{df_{s_o}}{d\alpha} + \frac{df_{s_D}}{d\alpha} \right\}_{\alpha=0} \\ &= \left\{ \int_0^D \left[\frac{\partial f}{\partial \theta} - \frac{d}{dz} \frac{\partial f}{\partial \theta'} \right] v(z) dz \right\}_{\alpha=0} \\ &\quad + \left\{ \left[\frac{\partial f}{\partial \theta'} \right]_{z=D} + \frac{\partial f_{s_D}}{\partial \theta} \right\}_{\alpha=0} v(D) \\ &\quad + \left\{ \left[-\frac{\partial f}{\partial \theta'} \right]_{z=0} + \frac{\partial f_{s_o}}{\partial \theta} \right\}_{\alpha=0} v(D) \end{aligned}$$

Case 1 \int_{0-hg}^{D-ht} Takahashi [Jpn. J. Appl. Phys. 37, 1865 (1998)]

$$-\left. \frac{\partial f}{\partial \theta'} \right|_{z=0} + \left. \frac{\partial f_{s_0}}{\partial \theta} \right|_{z=0} = 0$$

hg: $f_{s_0}(\theta) = \frac{1}{2} A_{\theta_0} \sin^2(\theta_0 - \theta_{0_{easy}})$

$$-f_{elas}(\theta_0) \left. \frac{\partial \theta}{\partial z} \right|_{z=0} - f_{flex}(\theta_0) \left. \frac{\partial \phi}{\partial z} \right|_{z=0} + \frac{1}{2} A_{\theta_0} \sin^2(\theta_0 - \theta_{0_{easy}}) = 0$$

$$\left. \frac{\partial f}{\partial \theta'} \right|_{z=D} + \left. \frac{\partial f_{s_D}}{\partial \theta} \right|_{z=D} = 0$$

ht: $f_{s_D}(\theta) = \frac{1}{2} A_{\theta_D} \sin^2(\theta_D - \theta_{D_{easy}})$

$$f_{elas}(\theta_D) \left. \frac{\partial \theta}{\partial z} \right|_{z=D} + f_{flex}(\theta_D) \left. \frac{\partial \phi}{\partial z} \right|_{z=D} + \frac{1}{2} A_{\theta_D} \sin^2(\theta_D - \theta_{D_{easy}}) = 0$$

Case 2 $\int_{D-ht \neq 0}^{0-hg \neq D}$ Theory

homeotropic surface (ht):
$$\left. \frac{\partial f}{\partial \theta'} \right|_{z=D} + \left. \frac{\partial f_{s_D}}{\partial \theta} \right|_{z=D} = 0$$

homogeneous surface (hg):
$$-\left. \frac{\partial f}{\partial \theta'} \right|_{z=0} + \left. \frac{\partial f_{s_0}}{\partial \theta} \right|_{z=0} = 0$$

\Rightarrow same boundary conditions as Takahashi

but

	Takahashi	Theory
Hg	0	D
Ht	D	0

Appendix E: Self Consistent Method

The self consistent method [T. Takahashi, S. Hashidate, H. Nishijou, M. Kimura and T. Akahane, Jpn. J. Appl. Phys. **37**, 1865 (1998)] used

$$\frac{\partial \phi}{\partial z} = \frac{f_{flex}(\theta)}{f_{diel}(\theta)} \frac{\partial \theta}{\partial z} - \left\{ \int_0^D \frac{f_{flex}(\theta)}{f_{diel}(\theta)} \frac{\partial \theta}{\partial z} dz - E \right\} / \left\{ f_{diel}(\theta) \int_0^D \frac{1}{f_{diel}(\theta)} dz \right\} \quad (E.1)$$

During the first iteration the electric field, E , is assumed to be constant across the cell. After the first iteration the function $\partial \phi / \partial z$ can be used in place of E . This cycle is repeated until successive θ and ϕ curves are the same as the θ and ϕ curves from the previous iteration.

In finite difference method equation (E.1) becomes:

$$\Delta \phi_{new} = \frac{f_{flex}(\theta)}{f_{diel}(\theta)} \Delta \theta - \left\{ \sum_{z=0}^D \frac{f_{flex}(\theta)}{f_{diel}(\theta)} \Delta \theta \cdot \Delta z - \Delta \phi_{old} \cdot \Delta z \right\} / \left\{ f_{diel}(\theta) \sum_{z=0}^D \frac{\Delta z}{f_{diel}(\theta)} \right\} \quad (E.2)$$

Initially the problem that we had with this method was that it was appearing to result in the 'wrong kind' of asymmetry of the transmittance curves. Because of this we examined the θ -curves that had resulted in the transmittance and what we observed was that, near the homogeneous alignment layer, the θ -curves would oscillate before reaching θ_{0easy} . This was alarming and cast doubt as to the validity of the solutions that this method found. Once we had obtained the relationship:

$$f_{diel}(\theta) \frac{\partial \phi}{\partial z} - f_{flex}(\theta) \frac{\partial \theta}{\partial z} = Const \quad (B.6)$$

we had a means by which to check if these solutions were valid by whether or not their θ and ϕ curves adhered to this constraint. We found that they did not. Instead we had to employ the method described in sections 1.2 and 1.3.

Appendix F: Infinite Anchoring Energies Case

What we also found is that if we use this form of the above equation:

$$f_{diel}(\theta) \frac{\partial \phi}{\partial z} - f_{flex}(\theta) \frac{\partial \theta}{\partial z} = Const \quad (B.6)$$

we are able to say that:

$$f_{diel}(\theta_0) \frac{\partial \phi}{\partial z} \Big|_{z=0} - f_{flex}(\theta_0) \frac{\partial \theta}{\partial z} \Big|_{z=0} = f_{diel}(\theta_D) \frac{\partial \phi}{\partial z} \Big|_{z=D} - f_{flex}(\theta_D) \frac{\partial \theta}{\partial z} \Big|_{z=D}$$

Recall equation (1.3)

$$f_{diel}(\theta) = \varepsilon_o (\Delta \varepsilon \sin^2(\theta) + \varepsilon_n), \quad (1.3)$$

where

$$\Delta \varepsilon = \varepsilon_p - \varepsilon_n, \quad (1.4)$$

and recalling equation (1.5)

$$f_{flex}(\theta) = (e_{11} + e_{33}) \cos(\theta) \sin(\theta), \quad (1.5)$$

$$\theta_0 = 90^\circ$$

$$\theta_D = 0^\circ$$

if

$$f_{flex}(\theta_0) = 0$$

$$f_{flex}(\theta_D) = 0$$

then

$$f_{diel}(\theta_0) = \varepsilon_o \varepsilon_p$$

$$f_{diel}(\theta_D) = \varepsilon_o \varepsilon_n$$

therefore

$$\begin{aligned}
 f_{diel}(\theta_0) \frac{\partial \phi}{\partial z} \Big|_{z=0} &= f_{diel}(\theta_D) \frac{\partial \phi}{\partial z} \Big|_{z=D} \\
 \epsilon_0 \epsilon_p \frac{\partial \phi}{\partial z} \Big|_{z=0} &= \epsilon_0 \epsilon_n \frac{\partial \phi}{\partial z} \Big|_{z=D} \\
 \frac{\partial \phi}{\partial z} \Big|_{z=0} &= \frac{\epsilon_n}{\epsilon_p} \frac{\partial \phi}{\partial z} \Big|_{z=D}
 \end{aligned}$$

The resulting transmittance curves were symmetric curves with a voltage offset due to the flexoelectric effect. The resulting curves were negligibly different from what we would see for the high anchoring energies case (e.g. see figure (1.4.15))

Appendix G: Takahashi's In-Plane Device Formalism

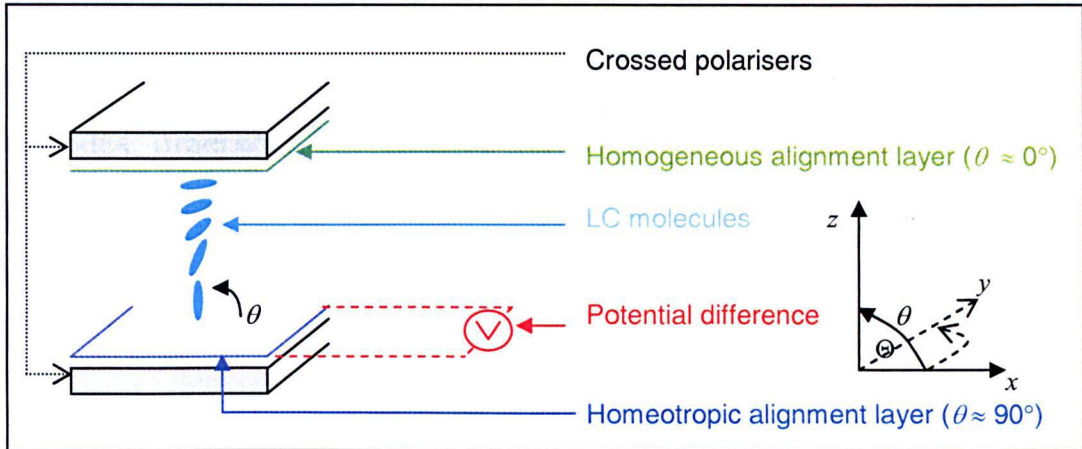


Figure F.1: Schematic of an in-plane HAN cell. The potential difference (red) is applied in the y -direction. The homeotropic (blue) and homogeneous (green) alignment layers impose a distortion in the director profile, which is depicted here as a change in the angle, θ , of the molecules (turquoise).

Takahashi et al. [Jpn. J. Appl. Phys. **37**, 1865 (1998)] assumed that the cell was invariant in the x - y plane. In their paper the in-plane device had applied the voltage *perpendicular* to the rubbing direction of the homogeneous alignment layer (see figure (F.1)). This is only appropriate when the molecular dipole moment is perpendicular to the molecular director (but in this case the electrical field would have little effect on the optical properties of the cell because it would not change the angle of orientation in the important z - x plane).

If, however, the molecular dipole is parallel to the director, then we would need to apply the voltage in the same direction as the rubbing direction. As most molecular dipole moments are at some other angle to the director, an electric field applied either parallel or perpendicular to the direction of the rubbed alignment layer would introduce an additional angular distortion (to that in the z - x plain), i.e. in the x - y plane. This would make the assumption of invariance in the x - y plain void.

Even in the *very* special cases described above (were we have oriented our electrodes parallel to the molecular dipole moments of the LC molecules at the homogeneous alignment layer), we would need to use vertical electrodes, otherwise our electric field lines would be curved. This would also make any assumptions about the systems x and y invariance invalid.

Appendix H: Relationship between Dipole Moments, Permittivities and Order Parameters

The order parameter, S , is given by

$$S = 1 - \frac{3}{2} \overline{\sin^2 \Theta}$$

where Θ is the angle of the director.

$$\frac{4}{3} \pi N a^3 = 1$$

with

$$N = N_L \rho / M$$

$$h = \frac{3\bar{\varepsilon}}{2\varepsilon + 1}, f = \frac{2\bar{\varepsilon} - 2}{2\varepsilon + 1} \frac{1}{a^3}$$

$$\bar{\varepsilon} = \frac{1}{3}(\varepsilon_1 + 2\varepsilon_2),$$

$$F = \frac{1}{1 - \bar{\alpha}f},$$

$$\bar{\alpha} = \frac{1}{3}(\alpha_1 + 2\alpha_q),$$

$$\overline{\mu_1^*} = \frac{\int_0^\pi \int_0^{2\pi} \int_0^{2\pi} (1 + \mu_z^* h F E_1 / kT) \mu_z^* W(\Theta) \sin(\Theta) d\vartheta d\vartheta' d\Theta}{\int_0^\pi \int_0^{2\pi} \int_0^{2\pi} (1 + \mu_z^* h F E_1 / kT) W(\Theta) \sin(\Theta) d\vartheta d\vartheta' d\Theta} \quad (8)$$

$$\overline{\mu_2^*} = \frac{\int_0^\pi \int_0^{2\pi} \int_0^{2\pi} (1 + \mu_x^* h F E_2 / kT) \mu_x^* W(\Theta) \sin(\Theta) d\vartheta d\vartheta' d\Theta}{\int_0^\pi \int_0^{2\pi} \int_0^{2\pi} (1 + \mu_x^* h F E_2 / kT) W(\Theta) \sin(\Theta) d\vartheta d\vartheta' d\Theta} \quad (9)$$

with

$$\mu_z^* = \mu^* [\cos \beta \cos \Theta + \sin \beta \sin \vartheta \sin \Theta]$$

and

$$\mu_x^* = \mu^* [\cos \beta \sin \vartheta' \sin \Theta + \sin \beta (\cos \vartheta \cos \vartheta' - \sin \vartheta \sin \vartheta' \cos \Theta)]$$

$$\begin{aligned} \mu_1^* &= \frac{\mu^*}{2kT} [2 \cos^2 \beta (1 - \overline{\sin^2 \Theta}) + \sin^2 \beta (1 - \overline{\sin^2 \Theta})] hF^2 E_1 \\ &= \frac{\mu^*}{3kT} [1 - (1 - 3 \cos^2 \beta) S] hF^2 E_1 \end{aligned} \quad (10 \text{ a \& b})$$

$$\begin{aligned} \mu_2^* &= \frac{\mu^*}{2kT} [\cos^2 \beta \overline{\sin^2 \Theta} + \sin^2 \beta (1 - \frac{1}{2} \overline{\sin^2 \Theta})] hF^2 E_2 \\ &= \frac{\mu^*}{3kT} [1 + \frac{1}{2} (1 - 3 \cos^2 \beta) S] hF^2 E_2 \end{aligned} \quad (11 \text{ a \& b})$$

$$\mu_l = \mu \cos \beta$$

$$\mu_q = \mu \sin \beta$$

$$\overline{\mu_1^*} = \left[\frac{\mu_l^2}{kT} \overline{\cos^2 \Theta} + \frac{\mu_q^2}{2kT} \overline{\sin^2 \Theta} \right] hF^2 E_1 \quad (10c)$$

$$\overline{\mu_2^*} = \left[\frac{\mu_l^2}{2kT} \overline{\sin^2 \Theta} + \frac{\mu_q^2}{2kT} \left(1 - \frac{1}{2} \overline{\sin^2 \Theta} \right) \right] hF^2 E_2 \quad (11c)$$

from (10b) and (11b) we get

$$\overline{\mu_1^*} = \left[\frac{\mu^2}{3kT} (1 - S) + \frac{\mu_l^2}{kT} S \right] hF^2 E \quad (10d)$$

$$\overline{\mu_2^*} = \left[\frac{\mu^2}{3kT} (1 - S) + \frac{\mu_q^2}{2kT} S \right] hF^2 E \quad (11d)$$

$$(\varepsilon_1 - 1) / 4\pi$$

&

$$(\varepsilon_2 - 1) / 4\pi$$

$$\frac{\varepsilon_1 - 1}{4\pi} = NhF \left\{ \bar{\alpha} + \frac{2}{3} \Delta\alpha S + F \frac{\mu^2}{3kT} \left[1 + (1 - \cos^2 \beta) S \right] \right\} \quad (12)$$

$$\frac{\varepsilon_2 - 1}{4\pi} = NhF \left\{ \bar{\alpha} + \frac{1}{3} \Delta\alpha S + F \frac{\mu^2}{3kT} \left[1 + \frac{1}{2} (1 - 3 \cos^2 \beta) S \right] \right\} \quad (13)$$

$$\Delta\varepsilon \equiv \varepsilon_1 - \varepsilon_2$$

$$\frac{\Delta\varepsilon}{4\pi} = NhF \left[\Delta\alpha - F \frac{\mu^2}{2kT} (1 - 3 \cos^2 \beta) \right] S$$

therefore

$$\Delta\varepsilon \propto S$$

$$\propto \text{const} - \mu^2$$

$$\propto (\text{const} - \mu^2) S$$

$$h = \frac{3\bar{\varepsilon}}{2\bar{\varepsilon} + 1}, f = \frac{2\bar{\varepsilon} - 2}{2\bar{\varepsilon} + 1} \frac{4\pi}{3} N_L \frac{\rho}{M}, F = \frac{1}{1 - \alpha f},$$

$$\bar{\varepsilon} = \frac{1}{3} (\varepsilon_1 + 2\varepsilon_2), \bar{\alpha} = \frac{1}{3} (\alpha_l + 2\alpha_q)$$

$$\frac{\varepsilon_{is} - 1}{4\pi} = NhF \left[\bar{\alpha} - F \frac{\mu^2}{3kT} \right]$$

$$\frac{\varepsilon_1 - 1}{4\pi} = NhF \left[\alpha_l - \frac{\mu_l^2}{kT} F \right]$$

$$\frac{\varepsilon_{is} - 1}{4\pi} = NhF \left[\alpha_q - \frac{\mu_q^2}{2kT} F \right]$$

Appendix I: Parameters used in Normalization of
Experimental Data for HAN Cells

$$Y = \frac{(A-a) + (B-b)x + (C-c)x^2 + (D-d)x^3 + (E-e)x^4 + (F-f)x^5 + (G-g)x^6 + (H-h)x^7 \dots}{(y - (a+bx+cx^2+dx^3+ex^4+fx^5+gx^6+hx^7 \dots))}$$

MBBA	JHW172	JHW131	JHW33	JHW29	E7	
0.771932812	2.508427685	2.75865031	2.10661747	3.48767295	1.18820557	<i>A</i>
0.027386267	-2.292687	0.488440964	0.357079897	0.049836325	0.226732364	<i>a</i>
-0.038825521	-0.001102198	0.026086536	-0.003978814	0.030679788	0.001955619	<i>B</i>
-0.006930798	-0.076131202	0.004771741	0.0008422	-0.006949422	-0.002172762	<i>b</i>
-0.008580729	0.111663961	0.110687268	0.24012602	0.0859408	0.318279935	<i>C</i>
0.014444075	-0.002034721	-0.048772622	-0.08155093	-0.010669864	-0.066246348	<i>c</i>
0.005273438	-0.03922429	0	0.008730235	0.032815203	-0.0006812	<i>D</i>
0.002969457	0.0681776	0	0.001364974	-0.000562833	0.003417352	<i>d</i>
0	0.058363411	0	0	0	0.041626475	<i>E</i>
0	-0.0202247	0	0	0	-0.002732431	<i>e</i>
0	-0.002730797	0	0	0	0	<i>H</i>
0	-0.013578325	0	0	0	0	<i>h</i>
0	-0.002174334	0	0	0	0	<i>I</i>
0	0	0	0	0	0	<i>i</i>

Appendix J: ANSI C Code Used to Solve PDEs

Commented out details have been included in a grey font, as they may be of interest to some. These also include typical input parameters for MBBA and E7 systems.

```
/* TO COMPILE:          cc -Aa CUTUP.c -o CUTUP -lm
   TO RUN:              CUT_UP
```

THIS PROGRAM'S MAIN FUNCTION IS TO CALCULATE THE TRANSMITTANCE vs APPLIED VOLTAGE CURVE FOR A GIVEN HAN CELL THIS DATA IS OUTPUTTED IN THE FILE "EandTrans.x"

HOWEVER, THE TRANSMITTANCE CURVES ARE DIFFICULT TO INTERPRET ON THEIR OWN SO ALSO INCLUDED IS THE PHASE DIFFERENCE vs APPLIED VOLTAGE CURVE THIS DATA IS OUTPUTTED IN THE FILE "EandPhase.x"

TO BE SMOOTH CURVES BOTH THESE FILES NEED A LARGE NUMBER OF POINTS TO BE PLOTTED ie recommended $kmax > 100$

other useful information can be gained from examining the director profiles and potentials across the cell for different voltages. this data is outputted in the files "Theta.x" and "Phi.x" respectively. The number of sets outputted in each of these files is $kmax$; Xmgr can read a maximum of 30 sets into any one graph so we recommend that $kmax$ is changed so that it is < 30 .

THE VALUES $dPhiRange$ & $PhiMin$ ARE VERY IMPORTANT. The program DOES NOT know in advance what the applied voltage across the cell is. If their values result in any DPHI falling outside "some range" (roughly $\pm 10V$) then the program will never finish running.

intervals that have been tried and have generally worked:

```
double      dPhiRange=1.5e-01, PhiMin=-3.0e-02; RECOMMENDED FOR MOST USES
double      dPhiRange=0.15e-01, PhiMin=-0.5e-02; BETTER IF YOU WANT TO FIND CENTRAL MINIMUM
ACCURATELY
double      dPhiRange=1.3e-01, PhiMin=-3.5e-02;
double      dPhiRange=0.5e-01, PhiMin=-1.5e-02;
** THESE VALUES WILL PROBABLY NEED TO BE CHANGED IF YOU CHANGE THE VALUE OF npoints **
```

DEFAULT SETTINGS FOR E7: (KEVIN BARTLE)

```
double      lambda      =      633E-9;          WAVELENGTH OF LIGHT in metres
double      epsilonO =      8.854e-12;          permitivity of free space
double      kmax         =      200;            NUMBER OF POINTS on the transmittance
vs Applied voltage curve
double      D            =      30.2e-6;        CELL THICKNESS in metres
double      ybegin       =      90.0;           Theta0 (in Degrees)
double      yend         =      2.0;           ThetaEND (in Degrees)
double      K11          =      11.1E-12;        SPLAY ELASTIC CONST
double      K33          =      17.1E-12;        BEND ELASTIC CONST
double      A_0          =      1e-4;           Anchoring energy at z = 0
double      A_d          =      5e-2;           Anchoring energy at z = D
double      e44          =      -5e-11;         flexoelectric constant e11 + e33
double      nO           =      1.51821;        ordinary refractive index
double      nE           =      1.73283;        extraordinary refractive index
double      epsilonN =      5.2;               Normal Permittivity
double      epsilonP =      19.0;              Parallel Permittivity
```

DEFAULT SETTINGS FOR MBBA: (TAKAHASHI)

```
double      lambda      =      550E-9;
```

```

double    epsilonO    =    8.854e-12;
double    kmax        =    200;
double    D           =    28.5e-6;
double    ybegin     =    90.0;
double    yend       =    2.0;
double    K11        =    6.4E-12;
double    K33        =    8.2E-12;
double    A_0        =    1.2e-5;
double    A_d        =    5e-2;
double    e44        =    -5e-11;
double    nO         =    1.57;
double    nE         =    1.80;
double    epsilonN   =    5.4;
double    epsilonP   =    4.7;

```

```

double    D           =    28.5e-6;
double    ybegin     =    90.0;
double    yend       =    2.0;
double    K11        =    6.4E-12;
double    K33        =    8.2E-12;
double    A_0        =    1.2e-5;
double    A_d        =    5e-2;
double    e44        =    -5e-11;
double    nO         =    1.57;
double    nE         =    1.80;
double    epsilonN   =    5.4;
double    epsilonP   =    4.7;
double    dPhiRange  =    1.15e-01;
double    PhiMin     =    -2.6e-02;
double    kmax       =    300;

```

*/

```
#define    npoints    200
```

```
#include <math.h>
```

```
#include <stdio.h>
```

```
#include <stdlib.h>
```

```

double    lambda     =    633E-9;
double    epsilonO   =    8.854e-12;
double    D          =    30.2e-6;
double    ybegin     =    90.0;
double    yend       =    2.0;
double    K11        =    11.1E-12;
double    K33        =    17.1E-12;
double    A_0        =    1e-4;
double    A_d        =    5e-2;
double    e44        =    -5e-11;
double    nO         =    1.51821;
double    nE         =    1.73283;
double    epsilonN   =    5.2;
double    epsilonP   =    19.0;
double    kmax       =    198;

```

```
/*make sure kmax is a multiple of 11*/
```

```
/*double dPhiRange = 1.20e-01;
```

```
double PhiMin = -3.0e-02; */
```

```
double    dPhiRange  =    0.60e-01;
```

```
double    PhiMin     =    -1.0e-02;
```

```
double fe(double THETA);
```

```
double fd(double THETA);
```

```
double fde(double THETA);
```

```
double fdd(double THETA);
```

```
double ff(double THETA);
```

```
double fdf(double THETA);
```

```

main(void)
{
/*int      i, j, S, Snew, r, T, Tnew, k, l=1, lmax, kmaxint=kmax/30; */
int      i, j, S, Snew, r, T, Tnew, k, l=1, lmax, kmaxint=kmax/11;
double   x, dx, m, n, p, q, pi = 3.1415927;
double   D2Phi, A, B, C, J, L, M, N, P;
double   Npoints = npoints * 1.0, l;
double   Psi, dTheta0, Dthetad, NablaThetad, BOB_0, BOB_d;
double   DeltaEpsilon = epsilonP-epsilonN, NablaTheta0;
double   V, Dz = D/(Npoints), Dphase, ploppy;
double   R = (nE*nE-nO*nO)/(nE*nE);
double   Phi[npoints+1], Integrand[npoints+1], dPhi[npoints], dtheta[npoints];
double   ENERGY, FF, FE, FDE, FD, FDD, Theta0; /* where      FF=f_flex(theta)
                                                                FD=f_diel(theta)
                                                                FE=f_elas(theta)
                                                                FDD=f'_diel(theta)
                                                                FDE=f'_elas(theta) */

/*double   dPhiRange=1.3e-01, PhiMin=-3.5e-02;*/
double   E, DPHI, CONST, con, dE, Erange=0.2;
typedef struct {
    double a, b, c, d, e, f;
}Output;

typedef struct {
    double a, b;
}output;

output   *theta, *theta_start;
Output   *Trans, *Trans_start;
FILE     *fp, *fp2, *fp1, *fp3, *fp4;
if ((fp1 = fopen("Theta.x", "w"))==NULL)
    {
    printf("Cannot Create Output File");
    exit(1);
    }
if ((fp = fopen("EandTrans.x", "w"))==NULL)
    {
    printf("Cannot Create Output File");
    exit(1);
    }
if ((fp2 = fopen("EandPhase.x", "w"))==NULL)
    {
    printf("Cannot Create Output File");
    exit(1);
    }
if ((fp3 = fopen("Phi.x", "w"))==NULL)
    {
    printf("Cannot Create Output File");
    exit(1);
    }
if ((fp4 = fopen("EandDPhase.x", "w"))==NULL)
    {
    printf("Cannot Create Output File");
    exit(1);
    }
Trans_start = (Output *)calloc(kmax, sizeof(Output));
if (!Trans_start)
    {
    printf ("ALLOCATION ERROR - ABORTING. \n");
    exit(1);
    }
theta_start = (output *)calloc(npoints+1, sizeof(output));

```

```

if (!theta_start)
    {
    printf ("ALLOCATION ERROR - ABORTING. \n");
    exit(1);
    }
CONST=0;
/*LOOP 1*/ for(k=0 ; k< kmax; k++)
    {
    T=+1;
    Theta0=ybegin*pi/180;
    dTheta0=pi/180;
    Phi[0]=0.0;
    DPHI= dPhiRange/(2.0*kmax*1.0);
    Phi[1]=PhiMin+k*DPHI;
    dtheta[0]=-ff(Theta0)*Phi[1]/fe(Theta0);
    Trans=Trans_start;
    theta=theta_start;
/*LOOP 2*/ while (T!= 0)
    {
    theta[0].a = 0.0*Dz;
    theta[0].b = Theta0;
    theta[1].a = 1.0*Dz;
    dtheta[0]=(0.5*Dz*A_0*sin(2*(Theta0-ybegin*pi/180))-
ff(Theta0)*Phi[1])/fe(Theta0);
    theta[1].b = Theta0+dtheta[0];
    CONST = (fd(theta[0].b) * (Phi[1]-Phi[0]) - ff(theta[0].b) * (theta[1].b-
theta[0].b))/Dz;
    for(i=1 ; i<npoints ; i++)
        {
        theta[i].a = i*Dz;
        /* modified version */
        FF=(ff(theta[i-1].b)+ff(theta[i].b))/2;
        FE=(fe(theta[i-1].b)+fe(theta[i].b))/2;
        FD=(fd(theta[i-1].b)+fd(theta[i].b))/2;
        FDD=(fdd(theta[i-1].b)+fdd(theta[i].b))/2;
        FDE=(fde(theta[i-1].b)+fde(theta[i].b))/2;
        dPhi[i-1] = Phi[i] - Phi[i-1];
        dtheta[i-1] = theta[i].b - theta[i-1].b;
        L=CONST*Dz/FD;
        M=FF/(2*FE*FD);
        N=FDE*dtheta[i-1]*dtheta[i-1]+FDD*dPhi[i-1]*dPhi[i-1]-
2*FF*(Phi[i]+dPhi[i-1]);
        P=FF*dtheta[i-1]/FD;
        Phi[i+1]=(L-M*N+P+Phi[i])*FE*FD/(FE*FD+FF*FF);
        D2Phi=Phi[i+1]-2*Phi[i]+Phi[i-1];
        theta[i+1].b=- (FDE*dtheta[i-1]*dtheta[i-1]+FDD*dPhi[i-1]*dPhi[i-
1]+2*FF*D2Phi)/(2*FE)+theta[i].b+dtheta[i-1];
        }
    dPhi[npoints-1] = Phi[npoints] - Phi[npoints-1];
    dtheta[npoints-1] = theta[npoints].b - theta[npoints-1].b;
    Dthetaad=theta[npoints].b-yend*pi/180;
    NablaThetad=0.5*A_d*sin(2*Dthetaad);
    dtheta[0]=theta[0].b-ybegin*pi/180;
    NablaTheta0=0.5*A_0*sin(2*dtheta[0]);
    BOB_d=fe(theta[npoints].b)*(theta[npoints].b-theta[npoints-1].b)/Dz
    +ff(theta[npoints].b)*(Phi[npoints]+Phi[npoints-1])/Dz+NablaThetad;
    BOB_0=fe(theta[0].b)*(theta[1].b-theta[0].b)/Dz
    +ff(theta[0].b)*(Phi[1]+ Phi[0])/Dz-NablaTheta0;
    if (theta[npoints].b*180/pi <(yend-60)) Tnew = +1;
    else if (theta[npoints].b*180/pi > (yend+60)) Tnew = -1;

```

```

else {
    if (BOB_d<-1e-9) Tnew = +1;
    else if (BOB_d>1e-9) Tnew = -1;
    else Tnew = 0;
}
if (T*Tnew > 0) dTheta0=dTheta0 ;
else if (T*Tnew < 0) dTheta0 = dTheta0/2.0;
else dTheta0 = 0;
Theta0 =Theta0 +Tnew*dTheta0 ;
T=Tnew;
}
/*END LOP 2 HERE*/
/*Need to put something in here that means that i only write to file every so often... so that i end up with 30 sets of
data for phi and theta (each)*/
/*if k = kmax/30 * 1, 2, 3 ... 30 do the following otherwise skip
for(k=0; k = kmaxint*n; n++)
    printf( "kmaxint=%d\n",kmaxint);
    printf( "k=%d\n",k);
*/
    if (k==kmaxint*(l-1))
    {
        fprintf(fp1, "@TYPE xy\n");
        for (i=0 ; i<npoints ; i++)
        {
            fprintf( fp1, "\t%g \t%g\n", theta[i].a, (theta[i].b*180/pi));
        }
        fprintf(fp1, "&\n");
        fprintf(fp3, "@TYPE xy\n");
        for (i=0 ; i<npoints ; i++)
        {
            fprintf( fp3, "\t%g \t%g\n", theta[i].a, Phi[i]);
        }
        fprintf(fp3, "&\n");
        /*
        printf( "l=%d\n",l);
        printf( "kmaxint*(l-1)=%d\n",k);
*/
        l++;
    }
/*CHECK THAT E FIELD IS CONSISTANT WITH APPLIED VOLTAGE*/
Psi=(e44/(2*DeltaEpsilon*epsilonO))*log(fd(theta[npoints].b)/fd(theta[0].b));
/*V=Phi[npoints]-Psi;*/
V=Phi[npoints];
/* how do i re adjust voltages so that they go from -v/2 tp +v/2 instead of 0 to v?
is it possible to avoid having to do this?... i'm thinking no.
ie can we define the charge densities in term of an absolute rather than a arbitrary value*/
ploppy=0.0;
/*CALCULATE TRANSMITTANCE*/
for (i=0 ; i<npoints ; i++)
{
    Integrand[i]=(1/(sqrt(1.0-R*(sin(pi/2-theta[i].b)*sin(pi/2-theta[i].b)))))-1.0;
    ploppy += Integrand[i];
}
Dphase = (2.0*pi*nO*ploppy*Dz)/lambda;
l = (1.0 - cos(Dphase))/2.0;

Trans[k].a = V;
/*Trans[k].b = Psi;*/
Trans[k].b = l;
Trans[k].c = Dphase;

```

```

Trans[k].d = ENERGY;

/*printf("k = %3d, BOBo =%16.10f, BOBd =%16.10f \t", k, BOB_0, BOB_d);
printf("k = %3d, \t", k);
printf("Theta0 = %18.13f, Thetad = %18.13f, dTheta0 = %18.13f, dThetad = %18.13f, dPhi0 =
%4.2e, dPhid = %18.13e, Voltage = %f\n", (theta[0].b)*180/pi, (theta[npoints].b)*180/pi, (dtheta[0])*180/pi,
(dtheta[npoints-1])*180/pi, dPhi[0], dPhi[npoints-1], Phi[npoints]); */
}
/*END OF LOOP 1*/

/*SEPARATED DATA SETS*/
fprintf(fp, "@TYPE xy\n");
fprintf(fp2, "@TYPE xy\n");
fprintf(fp4, "@TYPE xy\n");
for(k=0 ; k<kmax ; k++) fprintf(fp, "%18.13g %18.13g\n", Trans[k].a, Trans[k].b);
for(k=0 ; k<kmax ; k++) fprintf(fp2, "%18.13g %18.13g\n", Trans[k].a, Trans[k].c/(pi));
for(k=0 ; k<(kmax-1) ; k++) fprintf(fp4, "%18.13g %18.13g\n", (Trans[k+1].a+Trans[k].a)/2, (Trans[k+1].c-
Trans[k].c)/((Trans[k+1].a-Trans[k].a)*pi));
fclose(fp1);
fclose(fp);
fclose(fp2);
fclose(fp3);
fclose(fp4);
free(Trans_start);
free(theta_start);
printf("%c",7);
}
double fe(double THETA)
{
return K11*cos(THETA)*cos(THETA)+K33*sin(THETA)*sin(THETA);
}
double fd(double THETA)
{
double DeltaEpsilon, poop;
DeltaEpsilon = epsilonP-epsilonN;
poop=epsilonO*(DeltaEpsilon*sin(THETA)*sin(THETA)+epsilonN);
return poop;
}
double fde(double THETA)
{
return (K33-K11)*sin(2*THETA);
}
double fdd(double THETA)
{
double DeltaEpsilon;
DeltaEpsilon = epsilonP-epsilonN;
return 2*epsilonO*DeltaEpsilon*sin(THETA)*cos(THETA);
}
double ff(double THETA)
{
return e44*sin(THETA)*cos(THETA);
}
double fdf(double THETA)
{
return e44*cos(2*THETA);
}

```

Appendix K: The Equimolar Surface

For an arbitrary choice of dividing surface, the following equation from thermodynamics is true:

$$dE = TdS + \sum_i \mu_i dm_i - P^\alpha dV^\alpha - P^\beta dV^\beta + \sigma dA + C_1 dc_1 + C_2 dc_2$$

where c_1 and c_2 denote the two curvatures describing the surface (reciprocal of the radii of curvature) and C_1 and C_2 are constants. This can be rewritten as:

$$dE = TdS + \sum_i \mu_i dm_i - P^\alpha dV^\alpha - P^\beta dV^\beta + \sigma dA + \frac{1}{2}(C_1 + C_2)d(c_1 + c_2) + \frac{1}{2}(C_1 - C_2)d(c_1 - c_2) \quad (\text{K.1})$$

We choose the dividing surface such that $C_1 + C_2 = 0$ and for flat or spherical surfaces $d(c_1 - c_2) = 0$. Thus equation (K.1) simplifies to

$$dE = TdS + \sum_i \mu_i dm_i - P^\alpha dV^\alpha - P^\beta dV^\beta + \sigma dA$$

This is true for the Gibbs surface [Adamson]. The Gibbs surface is given by:

$$r_e^3 = \frac{1}{\rho_g - \rho_l} \int_0^\infty \frac{d\rho(r)}{dr} r^3 dr$$

What has been found in previous research is that the following function (equation (K.2)) shows very high correlation to the shape of the density profile obtained from computer simulations [Adamson]

$$\rho(r) = \frac{1}{2}(\rho_l + \rho_g) - \frac{1}{2}(\rho_l - \rho_g) \tanh \frac{2(r-r_0)}{d_s} \quad (\text{K.2})$$

where ρ_l and ρ_g are the fluid densities in the liquid and the gas phases respectively, $\rho(r)$ is the fluid's density at a given radius r , r_0 is an estimate for the droplet's radius (typically quite close to the Gibbs surface) and d_s is a measure of the surface thickness. Given that the curve fit has rotational symmetry at r_0 it is fair to say that this is the equimolar surface.

[Adamson] A. W. Adamson, *Chemistry of Surfaces* 3rd Edition, Wiley New York (1976)

Appendix L: Exponential Regression on Temperature versus Surface Tensions Graph

The regressions in figure 2.8 were performed by XMGR and were used as a guide to the eye. These regression data from XMGR for the droplets are shown below.

4,000 droplet

Regression of set 0 results to set 6

Number of observations	=	13
Mean of independent variable	=	63.84615
Mean of dependent variable	=	-3.098821
Standard dev. of ind. variable	=	22.14101
Standard dev. of dep. variable	=	0.4781439
Correlation coefficient	=	-0.7108349
Regression coefficient (SLOPE)	=	-0.01535076
Standard error of coefficient	=	0.00457975
t - value for coefficient	=	-3.351877
Regression constant (INTERCEPT)	=	-2.118734
Standard error of constant	=	0.3082021
t - value for constant	=	-6.874496

Analysis of variance

Source	d.f	Sum of squares	Mean Square	F
Regression	1	1.386232	1.386232	11.23508
Residual	11	1.357227	0.1233843	
Total	12	2.743459		

2,000 droplet

Regression of set 1 results to set 7

Number of observations	= 6
Mean of independent variable	= 45
Mean of dependent variable	= -3.283744
Standard dev. of ind. variable	= 18.70829
Standard dev. of dep. variable	= 0.5862105
Correlation coefficient	= -0.992287
Regression coefficient (SLOPE)	= -0.03109259
Standard error of coefficient	= 0.001942123
t - value for coefficient	= -16.00959
Regression constant (INTERCEPT)	= -1.884578
Standard error of constant	= 0.09347782
t - value for constant	= -20.16069

Analysis of variance

Source	d.f	Sum of squares	Mean Square	F
Regression	1	1.691811	1.691811	256.3069
Residual	4	0.0264029	0.006600725	
Total	5	1.718214		

1,000 droplet

Regression of set 2 results to set 8

Number of observations	= 6
Mean of independent variable	= 45
Mean of dependent variable	= -3.52831
Standard dev. of ind. variable	= 18.70829
Standard dev. of dep. variable	= 0.5644585
Correlation coefficient	= -0.980157
Regression coefficient (SLOPE)	= -0.02957288
Standard error of coefficient	= 0.002990348
t - value for coefficient	= -9.889444
Regression constant (INTERCEPT)	= -2.197531
Standard error of constant	= 0.1439307
t - value for constant	= -15.26797

Analysis of variance

Source	d.f	Sum of squares	Mean Square	F
Regression	1	1.530472	1.530472	97.8011
Residual	4	0.06259527	0.01564882	
Total	5	1.593067		

500 droplet

Regression of set 3 results to set 9

Number of observations	= 6
Mean of independent variable	= 45
Mean of dependent variable	= -4.060826
Standard dev. of ind. variable	= 18.70829
Standard dev. of dep. variable	= 0.8246918
Correlation coefficient	= -0.9738619
Regression coefficient (SLOPE)	= -0.04292942
Standard error of coefficient	= 0.005006368
t - value for coefficient	= -8.574963
Regression constant (INTERCEPT)	= -2.129002
Standard error of constant	= 0.2409653
t - value for constant	= -8.835305

Analysis of variance

Source	d.f	Sum of squares	Mean Square	F
Regression	1	3.225137	3.225137	73.53
Residual	4	0.175446	0.04386151	
Total	5	3.400583		

The data for the 4,000* curve has not been included as its value was qualitative rather than quantitative, i.e. it gave a curve fit that was visually pleasing but discounted numerous data points without more rigorous reasoning.

Appendix M: Ansi C Code Used on Cerius² Output Data, for 10 Data Sets per Droplet.

The form that a Cerius² output file takes does not appear to be restricted by concerns of conciseness, but outwardly is instead a quagmire of apparently superfluous formatting information. This makes it more difficult to extract the relevant data. However, as a general understanding of the idiosyncrasies of Cerius² files and C programming was not strictly relevant to the main body of the text, they have been included here instead for those with a specific interest in these areas. N.B. commented out details have been included in a lighter grey font as they may still be of interest to some.

```

/*
THIS IS A FURTHER ADDAPTATION TO THE PROGRAMS... THE IDEA BEING THIS
PROGRAM WILL DEAL WITH 10
INPUT FILES PRODUCE ALL THE OUT FILES AND ALSO CALCULATE THE AVERAGE
DATA CURVES.
THE ONLY PROBLEM THAT YOU NEED TO BE AWARE OF WITH THIS VERSION IS
THAT YOU NEED TO REEDIT THE
PROGRAM AND PUT IN THE NAMES OF THE NEW TEN INPUT FILES.... SORT THAT
ONE OUT NEXT TIME.
or you can copy the ten files you are looking at to Ar(1to10).msi
old blurb:
THIS PROGAM READS THE IMPUT MSI FILE (Ar.msi) CONVERTS INTO DATA IT CAN
USE, RESETS THE ORIGIN
AS THE CENTRE OF MASS, CALCULATES THE FORCES AND ENENERGIES OF/ON
EACH PARTICLE, ORDERS THE DATA
ACCORDING TO RADIAL DISTANCES FROM THE CENTRE OF MASS, AND THEN
CALCULATES THE AVERAGE OF THERE
FOR A GIVEN RADIAL REGION AND THEN OUTPUTS THIS DATA TO FILES
HisterE.DROP & HisterF.DROP
ps... this version now excludes 0 outputs in the Hister
files so a different version of adding.c will be needed
(not so for the same program on faraday and humus)*/
#define NI      60
#define ni      60.0
#include <math.h>
#include <stdio.h>
#include <stdlib.h>
#include <string.h>
double      sqr(double y);
double      twothesix(double x);
void main(void)
{
FILE          *in1, *in2, *in3, *in4, *in5, *in6, *in7, *in8, *in9, *in10;
FILE          *outE, *avE;
FILE          *outF, *avF;
char          c, string[100];
int           i = 0, j = 0, iMax, n = 13, counter, J[10][NI], K[NI];
double        MAXIMUM=6E-9, delta=(MAXIMUM/ni), pi=3.1415927;
double        x, y, z, xcm1 = 0, ycm1 = 0, zcm1 = 0, R, RSqrd, Radius, RadiusSqrd;
double        xcm2 = 0, ycm2 = 0, zcm2 = 0;
double        xcm3 = 0, ycm3 = 0, zcm3 = 0;
double        xcm4 = 0, ycm4 = 0, zcm4 = 0;
double        xcm5 = 0, ycm5 = 0, zcm5 = 0;
double        xcm6 = 0, ycm6 = 0, zcm6 = 0;

```

```

double      xcm7 = 0, ycm7 = 0, zcm7 = 0;
double      xcm8 = 0, ycm8 = 0, zcm8 = 0;
double      xcm9 = 0, ycm9 = 0, zcm9 = 0;
double      xcm10 = 0, ycm10 = 0, zcm10 = 0;
double      D, r, rm = 3.8680E-10,
            Av=6.022E+23, f1, e1, f2, e2, f3, e3, f4, e4, f5, e5, f6, e6, f7, e7, f8, e8,
f9, e9, f10, e10, R6, RM6,
            deltaradius, DeltaRadius,
            Rsq, Average;
double      temp1, temp2, temp3, temp4;
typedef struct {
    double X, Y, Z, R;
}coords;
coords      *cart1, *cart1_start;
coords      *cart2, *cart2_start;
coords      *cart3, *cart3_start;
coords      *cart4, *cart4_start;
coords      *cart5, *cart5_start;
coords      *cart6, *cart6_start;
coords      *cart7, *cart7_start;
coords      *cart8, *cart8_start;
coords      *cart9, *cart9_start;
coords      *cart10, *cart10_start;
typedef struct {
    double R, V;
}DATA;
DATA        *F1, *F1_start, *E1, *E1_start, *F2, *F2_start, *E2, *E2_start, *F3,
*F3_start, *E3, *E3_start;
DATA        *F4, *F4_start, *E4, *E4_start, *F5, *F5_start, *E5, *E5_start, *F6,
*F6_start, *E6, *E6_start;
DATA        *F7, *F7_start, *E7, *E7_start, *F8, *F8_start, *E8, *E8_start, *F9,
*F9_start, *E9, *E9_start, *F10, *F10_start, *E10, *E10_start;
DATA        *outDataE1, *outDataE1_start, *outDataF1, *outDataF1_start, *outDataE2,
*outDataE2_start, *outDataF2, *outDataF2_start;
DATA        *outDataE3, *outDataE3_start, *outDataF3, *outDataF3_start, *outDataE4,
*outDataE4_start, *outDataF4, *outDataF4_start;

```

```

DATA        *outDataE5, *outDataE5_start, *outDataF5, *outDataF5_start, *outDataE6,
*outDataE6_start, *outDataF6, *outDataF6_start;
DATA        *outDataE7, *outDataE7_start, *outDataF7, *outDataF7_start, *outDataE8,
*outDataE8_start, *outDataF8, *outDataF8_start;
DATA        *outDataE9, *outDataE9_start, *outDataF9, *outDataF9_start, *outDataE10,
*outDataE10_start, *outDataF10, *outDataF10_start;
DATA        *AVF, *AVF_start, *AVE, *AVE_start;
if ((in1 = fopen("Ar1.msi", "r"))==NULL) {
    printf("Unable to open input file");
    exit(1);
}
if ((in2 = fopen("Ar2.msi", "r"))==NULL) {
    printf("Unable to open input file");
    exit(1);
}
if ((in3 = fopen("Ar3.msi", "r"))==NULL) {
    printf("Unable to open input file");
    exit(1);
}
if ((in4 = fopen("Ar4.msi", "r"))==NULL) {
    printf("Unable to open input file");
    exit(1);
}
if ((in5 = fopen("Ar5.msi", "r"))==NULL) {
    printf("Unable to open input file");
    exit(1);
}
if ((in6 = fopen("Ar6.msi", "r"))==NULL) {
    printf("Unable to open input file");
    exit(1);
}
if ((in7 = fopen("Ar7.msi", "r"))==NULL) {
    printf("Unable to open input file");
    exit(1);
}
if ((in8 = fopen("Ar8.msi", "r"))==NULL) {

```

```

printf("Unable to open input file");
exit(1);
}
if ((in9 = fopen("Ar9.msi", "r"))==NULL) {
printf("Unable to open input file");
exit(1);
}
if ((in10 = fopen("Ar10.msi", "r"))==NULL) {
printf("Unable to open input file");
exit(1);
}
printf("Output files are called HisterE.DROP & HisterF.DROP and AverageE.DROP and
AverageF.DROP\n");
if ((outE=fopen("HisterE.DROP", "w"))==NULL) {
printf("Unable to open output file.\n");
exit(1);
}
if ((outF=fopen("HisterF.DROP", "w"))==NULL) {
printf("Unable to open output file.\n");
exit(1);
}
if ((avE=fopen("AverageE.DROP", "w"))==NULL) {
printf("Unable to open output file.\n");
exit(1);
}
if ((avF=fopen("AverageF.DROP", "w"))==NULL) {
printf("Unable to open output file.\n");
exit(1);
}
/*only need to do this once because all files should have the same number of particles
unless something has gone horribly wrong*/
while (!fgets(string, n, in1 )==0)
{
if (strcmp(string, " (A D XYZ (" )==0) i++;
};
iMax = i;

```

```

printf("iMax=%d\n", iMax);
D = 0.1850*4.186E+3*iMax/Av;
cart1_start = (coords *)calloc(iMax, sizeof(coords));
if (!cart1_start) {
printf ("ALLOCATION ERROR - ABORTING. \n");
exit(1);
} cart1=cart1_start;
cart2_start = (coords *)calloc(iMax, sizeof(coords));
if (!cart2_start) {
printf ("ALLOCATION ERROR - ABORTING. \n");

exit(1);
} cart2=cart2_start;
cart3_start = (coords *)calloc(iMax, sizeof(coords));
if (!cart3_start) {
printf ("ALLOCATION ERROR - ABORTING. \n");
exit(1);
} cart3=cart3_start;
cart4_start = (coords *)calloc(iMax, sizeof(coords));
if (!cart4_start) {
printf ("ALLOCATION ERROR - ABORTING. \n");
exit(1);
} cart4=cart4_start;
cart5_start = (coords *)calloc(iMax, sizeof(coords));
if (!cart5_start) {
printf ("ALLOCATION ERROR - ABORTING. \n");
exit(1);
} cart5=cart5_start;
cart6_start = (coords *)calloc(iMax, sizeof(coords));
if (!cart6_start) {
printf ("ALLOCATION ERROR - ABORTING. \n");
exit(1);
} cart6=cart6_start;
cart7_start = (coords *)calloc(iMax, sizeof(coords));
if (!cart7_start) {
printf ("ALLOCATION ERROR - ABORTING. \n");

```

```

    exit(1);
    } cart7=cart7_start;
cart8_start = (coords *)calloc(iMax, sizeof(coords));
if (!cart8_start) {
    printf ("ALLOCATION ERROR - ABORTING. \n");
    exit(1);
    } cart8=cart8_start;
cart9_start = (coords *)calloc(iMax, sizeof(coords));
if (!cart9_start) {
    printf ("ALLOCATION ERROR - ABORTING. \n");
    exit(1);
    } cart9=cart9_start;
cart10_start = (coords *)calloc(iMax, sizeof(coords));
if (!cart10_start) {
    printf ("ALLOCATION ERROR - ABORTING. \n");
    exit(1);
    } cart10=cart10_start;
E1_start = (DATA *)calloc(iMax , sizeof(DATA));
if (!E1_start) {
    printf ("ALLOCATION ERROR - ABORTING. \n");
    exit(1);
    } E1=E1_start;
E2_start = (DATA *)calloc(iMax , sizeof(DATA));
if (!E2_start) {
    printf ("ALLOCATION ERROR - ABORTING. \n");
    exit(1);
    } E2=E2_start;
E3_start = (DATA *)calloc(iMax , sizeof(DATA));
if (!E3_start) {
    printf ("ALLOCATION ERROR - ABORTING. \n");
    exit(1);
    } E3=E3_start;
E4_start = (DATA *)calloc(iMax , sizeof(DATA));
if (!E4_start) {
    printf ("ALLOCATION ERROR - ABORTING. \n");
    exit(1);

```

```

    } E4=E4_start;
E5_start = (DATA *)calloc(iMax , sizeof(DATA));
if (!E5_start) {
    printf ("ALLOCATION ERROR - ABORTING. \n");
    exit(1);
    } E5=E5_start;
E6_start = (DATA *)calloc(iMax , sizeof(DATA));
if (!E6_start) {
    printf ("ALLOCATION ERROR - ABORTING. \n");
    exit(1);
    } E6=E6_start;
E7_start = (DATA *)calloc(iMax , sizeof(DATA));
if (!E7_start) {
    printf ("ALLOCATION ERROR - ABORTING. \n");
    exit(1);
    } E7=E7_start;
E8_start = (DATA *)calloc(iMax , sizeof(DATA));
if (!E8_start) {
    printf ("ALLOCATION ERROR - ABORTING. \n");
    exit(1);
    } E8=E8_start;
E9_start = (DATA *)calloc(iMax , sizeof(DATA));
if (!E9_start) {
    printf ("ALLOCATION ERROR - ABORTING. \n");
    exit(1);
    } E9=E9_start;
E10_start = (DATA *)calloc(iMax , sizeof(DATA));
if (!E10_start) {
    printf ("ALLOCATION ERROR - ABORTING. \n");
    exit(1);
    } E10=E10_start;
outDataE1_start = (DATA*)calloc(NI, sizeof(DATA));
if (!outDataE1_start) {
    printf ("ALLOCATION ERROR - ABORTING. \n");
    exit(1);
    } outDataE1=outDataE1_start;

```

```

outDataE2_start = (DATA*)calloc(NI, sizeof(DATA));
if (!outDataE2_start) {
    printf ("ALLOCATION ERROR - ABORTING. \n");
    exit(1);
} outDataE2=outDataE2_start;
outDataE3_start = (DATA*)calloc(NI, sizeof(DATA));
if (!outDataE3_start) {
    printf ("ALLOCATION ERROR - ABORTING. \n");
    exit(1);
} outDataE3=outDataE3_start;
outDataE4_start = (DATA*)calloc(NI, sizeof(DATA));
if (!outDataE4_start) {
    printf ("ALLOCATION ERROR - ABORTING. \n");
    exit(1);
} outDataE4=outDataE4_start;
outDataE5_start = (DATA*)calloc(NI, sizeof(DATA));
if (!outDataE5_start) {
    printf ("ALLOCATION ERROR - ABORTING. \n");
    exit(1);
} outDataE5=outDataE5_start;
outDataE6_start = (DATA*)calloc(NI, sizeof(DATA));
if (!outDataE6_start) {
    printf ("ALLOCATION ERROR - ABORTING. \n");
    exit(1);
} outDataE6=outDataE6_start;
outDataE7_start = (DATA*)calloc(NI, sizeof(DATA));
if (!outDataE7_start) {
    printf ("ALLOCATION ERROR - ABORTING. \n");
    exit(1);
} outDataE7=outDataE7_start;
outDataE8_start = (DATA*)calloc(NI, sizeof(DATA));
if (!outDataE8_start) {
    printf ("ALLOCATION ERROR - ABORTING. \n");
    exit(1);
} outDataE8=outDataE8_start;
outDataE9_start = (DATA*)calloc(NI, sizeof(DATA));
if (!outDataE9_start) {
    printf ("ALLOCATION ERROR - ABORTING. \n");
    exit(1);
} outDataE9=outDataE9_start;
outDataE10_start = (DATA*)calloc(NI, sizeof(DATA));
if (!outDataE10_start) {
    printf ("ALLOCATION ERROR - ABORTING. \n");
    exit(1);
} outDataE10=outDataE10_start;
outDataF1_start = (DATA*)calloc(NI, sizeof(DATA));
if (!outDataF1_start) {
    printf ("ALLOCATION ERROR - ABORTING. \n");
    exit(1);
} outDataF1=outDataF1_start;
outDataF2_start = (DATA*)calloc(NI, sizeof(DATA));
if (!outDataF2_start) {
    printf ("ALLOCATION ERROR - ABORTING. \n");
    exit(1);
} outDataF2=outDataF2_start;
outDataF3_start = (DATA*)calloc(NI, sizeof(DATA));
if (!outDataF3_start) {
    printf ("ALLOCATION ERROR - ABORTING. \n");
    exit(1);
} outDataF3=outDataF3_start;
outDataF4_start = (DATA*)calloc(NI, sizeof(DATA));
if (!outDataF4_start) {
    printf ("ALLOCATION ERROR - ABORTING. \n");
    exit(1);
} outDataF4=outDataF4_start;
outDataF5_start = (DATA*)calloc(NI, sizeof(DATA));
if (!outDataF5_start) {
    printf ("ALLOCATION ERROR - ABORTING. \n");
    exit(1);
} outDataF5=outDataF5_start;
outDataF6_start = (DATA*)calloc(NI, sizeof(DATA));
if (!outDataF6_start) {

```

```

    printf ("ALLOCATION ERROR - ABORTING. \n");
    exit(1);
}
outDataF6=outDataF6_start;
outDataF7_start = (DATA*)calloc(NI, sizeof(DATA));
if (!outDataF7_start) {
    printf ("ALLOCATION ERROR - ABORTING. \n");
    exit(1);
}
outDataF7=outDataF7_start;
outDataF8_start = (DATA*)calloc(NI, sizeof(DATA));
if (!outDataF8_start) {
    printf ("ALLOCATION ERROR - ABORTING. \n");
    exit(1);
}
outDataF8=outDataF8_start;
outDataF9_start = (DATA*)calloc(NI, sizeof(DATA));
if (!outDataF9_start) {
    printf ("ALLOCATION ERROR - ABORTING. \n");
    exit(1);
}
outDataF9=outDataF9_start;
outDataF10_start = (DATA*)calloc(NI, sizeof(DATA));
if (!outDataF10_start) {
    printf ("ALLOCATION ERROR - ABORTING. \n");
    exit(1);
}
outDataF10=outDataF10_start;
F1_start = (DATA*)calloc(iMax, sizeof(DATA));
if (!F1_start) {
    printf ("ALLOCATION ERROR - ABORTING. \n");
    exit(1);
}
F1=F1_start;
F2_start = (DATA*)calloc(iMax, sizeof(DATA));
if (!F2_start) {
    printf ("ALLOCATION ERROR - ABORTING. \n");
    exit(1);
}
F2=F2_start;
F3_start = (DATA*)calloc(iMax, sizeof(DATA));
if (!F3_start) {
    printf ("ALLOCATION ERROR - ABORTING. \n");
    exit(1);
}
F3=F3_start;
F4_start = (DATA*)calloc(iMax, sizeof(DATA));
if (!F4_start) {
    printf ("ALLOCATION ERROR - ABORTING. \n");
    exit(1);
}
F4=F4_start;
F5_start = (DATA*)calloc(iMax, sizeof(DATA));
if (!F5_start) {
    printf ("ALLOCATION ERROR - ABORTING. \n");
    exit(1);
}
F5=F5_start;
F6_start = (DATA*)calloc(iMax, sizeof(DATA));
if (!F6_start) {
    printf ("ALLOCATION ERROR - ABORTING. \n");
    exit(1);
}
F6=F6_start;
F7_start = (DATA*)calloc(iMax, sizeof(DATA));
if (!F7_start) {
    printf ("ALLOCATION ERROR - ABORTING. \n");
    exit(1);
}
F7=F7_start;
F8_start = (DATA*)calloc(iMax, sizeof(DATA));
if (!F8_start) {
    printf ("ALLOCATION ERROR - ABORTING. \n");
    exit(1);
}
F8=F8_start;
F9_start = (DATA*)calloc(iMax, sizeof(DATA));
if (!F9_start) {
    printf ("ALLOCATION ERROR - ABORTING. \n");
    exit(1);
}
F9=F9_start;
F10_start = (DATA*)calloc(iMax, sizeof(DATA));
if (!F10_start) {
    printf ("ALLOCATION ERROR - ABORTING. \n");
    exit(1);
}

```

```

    }    F10=F10_start;
    AVF_start = (DATA*)calloc(NI, sizeof(DATA));
    if (!AVF_start) {
        printf ("ALLOCATION ERROR - ABORTING. \n");
        exit(1);
    }    AVF=AVF_start;
    AVE_start = (DATA*)calloc(NI, sizeof(DATA));
    if (!AVE_start) {
        printf ("ALLOCATION ERROR - ABORTING. \n");
        exit(1);
    }    AVE=AVE_start;
    rewind(in1);
    i=0;
    while (!fgets(string, n, in1)==0)
        {
            if (strcmp(string, " A D XYZ")==0)
                {
                    fscanf(in1, "%lf %lf %lf", &x, &y, &z);
                    /* -10=Slunits/-4=microns: input in Amstrongs */
                    cart1[i].X = x*1e-10;
                    cart1[i].Y = y*1e-10;
                    cart1[i].Z = z*1e-10;
                    xcm1 += cart1[i].X;
                    ycm1 += cart1[i].Y;
                    zcm1 += cart1[i].Z;
                    i++;
                };
        };
    i=0;
    while (!fgets(string, n, in2)==0)
        {
            if (strcmp(string, " A D XYZ")==0)
                {
                    fscanf(in2, "%lf %lf %lf", &x, &y, &z);
                    cart2[i].X = x*1e-10;
                    cart2[i].Y = y*1e-10;
                    cart2[i].Z = z*1e-10;
                    xcm2 += cart2[i].X;
                    ycm2 += cart2[i].Y;
                    zcm2 += cart2[i].Z;
                    i++;
                };
        };
    i=0;
    while (!fgets(string, n, in3)==0)
        {
            if (strcmp(string, " A D XYZ")==0)
                {
                    fscanf(in3, "%lf %lf %lf", &x, &y, &z);
                    cart3[i].X = x*1e-10;
                    cart3[i].Y = y*1e-10;
                    cart3[i].Z = z*1e-10;
                    xcm3 += cart3[i].X;
                    ycm3 += cart3[i].Y;
                    zcm3 += cart3[i].Z;
                    i++;
                };
        };
    i=0;
    while (!fgets(string, n, in4)==0)
        {
            if (strcmp(string, " A D XYZ")==0)
                {
                    fscanf(in4, "%lf %lf %lf", &x, &y, &z);
                    cart4[i].X = x*1e-10;
                    cart4[i].Y = y*1e-10;
                    cart4[i].Z = z*1e-10;
                    xcm4 += cart4[i].X;
                    ycm4 += cart4[i].Y;
                    zcm4 += cart4[i].Z;
                    i++;
                };
        };

```

```

};
i=0;
while (!fgets(string, n, in5)==0)
{
if (strcmp(string, " (A D XYZ (") == 0)
{
fscanf(in5, "%lf %lf %lf", &x, &y, &z);
cart5[i].X = x*1e-10;
cart5[i].Y = y*1e-10;
cart5[i].Z = z*1e-10;
xcm5 += cart5[i].X;
ycm5 += cart5[i].Y;
zcm5 += cart5[i].Z;
i++;
};
};

```

```

i=0;
while (!fgets(string, n, in6)==0)
{
if (strcmp(string, " (A D XYZ (") == 0)
{
fscanf(in6, "%lf %lf %lf", &x, &y, &z);
cart6[i].X = x*1e-10;
cart6[i].Y = y*1e-10;
cart6[i].Z = z*1e-10;
xcm6 += cart6[i].X;
ycm6 += cart6[i].Y;
zcm6 += cart6[i].Z;
i++;
};
};

```

```

i=0;
while (!fgets(string, n, in7)==0)
{
if (strcmp(string, " (A D XYZ (") == 0)
{

```

```

fscanf(in7, "%lf %lf %lf", &x, &y, &z);
cart7[i].X = x*1e-10;
cart7[i].Y = y*1e-10;
cart7[i].Z = z*1e-10;
xcm7 += cart7[i].X;
ycm7 += cart7[i].Y;
zcm7 += cart7[i].Z;
i++;
};
};

```

```

i=0;
while (!fgets(string, n, in8)==0)
{
if (strcmp(string, " (A D XYZ (") == 0)
{
fscanf(in8, "%lf %lf %lf", &x, &y, &z);
cart8[i].X = x*1e-10;
cart8[i].Y = y*1e-10;
cart8[i].Z = z*1e-10;
xcm8 += cart8[i].X;
ycm8 += cart8[i].Y;
zcm8 += cart8[i].Z;
i++;
};
};

```

```

i=0;
while (!fgets(string, n, in9)==0)
{
if (strcmp(string, " (A D XYZ (") == 0)
{
fscanf(in9, "%lf %lf %lf", &x, &y, &z);
cart9[i].X = x*1e-10;
cart9[i].Y = y*1e-10;
cart9[i].Z = z*1e-10;
xcm9 += cart9[i].X;
ycm9 += cart9[i].Y;

```

```

        zcm9 += cart9[i].Z;
        i++;
    };
};
i=0;
while (!fgets(string, n, in10)==0)
{
    if (strcmp(string, " (A D XYZ (")==0)
    {
        fscanf(in10, "%lf %lf %lf", &x, &y, &z);
        cart10[i].X = x*1e-10;
        cart10[i].Y = y*1e-10;
        cart10[i].Z = z*1e-10;
        xcm10 += cart10[i].X;
        ycm10 += cart10[i].Y;
        zcm10 += cart10[i].Z;
        i++;
    };
};
xcm1 = xcm1/iMax;
ycm1 = ycm1/iMax;
zcm1 = zcm1/iMax;
xcm2 = xcm2/iMax;
ycm2 = ycm2/iMax;
zcm2 = zcm2/iMax;
xcm3 = xcm3/iMax;
ycm3 = ycm3/iMax;
zcm3 = zcm3/iMax;
xcm4 = xcm4/iMax;
ycm4 = ycm4/iMax;
zcm4 = zcm4/iMax;
xcm5 = xcm5/iMax;
ycm5 = ycm5/iMax;
zcm5 = zcm5/iMax;
xcm6 = xcm6/iMax;
ycm6 = ycm6/iMax;

```

```

zcm6 = zcm6/iMax;
xcm7 = xcm7/iMax;
ycm7 = ycm7/iMax;
zcm7 = zcm7/iMax;
xcm8 = xcm8/iMax;
ycm8 = ycm8/iMax;
zcm8 = zcm8/iMax;
xcm9 = xcm9/iMax;
ycm9 = ycm9/iMax;
zcm9 = zcm9/iMax;
xcm10 = xcm10/iMax;
ycm10 = ycm10/iMax;
zcm10 = zcm10/iMax;
j=0;
for(i=0; i<(iMax); i++)
{
    cart1[i].X=cart1[i].X-xcm1;
    cart1[i].Y=cart1[i].Y-ycm1;
    cart1[i].Z=cart1[i].Z-zcm1;
    cart1[i].R = sqrt(cart1[i].X * cart1[i].X + cart1[i].Y * cart1[i].Y + cart1[i].Z *
cart1[i].Z);
    cart2[i].X=cart2[i].X-xcm2;
    cart2[i].Y=cart2[i].Y-ycm2;
    cart2[i].Z=cart2[i].Z-zcm2;
    cart2[i].R = sqrt(cart2[i].X * cart2[i].X + cart2[i].Y * cart2[i].Y + cart2[i].Z *
cart2[i].Z);
    cart3[i].X=cart3[i].X-xcm3;
    cart3[i].Y=cart3[i].Y-ycm3;
    cart3[i].Z=cart3[i].Z-zcm3;
    cart3[i].R = sqrt(cart3[i].X * cart3[i].X + cart3[i].Y * cart3[i].Y + cart3[i].Z *
cart3[i].Z);
    cart4[i].X=cart4[i].X-xcm4;
    cart4[i].Y=cart4[i].Y-ycm4;
    cart4[i].Z=cart4[i].Z-zcm4;
    cart4[i].R = sqrt(cart4[i].X * cart4[i].X + cart4[i].Y * cart4[i].Y + cart4[i].Z *
cart4[i].Z);

```

```

    cart5[i].X=cart5[i].X-xcm5;
    cart5[i].Y=cart5[i].Y-ycm5;
    cart5[i].Z=cart5[i].Z-zcm5;
    cart5[i].R = sqrt(cart5[i].X * cart5[i].X + cart5[i].Y * cart5[i].Y + cart5[i].Z *
cart5[i].Z);
    cart6[i].X=cart6[i].X-xcm6;
    cart6[i].Y=cart6[i].Y-ycm6;
    cart6[i].Z=cart6[i].Z-zcm6;
    cart6[i].R = sqrt(cart6[i].X * cart6[i].X + cart6[i].Y * cart6[i].Y + cart6[i].Z *
cart6[i].Z);
    cart7[i].X=cart7[i].X-xcm7;
    cart7[i].Y=cart7[i].Y-ycm7;
    cart7[i].Z=cart7[i].Z-zcm7;
    cart7[i].R = sqrt(cart7[i].X * cart7[i].X + cart7[i].Y * cart7[i].Y + cart7[i].Z *
cart7[i].Z);
    cart8[i].X=cart8[i].X-xcm8;
    cart8[i].Y=cart8[i].Y-ycm8;
    cart8[i].Z=cart8[i].Z-zcm8;
    cart8[i].R = sqrt(cart8[i].X * cart8[i].X + cart8[i].Y * cart8[i].Y + cart8[i].Z *
cart8[i].Z);
    cart9[i].X=cart9[i].X-xcm9;
    cart9[i].Y=cart9[i].Y-ycm9;
    cart9[i].Z=cart9[i].Z-zcm9;
    cart9[i].R = sqrt(cart9[i].X * cart9[i].X + cart9[i].Y * cart9[i].Y + cart9[i].Z *
cart9[i].Z);
    cart10[i].X=cart10[i].X-xcm10;
    cart10[i].Y=cart10[i].Y-ycm10;
    cart10[i].Z=cart10[i].Z-zcm10;
    cart10[i].R = sqrt(cart10[i].X * cart10[i].X + cart10[i].Y * cart10[i].Y + cart10[i].Z *
cart10[i].Z);
}
for(i=0 ; i<(iMax) ; i++)
{
    F1[i].R = cart1[i].R;
    F2[i].R = cart2[i].R;
    F3[i].R = cart3[i].R;
    F4[i].R = cart4[i].R;
    F5[i].R = cart5[i].R;
    F6[i].R = cart6[i].R;
    F7[i].R = cart7[i].R;
    F8[i].R = cart8[i].R;
    F9[i].R = cart9[i].R;
    F10[i].R = cart10[i].R;
    E1[i].V=0.0;
    E2[i].V=0.0;
    E3[i].V=0.0;
    E4[i].V=0.0;
    E5[i].V=0.0;
    E6[i].V=0.0;
    E7[i].V=0.0;
    E8[i].V=0.0;
    E9[i].V=0.0;
    E10[i].V=0.0;
    E1[i].R = F1[i].R;
    E2[i].R = F2[i].R;
    E3[i].R = F3[i].R;
    E4[i].R = F4[i].R;
    E5[i].R = F5[i].R;
    E6[i].R = F6[i].R;
    E7[i].R = F7[i].R;
    E8[i].R = F8[i].R;
    E9[i].R = F9[i].R;
    E10[i].R = F10[i].R;
    F1[i].V=0.0;
    F2[i].V=0.0;
    F3[i].V=0.0;
    F4[i].V=0.0;
    F5[i].V=0.0;
    F6[i].V=0.0;
    F7[i].V=0.0;
    F8[i].V=0.0;
    F9[i].V=0.0;

```

```

F10[i].V=0.0;
RM6 = twothesix(rm);
for(j=0; j<iMax ; j++)
{
if(i==j) j++;
r = sqrt((cart1[i].X - cart1[j].X) * (cart1[i].X - cart1[j].X) + (cart1[i].Y - cart1[j].Y) * (cart1[i].Y - cart1[j].Y) + (cart1[i].Z - cart1[j].Z) * (cart1[i].Z - cart1[j].Z));
R6 = twothesix(r);
f1 = -12 * D * ( RM6/(r * R6) - sqrt(RM6/R6)/r)/2;
e1 = D * (sqrt(RM6/R6)-2*(RM6/R6))/2;
F1[i].V += f1;
E1[i].V += e1;
r = sqrt((cart2[i].X - cart2[j].X) * (cart2[i].X - cart2[j].X) + (cart2[i].Y - cart2[j].Y) * (cart2[i].Y - cart2[j].Y) + (cart2[i].Z - cart2[j].Z) * (cart2[i].Z - cart2[j].Z));
R6 = twothesix(r);
f2 = -12 * D * ( RM6/(r * R6) - sqrt(RM6/R6)/r)/2;
e2 = D * (sqrt(RM6/R6)-2*(RM6/R6))/2;
F2[i].V += f2;
E2[i].V += e2;
r = sqrt((cart3[i].X - cart3[j].X) * (cart3[i].X - cart3[j].X) + (cart3[i].Y - cart3[j].Y) * (cart3[i].Y - cart3[j].Y) + (cart3[i].Z - cart3[j].Z) * (cart3[i].Z - cart3[j].Z));
R6 = twothesix(r);
f3 = -12 * D * ( RM6/(r * R6) - sqrt(RM6/R6)/r)/2;
e3 = D * (sqrt(RM6/R6)-2*(RM6/R6))/2;
F3[i].V += f3;
E3[i].V += e3;
r = sqrt((cart4[i].X - cart4[j].X) * (cart4[i].X - cart4[j].X) + (cart4[i].Y - cart4[j].Y) * (cart4[i].Y - cart4[j].Y) + (cart4[i].Z - cart4[j].Z) * (cart4[i].Z - cart4[j].Z));
R6 = twothesix(r);
f4 = -12 * D * ( RM6/(r * R6) - sqrt(RM6/R6)/r)/2;
e4 = D * (sqrt(RM6/R6)-2*(RM6/R6))/2;
F4[i].V += f4;
E4[i].V += e4;
r = sqrt((cart5[i].X - cart5[j].X) * (cart5[i].X - cart5[j].X) + (cart5[i].Y - cart5[j].Y) * (cart5[i].Y - cart5[j].Y) + (cart5[i].Z - cart5[j].Z) * (cart5[i].Z - cart5[j].Z));
R6 = twothesix(r);

```

```

f5 = -12 * D * ( RM6/(r * R6) - sqrt(RM6/R6)/r)/2;
e5 = D * (sqrt(RM6/R6)-2*(RM6/R6))/2;
F5[i].V += f5;
E5[i].V += e5;
r = sqrt((cart6[i].X - cart6[j].X) * (cart6[i].X - cart6[j].X) + (cart6[i].Y - cart6[j].Y) * (cart6[i].Y - cart6[j].Y) + (cart6[i].Z - cart6[j].Z) * (cart6[i].Z - cart6[j].Z));
R6 = twothesix(r);
f6 = -12 * D * ( RM6/(r * R6) - sqrt(RM6/R6)/r)/2;
e6 = D * (sqrt(RM6/R6)-2*(RM6/R6))/2;
F6[i].V += f6;
E6[i].V += e6;
r = sqrt((cart7[i].X - cart7[j].X) * (cart7[i].X - cart7[j].X) + (cart7[i].Y - cart7[j].Y) * (cart7[i].Y - cart7[j].Y) + (cart7[i].Z - cart7[j].Z) * (cart7[i].Z - cart7[j].Z));
R6 = twothesix(r);
f7 = -12 * D * ( RM6/(r * R6) - sqrt(RM6/R6)/r)/2;
e7 = D * (sqrt(RM6/R6)-2*(RM6/R6))/2;
F7[i].V += f7;
E7[i].V += e7;
r = sqrt((cart8[i].X - cart8[j].X) * (cart8[i].X - cart8[j].X) + (cart8[i].Y - cart8[j].Y) * (cart8[i].Y - cart8[j].Y) + (cart8[i].Z - cart8[j].Z) * (cart8[i].Z - cart8[j].Z));
R6 = twothesix(r);
f8 = -12 * D * ( RM6/(r * R6) - sqrt(RM6/R6)/r)/2;
e8 = D * (sqrt(RM6/R6)-2*(RM6/R6))/2;
F8[i].V += f8;
E8[i].V += e8;
r = sqrt((cart9[i].X - cart9[j].X) * (cart9[i].X - cart9[j].X) + (cart9[i].Y - cart9[j].Y) * (cart9[i].Y - cart9[j].Y) + (cart9[i].Z - cart9[j].Z) * (cart9[i].Z - cart9[j].Z));
R6 = twothesix(r);
f9 = -12 * D * ( RM6/(r * R6) - sqrt(RM6/R6)/r)/2;
e9 = D * (sqrt(RM6/R6)-2*(RM6/R6))/2;
F9[i].V += f9;
E9[i].V += e9;
r = sqrt((cart10[i].X - cart10[j].X) * (cart10[i].X - cart10[j].X) + (cart10[i].Y - cart10[j].Y) * (cart10[i].Y - cart10[j].Y) + (cart10[i].Z - cart10[j].Z) * (cart10[i].Z - cart10[j].Z));
R6 = twothesix(r);
f10 = -12 * D * ( RM6/(r * R6) - sqrt(RM6/R6)/r)/2;

```

```

e10= D * (sqr(RM6/R6)-2*(RM6/R6))/2;
F10[i].V += f10;
E10[i].V += e10;
};
}
counter=1;
while (counter > 0)
{
counter=0;
for(i=0 ; i<(iMax-1) ; i++)
{
if (F1[i].R > F1[i+1].R)
{
temp1=E1[i].R;
E1[i].R=E1[i+1].R;
E1[i+1].R=temp1;
temp2=E1[i].V;
E1[i].V=E1[i+1].V;
E1[i+1].V=temp2;
temp3=F1[i].R;
F1[i].R=F1[i+1].R;
F1[i+1].R=temp3;
temp4=F1[i].V;
F1[i].V=F1[i+1].V;
F1[i+1].V=temp4;
counter++;
}
}
}
counter=1;
while (counter > 0)
{
counter=0;
for(i=0 ; i<(iMax-1) ; i++)
{
if (F2[i].R > F2[i+1].R)
{
temp1=E2[i].R;
E2[i].R=E2[i+1].R;
E2[i+1].R=temp1;
temp2=E2[i].V;
E2[i].V=E2[i+1].V;
E2[i+1].V=temp2;
temp3=F2[i].R;
F2[i].R=F2[i+1].R;
F2[i+1].R=temp3;
temp4=F2[i].V;
F2[i].V=F2[i+1].V;
F2[i+1].V=temp4;
counter++;
}
}
}
counter=1;
while (counter > 0)
{
counter=0;
for(i=0 ; i<(iMax-1) ; i++)
{
if (F3[i].R > F3[i+1].R)
{
temp1=E3[i].R;
E3[i].R=E3[i+1].R;
E3[i+1].R=temp1;
temp2=E3[i].V;
E3[i].V=E3[i+1].V;
E3[i+1].V=temp2;
temp3=F3[i].R;
F3[i].R=F3[i+1].R;
F3[i+1].R=temp3;
temp4=F3[i].V;
F3[i].V=F3[i+1].V;
}
}
}
}

```

```

        F3[i+1].V=temp4;
        counter++;
    }
}
counter=1;
while (counter > 0)
{
    counter=0;
    for(i=0 ; i<(iMax-1) ; i++)
    {
        if (F4[i].R > F4[i+1].R)
        {
            temp1=E4[i].R;
            E4[i].R=E4[i+1].R;
            E4[i+1].R=temp1;
            temp2=E4[i].V;
            E4[i].V=E4[i+1].V;
            E4[i+1].V=temp2;
            temp3=F4[i].R;
            F4[i].R=F4[i+1].R;
            F4[i+1].R=temp3;
            temp4=F4[i].V;
            F4[i].V=F4[i+1].V;
            F4[i+1].V=temp4;
            counter++;
        }
    }
}
counter=1;
while (counter > 0)
{
    counter=0;
    for(i=0 ; i<(iMax-1) ; i++)
    {
        if (F5[i].R > F5[i+1].R)
        {
            temp1=E5[i].R;
            E5[i].R=E5[i+1].R;
            E5[i+1].R=temp1;
            temp2=E5[i].V;
            E5[i].V=E5[i+1].V;
            E5[i+1].V=temp2;
            temp3=F5[i].R;
            F5[i].R=F5[i+1].R;
            F5[i+1].R=temp3;
            temp4=F5[i].V;
            F5[i].V=F5[i+1].V;
            F5[i+1].V=temp4;
            counter++;
        }
    }
}
counter=1;
while (counter > 0)
{
    counter=0;
    for(i=0 ; i<(iMax-1) ; i++)
    {
        if (F6[i].R > F6[i+1].R)
        {
            temp1=E6[i].R;
            E6[i].R=E6[i+1].R;
            E6[i+1].R=temp1;
            temp2=E6[i].V;
            E6[i].V=E6[i+1].V;
            E6[i+1].V=temp2;
            temp3=F6[i].R;
            F6[i].R=F6[i+1].R;
            F6[i+1].R=temp3;
            temp4=F6[i].V;
        }
    }
}

```

```

        F6[i].V=F6[i+1].V;
        F6[i+1].V=temp4;
        counter++;
    }
}
counter=1;
while (counter > 0)
{
    counter=0;
    for(i=0 ; i<(iMax-1) ; i++)
    {
        if (F7[i].R > F7[i+1].R)
        {
            temp1=E7[i].R;
            E7[i].R=E7[i+1].R;
            E7[i+1].R=temp1;
            temp2=E7[i].V;
            E7[i].V=E7[i+1].V;
            E7[i+1].V=temp2;
            temp3=F7[i].R;
            F7[i].R=F7[i+1].R;
            F7[i+1].R=temp3;
            temp4=F7[i].V;
            F7[i].V=F7[i+1].V;
            F7[i+1].V=temp4;
            counter++;
        }
    }
}
counter=1;
while (counter > 0)
{
    counter=0;
    for(i=0 ; i<(iMax-1) ; i++)
    {
        if (F7[i].R > F7[i+1].R)
        {
            temp1=E7[i].R;
            E7[i].R=E7[i+1].R;
            E7[i+1].R=temp1;
            temp2=E7[i].V;
            E7[i].V=E7[i+1].V;
            E7[i+1].V=temp2;
            temp3=F7[i].R;
            F7[i].R=F7[i+1].R;
            F7[i+1].R=temp3;
            temp4=F7[i].V;
            F7[i].V=F7[i+1].V;
            F7[i+1].V=temp4;
            counter++;
        }
    }
}
counter=1;
while (counter > 0)
{
    counter=0;
    for(i=0 ; i<(iMax-1) ; i++)
    {
        if (F8[i].R > F8[i+1].R)
        {
            temp1=E8[i].R;
            E8[i].R=E8[i+1].R;
            E8[i+1].R=temp1;
            temp2=E8[i].V;
            E8[i].V=E8[i+1].V;
            E8[i+1].V=temp2;
            temp3=F8[i].R;
            F8[i].R=F8[i+1].R;
            F8[i+1].R=temp3;
            temp4=F8[i].V;
            F8[i].V=F8[i+1].V;
            F8[i+1].V=temp4;
            counter++;
        }
    }
}
counter=1;
while (counter > 0)
{
    counter=0;
    for(i=0 ; i<(iMax-1) ; i++)
    {
        if (F9[i].R > F9[i+1].R)
        {
            temp1=E9[i].R;
            E9[i].R=E9[i+1].R;
            E9[i+1].R=temp1;
            temp2=E9[i].V;
            E9[i].V=E9[i+1].V;
            E9[i+1].V=temp2;
            temp3=F9[i].R;
            F9[i].R=F9[i+1].R;
            F9[i+1].R=temp3;
            temp4=F9[i].V;
        }
    }
}

```

```

        F9[i].V=F9[i+1].V;
        F9[i+1].V=temp4;
        counter++;
    }
}
counter=1;
while (counter > 0)
{
    counter=0;
    for(i=0 ; i<(iMax-1) ; i++)
    {
        if (F10[i].R > F10[i+1].R)
        {
            temp1=E10[i].R;
            E10[i].R=E10[i+1].R;
            E10[i+1].R=temp1;
            temp2=E10[i].V;
            E10[i].V=E10[i+1].V;
            E10[i+1].V=temp2;
            temp3=F10[i].R;
            F10[i].R=F10[i+1].R;
            F10[i+1].R=temp3;
            temp4=F10[i].V;
            F10[i].V=F10[i+1].V;
            F10[i+1].V=temp4;
            counter++;
        }
    }
}
for (i=0 ; i<(iMax) ; i++)
{
    j=0;
    J[0][j] = 0;
    for (j=0 ; j<(NI) ; j++)
    {
        outDataF1[j].R = (j+0.5)*delta;
        outDataE1[j].R = (j+0.5)*delta;
        R=F1[j].R;
        if (((j*delta) < R) && (R < ((j+1)*delta)))
        {
            outDataE1[j].V = outDataE1[j].V +E1[i].V ;
            outDataF1[j].V = outDataF1[j].V +F1[i].V ;
            J[0][j]+=1;
        }
    }
}
for (i=0 ; i<(iMax) ; i++)
{
    j=0;
    J[1][j] = 0;
    for (j=0 ; j<(NI) ; j++)
    {
        outDataF2[j].R = (j+0.5)*delta;
        outDataE2[j].R = (j+0.5)*delta;
        R=F2[i].R;
        if (((j*delta) < R) && (R < ((j+1)*delta)))
        {
            outDataE2[j].V = outDataE2[j].V +E2[i].V ;
            outDataF2[j].V = outDataF2[j].V +F2[i].V ;
            J[1][j]+=1;
        }
    }
}
for (i=0 ; i<(iMax) ; i++)
{
    j=0;
    J[2][j] = 0;
    for (j=0 ; j<(NI) ; j++)
    {
        outDataF3[j].R = (j+0.5)*delta;
        outDataE3[j].R = (j+0.5)*delta;
    }
}

```



```

        outDataF7[j].V = outDataF7[j].V + F7[i].V ;
        J[6][j] += 1;
    }
}
for (i=0 ; i<(iMax) ; i++)
{
    j=0;
    J[7][j] = 0;
    for (j=0 ; j<(NI) ; j++)
    {
        outDataF8[j].R = (j+0.5)*delta;
        outDataE8[j].R = (j+0.5)*delta;
        R=F8[j].R;
        if (((j*delta) < R) && (R < ((j+1)*delta)))
        {
            outDataE8[j].V = outDataE8[j].V + E8[i].V ;
            outDataF8[j].V = outDataF8[j].V + F8[i].V ;
            J[7][j] += 1;
        }
    }
}
for (i=0 ; i<(iMax) ; i++)
{
    j=0;
    J[8][j] = 0;
    for (j=0 ; j<(NI) ; j++)
    {
        outDataF9[j].R = (j+0.5)*delta;
        outDataE9[j].R = (j+0.5)*delta;
        R=F9[j].R;
        if (((j*delta) < R) && (R < ((j+1)*delta)))
        {
            outDataE9[j].V = outDataE9[j].V + E9[i].V ;
            outDataF9[j].V = outDataF9[j].V + F9[i].V ;
            J[8][j] += 1;
        }
    }
}
        outDataF7[j].V = outDataF7[j].V + F7[i].V ;
        J[6][j] += 1;
    }
}
for (i=0 ; i<(iMax) ; i++)
{
    j=0;
    J[9][j] = 0;
    for (j=0 ; j<(NI) ; j++)
    {
        outDataF10[j].R = (j+0.5)*delta;
        outDataE10[j].R = (j+0.5)*delta;
        R=F10[j].R;
        if (((j*delta) < R) && (R < ((j+1)*delta)))
        {
            outDataE10[j].V = outDataE10[j].V + E10[i].V ;
            outDataF10[j].V = outDataF10[j].V + F10[i].V ;
            J[9][j] += 1;
        }
    }
}
for (j=0 ; j<(NI) ; j++)
{
    if (J[0][j] != 0) {
        outDataE1[j].V = outDataE1[j].V / (1.00 * J[0][j]);
        outDataF1[j].V = outDataF1[j].V / (1.00 * J[0][j]);
    }
    if (J[1][j] != 0) {
        outDataE2[j].V = outDataE2[j].V / (1.00 * J[1][j]);
        outDataF2[j].V = outDataF2[j].V / (1.00 * J[1][j]);
    }
    if (J[2][j] != 0) {
        outDataE3[j].V = outDataE3[j].V / (1.00 * J[2][j]);
        outDataF3[j].V = outDataF3[j].V / (1.00 * J[2][j]);
    }
    if (J[3][j] != 0) {
        outDataE4[j].V = outDataE4[j].V / (1.00 * J[3][j]);
    }
}

```

```

        outDataF4[j].V=outDataF4[j].V/(1.00*J[3][j]);
    }
    if (J[4][j]!=0) {
        outDataE5[j].V=outDataE5[j].V/(1.00*J[4][j]);
        outDataF5[j].V=outDataF5[j].V/(1.00*J[4][j]);
    }
    if (J[5][j]!=0) {
        outDataE6[j].V=outDataE6[j].V/(1.00*J[5][j]);
        outDataF6[j].V=outDataF6[j].V/(1.00*J[5][j]);
    }
    if (J[6][j]!=0) {
        outDataE7[j].V=outDataE7[j].V/(1.00*J[6][j]);
        outDataF7[j].V=outDataF7[j].V/(1.00*J[6][j]);
    }
    if (J[7][j]!=0) {
        outDataE8[j].V=outDataE8[j].V/(1.00*J[7][j]);
        outDataF8[j].V=outDataF8[j].V/(1.00*J[7][j]);
    }
    if (J[8][j]!=0) {
        outDataE9[j].V=outDataE9[j].V/(1.00*J[8][j]);
        outDataF9[j].V=outDataF9[j].V/(1.00*J[8][j]);
    }
    if (J[9][j]!=0) {
        outDataE10[j].V=outDataE10[j].V/(1.00*J[9][j]);
        outDataF10[j].V=outDataF10[j].V/(1.00*J[9][j]);
    }
}
for (j=0 ; j<(NI) ; j++)
{
    K[j]=0;
    for (i=0 ; i<10 ; i++)
    {
        if (J[i][j]!=0) K[j]++;
    }
}

```

```

for (j=0 ; j<(NI) ; j++) {
    AVE[j].R = (j+0.5)*delta;
    AVF[j].R = (j+0.5)*delta;
    if (K[j]!=0) {
        AVE[j].V=(outDataE1[j].V+outDataE2[j].V+outDataE3[j].V+outDataE4[j].V+outDataE5[j].V+
        outDataE6[j].V+outDataE7[j].V+outDataE8[j].V+outDataE9[j].V+outDataE10[j].V)/K[j];
        AVF[j].V=(outDataF1[j].V+outDataF2[j].V+outDataF3[j].V+outDataF4[j].V+outDataF5[j].V+o
        utDataF6[j].V+outDataF7[j].V+outDataF8[j].V+outDataF9[j].V+outDataF10[j].V)/K[j];
    }
    else {
        AVE[j].V=0;
        AVF[j].V=0;
    }
}
fprintf(outE, "@TYPE xy\n");
fprintf(outF, "@TYPE xy\n");
for (j=0 ; j<(NI) ; j++)
{
    if (J[0][j]!=0) {
        fprintf(outE, "%10.6le %10.6le\n", outDataE1[j].R , outDataE1[j].V);
        fprintf(outF, "%10.6le %10.6le\n", outDataF1[j].R , outDataF1[j].V);
    }
}
fprintf(outE, "&\n");
fprintf(outF, "&\n");
fprintf(outE, "@TYPE xy\n");
fprintf(outF, "@TYPE xy\n");
for (j=0 ; j<(NI) ; j++)
{
    if (J[1][j]!=0) {
        fprintf(outE, "%10.6le %10.6le\n", outDataE2[j].R , outDataE2[j].V);
        fprintf(outF, "%10.6le %10.6le\n", outDataF2[j].R , outDataF2[j].V);
    }
}
fprintf(outE, "&\n");
fprintf(outF, "&\n");

```

```

fprintf(outE, "@TYPE xy\n");
fprintf(outF, "@TYPE xy\n");
for (j=0 ; j<(NI) ; j++)
    {
        if (J[2][j]!=0) {
            fprintf(outE, "%10.6le %10.6le\n", outDataE3[j].R , outDataE3[j].V);
            fprintf(outF, "%10.6le %10.6le\n", outDataF3[j].R , outDataF3[j].V);
        }
    }
fprintf(outE, "&\n");
fprintf(outF, "&\n");
fprintf(outE, "@TYPE xy\n");
fprintf(outF, "@TYPE xy\n");
for (j=0 ; j<(NI) ; j++)
    {
        if (J[3][j]!=0) {
            fprintf(outE, "%10.6le %10.6le\n", outDataE4[j].R , outDataE4[j].V);
            fprintf(outF, "%10.6le %10.6le\n", outDataF4[j].R , outDataF4[j].V);
        }
    }
fprintf(outE, "&\n");
fprintf(outF, "&\n");
fprintf(outE, "@TYPE xy\n");
fprintf(outF, "@TYPE xy\n");
for (j=0 ; j<(NI) ; j++)
    {
        if (J[4][j]!=0) {
            fprintf(outE, "%10.6le %10.6le\n", outDataE5[j].R , outDataE5[j].V);
            fprintf(outF, "%10.6le %10.6le\n", outDataF5[j].R , outDataF5[j].V);
        }
    }
fprintf(outE, "&\n");
fprintf(outF, "&\n");
fprintf(outE, "@TYPE xy\n");
fprintf(outF, "@TYPE xy\n");
for (j=0 ; j<(NI) ; j++)

```

```

    {
        if (J[5][j]!=0) {
            fprintf(outE, "%10.6le %10.6le\n", outDataE6[j].R , outDataE6[j].V);
            fprintf(outF, "%10.6le %10.6le\n", outDataF6[j].R , outDataF6[j].V);
        }
    }
fprintf(outE, "&\n");
fprintf(outF, "&\n");
fprintf(outE, "@TYPE xy\n");
fprintf(outF, "@TYPE xy\n");
for (j=0 ; j<(NI) ; j++)
    {
        if (J[6][j]!=0) {
            fprintf(outE, "%10.6le %10.6le\n", outDataE7[j].R , outDataE7[j].V);
            fprintf(outF, "%10.6le %10.6le\n", outDataF7[j].R , outDataF7[j].V);
        }
    }
fprintf(outE, "&\n");
fprintf(outF, "&\n");
fprintf(outE, "@TYPE xy\n");
fprintf(outF, "@TYPE xy\n");
for (j=0 ; j<(NI) ; j++)
    {
        if (J[7][j]!=0) {
            fprintf(outE, "%10.6le %10.6le\n", outDataE8[j].R , outDataE8[j].V);
            fprintf(outF, "%10.6le %10.6le\n", outDataF8[j].R , outDataF8[j].V);
        }
    }
fprintf(outE, "&\n");
fprintf(outF, "&\n");
fprintf(outE, "@TYPE xy\n");
fprintf(outF, "@TYPE xy\n");
for (j=0 ; j<(NI) ; j++)
    {
        if (J[8][j]!=0) {
            fprintf(outE, "%10.6le %10.6le\n", outDataE9[j].R , outDataE9[j].V);

```

```

        fprintf(outF, "%10.6le %10.6le\n", outDataF9[j].R, outDataF9[j].V);
    }
}
fprintf(outE, "&\n");
fprintf(outF, "&\n");
fprintf(outE, "@TYPE xy\n");
fprintf(outF, "@TYPE xy\n");
for (j=0 ; j<(NI) ; j++)
{
    if (J[9][j]!=0) {
        fprintf(outE, "%10.6le %10.6le\n", outDataE10[j].R, outDataE10[j].V);
        fprintf(outF, "%10.6le %10.6le\n", outDataF10[j].R, outDataF10[j].V);
    }
}
fprintf(outE, "&\n");
fprintf(outF, "&\n");
for (j=0 ; j<(NI) ; j++) {
    if (K[j]!=0) {
        fprintf(avE, "%10.6le %10.6le\n", AVE[j].R, AVE[j].V);
        fprintf(avF, "%10.6le %10.6le\n", AVF[j].R, AVF[j].V);
    }
}
fclose(in1);
fclose(in2);
fclose(in3);
fclose(in4);
fclose(in5);
fclose(in6);
fclose(in7);
fclose(in8);
fclose(in9);
fclose(in10);
fclose(outE);
fclose(outF);
fclose(avE);
fclose(avF);

free(cart1_start);
free(cart2_start);
free(cart3_start);
free(cart4_start);
free(cart5_start);
free(cart6_start);
free(cart7_start);
free(cart8_start);
free(cart9_start);
free(cart10_start);
free(E1_start);
free(E2_start);
free(E3_start);
free(E4_start);
free(E5_start);
free(E6_start);
free(E7_start);
free(E8_start);
free(E9_start);
free(E10_start);
free(F1_start);
free(F2_start);
free(F3_start);
free(F4_start);
free(F5_start);
free(F6_start);
free(F7_start);
free(F8_start);
free(F9_start);
free(F10_start);
free(outDataF1_start);
free(outDataF2_start);
free(outDataF3_start);
free(outDataF4_start);
free(outDataF5_start);
free(outDataF6_start);

```

```
free(outDataF7_start);
free(outDataF8_start);
free(outDataF9_start);
free(outDataE10_start);
free(outDataE1_start);
free(outDataE2_start);
free(outDataE3_start);
free(outDataE4_start);
free(outDataE5_start);
free(outDataE6_start);
free(outDataE7_start);
free(outDataE8_start);
free(outDataE9_start);
free(outDataF10_start);
```

```
free(AVE_start);
free(AVF_start);
printf("%c",7);
}
double sqr(double y)
{
    y=y*y;
    return(y);
}
double twosix(double x)
{
    x=x*x*x*x*x*x;
    return(x);
}
```